



Journal of Engineering

ISSN 1726-4073



A Scientific Refereed Journal
Published by College of
Engineering University of
Baghdad

Number 0
Volume 21

May

٢٠١٥

ISSN 1726-4073

مجلة الهندسة



مجلة علمية محكمة تصدرها
كلية الهندسة - جامعة بغداد

العدد ٥

المجلد ٢١



ISSN 1726 - 4073



Journal of Engineering



**A Scientific Refereed Journal
Published by
College of Engineering
University of Baghdad**

**May
2015**

**Number 5
Volume 21**

ISSN 1726 - 4073



مجلة الهندسة



مجلة علمية محكمة تصدرها
كلية الهندسة - جامعة بغداد

العدد 5
المجلد ٢١



English Section

The text "English Section" is rendered in a bold, blue, sans-serif font with a slight 3D effect. It is positioned above a dark grey, fan-shaped base that tapers to a point at the bottom. The base consists of multiple dark grey, triangular segments that radiate from a central point at the bottom, creating a fan-like appearance. The overall design is clean and modern.

القسم العربي

Editorial Board

➤ **Chief Editor**

Prof. Dr. Najdat Nashat Abdullah

➤ **Members**

Prof. Dr. Safa N. Hamad

Prof. Dr. Thamir K. Mahmood

Prof. Dr. Ghada M.R. Razzouqi Al Siahq

Prof. Dr. Adanan Naji Jamael

Asst. Prof. Dr. Sameera M. Hamad-Allah

Asst. Prof. Dr. Zainab Ziad Ismail

Asst. Prof. Hasan Farhood Makki

Asst. Prof. Dr. Firas Mohammed Tuaimah

Asst. Prof. Dr. Nadia Adnan Shiltagh

➤ **Scientific Consultant Committee**

Prof. Dr. Saleem Mohammed Ridha Ali Taha

Prof. Dr. Saba Jabbar Neamah Al Khafaji

Prof. Dr. Yasin Khdear Salman

Prof. Dr. Ala Nasir Aljorany

Prof. Dr. Hussein Yousif Mahmood

Prof. Dr. Riyadh Zuhair Al Zubaidy

Prof. Dr. Majid Ibrahim Abdulwahab

Prof. Dr. Raad Sami Fyath

Prof. Dr. Mohammed Othman Abdul-Razaq

Prof. Dr. Abdul-Rassol Hamodi Shahab

➤ **Technical Supervision**

Rafel M. Ali

The Journal of Engineering is a monthly refereed periodical
Correspondence should be addressed to:

**THE EDITOR
JOURNAL OF ENGINEERING
COLLEGE OF ENGINEERING
UNIVERSITY OF BAGHDAD
P. O. BOX 47024 JADERIYAH
BAGHDAD – IRAQ**

مجلة الهندسة

جامعة بغداد

كلية الهندسة

هيئة التحرير

➤ رئيس التحرير:

أ.د. نجدة نشأت عبد الله

◀ الأعضاء:

◀ أ.د. صفاء نوري حمد

◀ أ.د. ثامر خضير محمود

◀ أ.د. غادة موسى رزوقي

◀ أ.د. عدنان ناجي جميل

◀ أ.م.د. سميرة محمد حمد الله

◀ أ.م.د. زينب زياد اسماعيل

◀ أ.م.د. حسن فرهود مكي

◀ أ.م.د. فراس محمد طعيمة

◀ أ.م.د. نادية عدنان شلتاغ

* الهيئة الاستشارية العلمية :

◀ أ.د. سليم محمد رضا علي طه

◀ أ.د. صبا جبار نعمة الخفاجي

◀ أ.د. ياسين خضير سلمان

◀ أ. علاء ناصر الجوراني

◀ أ.د. حسين يوسف محمود

◀ أ.د. رياض زهير الزبيدي

◀ أ.د. ماجد ابراهيم عبد الوهاب

◀ أ.د. رعد سامي فياض

◀ أ.د. محمد عثمان عبد الرزاق

◀ أ.د. عبد الرسول حمودي شهاب

◀ الأهرافض الفني:

رفل محمد علي

مجلة الهندسة: مجلة شهرية محكمة

تعنون كافة المراسلات وطلبات الاشتراك الى:

رئيس التحرير
مجلة الهندسة
كلية الهندسة
صندوق بريد ٤٧٠٢٤ الجادرية
بغداد - العراق

List of Contents

English Section:	Page
A Real-Coded Genetic Algorithm with System Reduction and Restoration for Rapid and Reliable Power Flow Solution of Power Systems	1 - 19
<i>Asst. Prof. Dr. Hassan Abdullah Kubba Alaa Suheib Rodhan</i>	
Non-Conventional Material to Remove Cu⁺² Ions from Aqueous Solutions using Chemical Coagulation	20 – 34
<i>Muna Yousif Abdul. Ahad Samer Jalil Ibrahim</i>	
Brackish Water Desalination Coupled with Wastewater Treatment and Electricity Generation	35 – 44
<i>Dr. Zainab Ziad Ismail Mohammed Abdulkhaleq Ibrahim</i>	
Resistance to Moisture Damage of Recycled Asphalt Concrete Pavement	45 – 54
<i>Prof. Saad Issa Sarsam Israa Lutfi AL-Zubaidi</i>	
Experimental Study of the Thermal Performance of Flat Plate Solar Collectors Array by Different Connection Configurations	55 – 71
<i>Dr. Jafar Mehdi Hassan Dr. Qussai Jihad Abdul-Ghafour Mohammed Fowzi Mohammed</i>	
Strength Improvement of Clay Soil by using Stone Powder	72 – 84
<i>Ahmed Sameer Abdulrasool</i>	
On Gradient Descent Localization in 3-D Wireless Sensor Networks	85 – 97
<i>Prof. Nuha Abdul Sahib Alwan Alaa Shakir Mahmood</i>	
Cooling Load Calculations For Typical Iraqi Roof and Wall Constructions using Ashrae's RTS Method	98– 114
<i>Khalid Ahmed Joudi Ali Naser Hussien</i>	
Using Spatial Videos, Google Earth[™] and Geographic Information System to Dynamically Monitor Built Environment Changes in a Challenging Environment: Baghdad, Iraq.	115-130

Husham AbdMunaf Atta
Andrew Curtis



A Real-Coded Genetic Algorithm with System Reduction and Restoration for Rapid and Reliable Power Flow Solution of Power Systems

Asst. Prof. Dr. Hassan Abdullah Kubba
Department of Electrical Engineering
College of Engineering/ University of Baghdad
E-mail: hassankubba@yahoo.com

Alaa Suheib Rodhan
M.Sc. Electrical Engineering
College of Engineering/ University of Baghdad
E-mail: alaa.rodhan@gmail.com

ABSTRACT

The paper presents a highly accurate power flow solution, reducing the possibility of ending at local minima, by using Real-Coded Genetic Algorithm (RCGA) with system reduction and restoration. The proposed method (RCGA) is modified to reduce the total computing time by reducing the system in size to that of the generator buses, which, for any realistic system, will be smaller in number, and the load buses are eliminated. Then solving the power flow problem for the generator buses only by real-coded GA to calculate the voltage phase angles, whereas the voltage magnitudes are specified resulted in reduced computation time for the solution. Then the system is restored by calculating the voltages of the load buses in terms of the calculated voltages of the generator buses, after a derivation of equations for calculating the voltages of the load busbars. The proposed method was demonstrated on 14-bus IEEE test systems and the practical system 362-busbar IRAQI NATIONAL GRID (ING). The proposed method has reliable convergence, a highly accurate solution and less computing time for on-line applications. The method can conveniently be applied for on-line analysis and planning studies of large power systems.

Keywords: load flow analysis, load modeling, power system modeling, real coded genetic algorithms, simulation, voltage measurement

الحل السريع والموثوق لسريان الحمل الكهربائي باستخدام الخوارزمية الجينية ذات التشفير الحقيقي مع اختزال الشبكة وأعادتها

علاء سحيب روضان
قسم الهندسة الكهربائية
كلية الهندسة/جامعة بغداد

أ.م. د. حسن عبدالله كية
قسم الهندسة الكهربائية
كلية الهندسة/جامعة بغداد

الخلاصة

يقدم البحث طريقة عالية الدقة لحساب سريان الحمل الكهربائي و تقليل احتمالية الانتهاء في الحدود الدنيا المحلية باستخدام الخوارزمية الجينية ذات التشفير الحقيقي مع اختزال الشبكة وأعادتها وتم تطوير الطريقة المقترحة (الخوارزمية الجينية ذات التشفير الحقيقي) لتقليل زمن الحساب الكلي بتقليل حجم النظام الى عدد محطات التوليد فقط، بعد اختزال عدد محطات الأحمال في النظام الحقيقي أو الواقعي لتقليل الزمن اللازم للحساب ، ومن ثم يتم حساب زاوية طور الفولتية بعد تحديد مقدار الفولتية لكل محطة توليد باستخدام الخوارزمية الجينية ذات التشفير الحقيقي ، بعد ذلك يتم إعادة تمثيل النظام ككل وحساب مقدار وزاوية طور الفولتية لكل محطات الأحمال باستخدام النتائج المستحصلة لمقدار وزاوية طور الفولتية لكل محطات التوليد بعد اشتقاق المعادلات المطلوبة لحساب مقدار وزاوية طور فولتية لكل محطات الأحمال بصيغة مقدار وزاوية فولتية محطات التوليد ، الطريقة المقترحة تم تطبيقها للعمل على الشبكة الوطنية العراقية الطريقة المقترحة عالية الدقة، موثوقة والزمن اللازم للوصول الى الحل قليل وكذلك ممكن تطبيقها في دراسات التحليل والتخطيط للأنظمة الكهربائية كبيرة الحجم وأثناء اشتغال المنظومة .

الكلمات الرئيسية: تحليل تدفق الحمل ، تمثيل الحمل ، تمثيل نظام القدرة الكهربائية ، الخوارزمية الجينية ذات التمثيل الحقيقي ، المحاكاة ، وحساب الفولتية.



1. INTRODUCTION

The power flow problem, which is to determine the power system static states (voltage magnitudes and voltage phase angles) at each busbar to find the steady state operating condition of a system, is very important and the most frequently carried out study by electrical power utilities for power system on-line operation, planning and control. The mathematical formulation of the electrical power flow problem results in a set of non-linear algebraic equations. The optimization numerical methods such as Newton-Raphson method or the artificial intelligence methods such as Genetic Algorithm (GA) are applied to solve the power flow problem. The power flow problem has multiple solutions, **Kubba, 1991**. The numerical methods and some of the artificial intelligence methods suffer from the local minima problem. Also there are many criteria which should be taken into consideration such as the speed of solution, storage requirement and the degree of solution accuracy. With increasing computer speeds, researchers are increasingly applying artificial and computational intelligence techniques, especially in power system problems. These methods offer several advantages over traditional numerical methods. Among these techniques is that of *genetic algorithm*. Genetic algorithms (GAs) are efficient stochastic search techniques that emulate natural phenomena. They have been used successfully to solve a wide range of optimization problems. Because of existence of local minima, these algorithms offer promise in solving large-scale problems. A genetic algorithm mimics *Darwin's evolution process* by implementing "*survival of the fittest*" strategy. Genetic algorithm solves linear and nonlinear problems by exploring all regions of the search space and exponentially exploiting promising areas through *selection, crossover, and mutation* operations. They have been proven to be an effective and flexible optimization tool that can find optimal or near-optimal solutions, **Wong, et al., 1999**. In this study, an improved genetic algorithm solution of the load flow problem is presented in order to minimize the total *active and reactive power mismatches* of the given systems, a *real-coded* genetic algorithm has been implemented. The proposed method has been demonstrated on a typical test system, and was used to solve the Iraqi National Grid load flow problem.

2. THE REAL-CODED (CONTINUOUS) GENETIC ALGORITHM (RCGA)

The binary genetic algorithm is conceived to solve many optimization problems that stump traditional techniques. But, the attempting to solve a problem where the values of the variables are continuous and want to define them to the full machine precision. In such a problem, each variable requires many bits to represent it. If the number of variables is large, the size of the chromosome is also large. In principle, any conceivable representation could be used for encoding the variables. When the variables are naturally quantized, the binary genetic algorithm fits nicely. However, when the variables are continuous, it is more logical to represent them by *floating-point numbers, i.e., real number*. In addition, since the binary genetic algorithm has its precision limited by the binary representation of variables, using floating-point numbers instead easily allows representation to the machine precision. This continuous genetic algorithm also has the advantage of requiring less storage than the binary genetic algorithm because a single floating-point number represents the variable instead of N_{bits} integers. The continuous genetic algorithm is inherently faster than the binary genetic algorithm, because the chromosomes do not have to be decoded prior to the evaluation of the *cost function (objective function)*, **Ippolito, et al., 2006**. Since the continuous GA is implemented using floating point numbers, i.e., real numbers we have called this as Real-Coded GA (RCGA).

3. MATHEMATICAL DESCRIPTION AND COMPONENTS OF A CONTINUOUS GENETIC ALGORITHM (RCGA)

The real-coded genetic algorithm is very similar to the binary genetic algorithm, but the primary difference is the fact that variables are no longer represented by bits of zeros and ones, but instead by floating-point real numbers over whatever range is deemed appropriate. However, this simple fact adds some nuances to the application technique that must be carefully considered. In particular, we will present the RCGA operators, which are used in this research.

3.1 The Variables and Cost Function

A cost function generates an output from a set of input variables (a chromosome). The cost function may be a mathematical function, or from experiment. The objective is to modify the output in some desirable fashion by finding the appropriate values for the input variables. The goal is to solve some optimization problem where we search for an optimum (minimum) solution in terms of the variables of the problem. The term fitness is extensively used to designate the output of the *objective function* in the genetic algorithm literature. Fitness implies a maximization problem. Fitness has a closer association with biology than the term cost, and thus we have adopted the term cost, since most of the optimization literature deals with minimization, hence cost. They are equivalent. If the chromosome has N_{var} variables (a 2N-dimensional optimization problem) given by $(b_1, b_2, \dots, b_{N_{var}})$ where N is the number of buses, then the chromosome is written as an array with $(1 \times N_{var})$ elements so that:

$$chromosome = [b_1, b_2, b_3, \dots, b_{N_{var}}] \quad (1)$$

In power flow problem, the chromosome is written in terms of the voltages magnitudes and voltages phase angles variables of all the buses as follows:

$$chromosome = [V_1, V_2, \dots, V_N, \theta_1, \theta_2, \dots, \theta_N] \quad (1.1)$$

In this case, the variable values are represented as floating-point numbers. Each chromosome has a cost found by evaluating the cost function (f) at the variables $(V_1, V_2, \dots, V_N, \theta_1, \theta_2, \dots, \theta_N)$.

$$cost = f(chromosome) = f(b_1, b_2, \dots, b_{N_{var}}) \quad (2)$$

Equations (1) and (2) along with applicable constraints constitute the problem to be solved. Our primary problem in this research is the continuous functions introduced below. The two cost functions are:

$$\Delta P_i = P_i^{sp} - V_i \sum_{k=1}^N V_k (G_{ik} \cos \theta_{ik} + B_{ik} \sin \theta_{ik}) \quad (3)$$

Where P_i^{sp} is the specified active power at bus i, eqn.3 is for "PV" (generator buses), and "PQ" (load buses),

$$\Delta Q_i = Q_i^{sp} - V_i \sum_{k=1}^N V_k (G_{ik} \sin \theta_{ik} - B_{ik} \cos \theta_{ik}) \quad (4)$$

Where Q_i^{sp} is the specified reactive power at bus i, eqn.4 is for PQ buses only, Where $\theta_{ik} = \theta_i - \theta_k$ and, (ΔP_i) is the mismatch active power at bus (i) and (ΔQ_i) is the mismatch reactive power at bus (i). $(V_i, V_k, \theta_i, \theta_k)$ are the voltage magnitude and angle at buses (i) and (k) respectively, which are the variables of the two cost functions and (N) is the number of buses, **Kubba, 2008**.

3.2 Variable Encoding, Precision, and Bounds

Here, the difference between binary and continuous genetic algorithms is shown. It is no longer needed to consider how many bits are necessary to represent accurately a value. Instead, (V) and (θ) have continuous values that are limited between appropriate bounds which are in our problem,

$0.9 \leq V \leq 1.1$ and $-20 \leq \theta \leq 20$. Since the genetic algorithm is a search technique, it must be limited to exploring a reasonable region of variable space. Sometimes, this is done by imposing a constraint on the problem. If one does not know the initial search region, there must be enough diversity in the initial population to explore a reasonably sized variable space before focusing on the most promising regions.

3.3 Initial Population

The genetic algorithm starts with a group of chromosomes known as the *population*. A matrix represents the population with each row in the matrix being a $(1 \times N_{\text{var}})$ array (chromosome) of continuous values. Given an initial population of N_{ind} chromosomes, the full matrix of $(N_{\text{ind}} \times N_{\text{var}})$ random values is generated. All variables are normalized to have values between 0 and 1, the range of a uniform random number generator. The values of a variable are “unnormalized” in the cost function. If the range of values is between b_{lo} and b_{hi} , then the unnormalized values are given by:

$$b = (b_{\text{hi}} - b_{\text{lo}})b_{\text{norm}} + b_{\text{lo}} \quad (5)$$

where, b_{hi} is highest number in the variable range, b_{lo} is lowest number in the variable range, and b_{norm} is normalized value of variable. This society of chromosomes is not a democracy; the individual chromosomes are not all created equal. Each one's worth is assessed by the cost function. So at this point, the chromosomes are passed to the cost function for evaluation. In this research, we had used a population size (initial population) of 20 individuals (chromosomes) for 14-bus IEEE system power flow solution and 500 individuals for 362-bus Iraqi National Grid (ING) power flow solution which depends on the number of variables for each system. These population sizes are kept constant throughout the whole solution process.

3.4 Natural Selection

Survival of the fittest translates into discarding the chromosomes with the higher costs. First, the N_{ind} costs and associated chromosomes are ranked from lowest cost to highest cost. Then, only the best are selected to continue, while the rest are deleted. The selection rate, X_{rate} , is the fraction of N_{ind} that survives for the next step of mating. The number of chromosomes that are kept each generation is:

$$N_{\text{keep}} = X_{\text{rate}} \cdot N_{\text{ind}} \quad (6)$$

Natural selection occurs each generation or iteration of the algorithm. Of the N_{ind} chromosomes, only the top N_{keep} survive for mating, and the bottom $(N_{\text{ind}} - N_{\text{keep}})$ are discarded to make room for the new offspring. Deciding how many chromosomes to keep is somewhat arbitrary. Letting only a few chromosomes survive to the next generation limits the available genes in the offspring. Keeping too many chromosomes allows bad performers a chance to contribute their traits to the next generation. We use 50% ($X_{\text{rate}}=0.5$) in the natural selection process. Another approach to natural selection is called *thresholding* (Truncation Selection) is used in this research. In this approach, all chromosomes that have a cost function lower than some truncation threshold survive. The threshold must allow some chromosomes to continue in order to have parents to produce offspring. Otherwise, a whole new population must be generated to find some chromosomes that pass the test. At first, only a few chromosomes may survive. In later generations, however, most of the chromosomes will survive unless the threshold is changed. An attractive feature of this technique is that the population does not have to be sorted.

3.5 Selection

In this process, two chromosomes are selected from the mating pool of N_{keep} chromosomes to produce two new offspring. Pairing takes place in the mating population until $(N_{ind} - N_{keep})$ offspring are born to replace the discarded chromosomes. Pairing chromosomes in a genetic algorithm can be as interesting and varied as pairing in an animal species. Two types of selection are used in this research, which are:

3.5.1. Rank-weighted roulette wheel: This approach uses a uniform random number generator to select chromosomes. The row numbers of the parents are found using:

$$ma = \text{ceil}(N_{keep} * \text{rand}(1, N_{keep}/2))$$
$$pa = \text{ceil}(N_{keep} * \text{rand}(1, N_{keep}/2)),$$

Where *ceil* rounds the value to the next highest integer and *rand* generates arrays of random numbers whose elements are uniformly distributed in the interval (0, 1). This approach is problem independent and finds the probability from the rank of the chromosome. Rank weighting is slightly more difficult to program than the other selection types. Small populations have a high probability of selecting the same chromosome. The probabilities only have to be calculated once. We tend to use rank weighting because the probabilities do not change each generation. This approach of selection had been used in 14-bus IEEE-system.

3.5.2. Tournament selection: Another approach that closely mimics mating competition in nature is to randomly pick a small subset of chromosomes (two or three) from the mating pool, and the chromosome with the lowest cost in this subset becomes a parent. The typical value accepted by many applications is $k=2$ (so-called tournament size). The tournament repeats for every parent needed. Thresholding and tournament selection make a nice pair, because the population never needs to be sorted. Tournament selection works best for large population sizes because sorting becomes time-consuming for large populations. Each of the parent selection schemes results in a different set of parents. As such, the composition of the next generation is different for each selection scheme. Rank-weighted Roulette-wheel and tournament selection are standard for most genetic algorithms. It is very difficult to give advice on which selection scheme works best. In our problem, we follow the *roulette-wheel* and *tournament* parent selection procedures for 14-bus IEEE-system and 362-bus ING respectively, **Younes and Rahli, 2006**.

3.6 Crossover (Recombination)

As for the binary algorithm, two parents are chosen, and the offspring are some combination of these parents. Many different approaches have been tried for crossing over in continuous genetic algorithm. The simplest methods choose one or more points in the chromosome to mark as the *crossover points*. Then the variables between these points are merely swapped between the two parents. For example, consider the two parents to be:

$$\text{parent 1} = [b_{m1}, b_{m2}, b_{m3}, b_{m4}, b_{m5}, b_{m6}, \dots, b_{mNvar}]$$
$$\text{parent 2} = [b_{d1}, b_{d2}, b_{d3}, b_{d4}, b_{d5}, b_{d6}, \dots, b_{dNvar}]$$

Crossover points are randomly selected (at points (3, 4)), and then the variables in between are exchanged:

$$\text{offspring 1} = [b_{m1}, b_{m2}, b_{d3}, b_{d4}, b_{m5}, b_{m6}, \dots, b_{mNvar}]$$
$$\text{offspring 2} = [b_{d1}, b_{d2}, b_{m3}, b_{m4}, b_{d5}, b_{d6}, \dots, b_{dNvar}]$$

The extreme case is selecting N_{var} points and randomly choosing which of the two parents will contribute its variable at each position. Thus, one goes down the line of the chromosomes and, at each variable, randomly chooses whether or not to swap information between the two parents. This method is called *uniform crossover*:

$$\begin{aligned} \text{offspring } 1 &= [b_{m1}, b_{d2}, b_{m3}, b_{m4}, b_{d5}, b_{m6}, \dots, b_{dNvar}] \\ \text{offspring } 2 &= [b_{d1}, b_{m2}, b_{d3}, b_{d4}, b_{m5}, b_{d6}, \dots, b_{mNvar}] \end{aligned}$$

The problem with these point crossover methods is that no new information is introduced; each continuous value that was randomly initiated in the initial population is propagated to the next generation, only in different combinations. Although this strategy works fine for binary representations, there is now a continuum of values, and in this continuum we are merely interchanging two data points. These approaches totally rely on mutation to introduce new genetic material. The blending methods remedy this problem by finding ways to combine variable values from the two parents into new variable values in the offspring. A single offspring variable value b_{new} comes from a combination of the two corresponding parent's variable values:

$$b_{new} = \beta b_{mn} + (1 - \beta) b_{dn} \quad (7)$$

Where, β is a random number on the interval $[0,1]$, $b_{mn} = n^{\text{th}}$ variable in the mother chromosome, $b_{dn} = n^{\text{th}}$ variable in the father chromosome.

The same variable of the second offspring is merely the complement of the first (*i.e.* replacing β by $1 - \beta$). If $\beta = 1$, then b_{mn} propagates in it's entirely and b_{dn} dies. In contrast, if $\beta = 0$, then b_{dn} propagates in it's entirely and b_{mn} dies. When $\beta = 0.5$, the result is an average of the variables of the two parents. This method has been demonstrated to work well on several interesting problems. Choosing which variables to blend is the next issue. Sometimes, this linear combination process is done for all variables to the right or to the left of some crossover point, **Woon, 2004**. Any number of points can be chosen to blend, up to N_{var} values where all variables are linear combinations of those of the two parents. The variables can be blended by using the same β for each variable or by choosing different β 's for each variable. These blending methods effectively combine the information from the two parents and choose values of the variables between the values bracketed by the parents; however, they do not allow introduction of values beyond the extremes already represented in the population. Of course, the factor (0.5) is not the only one that can be used in such a method. Heuristic crossover is a variation where some random number β is chosen on the interval $[0, 1]$ and the variables of the offspring are defined by:

$$b_{new} = \beta(b_{mn} - b_{dn}) + b_{dn} \quad (8)$$

Variations on this theme include choosing any number of variables to modify and generating different β for each variable. This method also allows generation of offspring outside of the values of the two parent variables. Sometimes, values are generated outside of the allowed range. If this happens, the offspring is discarded and the algorithm tries another β . In our problem, we want to find a way to closely mimic the advantages of the binary genetic algorithm scheme. It begins by randomly selecting a variable c in the first pair of parents to be the crossover point, **Yin, 1993**.

$$c = \text{round up } \{ \text{random} * N_{var} \} \quad (9)$$

Where, (round up) is rounding mode that rounds to the nearest allowable quantized value. We'll let: parent 1 = $[b_{m1}, b_{m2}, \dots, b_{mc}, \dots, b_{mNvar}]$ parent 2 = $[b_{d1}, b_{d2}, \dots, b_{dc}, \dots, b_{dNvar}]$, Where (m) and (d) subscripts discriminate between the *mom* and *dad* parent. Then, the selected variables are combined to form new variables that will appear in the children:

$$\begin{aligned} b_{new1} &= b_{mc} - \beta (b_{mc} - b_{dc}) \\ b_{new2} &= b_{dc} + \beta (b_{mc} - b_{dc}) \end{aligned}$$

Where, β is also a random value between 0 and 1. The final step is to complete the crossover with the rest of the chromosome as in binary genetic algorithm:

$$\begin{aligned} \text{offspring } 1 &= [b_{m1}, b_{m2}, \dots, b_{new1}, \dots, b_{dNvar}] \\ \text{offspring } 2 &= [b_{d1}, b_{d2}, \dots, b_{new2}, \dots, b_{mNvar}] \end{aligned}$$

If the first variable of the chromosomes is selected, then only the variables to the right of the selected variable are swapped. If the last variable of the chromosomes is selected, then only the variables to the left of the selected variable are swapped. This method does not allow offspring variables outside the bounds set by the parent unless $\beta > 1$, **Younes and Rahli, 2006 and Jain, and Martin1, 1998.**

3.7 Mutation

Random mutations alter a certain percentage of the genes in the list of chromosomes. If care is not taken, the genetic algorithm can converge too quickly into one region of the *cost surface*. If this area is in the region of the *global minimum*, that is good. However, some functions, such as the one we are modeling, have many *local minima*. If nothing is done to solve this tendency to converge quickly, it may end up in a local rather than a global minimum. To avoid this problem of overly fast convergence (premature convergence), the routine is forced to explore other areas of the cost surface by randomly introducing changes, or mutations, in some of the variables. Mutation points are randomly selected from the $(N_{ind} \times N_{var})$, total number of genes in the population matrix.

Increasing the number of mutations increases the algorithm's freedom to search outside the current region of variable space. It also tends to distract the algorithm from converging on a popular solution. With the process of the crossover and mutation taking place, there is a high chance that the optimum solution could be lost as there is no guarantee that these operators will preserve the fittest string. To counteract this, *elitist* models are often used. In an elitist model, the best individual in the population is saved before any of these operations take place. After the new population is formed and evaluated, it is examined to see if this best structure has been preserved. If not, the saved copy is reinserted back into the population. The genetic algorithm then continues on as normal, **Ibrahim, 2005 and Vasconcelos, et al., 2002.**

4. PROPOSED TECHNIQUE

In the proposed method the load busbars are eliminated, retaining only generator busbars for the iterative process. The system equations in terms of generator busbars and load busbars can be written as:

$$\begin{bmatrix} I_G \\ I_L \end{bmatrix} = \begin{bmatrix} Y_{11} & Y_{12} \\ Y_{21} & Y_{22} \end{bmatrix} \begin{bmatrix} V_G \\ V_L \end{bmatrix} \quad (10)$$

If the voltage of the K^{th} load busbar is initially assumed to be $V_{Lk=1.0} \angle 0^\circ$. Then the current in the busbar to the load is:

$$I_{Lk} = \frac{P_{Lk} - jQ_{Lk}}{V^*_{Lk}} \quad (11)$$

From the second row of Eq.(10), we have

$$V_L = -Y_{22}^{-1} Y_{21} V_G + Y_{22}^{-1} I_L \quad (12)$$

Substituting Eq. (12) in the first row of Eq. (10), we get

$$I_G = Y_{11} V_G + Y_{12} (-Y_{22}^{-1} Y_{21} V_G + Y_{22}^{-1} I_L) \quad (13)$$

The above equation is written as

$$I_G = Y_{GG} V_G + Y_{GL} I_L \quad (14)$$

$$\text{Where: } Y_{GG} = Y_{11} - Y_{12} Y_{22}^{-1} Y_{21} \quad \text{and} \quad Y_{GL} = Y_{12} Y_{22}^{-1} \quad (15)$$

From Eq.(14), the i^{th} generator busbar is:

$$I_i = \sum_{k=1}^m Y_{ik} V_k + a_i, \quad \text{for } i=1,2,\dots,m. \quad (16)$$

Where a_i is the i^{th} element of the column vector A given by

$$A = Y_{GL} I_L \quad (17)$$

The complex power at the busbar is

$$S_i = V_i^* I_i = V_i^* \sum_{k=1}^m Y_{ik} V_k + V_i^* a_i \quad (18)$$

for $i=1,2,\dots,m$.

The real power injection at the busbar is

$$P_i = \text{Re } S_i = \sum_{k=1}^m e_i (e_k G_{ik} - f_k B_{ik}) + \sum_{k=1}^m f_i (e_k B_{ik} + f_k G_{ik}) + L_i \quad (19)$$

for $i=1,2,\dots,m$.

$$\text{Where } L_i = e_i c_i + f_i d_i \quad (20)$$

(L_i) can be considered as an equivalent local load at generator busbar i due to elimination of the load busbars, **Mithulanathan, et al., 2004**.

5. COMPUTER ALGORITHM OF THE PROPOSED METHOD

The computer algorithm for the proposed method is as follows:

1. Read the lines data and form the nodal admittance matrix.
2. Read the busbars data, such as the specified active power, voltage magnitude of the generator buses, specified active and reactive power of the load buses, slack bus voltage, and initial estimate of the voltage of the load buses, assuming (1.0 p.u., 0.1 MW/MVAr)

3. Eliminate the load busbars and reduce the network to the size of that of the generators busbars.
4. Compute (I_L) using Eq. (11) for all load buses, form the column vector (A) given by Eq. (17), then form (L_i) assuming (e_i) equal to the specified values, and (f_i) initially is zero.
5. Execute the Real-Coded Genetic Algorithm on the generator buses only to find the most recent value of the voltages, implementing all the GA operators such as Selection with Rank-Weighting Roulette Wheel, Tournament selection with truncation threshold, Single-point Crossover with blending method, and Mutation (rate of Mutation=0.2), we use initial population of 20 chromosomes for 14-bus IEEE system and 500 chromosomes for Iraqi National Grid (ING) system. At each generation (iteration) of the GA, we calculate the most recent values of (V_L) from Eq. (12), (I_L) from Eq. (11) and (L_i) , then calculate (P_i) from Eq. (19).
6. Convergence Test: The mismatch active powers for the generator buses (cost function) are calculated at each GA generation (iteration) according to the following equation:

$$\Delta P_i = P_i^{sp} - P_i^{cal}, \text{ for } i=1,2,\dots,m. \quad (21)$$

When the mismatch active powers (cost function) for all generator buses except the slack bus are less than a small tolerance value (usually 0.001), 0.1MW/MVAR then the solution has converged.

7. Restore the system and calculate the load busbars voltages using Eq. (12).
8. Print results and end.

6. IMPLEMENTATIONS AND RESULTS

Two test systems were used to demonstrate the performance of the proposed method, namely:
1. 14 busbars IEEE International test system, the lines and buses data are present in, **Kubba, 1991**. The "14- bus" test system consists of: 1 slack bus, 4 generator buses (PV) and 9 load buses(PQ).
2. The Iraqi National Grid (ING) which consists 362 busbars, 1 slack bus, 29 generator buses (PV) and 332 load buses (PQ) , **Al-Bakri, 1994**.

The load flow solution using real-coded genetic algorithm programs with and without the method of Reduction and Restoration have been developed by the use of MATLAB version 7, and tested with a Pentium 4, 3GHz (Cache 2M) PC with 2GB RAM. **Table 1**, illustrates the power flow solution for a 14-bus IEEE test system using conventional RCGA with two objective functions, which are the mismatch active and reactive powers at each bus according to its constraints except the slack bus. The sum of weighted cost multi-objective functions is used. The most straightforward approach to multi-objective optimization is to weight each function and add them together, **Abido, 2003**.

$$cost = \sum_{i=1}^h w_i f_i \quad (22)$$

Where f_i is the cost function (i), w_i is the weighting factor, h is the number of objective functions, and

$$\sum_{i=1}^h w_i = 1. \quad (23)$$

Implementing this multiple objective optimization approach in a real-coded genetic algorithm only requires modifying the cost function to fit the form of Eq. (22) and does not require any modification to the genetic algorithm. Thus, Eq. (22) becomes:

$$cost = w f_1 + (1-w) f_2 \quad (24)$$

Where f_1 and f_2 are the mismatch active and reactive powers respectively, and have the same rank of importance. This approach is adopted in this research for its simplicity, easy of programming and gives us the required accuracy. Here, (w) is chosen to be (0.5), **Ricciari and Falcao, 1999**.

Because of the stochastic nature of the genetic algorithm process, each independent run will probably produce a different number of generations and consequently the computation time and the best amongst these should be chosen. The best of the 10 implementations runs are shown in the tables. The total computation time was 7.156 sec. **Table 2**, illustrates the power flow solution of the same IEEE test system using RCGA with the method of system Reduction and Restoration (Proposed Method). Since, we only retain the generator buses for the GA process, so a single objective function (mismatch active power) is needed. The total computation time for the whole load flow solution was 0.18 second. The power flow solution results for the Iraqi National Grid (362-bus) by using RCGA with the method of system reduction and restoration were tabulated in **Tables (3) and (4)**. Since the proposed method (RCGA with system Reduction and Restoration) implements the complete cycles of the genetic algorithm on the generator busbars only which are the first thirty buses of the system, then **Table 3**, shows the results and number of generations for each generator busbar and the power flow solution for the total Iraqi National Grid are presented. **Table 4**, shows the voltages of load buses which are calculated after restoring the system, also the mismatch active and reactive powers of load buses are presented. The total computation time with conventional RCGA method was more than 72 hours, while the total computation time for the proposed method was 519 seconds for the whole load flow solution of 362-bus ING with the same accuracy. A ranked-weighted roulette wheel and Tournament selection process were used for 14-bus IEEE and ING respectively. **Fig.1** shows the evaluation process of the genetic algorithm for bus 2 of 14-bus IEEE system, the dotted curve represents the minimum cost of the solution (chromosome) which is converged with 15 generations and the solid curve represents the average value of the costs amongst generations versus the number of generations.

7. CONCLUSIONS

The proposed method which had presented in this paper is very much faster than the simple real-coded genetic algorithm, since the system is reduced to the size of that of the generator busbars which for any realistic system is small as we see for the 362-bus Iraqi National Grid, only 30 buses are generator busbars. We must take into consideration that the main drawback of the genetic algorithm is the large computation time. So, this contribution is especially for GA as an optimization technique. The objective function (cost function) for the generator buses is only the mismatch active power, so that multi-objective function techniques are not needed. Thus, it can be concluded that the proposed method is suitable for on-line implementation for small and medium-scale power systems and it can be used for planning study for large-scale systems. The proposed method has reliable convergence and high accuracy of solution. Whereas the traditional numerical techniques (Gauss-Seidel, Newton-Raphson, Fast decoupled,...etc.) use the characteristics of the problem to determine the next sampling point (*e.g.* gradient, linearity and continuity), genetic algorithm makes no such assumptions. Instead, the next sampled point is determined based on stochastic sampling or decision rules rather than on a set of deterministic decision rules. Genetic algorithms with the method of system reduction and restoration have been used to solve difficult problems with objective functions that possess properties such as *continuity*, *differentiability* and so forth. Also, whereas the traditional numerical techniques mentioned above use single point at a time to search the problem space, genetic algorithm uses a population of candidate solutions for solving the problem, thus reducing the possibility of ending at a local minima.



8. REFERENCES

- Al-Bakri, 1994, *A Study of Some Problems on the IRAQI NATION AL GRID and Establishing a Method Algorithm for Load Flow*, M.Sc Thesis , University of Baghdad,.
- Kubba, H. A., Hassan, A. S. and T. Krishnaparandhama, 1991, *Comparative Study of Different Load Flow Solution Methods*, Al-Muhandis, Referred Scientific Journal of Iraqi Engineers Society, Vol. 107, pp. 25-46.
- Kubba, H. A. 2009, *An Efficient and more Reliable Second Order Load Flow Solution Method*, Journal of Association for the Advancement of Modeling & Simulation Techniques in Enterprises.
- Kubba, H. A., Omar R, and Soltani j., 2008, *A Multi-Objective Genetic Algorithm for a Rapid and Efficient Load Flow Solution for Electrical Power Systems*. Proceedings of the international conference on modelling and simulation, Petra, Jordan; 18– 20 Nov., p.14–9.
- Yang, H. T., Yang, P.C. and Huang, C. L.1997, *A Parallel Genetic Algorithm Approach to Solving the Unit Commitment Problem: Implementation on the Transporter Networks," IEEE Transactions on Power Systems*, Vol. 12, No. 2, pp. 661-668.
- Vasconcelos, J. A., Adriano, R. L. , Vieira, D. A. G., Souza,G. F. D. and Azevedo,H. S., 2002 *NSGA with Elitism Applied to Solve Multi-Objective Optimization Problems*, Journal of Microwaves and Optoelectronics, Vol. 2 No. 6, pp. 59-69.
- Wong, K. P., Li, A. and Law, T. M., 1999, *Advanced Constrained Genetic Algorithm Load Flow Method*, presented in IEEE Proceedings on generator, transmission, distribution, Vol. 146, No. 6.
- Woon, L. C., 2004, *Genetic Algorithm for Load Flow Solution Techniques*, Master of engineering (electrical), Universiti Teknologi Malaysia, <http://www.sps.utm>.
- Ippolito, L. A., Cortiglia, La and Petrocelli, M., 2006, *Optimal Allocation of Facts Devices by Using Multi-Objective Optimal Power Flow and Genetic Algorithms*, International journal of emerging electric power systems, Vol. 7, No. 2, pp. 1-19.
- Jain, L. C., and Martin, N. M. 1998, *Fusion of Neural Networks, Fuzzy Systems and Genetic Algorithms: Industrial Applications*, CRC Press, CRC Press LLC.
- Younes, M.and Rahli, M., 2006, *On the Choice Genetic Parameter with Taguchi Method Applied in Economic Power Dispatch*, Leonardo Journal of Sciences, issue 9, pp. 9-24.
- Abido, M. A., 2003, *Environmental/Economic Power Dispatch using Multi- Objective Evolutionary Algorithms*, IEEE Trans. Power Syst., Vol. 18, No. 4, pp.1529–1537 .
- Mithulananthan N. O., Than, and Le Van Phu. 2004, *Distributed Generator Placement in Power Distribution System Using Genetic Algorithm to Reduce Losses*, Thammasat Int. J. Sc. Tech., Vol. 9, No. 3, pp. 55- 62.



- Riccieri, O. F. and Falcao D. M. 1999, *Meter Placement Method for State Estimation using Genetic Algorithms*, Intelligent System Application to Power Systems (ISPA), Rio de Janeiro, Brazil, pp. 360-364.
- Ibrahim S. B. M., 2005, *The PID Controller Design Using Genetic Algorithm*, A dissertation submit ted to University of Southern Queensland, Faculty of engineering and surveying, Electrical and Electronics Engineering.
- Bouktir, T. L. Slimani, and Belkacemi, M. A. 2004, *Genetic Algorithm for Solving the Optimal Power Flow Problem*, Leonardo journal of sciences, pp. 44-58.
- Yin, X, 1993, *Application of Genetic Algorithm to Multiple Load Flow Solution Problem in Electrical Power Systems*, presented in IEEE Proceedings of the 32nd conference on decision and control, San Antonio, Texas.

NOMENCLATURE

N = number of busbars in the system.

m = number of generator busbar in the system.

V_G = M -dimensional vector of voltages of generator busbars.

I_G = M -dimensional vector of currents of generator busbars.

V_L = $(N-M)$ dimensional vector of voltages of load busbars.

I_L = $(N-M)$ dimensional vector of currents of load busbars.

Y = admittance matrix of order $N \times N$.

$Y_{11}, Y_{12}, Y_{21}, Y_{22}$ = sub-matrices of Y of appropriate order.

V_k^* = conjugate of k^{th} busbar voltage V_k .

e_k, f_k = inphase and quadrature components of V_k .

c_i, d_i = real and imaginary parts of a_i .

sp = specified value.

cal = calculated.

G_{ik}, B_{ik} = real and imaginary parts of the admittance Y_{ik}

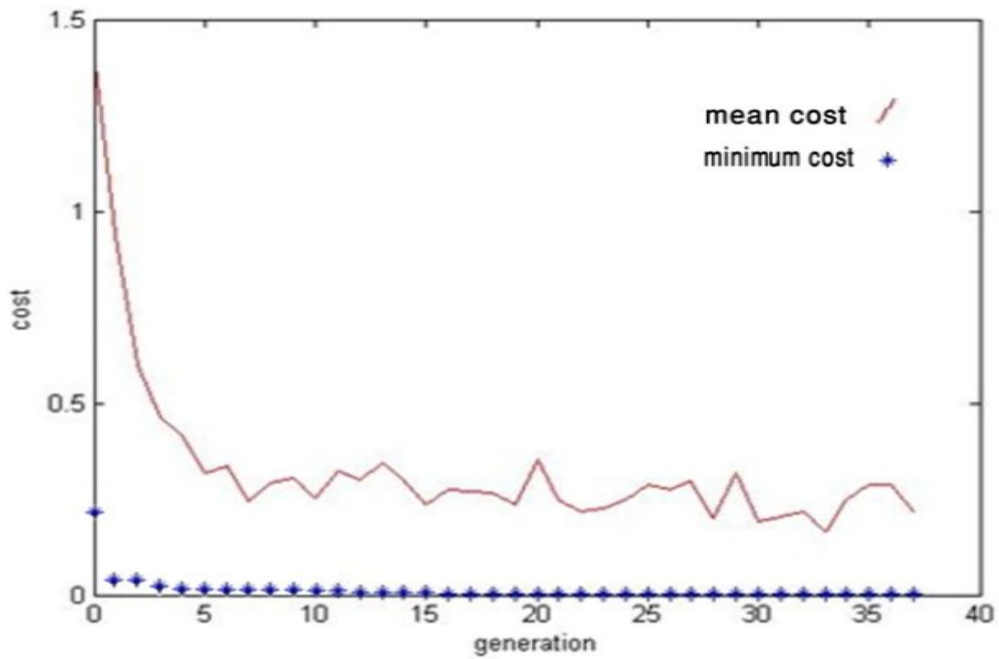


Figure1. Evaluation process for busbar (2), 14- bus IEEE test system.

Table 1. Power flow solution (14-Bus IEEE) test system with accuracy (0.001p.u.), using RCGA without reduction and restoration.

Bus	Active power	Reactive power	Voltage	Voltage	No. of
No	Mismatch	Mismatch	Magnitude (p.u)	Angle (deg)	Generations
1	Slack	Slack	1.06	0.00	—
2	0.000329	PV	1.045	3.2117	17
3	0.000131	PV	1.010	-4.3582	7
4	0.000484	PV	1.070	-6.1436	21
5	0.000890	PV	1.090	-12.423	47
6	0.000798	0.000481	1.057131	6.30252	95
7	0.000365	0.000060	1.0773818	-4.6541	107
8	0.000222	0.000773	1.0565362	-1.7120	193
9	0.000185	0.000682	1.0456395	1.44081	172
10	0.000273	0.000322	1.045163	-9.0031	18
11	0.000950	0.000223	1.057696	-5.4828	90
12	0.000411	0.000535	1.061725	7.67754	43
13	0.000770	0.000521	1.0482889	-11.028	29
14	0.000209	0.000762	1.0588537	-3.3446	47
	Total	Computational	Time:		7.156 sec.



Table 2. Power flow solution (14-Bus IEEE) test system with accuracy (0.001p.u.), using RCGA with reduction and restoration.

Bus	Active power	Reactive power	Voltage	Voltage	No. of
No.	Mismatch	Mismatch	Magnitude(p.u)	Angle(deg.)	Generations
1	Slack	Slack	1.06	0.00000	-
2	0.000373	PV	1.045	3.21170	15
3	0.000130	PV	1.010	-3.35826	5
4	0.000374	PV	1.070	-6.10062	21
5	0.000890	PV	1.090	-11.0235	40
6	0.000678	0.000444	1.0476131	6.30252	-
7	0.000360	0.0006	1.0573888	-4.69990	-
8	0.000223	0.000788	1.065092	-2.71203	-
9	0.000109	0.0005	1.0558895	1.63081	-
10	0.000223	0.000321	1.0551690	-9.03316	-
11	0.000850	0.000221	1.0476990	-4.08283	-
12	0.000407	0.000546	1.0762725	6.60054	-
13	0.000660	0.000512	1.0482889	-11.0208	-
14	0.000205	0.000769	1.0688837	-3.34469	-
Total	Computational	Time:			0.18 sec.

Table 3. Power flow solution for “IRAQI NATIONAL GRID” with accuracy (0.001p.u.), using RCGA with the method of reduction and restoration (only the generator busbars).

Bus	Active power	Reactive power	Voltage	Voltage	No. of
No.	Mismatch (p.u)	Mismatch (p.u)	Magnitude (p.u)	Angle(deg)	Generations
1	Slack	Slack	1.04	0	—
2	0.0005	PV	1	18.3805	262
3	0.00021334	PV	1	2.8233	57
4	0.0008081	PV	1	-9.5400	319
5	0.00011245	PV	1	13.6445	521
6	0.00043106	PV	1	-11.8520	34
7	0.0018487	PV	1	4.1875	500
8	0.00066843	PV	1	7.5529	244
9	0.00023882	PV	1	12.3150	30
10	0.00016648	PV	1	4.0006	134
11	0.0003391	PV	1	-19.7704	88
12	0.00045458	PV	1	-6.3530	266
13	0.00013682	PV	1	4.5221	424
14	0.00058912	PV	1	-6.9794	76
15	0.00054176	PV	1	-8.1968	353
16	0.00021063	PV	1	13.5898	42
17	0.00078201	PV	1	4.5766	39
18	2.4477*10 ⁻⁶	PV	1	11.1094	41
19	0.00090163	PV	1	7.0672	47
20	0.00089409	PV	1	-7.0275	9
21	0.00037127	PV	1	-3.2876	159
22	0.00014522	PV	1	-10.7986	24
23	0.00093387	PV	1	2.0421	216
24	0.00084462	PV	1	9.0268	47



25	0.00038532	PV	1	2.9669	17
26	0.00023586	PV	1	3.8338	52
27	7.2047*10 ⁻⁶	PV	1	-6.8666	88
28	0.00011686	PV	1	0.0252	50
29	0.00026843	PV	1	7.3612	333
30	0.0005791	PV	1	9.1833	134

*Total computing time (Genetic Algorithm without the method of Reduction and Restoration): more than 72 hours.

*Total computing time (Genetic Algorithm with the method of Reduction and Restoration): 519 sec., this time is for the total load flow solution of 362-bus ING system.

Table 4. Power flow solution for "IRAQI NATIONAL GRID" (load buses) after system restoration.

Bus No.	Active power Mismatch (p.u)	Reactive power Mismatch (p.u)	Voltage Magnitude (p.u)	Voltage Angle(deg.)
31	0.0003	0.0002	1.02247	12.3782
32	0.000310	0.00013264	1.03356	-12.5347
33	0.000761	0.00088425	0.955482	-18.8922
34	0.00048	0.000007	0.981021	-3.14901
35	0.00082	0.00019414	0.969731	-7.5778
36	0.0007	0.0004	0.999866	0.40992
37	0.00094	0.00059979	0.99142	-0.108361
38	0.00072	0.0000028	1.02766	2.41241
39	0.00010	0.000031	0.951085	8.90456
40	0.000073	0.000082	0.978972	7.68687
41	0.000003	0.00014068	0.954069	-2.09315
42	0.00056231	0.00034232	0.951974	10.2677
43	0.00015186	0.00084486	0.956778	9.06423
44	0.00093275	0.00060546	0.955108	-13.2829
45	0.00085845	0.0000039	1.00216	-8.97243
46	0.000025	0.00022034	0.955224	-7.08481
47	0.0005849	0.00025364	0.96548	-8.2154
48	0.0006	0.0009	0.96959	0.0359168
49	0.00046407	0.00068482	1.01733	8.11071
50	0.00064014	0.00040881	0.96882	16.9887
51	0.00081139	0.00073374	1.01725	12.1607
52	0.00063582	0.00036833	0.999238	0.015595
53	0.00064585	0.00073222	0.95709	7.0377
54	0.00039461	0.00031144	1.02049	4.97693
55	0.00050197	0.00051873	0.95678	18.5084
56	0.0006757	0.00066047	1.02961	13.4216
57	0.00048624	0.00046999	1.01989	13.0202
58	0.00026657	0.00078447	1.03154	-4.56727
59	0.00020212	0.00087574	0.998382	-0.133244
60	0.00099704	0.00040061	0.969316	-9.13924
61	0.0002	0.0005	1.09633	-3.3891
62	0.00062866	0.00048481	1.01166	3.0274
63	0.000034	0.00050729	1.00118	11.0695



64	0.00052304	0.0006	0.956323	0.126932
65	0.00039148	0.00027503	0.959269	-3.93418
66	0.0003338	0.00048038	0.959048	5.45821
67	0.00045369	0.00074015	1.03691	8.05995
68	0.00077681	0.00053799	0.962027	-0.556099
69	0.00027057	0.00061177	1.0712	5.11859
70	0.00040663	0.00054506	0.959477	-13.4194
71	0.00015602	0.00084029	1.0151	4.6136
72	0.00085314	0.0000044	0.9505	-9.4481
73	0.00082757	0.00056498	0.9587	14.8084
74	0.0000066	0.00028761	1.0205	-0.5232
75	0.00045213	0.00089712	0.9606	16.254
76	0.00026312	0.00099152	1.0235	-0.4562
77	0.0003	0.0002	0.9989	-15.9269
78	0.00060173	0.00081968	0.9569	9.3835
79	0.00097288	0.00093161	0.9615	-9.6373
80	0.00030775	0.00026214	1.0172	-11.3539
81	0.00028197	0.0003666	0.9567	10.958
82	0.0001	0.0007	0.9709	-9.6128
83	0.00017501	0.00031678	0.9538	0.5662
84	0.00060463	0.00055344	0.9689	12.4227
85	0.00049479	0.00025939	0.9917	-17.9393
86	0.00074739	0.000061	0.9976	11.2733
87	0.00073692	0.00062359	1.0459	3.6541
88	0.0002	0	0.9665	7.1323
89	0.000081	0.00089968	1.0154	-0.9266
90	0.00051316	0.00093613	1.0007	-15.3443
91	0.000031	0.00072166	1.0017	18.7953
92	0.00062835	0.00047428	0.9977	12.0889
93	0.0000047	0.00047299	1.0034	11.0409
94	0.00031952	0.00085516	0.9855	1.9537
95	0.00028333	0.00050642	1.0368	18.9362
96	0.0008504	0.00096063	1.0821	-15.1242
97	0.00038635	0.00026579	1.0445	-5.8019
98	0.00069584	0.00012365	0.9702	-8.2354
99	0.0007	0.0009	0.9562	16.788
100	0.00010717	0.0000085	0.9727	-10.4169
101	0.0006727	0.00077553	0.9557	8.5754
102	0.00053227	0.00015283	1.0827	-10.9894
103	0.00044692	0.00081571	0.9729	0.6583
104	0.00016048	0.000073	1.0319	0.9266
105	0.000025	0.00047994	0.9625	-2.6931
106	0.000048	0.00079433	0.9284	-10.2436
107	0.00084716	0.00015576	0.9641	4.4674
108	0.00068356	0.000055	1.0552	1.2291
109	0.00026455	0.00064387	1.0413	11.6445
110	0.00058321	0.00015476	1.02897	9.3654
111	0.00071167	0.00048416	1.089	16.4406
112	0.00094005	0.00097359	0.9736	12.9073
113	0.00084364	0.00061624	1.0071	19.928
114	0.00021032	0.00017141	0.9618	3.9724



115	0.00084827	0.00097626	0.9523	0.8467
116	0.00083	0.000547	0.9523	4.5623
117	0.00047	0.0007656	1.0258	-15.256
118	0.000455	0.00072	0.96136	16.2351
119	0.00092	0.0009962	0.992564	-9.2541
120	0.00012	0.0004547	1.03654	0.06541
121	0.001	0.0008	0.9618	2.2392
122	0.00013234	0.00093924	0.9884	11.3193
123	0.00096448	0.0005687	0.9523	-7.3612
124	0.00081065	0.0000031	1.0828	-6.4949
125	0.00030709	0.000083	0.9998	-11.0119
126	0.000048	0.00071905	0.9618	3.1288
127	0.00096313	0.00098343	0.9757	-4.9987
128	0.00093397	0.00077209	1.0843	-0.3262
129	0.00062329	0.00064654	1.0182	12.9015
130	0.00094189	0.00037681	0.9539	-8.8013
131	0.00014215	0.00057406	0.9571	1.6474
132	0.00041524	0.0005684	0.9583	10.7085
133	0.00020296	0.00046611	0.9638	6.3202
134	0.00037946	0.00062747	0.9987	9.103
135	0.00095745	0.00082409	0.9785	-1.7189
136	0.00027374	0.00046965	0.9706	1.4742
137	0.00020975	0.00085845	0.971	7.2577
138	0.00039402	0.00048299	1.0127	7.7591
139	0.00035319	0.00036285	0.9632	5.5677
140	0.0006075	0.0009984	0.95154	6.3214
141	0.0008155	0.0002237	0.95214	-14.2365
142	0.00011	0.0009845	1.0564	0.98745
143	0.0002734	0.0002717	0.9654	3.2145
144	0.0001812	0.000567	0.9628	-17.149
145	0.0004911	0.0006331	0.9752	-4.2187
146	0.0005208	0.000486	0.9962	0.05871
147	0.0005119	0.000886	1.0547	2.0154
148	0.0002753	0.0004816	0.9614	13.2974
149	0.0004286	0.0004054	1.0893	1.5647
150	0.0002753	0.0001582	0.9512	6.2354
151	0.0007	0	0.9544	3.5375
152	0.00013698	0.00027886	1.007	-0.8344
153	0.00020208	0.00023032	0.9965	-0.5292
154	0.00040253	0.00020923	0.9701	5.2631
155	0.00046085	0.00096044	0.9731	5.815
156	0.00029987	0.000035	0.9753	4.4393
157	0.00080446	0.00053457	0.9485	-8.8882
158	0.00035469	0.00015957	0.9687	13.5985
159	0.0003943	0.000029	0.9585	-1.0752
160	0.00073661	0.00017162	0.9279	13.6502
161	0.00065884	0.00028923	0.9548	-6.1351
162	0.00035578	0.00029898	0.9587	-2.3739
163	0.00075604	0.00092751	0.9521	2.898
164	0.000035	0.00038695	1.0067	8.9077
165	0.00099806	0.00071947	1.0691	-10.2774



166	0.00012425	0.000052	0.955	-8.262
167	0.00092219	0.00019175	0.9984	13.4656
168	0.00076628	0.00081641	0.9775	17.2191
169	0.00092571	0.000057	0.973	0.6329
170	0.00054766	0.00069843	0.9653	0.4959
171	0.00099334	0.00079967	0.9611	10.6166
172	0.00049608	0.00022697	0.9946	-1.0459
173	0.00055849	0.00042155	0.9421	-4.9939
174	0.00048618	0.000055	1.0338	3.6292
175	0.00014611	0.00072444	0.9827	10.898
176	0.00051741	0.00064903	0.9628	6.5469
177	0.00071172	0.00036796	0.9539	-1.5042
178	0.00019378	0.000039	0.9512	6.5171
179	0.00060168	0.0008397	1.0102	-7.9275
180	0.00059232	0.00022898	0.9634	6.5271
181	0.0001	0.0002	1.0054	4.2552
182	0.00044569	0.000618	1.0125	-6.0294
183	0.00055934	0.00041766	0.9865	3.0486
184	0.00020306	0.00096151	0.9548	7.0504
185	0.00088243	0.00045767	0.9413	-0.5076
186	0.00069729	0.00070518	0.9528	9.3272
187	0.000044	0.000333	0.9537	4.4252
188	0.000013	0.00044238	0.9582	2.137
189	0.00050756	0.00076265	0.9543	4.8151
190	0.00066192	0.00075837	0.9592	19.2249
191	0.0002513	0.00044497	0.9583	0.8323
192	0.00020302	0.00080563	0.9555	2.266
193	0.00030057	0.00094464	1.0024	-17.265
194	0.00046703	0.00042967	0.9994	11.0973
195	0	0	0.9507	18.5179
196	0.00093542	0.000085	0.9738	10.7321
197	0.00051919	0.00062756	0.9848	1.4284
198	0.00013828	0.00084404	1.067	6.9025
199	0.00052945	0.0002323	1.027	-17.4657
200	0.00054335	0.00038057	0.9445	-15.5822
201	0.00061187	0.00075132	0.9957	-18.0073
202	0.00096005	0.00091358	0.9778	-2.2563
203	0.00079194	0.00022214	0.9552	-3.3525
204	0.00026439	0.00095589	0.9802	0.5317
205	0.00056456	0.00087312	0.9946	18.2447
206	0.00054948	0.00055895	0.9555	8.0271
207	0.00077144	0.001	0.9546	3.8581
208	0.00075889	0.00027959	1.0049	8.4842
209	0.00056002	0.00040952	1.0468	-13.798
210	0.0006285	0.00057178	0.9503	-5.8999
211	0.00019025	0.00095178	0.9528	-5.8964
212	0.00059117	0.00056099	0.9572	-0.4872
213	0.00037677	0.00016316	0.9714	17.869
214	0.00088221	0.00063269	0.9555	-11.1881
215	0.00065945	0.00093676	0.9865	-2.8314
216	0.00087711	0.00089287	0.988	-0.0197



217	0.00093717	0.00011334	0.9586	-9.8487
218	0.00048357	0.0005098	1.0667	16.3454
219	0.000074	0.00050823	0.9713	8.419
220	0.00023902	0.00097386	0.9738	8.5508
221	0.00020321	0.00085756	1.0454	15.2306
222	0.00011518	0.00095031	1.0223	6.236
223	0.0009373	0.00031901	0.9452	1.1682
224	0.00063283	0.00047536	0.99	-4.223
225	0.00019285	0.000067	0.9426	-12.6611
226	0.000078	0.00023635	0.9599	-3.5077
227	0.00054555	0.000043	0.963	5.5577
228	0.0007854	0.000023	0.9515	2.3654
229	0.00021656	0.00064519	1.0196	-10.1812
230	0.00045404	0.00078516	1.0707	-17.4119
231	0.00026644	0.00016696	0.9708	-3.5614
232	0.00032806	0.0001135	1.0165	-17.2337
233	0.0008132	0.00026348	1.0561	0.7447
234	0.00049081	0.00047598	0.9979	6.2127
235	0.00042958	0.00037536	0.9598	3.4219
236	0.00099515	0.00014891	1.0225	6.0696
237	0.00084	0.00054738	0.9921	-3.3138
238	0.00019869	0.0005315	1.0221	5.5529
239	0.00069827	0.00070673	0.9505	-0.6187
240	0.00073886	0.0006194	0.9452	14.327
241	0.000012	0.00047631	1.0173	-11.6858
242	0.00052499	0.000039	0.945	-2.4259
243	0.00044988	0.00058049	0.9533	16.2874
244	0.00033758	0.00014153	0.9937	6.6786
245	0.00068628	0.00084693	0.9597	-4.9778
246	0.0004596	0.00037358	0.9885	9.4525
247	0.00051515	0.00045483	0.9546	4.6063
248	0.00032144	0.00068358	1.0714	7.7469
249	0.00043791	0.00041416	0.9966	-0.7901
250	0.00028647	0.00022116	0.9556	-2.497
251	0.0007	0.0003	0.95315	1.1601
252	0.000095	0.00054734	0.95733	-8.8202
253	0.00079549	0.00077536	0.98058	-5.4324
254	0.00032922	0.00065235	1.0836	-17.168
255	0.000085	0.00037146	0.959	8.3101
256	0.00094778	0.000036	0.98041	-19.965
257	0.00078819	0.00080088	0.95607	-13.439
258	0.0001091	0.00023452	1.0162	-4.7631
259	0.0008952	0.00047521	0.9842	1.5236
260	0.0009	0.0003	0.9574	-2.2963
261	0.0004	0.0008	1.0025	-3.0548
262	0.00066294	0.000013	0.9891	-1.1725
263	0.00048644	0.0001791	0.94889	8.6261
264	0.00015727	0.00054346	0.95678	-18.469
265	0.00033058	0.00075487	0.9502	8.8319
266	0.00060066	0.00054603	1.0306	6.2556
267	0.00052942	0.00042094	1.0529	14.874



Use of non-Conventional Material to Remove Cu^{+2} ions from Aqueous Solutions using Chemical Coagulation

Muna Yousif Abdul. Ahad

Assistant Professor

College of Engineering- University of Baghdad

Email: myabdulahad@yahoo.com

Samer Jalil Ibrahim

College of Engineering-University of Baghdad

Email: samerjalil44@yahoo.com

ABSTRACT

Coagulation - flocculation are basic chemical engineering method in the treatment of metal-bearing industrial wastewater because it removes colloidal particles, some soluble compounds and very fine solid suspensions initially present in the wastewater by destabilization and formation of flocs. This research was conducted to study the feasibility of using natural coagulant such as okra and mallow and chemical coagulant such as alum for removing Cu and increase the removal efficiency and reduce the turbidity of treated water. Fourier transform Infrared (FTIR) was carried out for okra and mallow before and after coagulant to determine their type of functional groups. Carbonyl and hydroxyl functional groups on the surface of okra and mallow were the major groups responsible for coagulation process. By using alum (conventional coagulants), okra and mallow (as a primary coagulant or in combination with the other two primary coagulants) and by the jar testing, the optimum pH-value and dose of the coagulants were determined. The results indicated that the optimal pH values were 6.7, 8 and 6 for alum, okra and mallow, respectively. Mathematical modeling show significant results (sig.<0.05) for the % Cu removal (dependent variable) with respect to coagulant dose (independent variable) for the okra as a primary coagulant, alum with okra and alum with mallow as binary coagulants and alum, okra and mallow as ternary coagulants .

Keywords: heavy metal; coagulant; jar test; flocculation.

استخدام المواد غير التقليدية لإزالة ايونات النحاس من المحاليل المائية
بطريقة التخثير الكيميائي

سامر جليل ابراهيم

كلية الهندسة | جامعة بغداد

منى يوسف عبد الاحد

كلية الهندسة | جامعة بغداد

الخلاصة

ان عمليتي التخثير والتلييد تلعبان دورا رئيسين ومهمين في معالجة المياه الملوثة والمياه الصناعية الملوثة ايضا من حيث ازالة المعادن الثقيلة مثل (النحاس) والمواد العالقة الذاتية من هذه المياه لخطورتها وسميتها للبيئة والصحة العامة. ومن الاساس ان تكون نسبها ضمن المحددات البيئية العالمية والمحلية المسموح بها. في هذا البحث تم استخدام مواد محلية ناتجة من النفايات الرخيصة الطبيعية والصديقة للبيئة مثل (مخلفات الباميا، اوراق الملوخية) كمخثرات لإزالة المعادن الثقيلة بطريقة اختبار الجرة. اضافة الى استخدام الشب الذي يعتبر من اكثر هذه المخثرات استخداما في هذه العمليات وقد استخدمت هذه المواد في هذه العملية لغرض زيادة وتحسين نسبة الازالة للعناصر الثقيلة وكذلك لتقليل نسبة العكورة الناتجة. حيث تم اجراء فحص التحليل الكيفي لورق الملوخية و مخلفات الباميا باستخدام جهاز الأشعة تحت الحمراء لغرض دراسة المركبات الكيميائية والمركبات المؤكسدة ومعرفة المجموعات الفعالة للمركبات العضوية مثل المجموعات الامينية الكربوكسيلية، الهيدروكسيل و الكربونيل على عملية التخثير والتلييد. كما تمت دراسة العوامل المؤثرة على عملية التخثير مثل قيمة الدالة الحامضية وكمية المواد المخثرة. ومن خلال نتائج البحث تبين ان قيم الدالة الحامضية المثلى كانت 6.7, 8, 6 لكل من الشب والباميا وورق الملوخية على التوالي. كما تم تطبيق موديل رياضي SPSS by (Multiple linear regression analysis) للمقارنة بين هذه المخثرات من حيث المعنوية واللامعنوية. هذا وتحتل عملية الفصل بالتخثير والتلييد مكانة كبيرة باعتبارها تقنية واعده في تكنولوجيا المياه النظيفة ومعالجة المياه الملوثة.

الكلمات الرئيسية: المعادن الثقيلة؛ المخثرات؛ جهاز فحص الجرة؛ التلييد.

1. INTRODUCTION

As a result of industrial activities and technological development, the amount of heavy metal ions discharged into streams and rivers by industrial and municipal wastewater have been increased incessantly. Heavy metals are member of a loosely-defined subset of elements that exhibit metallic properties, which mainly includes the transition metals, some metalloids, lanthanides, and actinides. Heavy metals such as copper, lead and zinc are main toxic pollutants in industrial wastewater, and they also become major surface and ground water contaminants. Heavy metals are discharged by various industries such as metal purification, metal finishing, chemical manufacturing, mining operations, smelting, battery manufacturing, and electroplating, **Issabayeva et al., 2010**. Removal of heavy metals from industrial wastewater is of primary importance because they are not only causing contamination of water bodies and are also toxic to many life forms. Most heavy metals are cations, carrying a positive charge, such as zinc, lead, copper, nickel and cadmium. Soil particles tend to have a variety of charged sites on their surfaces, some positive while some negative. The negative charges of these soil particles tend to attract and bind the positively charged metal cations, preventing them from becoming soluble and dissolve in water. The soluble form of metals is more dangerous because it is easily transported, hence more readily available to plants and animals. Metal behavior in the aquatic environment is surprisingly similar to that outside a water body. Sediments at the bed of streams, lakes and rivers exhibit the same binding characteristics as soil particles mentioned earlier. Hence, many heavy metals tend to be sequestered at the bottom of water bodies. The aquatic environment is more susceptible to the harmful effects of heavy metal pollution. Metal ions in the environment bioaccumulation and are biomagnified along the food chain. Therefore, their toxic effect is more pronounced in animals at higher trophic levels, **Ahluwalia and Goyal, 2005**. During the last years, rapid growth of population, urbanization, and industrial as well as agricultural activities have increased water demand, particularly in recent decades. Water



treatment industry is among the most important industries in many countries. Coagulation, flocculation, sedimentation, filtration and disinfection are the most common treatment processes used in the production of drinking water. Coagulation/flocculation processes are of great importance in solid-liquid separation practice ,**Yukselen, and Gregory, 2004.**

Coagulation

Coagulation is the process by which colloidal particles and very fine solid suspensions initially present in water are combined into larger agglomerates that can be separated via sedimentation, flocculation, filtration, centrifugation or other separation methods. Coagulation is commonly achieved by adding different types of chemicals (coagulants) to the water to promote destabilization of the colloid dispersion and agglomeration of the resulting individual colloidal particles. The addition of some common coagulants to water not only produces coagulation of colloids but also typically results in the precipitation of soluble compounds, such as phosphates, that can be present in the water. In addition, coagulation can also produce the removal of particles larger than colloidal particles due to the entrapment of such particles in the flocks formed during coagulation, **Metcalf and Eddy 2003.** This is achieved by rapid mixing of a coagulant in solution for short durations in order to achieve complete and uniform coagulant dispersion. Insufficient coagulant mixing may result in uneven coagulant dispersion throughout the solution, resulting in the presence of too much coagulant in certain areas and too little in others thereby degrading the overall process. Coagulant over-mixing on the other hand is not believed to have an effect on coagulation performance ,**Horne, 2005** and **Bratby, 2006.**

2. EXPERIMENTAL

2.1 Materials

Analytical grade reagents were used in the experimental studies. Copper Sulfate pent hydrated ($\text{CuSO}_4 \cdot 5\text{H}_2\text{O}$) from (E. MERK, Denmark) were used for preparing synthetic solutions. The properties of metal salts are given in **Table1.** Adjustments of pH were carried out by using 0.1N HCl and 0.1N NaOH.

2.2 Coagulants

2.2.1 Alum

Alum was used as a coagulant for the removal of heavy metal. The alum was milled, sieved and particles sizes ≤ 0.6 mm were selected for the investigation.

2.2.2 Mallow

Mallow leaves were washed with tap water then distilled water, dried at 50°C for 24 hours in the oven to remove the moisture content until constant weight. The dried mallow was milled, sieved and particles size ≤ 0.6 mm were selected for the investigation.

2.2.3 Okra

Okra pods were washed with tap water then distilled water, dried at 50°C for 24 hours in the oven to remove the moisture content until constant weight. The dried okra was milled, sieved and particles size ≤ 0.6 mm were selected for the investigation.

2.3 General Description for the Experimental Procedure

Experiments had been carried out to find the optimum pH, and optimum dose. The procedure involved filling the beakers with 1 L of heavy metal ion solution of 0.47 mg/L. Primary doses of (0, 0.35, 0.7, 1.4, 2.1 and 2.8) g/L for alum and (0, 0.2, 0.4, 0.5, 0.6 and 0.7) g/L for okra or mallow, respectively were added into the beakers. The suspensions were stirred rapidly (300 rpm) for 1 minute at G (275 S^{-1}) to ensure adequate mixing. The rapid mixing, then followed by slow mixing (50 rpm) for 15 minutes at G (16 S^{-1}) were performed to achieve opportunity for particle collisions and aggregate formation, Sulaymon et al., 2009. Experiments were carried out at initial pH values (5, 6, 6.7, 7, 8 and 9). The suspension was then allowed to settle for 15 minutes, and the sample is drawn at 6 cm depth from the supernatant to measure % Cu removal, and % residual turbidity. For the binary coagulants combinations, the optimum dosages from the primary experiments that are having the highest % Cu removal were selected. Combined binary doses of alum with okra or mallow of different percentages were used. The above procedure was repeated to estimate the optimum pH and dose for the highest %Cu removal. In the ternary coagulants combinations, the optimum doses and PH the binary experiments, which give the higher % Cu removal were selected. Combined ternary doses of alum, okra and mallow of different percentages were used. The procedure was repeated. Settling velocity, % residual turbidity, and conductivity for the selected optimum pH and coagulant dose combination were conducted and measured.

3. RESULTS AND DISCUSSION

3.1 FTIR Result

In order to understand the possible coagulant- metal ion interactions, it is essential to identify the functional groups present in this process. The main effective binding sites can be identified by FTIR spectral comparison of the coagulant. Coagulants were examined using (Shimadzo FTIR, 800 series spectra- photometer). Two flasks were filled with 1000 ml of the metal solution and 1gm of (okra and mallow), then placed in the jar and agitated continuously (1 minute for rapid mixing and 15 minute for slow mixing). Samples of the coagulant materials were dried by sun for 48 hours before FTIR tests., from Fig. 1. The FTIR spectral indicate the presence of amino, carboxylic, hydroxyl and carbonyl groups. Contribution of each functional group in this process is summarized in Table 2. Mallow before test has greatest changes in the peak values of bands than Okra before test, while the Okra after test was the lowest one.

3.2 Primary Coagulant Experiments

3.2.1 Optimum pH values

Samples of collected distilled water with Cu were placed in beakers and subjected repeatedly to a standard jar test using the following coagulants:-

1-Alum [$\text{Al}_2(\text{SO}_4)_3 \cdot 18\text{H}_2\text{O}$] at a dose 1400 mg/L

2-Okra at a dose 500 mg/L

3-Mallow at a dose 500 mg/L

Each beaker in the set of the standard jar test apparatus had its pH adjusted to different values (5, 6, 6.7, 7, 8, and 9).

Fig. 2 shows the effect of pH on the % removal of Cu in which generally, the % removal of Cu for alum>Okra>mallow.

3.2.2 Optimum coagulant dose

Jar tests were conducted to find the optimum coagulants doses, at the optimum pH 6.7, 8.0, 6.0 for alum, okra, and mallow. The results are shown in **Figs. 3, 4 and 5** respectively.

3.2.3 Effect of coagulant dose

The effects of different dosages of alum, okra and mallow are shown in **Figs. 3, 4, and 5**. The % removal of Cu increased with the increasing doses of the coagulants. It is observed that when the doses of alum, okra and mallow were greater than 1400 mg/L, 500 mg/L and 500 mg/L, respectively, the removal increased slowly. Thus, the optimum doses of alum, okra and mallow were 1400, 500 and 500 mg/L for the highest removal of heavy metal each in its related optimum pH value. These results are mainly due to the fact that the optimum coagulant dosage produces flocs that have a good structure and consistency. But in dosages lower and higher than optimum dosages, the produced flocs are small and influence the settling velocity of the sludge. A comparison between alum, okra and mallow for the removal of Cu at the optimum conditions, then relative abundance of coagulants after treating distilled wastewater with Cu followed the order: mallow>okra>alum as shown in **Fig. 6**.

3.3 Binary Combination Coagulants Experiments

The combination of alum as a primary coagulant with another coagulant aid (okra or mallow) for removal Cu were carried out and tabulated in **Table 2**.

3.4 Ternary Combination Coagulants Experiments

The combination of alum as a primary coagulant with another two coagulant aids (okra and mallow) for removal Cu were carried out and tabulated in **Table 3**.

3.5 Variation of Turbidity with Dose

Figs. 7, 8, and 9 show the residual turbidity with dose for the primary, binary and ternary coagulants, in which the residual turbidity decreased as the dose of coagulant increased.

3.6 Variation of Conductivity with Dose

Fig. 10 shows the variation of the conductivity with dose for the optimal ternary combination coagulants of pH= 7 and dose 0.725 g/L, the conductivity decreased as the dose increased which indicates that the Cu concentration in the supernatant becomes lower by increasing the coagulant dose.

3.7 Settling velocity

In the **Fig.11**, the settling velocity has been measured through the relation between time and height of interface for each successive point on the curve. **Fig. 12** shows the settling rate-concentration relationship for the optimal ternary combination coagulants of pH= 7 and dose 0.725 g/L by using alum, okra and mallow for Cu (0.47 mg/L).

3.8 Mathematical Modeling

Developing a mathematical model for the coagulation flocculation experiments, and generating quick decision-making information, using powerful statistics (multiple linear regression analysis MLR) by SPSS statistic software package (version 17.0), to understand and show an effective presentation for the results with a high quality of tabular and graphical modeling outputs. Equations of mathematical modeling for primary, binary and ternary coagulants show in **Table 4**.

4. CONCLUSION

The following results have been obtained:

1. The optimum coagulant doses in distilled water treatment with Cu concentration (0.47 mg/L) for alum, okra and mallow were 1400mg/L, 500mg/L and 500mg/L respectively.
2. The optimum pH values for coagulants (alum, okra and mallow) were 6.7, 8.0 and 6.0, respectively when used as primary coagulants.
3. Using okra and mallow as coagulant aids with alum (in binary and ternary combinations) cause quicker formation of flocs and that increases their rate of sedimentation.
4. Natural coagulants (when used as primary coagulants) seem to be more effective at higher turbidity levels.
5. Mathematical modeling shows significant results (sig.<0.05) for the % Cu removal (dependent variable) with respect to coagulant dose (independent variable) for the okra as a primary coagulant, alum with okra, and alum with mallow as binary coagulants, and alum, okra, and mallow as ternary coagulants.
6. Mathematical modeling shows significant results (sig.<0.05) for the % residual turbidity (dependent variable) with respect to coagulant dose (independent variable) for the alum, okra, and mallow as a primary coagulant, alum with mallow as binary coagulants, and alum, okra, and mallow as ternary coagulants.

REFERENCES

- Ahluwalia, S.S. and Goyal, D., 2005, *Microbial and Plant Derived Biomass for Removal of Heavy Metals from Wastewater*, Bioresource Technology, 98, 2243-2257.
- Bratby, J., 2006, *Coagulation and Flocculation in Water and Wastewater Treatment* 2nd Edition. IWA publishing, London, UK. TechBooks, India,
- Horne, W.J., 2005, *Evaluation and Optimization of Control Strategies for Management of Disinfection Byproduct Precursors within the Northeast Mississippi Water District*. Master's Thesis. Dave C. Swalm School of Chemical Engineering, Mississippi State University, Mississippi State, Mississippi
- Issabayeva, G., Aroua, M.K., and Sulaiman, N.M., 2010, *Study on Palm Shell Activated Carbon Adsorption Capacity to Remove Copper Ions from Aqueous Solution*, Desalination, 262, 94-98.
- Metcalf and Eddy, 2003, *Wastewater Engineering Treatment and Reuse*. 4th Hill Companies, Inc., New York,.
- Sulaymon A.H, Ali A. M. and Al Naseri S.K., 2009, *Natural Organic Matter from Tigris River Water in Baghdad, Iraq*, Desalination, 245, pp.155-168.

- Yukselen, M.A. and J. Gregory, 2004. *The Effect of Rapid Mixing on the Break-up and Re-Formation of Floccs*. J. Chem. Technol. Biot., 79: 782-788

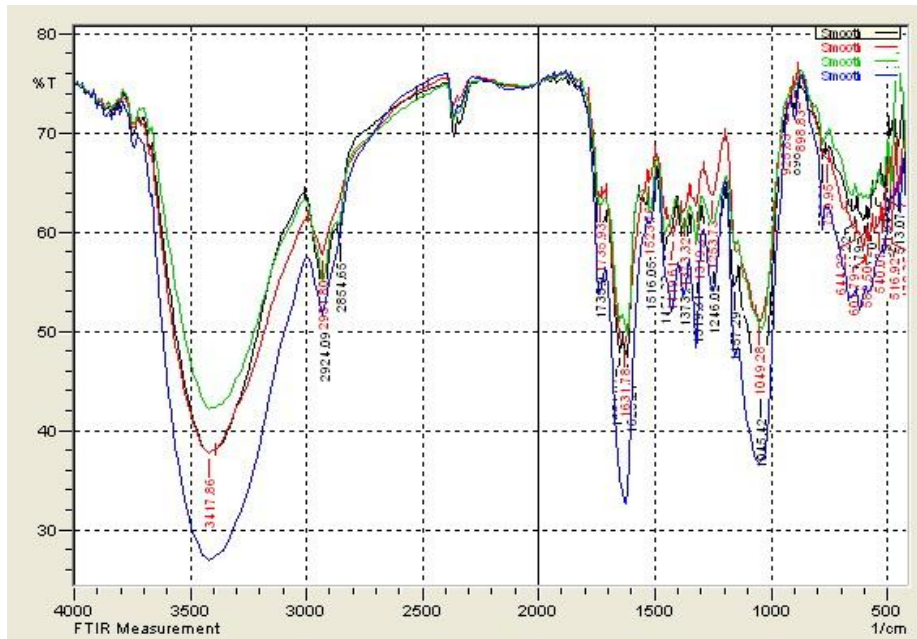


Figure 1. FTIR spectrum for Okra and Mallow before and after tests (• okra before test, • mallow before test, • okra after test, • mallow after test).

Table 1. Properties of metal salt.

Property	Copper sulfate CuSO ₄ .5H ₂ O
Molar mass g/mol	249.70
Atomic weight g/mol	63.546
Appearance	Blue
Density g/cm ³	2.284

Table 2. Function groups before and after okra and mallow coagulants with Copper ion.

Wave number (cm ⁻¹) Okra before test	Assignment groups	After coagulation Of Cu	Wave number (cm ⁻¹) Mallow before test	Assignment groups	After coagulation Of Cu
3417.86	Amides	3421.72	3417.86	Amides	3417.86
2931.80	Carboxylic acids	2927.94	2927.94	Carboxylic acids	2924.09
1735.93	Carboxylic acids,	1735.93	2854.65	Carboxylic acids	2854.65



	Aldehydes				
1631.78	Amides	1624.06	1735.93	Carboxylic acids, Aldehydes	1735.93
1523.76	Nitro groups, Amides	1516.05	1651.07	Amides,Imines	1651.07
1419.61	Aromatics	1423.47	1616.35	Amides	1620.21
1373.32	Alkylhalides, Nitro groups	1373.32	1516.05	Nitro groups, Amides	1516.05
1319.31	Alkylhalides, Nitro groups	1319.31	1454.33	Aromatics	1454.33
1253.73	Alcohols Ketones Alkylhalides	1249.87	1369.46	Alkylhalides, Nitro groups	1373.32
1049.28	Alcohols, Alkylhalides, Phosphines	1053.13	1319.31	Alkylhalides, Nitro groups	1319.31
898.83	Phosphines, Sulfonates	898.83	898.83	Phosphines, Sulfonates	898.83

Table 2. The percentages of the coagulant doses for binary coagulation .

Sample No.	1	2	3	4	5	6
Coagulants	85% of alum dose+15% one of (mallow or okra) dose (1.19g/L + 0.075g/L)	70% of alum dose+30% one of (mallow or okra) dose (0.98g/L + 0.15g/L)	55% of alum dose+45% one of (mallow or okra) dose (0.77g/L + 0.225g/L)	40% of alum dose+60% one of (mallow or okra) dose (0.56g/L + 0.3g/L)	25% of alum dose+75% one of (mallow or okra) dose (0.35g/L + 0.375g/L)	10% of alum dose+90% one of (mallow or okra) dose (0.14g/L + 0.45g/L)

**Table 3.** The percentage of the coagulant doses for ternary coagulation.

Sample No.	1	2	3	4	5	6
Coagulants	85% of alum dose+7.5% two of (mallow and okra) doses (1.19g/L + 0.0375g/L + 0.0375g/L)	70% of alum dose+15% two of (mallow and okra) doses (0.98g/L + 0.075g/L + 0.075g/L)	55% of alum dose+22.5% two of (mallow and okra) doses (0.77g/L + 0.1125g/L + 0.1125g/L)	40% of alum dose+30% two of (mallow and okra) doses (0.56g/L + 0.15g/L + 0.15g/L)	25% of alum dose+37.5% two of (mallow and okra) doses (0.35g/L + 0.1875g/L + 0.1875g/L)	10% of alum dose+45% two of (mallow and okra) doses (0.14g/L + 0.225g/L + 0.225g/L)

Table 4. Equations of mathematical modeling for primary, binary and ternary coagulants.

Stage	Coagulants	Equations	Significant
Primary	Alum	Y= 9.337x + (-25.14) for pH Y = 6.06x + 8.924 for dose	non-significant (0.132) non-significant (0.096)
	Okra	Y = 9.067x + (-24.47) for pH Y = 2.997x + 7.620 for dose	non-significant (0.132) significant (0.046)
	Mallow	Y = 5.945x + (-6.42) for pH Y = 5.776x + 15.832 for dose	non-significant (0.252) non-significant (0.067)
Binary	Alum + Okra	Y = 10.93x + (-33.11) for pH Y = 4.603x + 11.55 for dose	non-significant (0.093) significant (0.034)
	Alum + Mallow	Y = 10.22x + (-28.24) for pH Y = 4.604x + 11.084 for dose	non-significant (0.124) Significant (0.029)



Ternary	Alum + Okra + Mallow	$Y = 9.81x + (-21.878)$ for pH $Y = 4.703x + 12.497$ for dose	non-significant (0.193) significant (0.039)
---------	----------------------	--	--

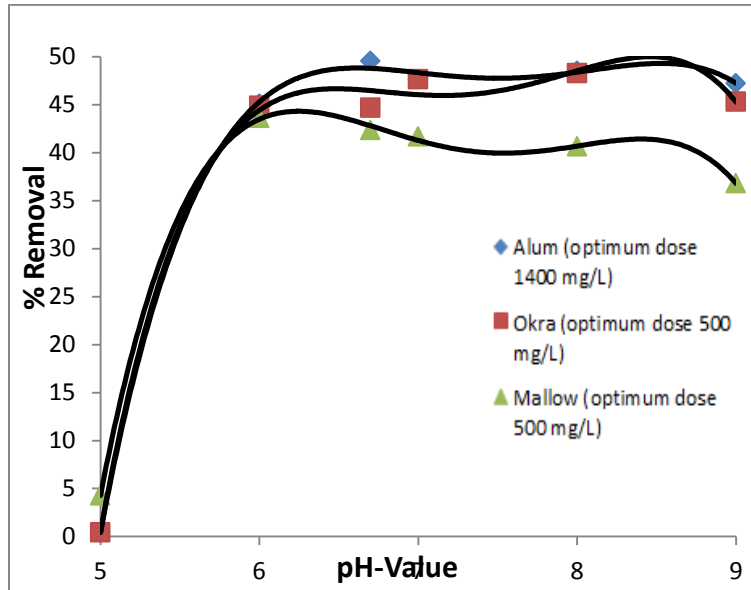


Figure 2. The effect of pH values on the % removal of Cu for the investigated coagulants.

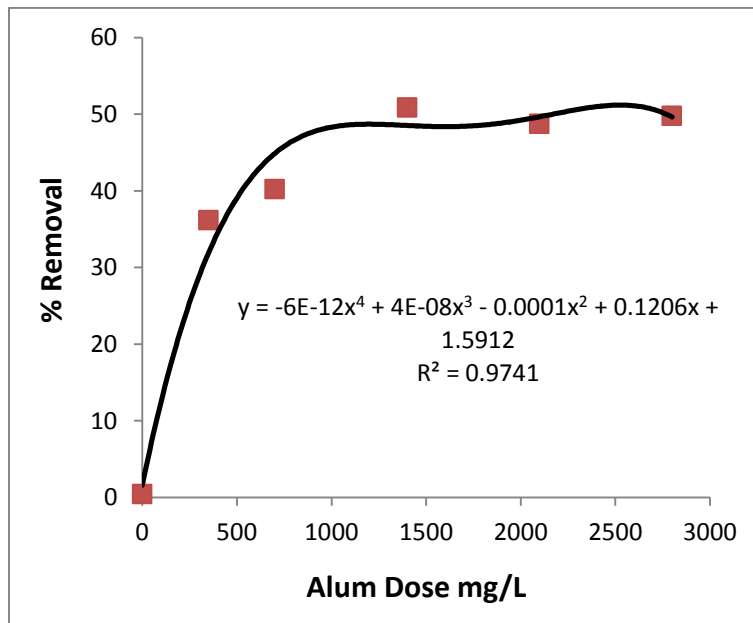


Figure 3. The effect of Alum coagulant dosages at optimum pH of 6.7 on Cu removal efficiencies of investigated coagulant.

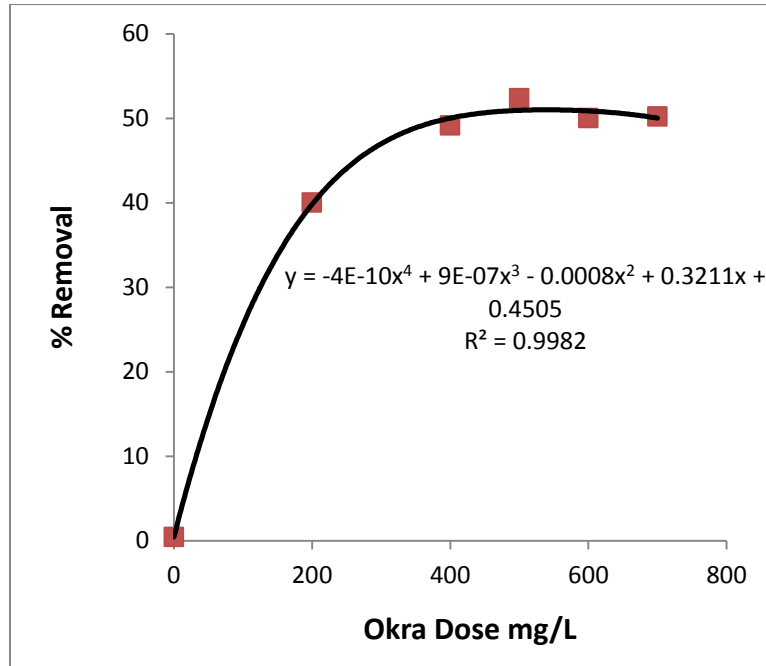


Figure 4. The effect of Okra coagulant dosages at optimum pH of 8.0 on Cu removal efficiencies of investigated coagulant.

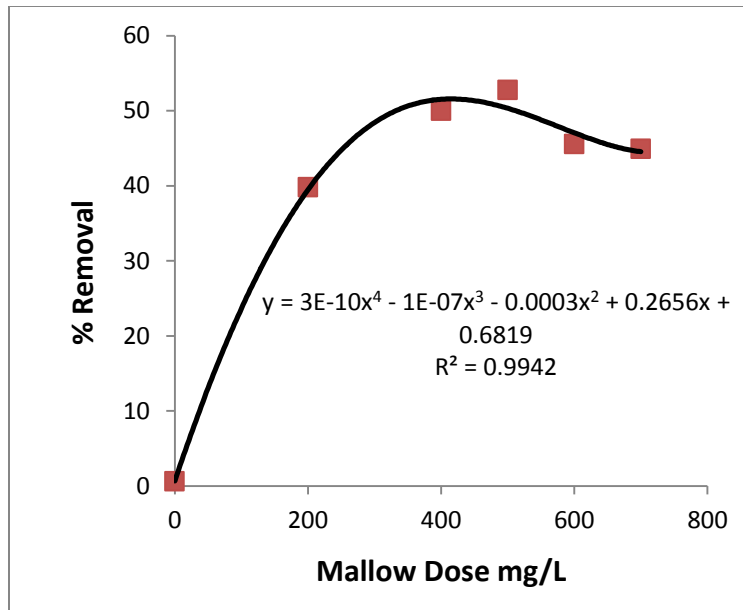


Figure 5. The effect of Mallow coagulant dosages at optimum pH of 6.0 on Cu removal efficiencies of investigated coagulant.

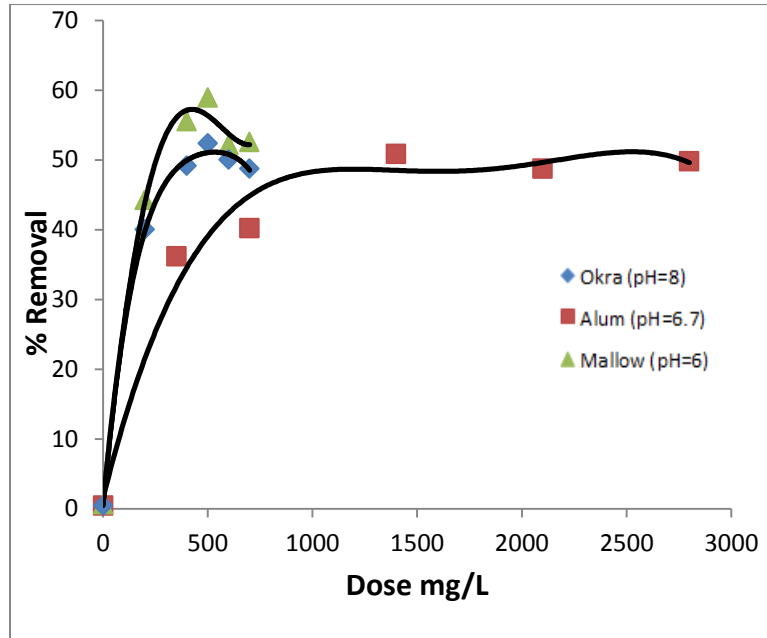


Figure 6. The effect of used coagulant and its dosages on the Cu removal efficiencies at their optimum pH.

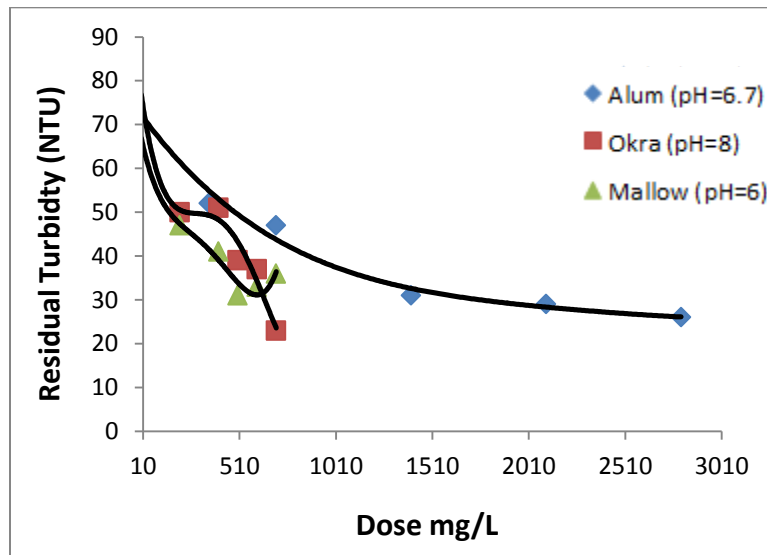


Figure 7. Residual turbidity vs. dose for primary coagulants.

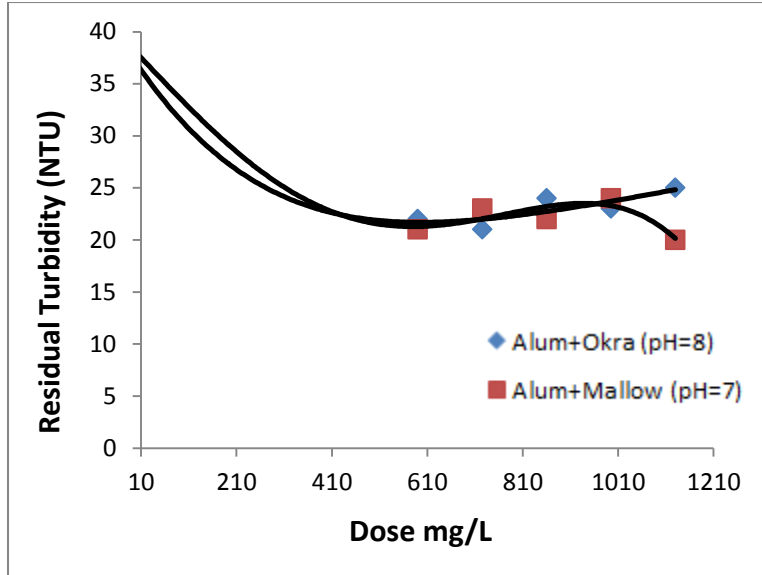


Figure 8. Residual turbidity vs. dose for binary combination coagulants.

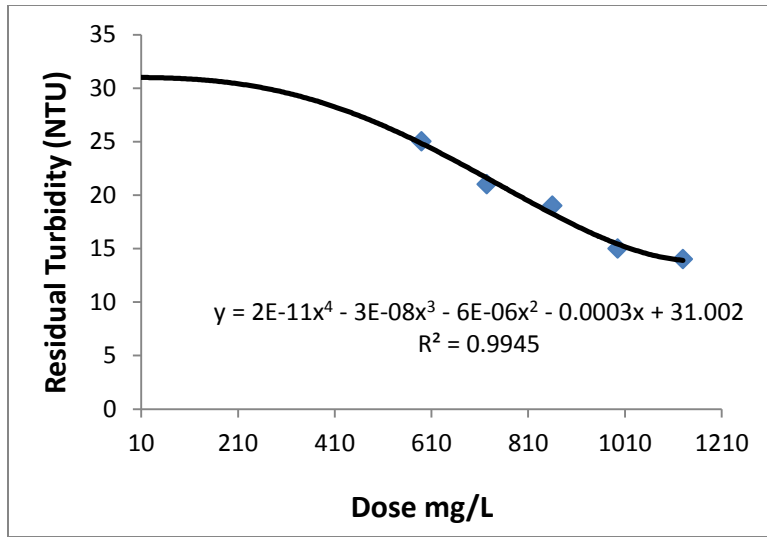


Figure 9. Residual turbidity vs. dose for ternary combination coagulants.

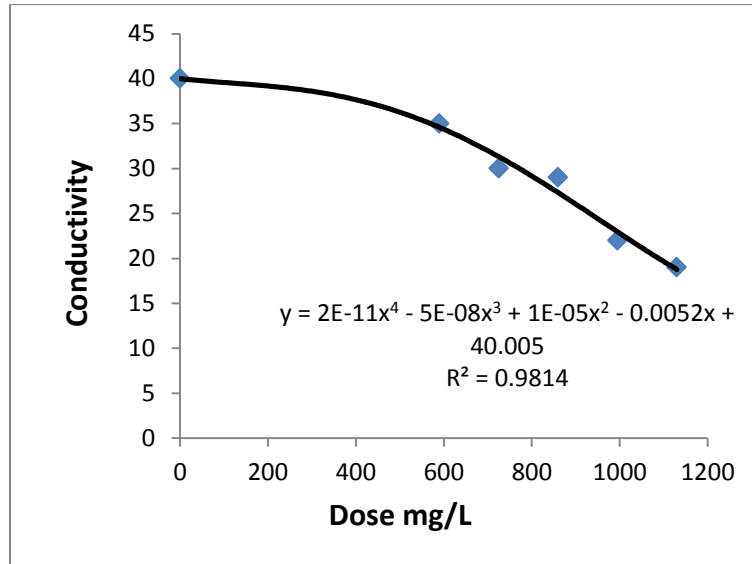


Figure 10. Conductivity vs. dose of alum in conjunction with okra and mallow for Cu (0.47mg/L) at pH= 7.

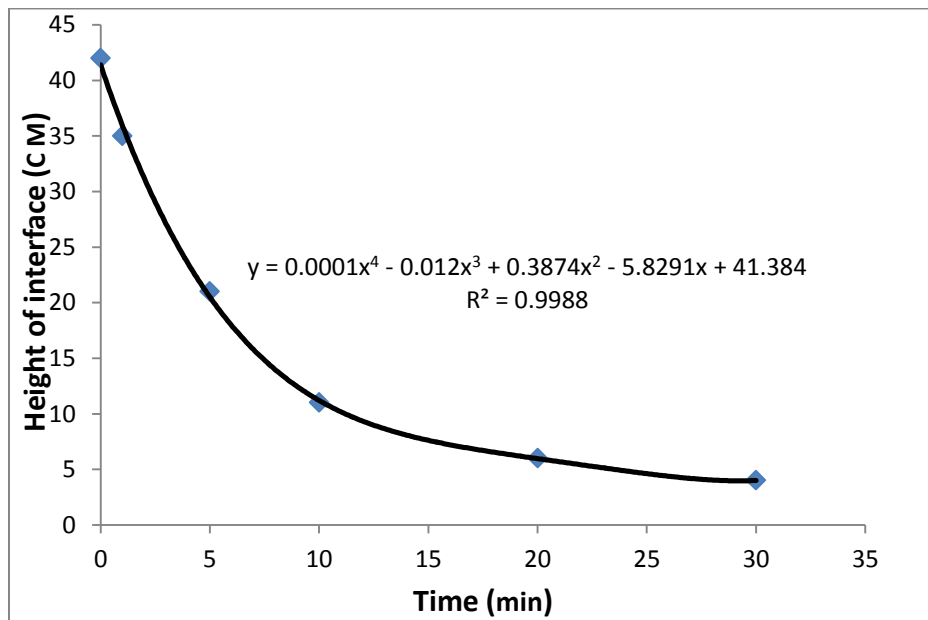


Figure 11. Height of interface vs. time for ternary combination coagulants.

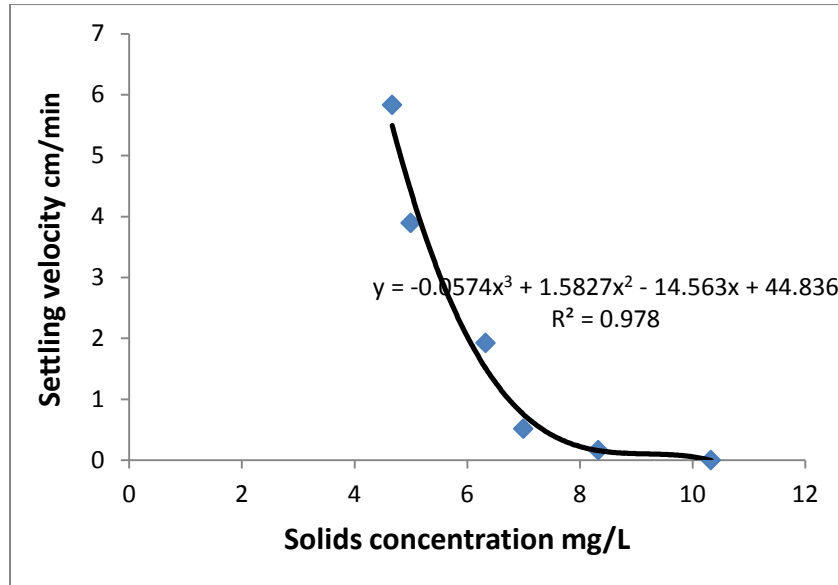


Figure 12. Settling rate vs. solids concentration.



Brackish Water Desalination Coupled With Wastewater Treatment and Electricity Generation

Dr. Zainab Ziad Ismail

Assistant Professor

College of Engineering -University of Baghdad

Email:zismail9@gmail.com

Mohammed Abdulkhaleq Ibrahim

Instructor

College of Engineering -Al-Nahrain University

Email: moh_env@yahoo.com

ABSTRACT

A new bio-electrochemical system was proposed for simultaneous removal of organic matters and salinity from actual domestic wastewater and synthetically prepared saline water, respectively. The performance of a three-chambered microbial osmotic fuel cell (MOFC) provided with forward osmosis (FO) membrane and cation exchange membrane (CEM) was evaluated with respect to the chemical oxygen demand (COD) removal from wastewater, electricity generation, and desalination of saline water. The MOFC was inoculated with activated sludge and fueled with actual domestic wastewater. Results revealed that maximum removal efficiency of COD from wastewater, TDS removal efficiency from saline water, power density, and current density were 96%, 90%, 30.02 mW/m², and 107.20 mA/m², respectively.

Key words: microbial fuel cell, desalination, osmosis, electricity generation, wastewater.

تحلية المياه المالحة مقترنة بمعالجة مياه المخلفات وتوليد الطاقة الكهربائية

محمد عبد الخالق ابراهيم

مدرس

كلية الهندسة – جامعة النهرين

د. زينب زياد اسماعيل

استاذ مساعد

كلية الهندسة – جامعة بغداد

الخلاصة

تم اقتراح تنفيذ منظومة احيائية كهروكيمياوية جديدة لأزالة المواد العضوية والملوحة من مياه الصرف الصحي الحقيقية والمياه المالحة المحضرة ، على التوالي. تم تقييم اداء خلية الوقود الاحيائية التناضحية ثلاثية الحجرات والمجهزة بغشاء تناضحي امامي (FO) وبغشاء أيوني (CEM) يسمح بمرور البروتونات على اساس ازالة المحتوى الكيميائي للاوكسجين (COD) من مياه الصرف، وتوليد الكهرباء وازالة الملوحة من الماء المالح. تم استخدام الحمأة المنشطة كمصدر للبكتيريا واستخدام مياه الصرف الصحي كمصدر وقود حيوي مستمر للخلية. اظهرت النتائج المختبرية لمنظومة الوقود الاحيائية التناضحية العاملة بالماء الملحي المحضر نسبة ازالة متطلب اوكسجين كيميائي و كفاءة ازالة الاملاح الذائبة و كثافة القدرة و كثافة التيار. كانت 96%، 90%، 30.02 ملي واط/م²، 107.20 ملي امبير/م² على التوالي.

الكلمات الرئيسية:خلية الوقود الاحيائي، ازالة الملوحة، التنافذ، توليد الكهرباء، مياه الصرف الصحي.



1. INTRODUCTION

It is well recognized that alternative sources of energy are urgently required. Current reliance on fossil fuels is unsustainable due to pollution and finite supplies. While much research is being conducted into a wide range of energy solutions, it does not appear that any single solution will be able to replace fossil fuels in its entirety. However, different alternatives will be required providing energy for a specific task in specialized ways in various situations, **Franks and Nevin, 2010**. Microbial fuel cell (MFC) technology is a promising approach for wastewater treatment because of its potential energy-creating benefits, and its diverse functions. The anode of an MFC can treat various wastewaters and wastes, including municipal and industrial wastewaters, petroleum wastes, and solid wastes. The cathode can be used to conduct denitrification, or the removal of heavy metals. MFCs that can accomplish contaminant removal, bioenergy production, and clean water extraction will become more competitive with existing wastewater treatment technologies. Extracting clean water from wastewater has been realized by using technologies such as forward osmosis (FO).

FO is the movement of water across a semi permeable membrane in order to induce flow from an area of high-water potential to an area of low-water potential. The driving force in the FO process is the concentrated solution (draw solution) on the permeate side of the membrane, which should have a high osmotic efficiency, and can be easily and inexpensively separated from the solution, leaving potable water. The advantages of using FO include low hydraulic pressure, high rejection of a wide range of contaminants, and less membrane fouling compared with pressure-driven membrane processes, **Zhang, et al., 2011**. A novel microbial osmotic fuel cell (MOFC) has been developed to simultaneously treat wastewater, extract clean water, and produce bioelectricity. MOFCs integrate both FO and MFCs into one bioreactor by replacing ion exchange membranes with FO membranes. This change helps to realize the extraction of high-quality water from the wastewater during the electricity-generating process, **Zhang and He, 2012**. The use of MOFCs represents a new approach for desalination, but the operational conditions and reactor designs have varied widely. Wastewater can be a good source for energy to desalinate salt water, but acetate has been used as the fuel for most studies in order to create uniform operating conditions for testing desalination aspects of the system performance. **Kim, and Logan, 2013 and Zhang and He, 2013**, developed a system consisting of two membrane-based bio-electrochemical reactors to treat artificial wastewater and desalinate saline water. The coupled system significantly improved desalination efficiency through both dilution (in the MOFC) and salt removal in the microbial desalination cell (MDC) and achieved more organic removal than an individual MDC. It was found that the COD removal 85% and energy production 0.160 kWh/m^3 could be achieved. **Werner, et al., 2013**, developed an air-cathode microbial osmotic fuel cell (MOFC) which has a forward osmosis (FO) membrane situated between the electrodes that enable desalinated water recovery along with power generation. The performance of this new design was compared to conventional microbial fuel cells containing a cation (CEM) or anion exchange membrane (AEM). Internal resistance of the MOFC was reduced with the FO membrane compared to the ion exchange membranes; resulting in a higher maximum power production of 43 W/m^3 compared to 40 W/m^3 and 23 W/m^3 obtained with AEM and CEM, respectively. The initial water flux declined by 28% from cycle 1 to cycle 3 of operation but stabilized at 4.1 LMH over the final three batch cycles. It is shown that MOFCs have less change in electrolyte solution pH compared to those with AEM and CEM membranes. **Pardeshi, and Mungray, 2014**, investigated the performance of a laboratory made FO



membrane in MOFC treating glucose as substrate and 2M NaCl as draw solution. The FO membrane was able to achieve $18.43 \text{ lm}^{-2} \text{ h}^{-1}$ (LMH) water flux and for fouled FO membrane it was $15.26 \text{ lm}^{-2} \text{ h}^{-1}$. The MOFC constantly produced bioelectricity and achieved maximum current density of 139.52 A/m^3 and power density 27.38 W/m^3 . The energy production of MOFC was 0.438 kWh/m^3 .

The present study aimed to investigate the performance of a continuously operated three-chambered microbial osmotic fuel cell (MOFC) for simultaneous wastewater treatment, saline water desalination, and power generation. The MOFC was fueled with actual domestic wastewater and inoculated with freshly collected activated sludge.

2. MATERIALS AND METHODS

2.1 MOFC System

The proposed MOFC consisted of three chambers: the anode, a mid desalination chamber, and the cathode chamber. The bio-electrochemical reactor was made from Plexiglas sheets, which were assembled with silicon tape. The anode compartment was placed at the left side with dimensions of $15 \text{ cm} \times 15 \text{ cm} \times 20 \text{ cm}$. The mid desalination cell had dimensions of $15 \text{ cm} \times 15 \text{ cm} \times 10 \text{ cm}$ and the cathode chamber was placed at the right side with dimensions of $15 \text{ cm} \times 15 \text{ cm} \times 20 \text{ cm}$. The anode chamber had three ports, one for wastewater inlet, the other for treated effluent, and the third for nitrogen flushing. The mid chamber had only two ports one for the brackish water inlet, and the other for discharging the treated brackish water. The cathode chamber had three ports, one for catholyte inlet, the other for catholyte replacement, and the third port for air sparging. The mid chamber had two membranes, FO membrane placed between the mid and the anode chamber and CEM membrane placed between the mid and cathode chamber. This was achieved by sandwiching each membrane between two perforated Plexiglas sheets containing 100 holes, each of 5 mm diameter distributed uniformly. Four identical plain uncoated graphite plates were used as electrodes for both anode and cathode. The dimensions of each electrode were $13 \text{ cm} \times 12 \text{ cm} \times 0.3 \text{ cm}$ with a total surface area for each electrode of 653 cm^2 in each chamber. The graphite electrodes were abraded by sand paper to enhance bacterial attachment. These electrodes were connected with copper wires by alligator clamps in order to provide connections to an external electrical circuit, through which the electrons were transferred. Before using the electrodes in the MOFC, they were soaked in deionized water for a period of 24 h.

2.2 Substrate, Inoculums, and Chemicals

Actual domestic wastewater samples were freshly collected from the outlet of the primary clarifier at Al-Rustamia Wastewater Treatment Plant (Baghdad) to continuously operate the MOFC system. The quality of actual domestic wastewater is given in **Table 1**.

The brackish water in this study represents the draw solution used in the mid chamber. This solution was prepared by dissolving 130000 mg NaCl, 10000 mg KCl, and 8000 mg MgSO_4 in one liter of distilled water resulted in a total TDS of 148000 mg/L.

The MOFC was inoculated with activated sludge samples collected from the bioreactor of Al-Rustamia Wastewater Treatment Plant. The collected sludge was considered as the source for the active biomass.

To enrich the microorganisms growth in the MOFC, mineral salts medium (MSM) was used. The MSM solution was prepared according to the procedure outlined in , **Jang, et al., 2004**. The solution was prepared by dissolving 0.56 g $(\text{NH}_4)_2\text{SO}_4$, 0.20 g $\text{MgSO}_4 \cdot 7\text{H}_2\text{O}$, 15 mg CaCl_2 , 1 mg $\text{FeCl}_3 \cdot 6\text{H}_2\text{O}$, 20 mg $\text{MnSO}_4 \cdot \text{H}_2\text{O}$, 0.42 g NaHCO_3 in one liter distilled water, and then the



solution was autoclaved at 121 °C for 20 min and cooled under oxygen-free nitrogen gas before use. The catholyte solution was used as an oxidant at the cathode chamber of the MOFC. The catholyte was a phosphate buffer solution (PBS) consisted of 20.7492 g/L Na₂HPO₄, 3.1167 g/L NaH₂PO₄, and 32.930 g/L of K₃Fe(CN)₆ prepared according to ,**Wei, et al., 2011**.

2.3 Set up of MOFC

Before the construction and set up of the MOFC system, all the components of the microbial fuel cell were cleaned very well with proper detergent, significantly and repeatedly rinsed with tap water, and then with distilled water.

The CEM membrane was soaked in a sodium chloride solution for 24 h before use. The FO membrane was soaked in deionized water for 30 min (as per manufacturer's instructions). When testing the FO membrane, extensive care was taken into consideration to ensure that the active layer was oriented toward the feed solution, with support layer oriented toward the draw solution. During the assembly of the MOFC, both the anodic and cathodic compartments were filled with deionized water, gently shaken, and then emptied followed by tight closing of the ports. The anode in particular, was pre-treated and sterilized with boiled distilled water for 1 h, and then washed and re-treated for additional 30 min using refresh boiled distilled water to insure the sterilization process.

2.4 Operation of MOFC

Inoculation of MOFC with active biomass at anaerobic condition was achieved by first; flushing the anode chamber with nitrogen gas for not less than 30 min, and then the biomass was added to the anodic section. The biomass was kept in the anode chamber for 14 days, before fueling the MOFC with the actual wastewater as the substrate which was fed continuously to the anode chamber at a constant rate of 2.72 cm³/ min providing a hydraulic retention time (HRT) of 28 h. At the same time air was purged into the cathode chamber at a rate of 100 cm³/ min.

Measurement of dissolved oxygen concentration in cathode chamber indicated saturated concentrations which improves the reduction reaction. While in the anode chamber, the dissolved oxygen concentration was observed to be almost zero indicating the existence of anaerobic conditions in the anode chamber.

The TDS and conductivity of the brackish water were continuously observed and measured at the mid chamber to evaluate the MOFC performance with respect to the desalination of brackish water with time.

Water flux from the anode chamber to the mid chamber was measured by using a digital scale recording the change of water flux within a certain period of time. Water flux was either expressed in mL or calculated as liter per surface area of the FO membrane per hour (LMH).

The performance of wastewater treatment with respect to the chemical oxygen demand (COD) concentration was carried out by daily sampling of both influent and effluent of wastewater in the anode chamber.

2.5 Analytical Techniques and Calculations

2.5.1 Power calculations

The power generated by a MFC is quantified in terms of power output as follows, **Barua, and Deka, 2010**.

$$P = V_{cell} \cdot I \quad (1)$$

The current produced in MFC is calculated by measuring the potential across the load (i.e. the external resistor, R_{ext}) and by using Ohm's Law, **Logan, 2008**.

$$I = \frac{V_{cell}}{R_{ext}} \quad (2)$$

Thus, the power output can be calculated by:

$$P = \frac{V_{cell}^2}{R_{ext}} \quad (3)$$

Where: P = power (W), V_{cell} = cell voltage (Volt), I = current (Amp), R_{ext} = external resistance (Ω).

2.5.2 Power output normalized by surface area

Knowing how much power is generated by a MFC does not sufficiently describe how efficiently that power is generated by the specific system architecture. Thus, it is common to normalize power production by the surface area of the anode, so that the power density produced by the MFC is calculated by using Eq. (4), **Shukla, et al., 2004**.

$$P_{An} = \frac{V_{cell}^2}{A_{An} \cdot R_{ext}} \quad (4)$$

Where: P_{An} = power density (W/m^2), A_{An} = anode surface area (m^2)

3. RESULTS AND DISCUSSION

3.1 Substrate Removal from Wastewater

The profile of COD removal from actual wastewater is given in **Fig. 1**. The COD removal efficiency was observed for 30 days. The COD loading rate was $0.54 \text{ kg COD}/m^3 \text{ d}$. Maximum COD removal > 96% was observed after 13 days of continuous operation, and then a steady state condition was achieved after almost 15 days with an average COD removal efficiency of 90%. These findings were comparable to the maximum COD removal up to 90% reported by **Werner, et al., 2013** or a microbial osmotic fuel cell operating with acetate-based synthetically prepared wastewater and NaCl solution as the draw solution. Biological oxygen demand (BOD) was measured along with to the chemical oxygen demand (COD) measurements. Maximum BOD removal was observed achieving 72% as given in **Fig. 2**.

3.2 Electricity Generation

The system was continuously operated for 30 days; the open circuit potential was 0.424 volt. For the closed circuit, the operation of MOFC consisted of 4 phases **Figs. 3** and **4**, a rapid increase in potential difference and current generation up to 0.28 volt and 7.0 mA was observed at the 5th day. This rapid increase is due to the high proton transfer resulting from high water flux between the two sides of the FO membrane. After 5 days, the potential and current maintained stable with a slight decrease until a rapid decrease appeared after 17 days of operation. This observation was most likely due to the water flux reduction resulting from the FO fouling which restricted the protons transfer through the FO membrane, and then a stable condition was observed after 21 days operation due to the fact that the FO membrane was significantly fouled. The maximum



obtained power density and current density were 30.02 mW/ m² and 107.2 mA/ m², respectively as given in **Fig. 5**.

3.3 Brackish Water Desalination

Results revealed that the initial TDS concentration (148000 mg/L) in the draw solution was reduced by more than 91 ± 1% (**Fig. 6**). These results are more favorable than the maximum TDS removal of 57.8% previously reported by **Zhang and He, 2012**, for an osmotic microbial desalination cell (ODMC).

4. CONCLUSIONS

This study demonstrated the validity of using a hybrid design of microbial osmotic fuel cell (MOFC) for simultaneous biotreatment of wastewater, desalination of brackish water, and generating bioelectricity as well. Significant relationship between COD removal from wastewater and power generation was obtained in the MOFC fed with real domestic wastewater indicating the validity of this bio-electrochemical system for the treatment of actual effluents. Results demonstrated that the highest removal efficiency of COD from wastewater in MOFC was up to 96% after 14 days of continuous operation. Experimental results indicated that FO membrane fouling has a superior effect on the MOFC performance with respect to electricity generation. A drop in the voltage, mainly due to FO membrane fouling was observed in MOFC after 17 days of continuous operation. Desalination of brackish water reached 91% which is more than the reported results in ODMC.

REFERENCES

- Barua, P.K., and Deka, D., 2010, *Electricity Generation from Biowaste Based Microbial Fuel Cells*, International Journal of Energy, Vol. 1, 77-92.
- Franks, A.E. and Nevin, K.P., 2010, *Microbial fuel Cells*, A Current Review, Vol. 3, pp. 899-919.
- Jang, J.K., Pham, T.H., Chang, I.S., Kang, K.H., Moon, H., Cho, K.S., Kim, and B.H., 2004, *Construction and Operation of Novel Mediator- and Membrane-Less Microbial Fuel Cell*. Process Biochemistry, Vol. 39, 1007–1012.
- Kim Y., and Logan, B.E., 2013, *Microbial Desalination Cells for Energy Production and Desalination*, Desalination, Vol. 308, 122-130.
- Logan, B. E., 2008, *Microbial Fuel Cells*, John Wiley & Sons, Inc., Hoboken, New Jersey, USA.
- Pardeshi, P., Mungray, A., 2014, *High Flux Layer by Layer Polyelectrolyte FO Membrane: Toward Enhanced Performance for Osmotic Microbial Fuel Cell*, International Journal of Polymeric Materials and Polymeric Biomaterials, Vol. 63, 595-601.
- Shukla, A.K., Suresh, P., Berchmans, S., and Rajendran, A., 2004, *Biological Fuel Cells and their Applications*, Current Science, Vol. 87, 455-468.



- Wei, L., Yuan, Z., Cui, M., Han, H., and Shen, J., 2011, *Study on Electricity-Generation Characteristic of Two-Chambered Microbial Fuel Cell in Continuous Flow Mode*, International Journal of Hydrogen energy, 1-7.
- Werner, Craig M., Logan, B.E., Saikaly, Pascal E., and Amy, G.L., 2013, *Wastewater Treatment, Energy Recovery and Desalination using a Forward Osmosis Membrane in an Air-Cathode Microbial Osmotic Fuel Cell*, Journal of Membrane Science, Vol. 428, 116-122.
- Zhang, B., and He, Z., 2012, *Integrated Salinity Reduction and Water Recovery in an Osmotic Microbial Desalination Cell*, The Royal Society of Chemistry, Vol. 2, 3265-3269.
- Zhang, B., and He, Z., 2013, *Improving Water Desalination by Hydraulically Coupling an Osmotic Microbial Fuel Cell with a Microbial Desalination Cell*, Journal of Membrane Science, Vol. 441, 18-24.
- Zhang, F., Brastad, K.S., and He, Z., 2011, *Integrating Forward Osmosis into Microbial Fuel Cells for Wastewater Treatment Water Extraction and Bioelectricity Generation*, Environmental Science and Technology, Vol. 45, 6690-6696.

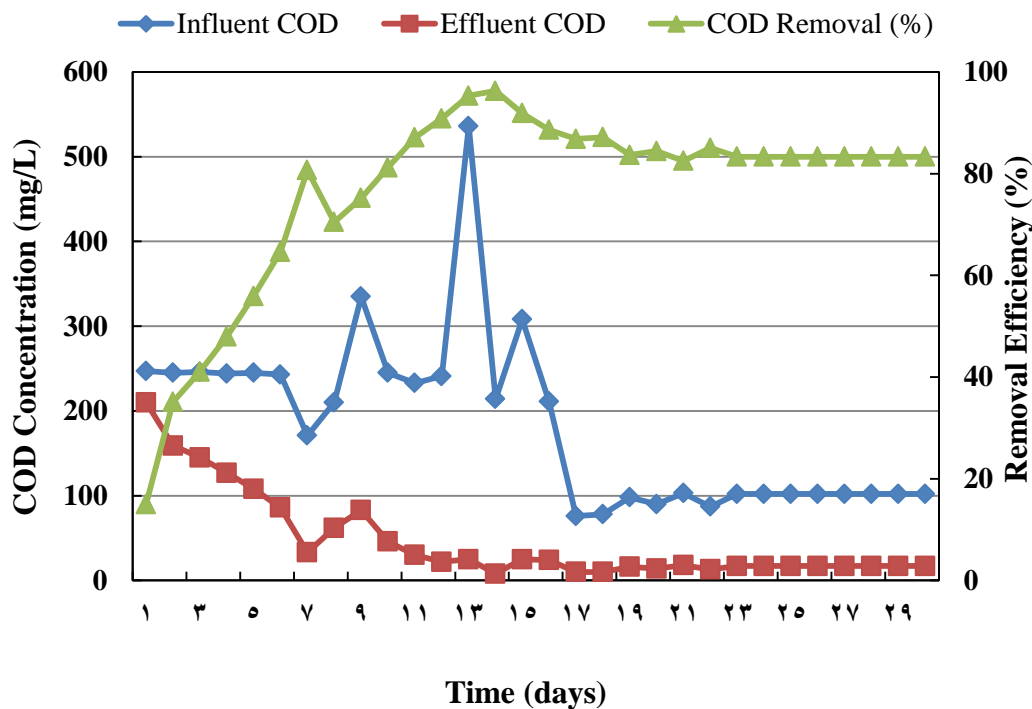


Figure 1. Profile of COD removal.

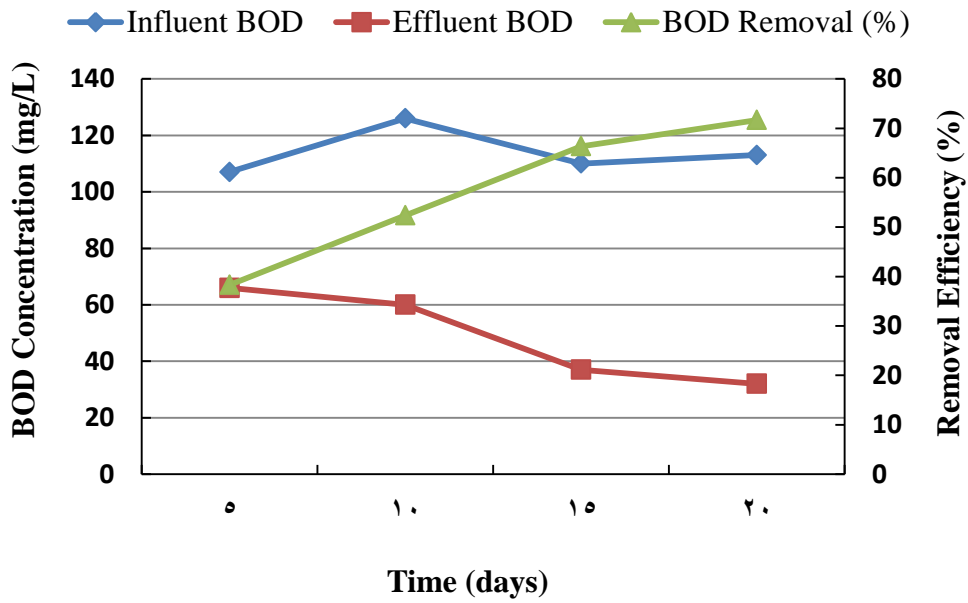


Figure 2. Profile of BOD removal efficiency.

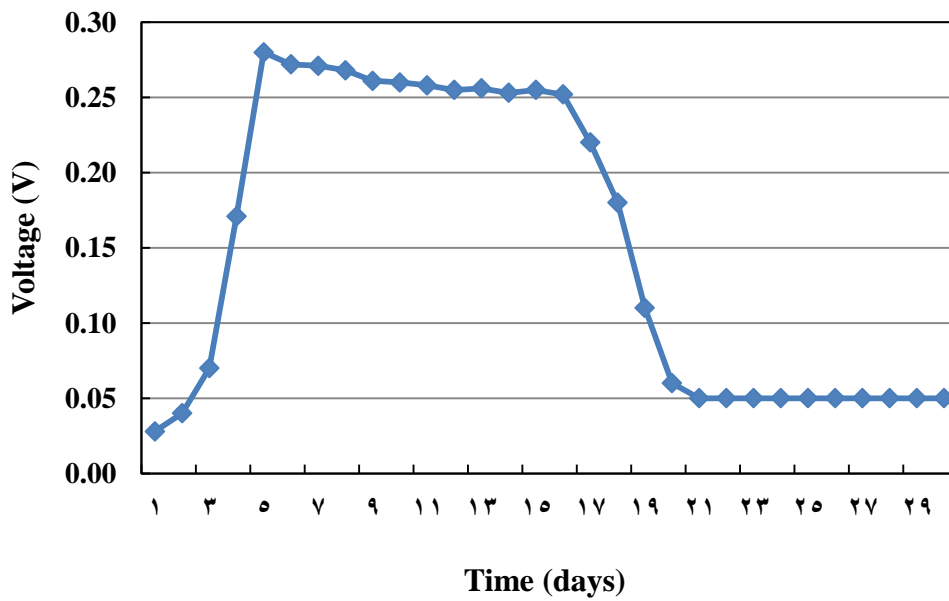


Figure 3. Variation of voltage with time.

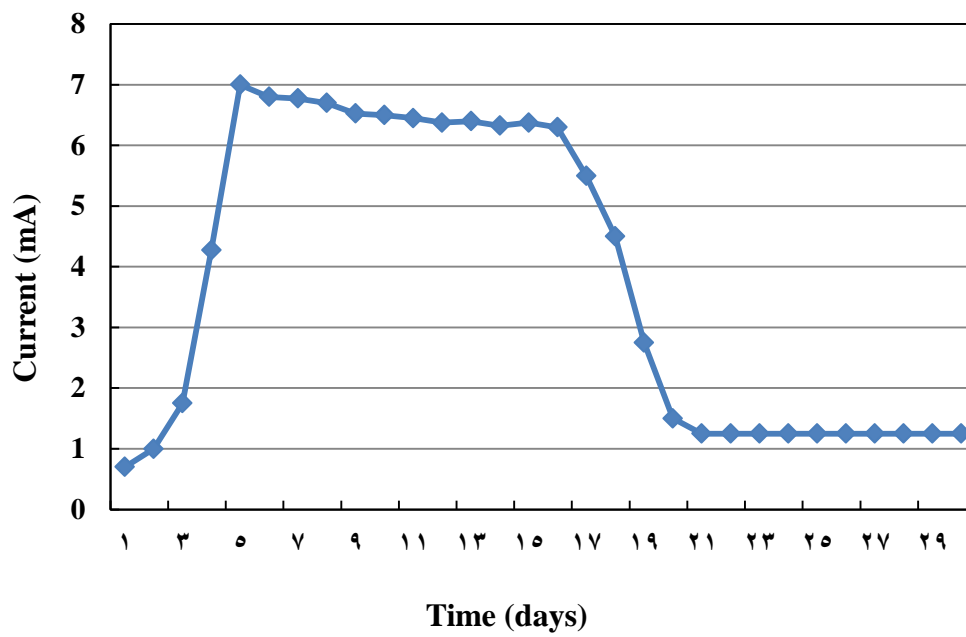


Figure 4. Variation of current with time.

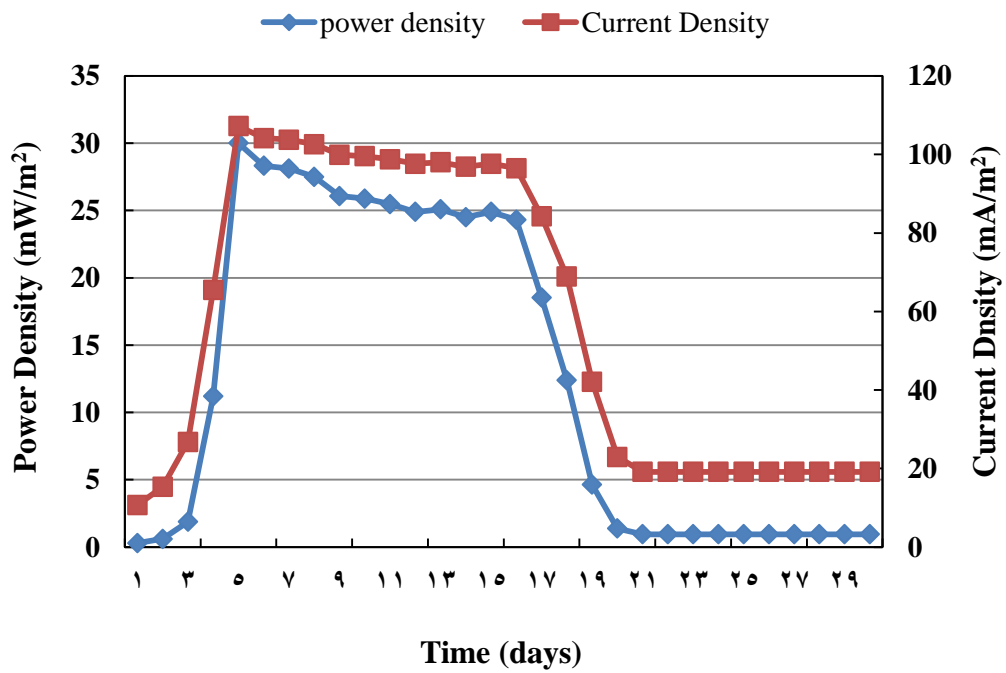


Figure 5. Variation of power and current densities with time.

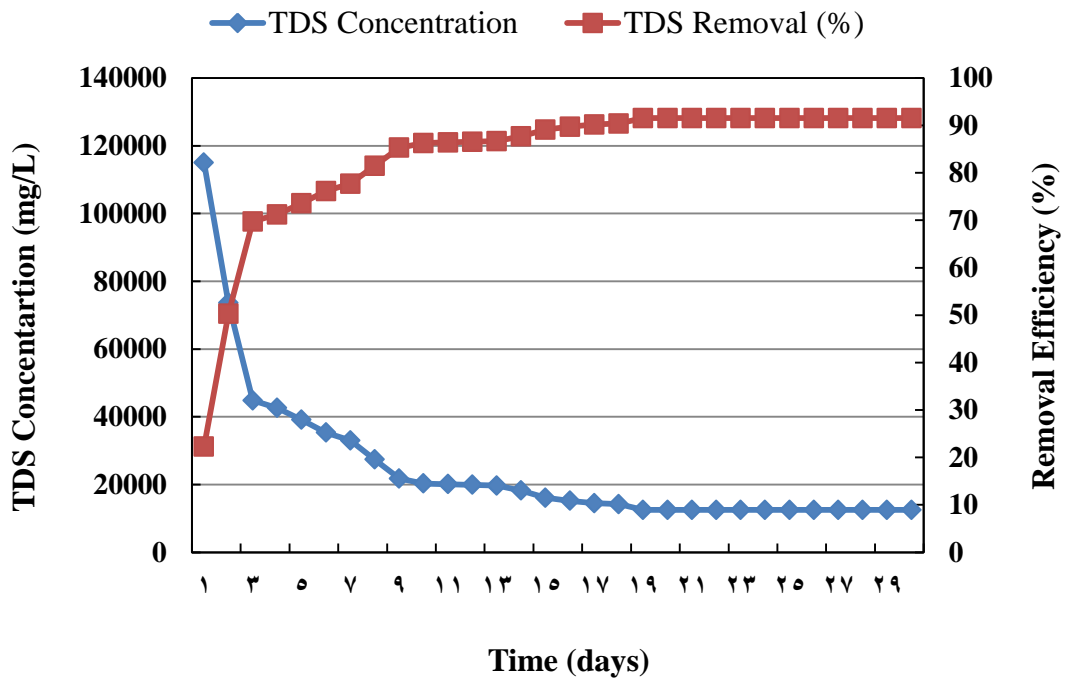


Figure 6. Profile of TDS removal.

Table 1. Quality of the actual domestic wastewater.

Constituent	Unit	Average concentration
BOD	mg/L	129
COD	mg/L	246
TSS	mg/L	105
TDS	mg/L	1750
PO ₄ ⁻³	mg/L	23.8
NO ₃ ⁻	mg/L	30
Cl ⁻	mg/L	625
SO ₄ ⁻²	mg/L	850
pH	---	7.3-7.7
Conductivity	μS/cm	2.57



Resistance to Moisture Damage of Recycled Asphalt Concrete Pavement

Prof. Saad Issa Sarsam

Department of civil Engineering

College of Engineering

University of Baghdad

saadisarsam@coeng.uobaghdad.edu.iq

Israa Lutfi AL-Zubaidi

Department of civil Engineering

College of Engineering

University of Baghdad

israaloutfi@yahoo.com

ABSTRACT

Recycled asphalt concrete mixture are prepared, artificially aged and processed in the laboratory to maintain the homogeneity of recycled asphalt concrete mixture gradation, and bitumen content. The loose asphalt concrete mix was subjected to cycle of accelerated aging, (short –term aging) and the compacted mix was subjected to (long -term aging) as per Super-pave procedure. Twenty four Specimens were constructed at optimum asphalt content according to Marshall Method. Recycled mixture was prepared from aged asphalt concrete using recycling agent (soft asphalt cement blended with silica fumes) by (1.5%) weight of mixture as recycling agent content. The effect of recycling agent on aging after recycling process behavior of asphalt concrete was determine. Aged specimens after recycling process were prepared by subjecting the recycled asphalt concrete to accelerated aging and tested for resistance to moisture damage. The improvement in the resistance to moisture damage of aged mixture after recycling with (soft asphalt cement blended with silica fumes) was 76.17% as compared to the corresponding aged mixture before recycling process. The ITS for unconditioned specimens for aged after recycling process mixture was less than reference by 67.1%, and less than that of aged before recycling process mixtures by 64.1%.

Key words: aged asphalt concrete; moisture damage; recycled asphalt concrete; recycling agent.

مقاومة الضرر بالرطوبة لرسفة الخرسانة الاسفلتية المعاد تدويرها

اسراء لطفي الزبيدي

طالبة ماجستير

قسم الهندسة المدنية

جامعة بغداد – كلية الهندسة

سعد عيسى سرسم

أستاذ

قسم الهندسة المدنية

جامعة بغداد – كلية الهندسة

المستخلص

الخرسانة الاسفلتية المعاد تدويرها تم تعريضها الى تقادم صناعي و جهزت بالمختبر للمحافظة على تجانس التدرج لخلطة الخرسانة الاسفلتية المعاد تدويرها وعلى محتوى الاسفلت. تم تحضير النماذج عند نسبة الاسفلت المثلى بواسطة تعريض خلطة الخرسانة الاسفلتية المفتتة الى دورة واحدة من التقادم المسرع (تقادم قصير الامد) ثم تحدل وتعرض الى دورة اخرى من التقادم المسرع (تقادم طويل الامد) كما في طريقة الرصف المتفوق. النماذج تم تحضيرها عند نسبة الاسفلت المثلى حسب طريقة مارشال.



الخلطة المعاد تدويرها حضرت من الخرسانة الاسفلتية المتقدمة بعد معاملتها بمنشط اعادة التدوير المكون من (الاسفلت الإسمنتي ذو الاحتراق العالي ممزوج مع غبار السليكا). كانت نسبة المنشط ١,٥ بالمئة من وزن الخلطة. تأثير منشط اعادة التدوير على خواص التقادم تم ايجاده بواسطة تحضير العينات المتقدمة بالمر بعد عملية اعادة التدوير بواسطة اعادة تعريض الخرسانة الاسفلتية المعاد تدويرها الى تقادم مسرع مرة ثانية وفحصها لمعرفة مقاومتها للضرر بالرطوبة. كانت نسبة التحسن في مقاومة الضرر بالرطوبة للخلطة المتقدمة بالمر بعد اعادة التدوير مع منشط اعادة التدوير (الاسفلت السمنتي ذو تدرج الاحتراق العالي الممزوج مع غبار السليكا) ٧٦,١٧% مقارنة مع الخلطات المتقدمة بنفس العمر قبل عملية اعادة التدوير. كانت قيم مقاومة الشد غير المباشر للنماذج المتقدمة بعد إعادة التدوير تقل بمقدار ٦٧,١% عن النماذج المرجعية كما كانت تقل بمقدار ٦٤,١% عن النماذج المتقدمة قبل إعادة التدوير.

الكلمات الرئيسية : الخرسانة الاسفلتية المعاد تدويرها، التقادم ، التقادم بعد عملية اعادة التدوير ، الضرر بالرطوبة.

1. INTRODUCTION

Most of pavement design methods are focusing on the selection of pavement structure that will have resistance to traffic and environmental conditions. The ability of the recycled asphalt concrete materials to withstand the effects of environmental conditions, such as water, ageing and temperature variations without any significant deterioration is considered as essential issue in the decision of recycling.

2. BACKGROUND

Moisture damage in asphalt concrete pavements is considered as primary cause of distresses in the asphalt pavement layers. The exposure of asphalt pavement to water is often one of the major factors affecting the durability of HMA. The water induced damage in HMA layers may be associated with two mechanisms: loss of adhesion and/loss of cohesion. In the first mechanism, the water gets trapped between the asphalt and aggregate and strips the asphalt film away, leaving aggregate without asphalt film coverage. This happens because the aggregates have a greater affinity for water than asphalt binder. The second mechanism includes the interaction of water with the asphalt cement that reduces the cohesion within the asphalt cement. This will lead to a severe reduction in the asphalt mixture strength, **Wasiuddin, 2007**.

Moisture susceptibility generally causes poor mixture durability. It may be caused by the loss of cohesive bond between binder and aggregate, usually due to moisture intrusion. This is called stripping, and it often starts at the top of the pavement and progresses downward, resulting in raveling. Moisture susceptibility can be evaluated in the laboratory by performing stability, resilient modulus, or tensile strength testing on unconditioned and moisture conditioned samples. Loss of strength is due to the weakening of the bond between the asphalt cement and aggregate. To help protect the pavement structure against moisture damage, it is necessary to determine if a mixture is susceptible to water damage in the event of water penetration , **Sondag et al., 2002**.

,Al-Rousan, et al., 2008. studied the moisture damage of recycled mixtures. Two mixtures were prepared, the first mix was composed of 100% fresh aggregate and virgin asphalt and the second mix was composed of 30% RAP and 70% fresh aggregate and virgin asphalt. Water susceptibility of the asphalt concrete mixes due to RAP usage in asphalt mixes was evaluated by measuring the reduction of the Indirect Tensile Strength (ITS) after immersion in water for 24 hours at 60°C, They concluded that the loss in ITS for mixtures containing RAP is much lower than mixtures containing



no RAP. This was attributed to the fact that RAP contains hardened asphalt that became more viscous as time passes.

Xiao et al., 2009, stated that the indirect tensile strength (ITS) and tensile strength ratio (TSR) test were conducted to evaluate the moisture susceptibility of an asphalt mixture. The results showed that the TSR values of all of the mixtures, except the virgin mix, were higher than 85%, the use of RAP in modified mixtures provided such benefits as decreasing the virgin asphalt binder content, increasing the ITS and TSR values, and thus improving the moisture resistance of HMA mixtures.

Sarsam, and Alwan 2014, studied the impact of moisture damage on pavement properties, It was concluded that the moisture-conditioned mix has lower resistance to permanent deformation (at 1000 cycles) by 93% as compared with the unconditioned mixture. Superpave asphalt concrete was shown to be durable against moisture damage by 81% at optimum asphalt content when compared to the requirement of **SCR B, 2007**.

Sarsam, and Al-Janabi 2014, studied the recycling of asphalt Mixtures with Soft asphalt or with asphalt and Sulfur, they concluded that recycled mixtures were less susceptible to moisture damage by an average value of 53% as compared to reclaimed mix and exceeded the I.R.S requirement of 70% value for virgin mixture.

Sarsam, and Alwan 2015, stated in the experimental results that, in general, the mixes subjected to moisture damage give low resistance to indirect tensile strength, low resilient modulus at 40 C, high permanent deformation at 40 C, low stiffness, and low fatigue life, by (19%, 21%, 93%, 62% and 70%) respectively as compared with unconditioned mixture.

3. RESEARCH OBJECTIVE

The main objectives for this study are evaluating the durability performance of recycled asphalt concrete mixture in terms of accelerated aging, moisture damage, and studying the effect of recycling agent on aging after recycling behavior of asphalt concrete, also investigating the effect of accelerated aging methods (Short-Term Aging) and (Long –Term Aging) on physical properties for recycled asphalt concrete.

4. MATERIALS

The Materials used in this study are locally available and selected from the currently used materials in road construction in Iraq. One type of asphalt cement (40-50) penetration grade from Dora Refinery was used in this study. Mineral aggregate (12.5 mm nominal maximum size gradation), with crushed coarse aggregate (retained on sieve no.4) was obtained from AL-Nibaae quarry. Crushed Sand and natural Sand are used as Fine aggregate (particle size distribution between sieve no.4 and sieve no.200). One type of mineral filler (Ordinary Portland Cement) has been used in this study, which is obtained from Badoush factory. **Tables 1, 2, and 3** show the physical properties of Asphalt cement, Coarse and Fine Aggregate and Filler respectively. **Fig.1** illustrates Aggregate gradation and specification limits.

5. ASPHALT CONCRETE

5.1 Mix Preparation

Asphalt concrete mixtures (Reference mixture) were prepared at optimum asphalt content (4.7%) using Marshall Method. A total of 24 asphalt concrete specimens have been prepared and tested.



5.2 Aged Materials

Reclaimed asphalt pavement (RAP) incorporated in this work was laboratory-prepared, and subjected to aging and recycling, aged asphalt concrete mixture were prepared from asphalt concrete mixture by subjecting the mix to two cycle of accelerated aging (Short-Term Aging) and then (Long –Term Aging) as per Superpave procedure. Asphalt concrete mixture was spread in shallow trays with 3 cm thickness, and subjected to two cycles of accelerated aging process by storage inside the oven at 135°C for 4 hours (Short –term aging) then compacted in accordance with ,**ASTM D1559, 2009** method. Specimens were subjected to accelerated aging process (Long – term aging) for five days at 85°C as per Superpave procedure.

5.3 Recycling Agent

Asphalt cement of penetration grade (100-150) from Al-Dura refinery was adopted in this study and blended with 2% of silica fumes which is obtained from local market; it is an ultra-fine powder consisting of nearly spherical particles around 100 times smaller than a grain of cement. Other percentages of silica fumes were also tried by testing the blend to (penetration, softening point and ductility) and 2% of silica fume was selected. Soft asphalt was heated to nearly 110°C, and the silica fumes were added to the asphalt cement with stirring until homogenous blend was achieved, the mixing and stirring was continued for 30 minutes by mechanical blender. **Tables 4 , 5 and 6** show the Physical properties of Silica Fumes, Physical properties of Soft asphalt Cement and Physical properties of recycling agent [Soft Asphalt Cement (100-150) blended with Silica fumes] respectively, Soft asphalt cement blended with silica fumes will be referred as "Soft AC+ Silica fumes" in this study.

5.3 Preparation of Recycled Mixture

Aged specimens were heated to 140° C to become loose. 1.5 % of the recycling agent based on previous work by ,**Sarsam, 2007**, was added and mixed for two minutes until all mixture is visually coated with recycling agent. Marshall Specimens were constructed from the loose recycled mix after heating the material to 150°C.

5.4 Preparation of Aged Mixture after Recycling

Recycled specimens were also heated to 140°C to become loose, then spread in shallow trays with 3cm thickness and subjected to two cycles of accelerated aging process by storage inside the oven at 135°C for 4 hours (Short –term aging). The aged asphalt concrete was then compacted in accordance with ,**ASTM D1559, 2009**, method and subjected to accelerated aging process (Long – term aging) for five days at 85°C as per Superpave procedure.

6. LABORATORY EVALUATION OF MOISTURE DAMAGE

6.1 Indirect Tensile Strength Ratio Test

The test was performed to evaluate the moisture damage resistance of mixtures, and the procedure followed ,**ASTM D4867, 2009**. A set of six specimens were prepared, three specimens were tested for indirect tensile strength by storing in a water bath at 25°C for 30 minutes, and an average value of ITS for these specimens was computed as SI (ITS for unconditioned specimens). The other three specimens were conditioned by placing in volumetric flask 4000-ml heavy- wall glass filled with



water at room temperature of 25°C, then a vacuum of 28mm Hg (3.74 kPa) was applied for 5 to 10 min. to obtain 55 to 80 % degree level of saturation. The specimens then placed in deep freeze at -18°C for 16 hours. The frozen specimens were moved to a water bath for 24 hours at 60°C, then they were placed in a water bath at 25°C for 1 hour, and they were tested for indirect tensile strength, the average value was computed as SII (ITS for moisture-conditioned specimens). The indirect tensile strength was calculated by Eq.(1)

$$ITS = \frac{2000 * P}{\pi * t * D} \dots\dots\dots(1)$$

Where:

- ITS = Indirect tensile strength, KPa
- P = Maximum load resistance at failure, N
- D = Diameter of specimen, mm
- T = Thickness of specimen immediately before test, mm.

The indirect tensile strength ratio was calculated using Eq. (2).

$$TSR = \frac{SII}{SI} * 100 \dots\dots\dots (2)$$

Where:

- TSR = Indirect tensile strength ratio, %
- SI = Average ITS for unconditioned specimens, kPa
- SII = Average ITS for moisture-conditioned specimens, kPa

7. ANALYSIS AND DISCUSSION OF TEST RESULTS

The ITS for unconditioned specimens for aged mixture was lower than reference mixture by 8.37%, it may be attributed to the fact that failure plane was different from that of Marshall test and it was very stiff mix in moderate temperature so it fails faster than others. For recycled mix, specimens showed higher deformation on failure (higher flexibility) of recycled mix when compared with the reference mixture, it was lower than that of reference by 42.21%, this might be related to the density of recycled mix which is lower than reference mix, and the higher viscosity of binder in recycled mix compared to reference mix. This agrees well with the findings addressed by **Celauro et al., 2010**, **Silva et al., 2012** and **Sarsam, 2007**. The tensile strength for aged after recycling process was less than reference by 67.1%, and less than aged mixtures by 64.1%, such behavior was related to decrease of stiffening of mixture in (STA and LTA) mix due to the effect of recycling agent.

Fig. 2 illustrates the ITS values for each mixture type.

Tensile strength ratio shows low values as compared with reference mixtures, (57.58%) for (STA+LTA) mixture. This could be due to aging process so the resistance to water damage decrease. On the other hand, the recycled mix shows higher values when compared with aged mixtures. This was due to recycling process so the resistance to water damage increase and become more susceptible to temperature due to the increase in binder content of this mixture, such finding agreed with **Sondag et al., 2002**, **Xiao and Amirkhanian, 2007**. TSR was lower than that of reference about 16.47%.



The result showed that tensile strength ratio of aging after recycling mixture shows good resistance to the action of water when compared to the aged mixture before recycling process. TSR was more than that of (STA+LTA) mixture by 76.17% and less than that of reference mix by 25.26%. **Fig.3** illustrates TSR for each mixture type.

8. CONCLUSIONS

1. The ITS for unconditioned specimens for aged after recycling process mixture was less than reference by 67.1%, and less than that of aged before recycling process mixtures by 64.1%, it was related to decreasing of stiffening of mixture in aged mix due to the effect of recycling agent.
2. Aged mixtures showed lower resistance to moisture damage, the percentages of variation for (STA+LTA) mixture as compared to reference mixture was -57.58%, On the other hand, an improvement in mixtures properties when recycled with (Soft Ac+ Silica Fume) recycling agent, properties was noticed when the percentages of variation of mixtures properties compared with reference mixture is about -16.47%.
3. Aged after recycling mixtures had good resistance for water damage, the percentage of improvement for aged after recycling process mixture was 76.17% as compared to aged mixture before recycling process.

REFERENCE

- Al-Rousan, T., Asi, I., Al-Hattamleh, O., and Al-Qablan, H., 2008, “*Performance of Asphalt Mixes Containing RAP*” Jordan Journal of Civil Engineering, Volume 2, No. 3, PP. 218-227.
- American Society for Testing and Materials, 2009, “*Annual Book of ASTM Standards, Road and Paving Materials; Vehicle-Pavement System*” Vol. 04.03.
- Celauro, C., Bernardo, C., and Gabriele, B., 2010, “*Production of Innovative, Recycled and High-Performance Asphalt for Road Pavements*” Resources, Conservation and Recycling, Vol. 54, PP. 337-347.
- Sarsam S.I., 2007, “*A Study on Aging and Recycling of Asphalt Concrete Pavement*” University of Sharjah Journal of Pure and Applied Sciences, Vol. 4, No. 2, pp. 79-96.
- Sarsam S.I. and Alwan A. H. 2014, “*Impact of Moisture Damage on Rutting Resistance, Shear and Tensile Properties of Asphalt Pavement*” International Journal of Scientific Research in Knowledge, IJSRK 2(10), pp. 453-462.
- Sarsam S.I. and Alwan A.H. , 2015 “*Properties of Superpave Asphalt Concrete Subjected to Impact of Moisture Damage*” Journal of Engineering, No. 1 Vol. 21 January, PP1-14, Iraq.



- Sarsam S.I. and AL-Janabi I.A., 2014, “Assessing Shear and Compressive Strength of Reclaimed Asphalt Concrete” International Journal of Scientific Research in Knowledge, IJSRK 2(8), pp. 352-361.
- Scholz, T. V., 1995, “Durability of Bituminous Paving Mixtures”, PhD Thesis. Nottingham Pavement Engineering Center. Nottingham, School of Civil Engineering, Nottingham University.
- Silva, H.M.R.D., Oliveira J.R.M., and Jesus, C.M.G., 2012, ”Are totally recycled Hot Mix Asphalts a Sustainable Alternative for Road Paving” Journal of Resources, Conservation and Recycling, VOL. 60, PP. 38-48.
- Sondag, M.S., Chadbourn, B.A., and Drescher, A., 2002, “ Investigation of Recycled Asphalt Pavement (RAP) Mixtures” Report No. MN/RC – 2002-15, Minnesota Department of Transportation.
- Wasiuddin, N., 2007, “Effect of Additives on Surface Free Energy Characteristics ofAggregates and Binders in Hot Mix Asphalt”, the Texas Transportation Institute (TTI).
- Xiao, F., Amir Khanian, S.N., Shen, J., and Putman, B., 2009, “ Influences of Crumb Rubber Size and Type on Reclaimed Asphalt Pavement (RAP) Mixtures” Construction and Building Materials, Vol. 23, PP. 1028-1034.
- Xiao F. and Amir Khanian S.N.,2007, “ Laboratory Investigation of Moisture Damage in Rubberized Asphalt Mixtures Containing Reclaimed Asphalt Pavement”, International Journal of Pavement Engineering, Department of Civil Engineering, Clemson University, Clemson, South Carolina 29634-0911, USA.

Table 1. Physical properties of asphalt cement.

Property	Test Conditions	ASTM Designation No.	Value	SCRB Specification
Penetration	25°C , 100gm , 5 sec	D5-06	41	40-50
Softening point	(ring & ball)	D36-895	49 °C	-
Ductility	25°c ,5cm/min	D113-99	>150	+100
Specific gravity	25°C	D70	1.04	-
Flash point	Cleveland open cup	D92-05	275 °C	>232
After thin film oven test properties D1754-97				
Retained penetration	25°C , 100gm , 5 sec	D5-06	60%	55>
Ductility of residue	25°C ,5cm/min	D113-99	85cm	25>
Loss on weight	163°C, 50g, 5 hrs.		0.3	-

**Table 2.** Physical properties of coarse and fine aggregate.

Property	Value	ASTM Designation No.
Coarse Aggregate		
Bulk specific gravity	2.584	C127-01
Apparent specific gravity	2.608	C127-01
Water absorption %	0.57%	C127-01
Wear % (Los Angeles abrasion)	13.08%	C131-03
Fine Aggregate		
Bulk specific gravity	2.604	C128-01
Apparent specific gravity	2.664	C128-01
Water absorption %	1.419%	C128-01

Table 3. Physical properties of filler (cement).

Property	Value
Bulk specific gravity	3.14
% Passing Sieve No.200	96

Table 4. Physical properties of silica fumes.

Property	Value
Bulk specific gravity	2.134
% Passing Sieve No.200	100

Table 5. Physical properties of soft asphalt cement.

Property	Test Conditions	ASTM Designation No.	Value
Penetration	25°C , 100gm , 5 sec	D5-06	120
Softening point	(ring & ball)	D36-95	25 ° C
Ductility	25°C ,5cm/min	D113-99	80cm
Flash point	Cleave land open cup	D92-05	250 °C
After thin film oven test properties D1754-97			
Retained penetration of residue	25°C , 100gm , 5 sec	D5-06	66%
Ductility of residue	25°C ,5cm/min	D113-99	30cm
Loss on weight	163°C,50g,5hr		0.35%

Table 6. Physical properties of soft asphalt cement (100-150) blended with silica fumes.

Property	Test Conditions	ASTM Designation No.	Value
Penetration	25°C , 100gm , 5 sec	D5-06	163
Softening point	(ring & ball)	D36-95	35° C
Ductility	25°C ,5cm/min	D113-99	88cm
Flash point	Cleveland open cup	D92-05	260 °C
After thin film oven test properties D1754-97			



Retained penetration of residue	25°C , 100gm , 5 sec	D5-06	53%
Ductility of residue	25°C ,5cm/min	D113-99	22cm
Loss on weight	163°C,50g,5hr		0.2%

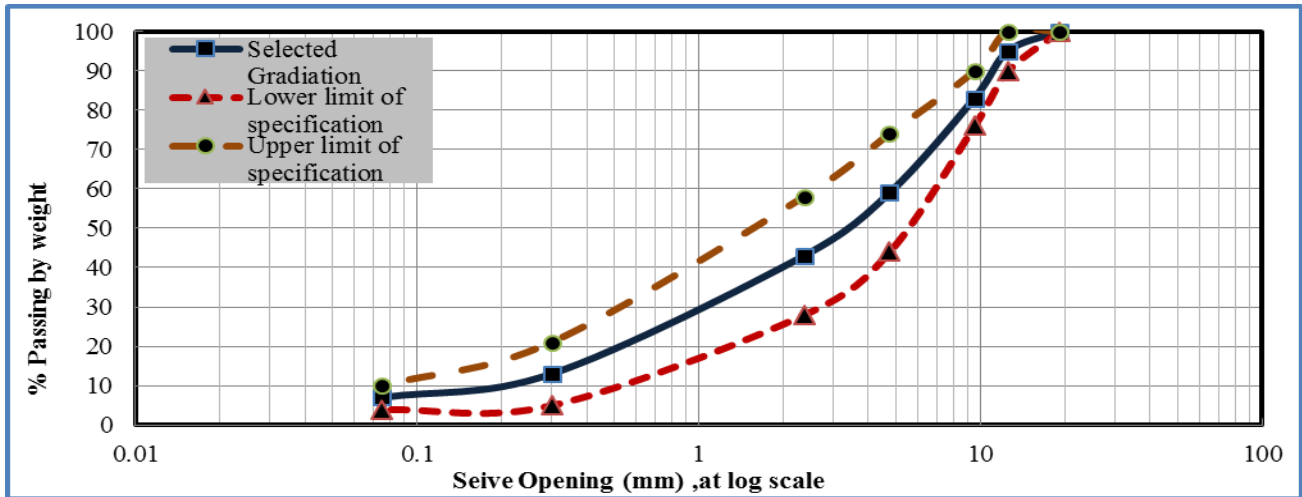


Figure 1. Selected aggregate gradation and specification limits.

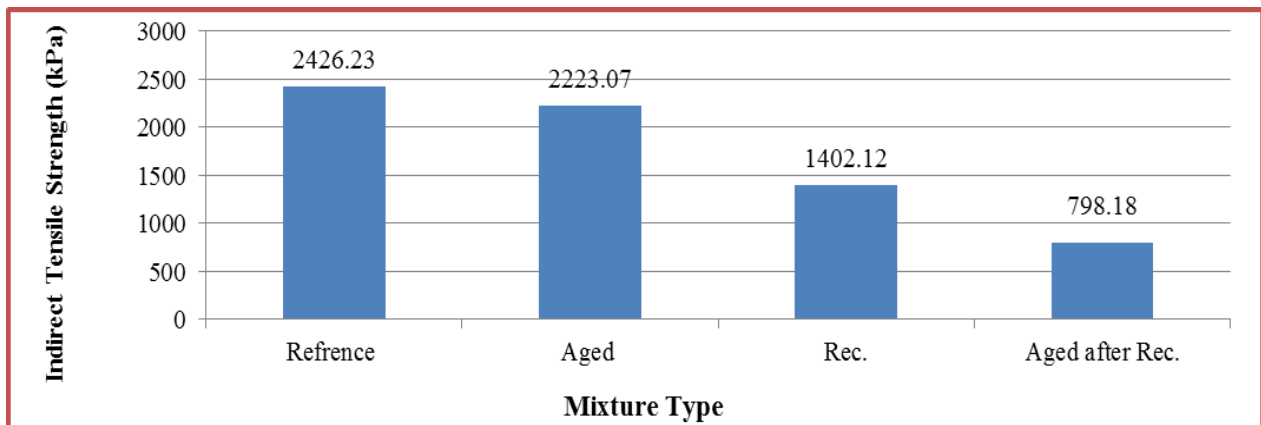


Figure 2. ITS values for each mixture type.

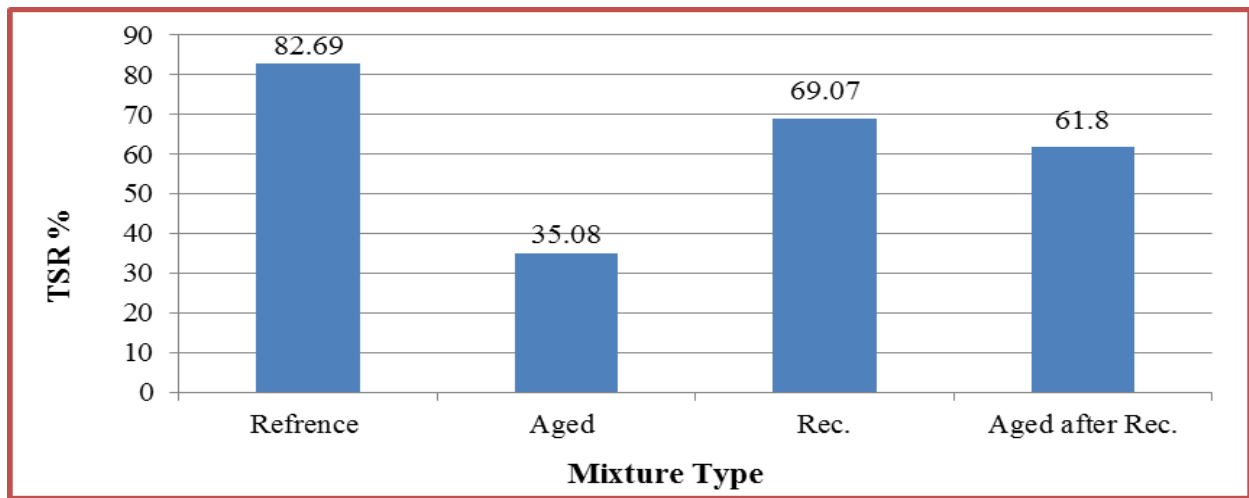


Figure 3. TSR for each mixture type.



Experimental Study of the Thermal Performance of Flat Plate Solar Collectors Array by Different Connection Configurations

Dr. Jafar Mehdi Hassan
Professor
Department of Mechanical Engineering
University of Technology
Email : Jafarmehdi1951@yahoo.com

Dr. Qussai Jihad Abdul-Ghafour
Assistant Professor
Department of Mechanical Engineering
University of Technology
Email: kaisyj@yahoo.com

Mohammed Fowzi Mohammed
Lecturer
Department of Mechanical Engineering
University of Technology
Email : mohammed2007msc@yahoo.com

ABSTRACT

The current research illustrates experimentally the effect of series and parallel connection (Z-I Configurations) of flat plate water solar collectors array on the thermal performance of closed loop solar heating system. The study includes the effect of changing the water flow rate on the thermal efficiency. The results show that, the collector's efficiency in series connection is higher than the parallel connection within flow rate level less than (100) ℓ/hr. Moreover, the collector efficiency in parallel connection of (I-Configurations) is more than the (Z- Configurations) with increasing the water flow rate .The maximum daily efficiency for parallel (I-Configurations) and (Z-Configurations) are (55%) and (51%) at water flow rate (150) ℓ/ hr. It was also noted that the thermal stratification of storage tank in case of series connection is higher than that of parallel connection. Also, when the flow rate increases, the thermal stratification of storage tank reduces.

Keywords: flat plate, solar collectors.

دراسة تجريبية للأداء الحراري لمصفوفة من المجمعات الشمسية المسطحة ذات اشكال ربط مختلفة

د. قصي جهاد عبد الغفور
استاذ مساعد
قسم الهندسة الميكانيكية
الجامعة التكنولوجية

د. جعفر مهدي حسن
استاذ
قسم الهندسة الميكانيكية
الجامعة التكنولوجية

محمد فوزي محمد
مدرس
قسم الهندسة الميكانيكية
الجامعة التكنولوجية

الخلاصة

يوضح البحث الحالي تجريبيا تأثير ربط التوالي، وربط التوازي (شكل-1-Z) لمصفوفة من المجمعات الشمسية المسطحة على الاداء الحراري لمنظومة تسخين بالطاقة الشمسية مغلقة الحلقة. تضمنت الدراسة تأثير تغير معدل التدفق على الكفاءة الحرارية. بينت النتائج العملية ان كفاءة المجمعات ذات ربط التوالي اعلى من ربط التوازي عند معدل التدفق اقل من ١٠٠ لتر/ ساعة . كما بينت التجارب العملية ان كفاءة المجمعات ذات ربط التوازي (شكل-1-) اعلى من (شكل-Z-) عند زيادة معدل التدفق. ان الكفاءة القصوى لربط التوازي (شكل-1-Z) خلال اليوم (55%) و(51%) عند معدل تدفق ١٥٠ لتر/ ساعة . كما لوحظ ان التدرج الحراري للخزان في حالة ربط التوالي اعلى من ربط التوازي . بالإضافة الى ان عند زيادة معدل التدفق تقلل من قيم التدرج الحراري للخزان .

الكلمات الرئيسية: صفيحة مستوية ، مجمعات شمسية.

1. INTRODUCTION

Many numerical and experimental studies were done by of many researchers. **Wang, and WU, 1990.** studied the performance of flat plate solar collector arrays connected in parallel by analysis a new discrete numerical model is proposed to calculate the flow and temperature distribution in solar collector arrays. The numerical results show that, there are some difference in flow and heat transfer between single collector and large collector array because of the flow non uniformity. **Bong, et al., 1993.** studied a theoretical model for the determination of efficiency, heat removal factor and the outlet water temperature of single collector and an array of flat heat pipe collectors. The results show that ,for flat plate heat pipe collector ,or when two or more collectors connected in series ,there is linear relationship between the efficiency and parameter $(T_{fi}-T_a)/I$ under steady state conditions . A solar heating system with a water source heat pump was investigated experimentally in north China by **,Kuang, et al., 2003.** The system consists of five flat plate solar collectors were combined in a parallel array with a total net area of (11 m^2) . The results show that, a good thermal performance because of the low operating temperature. The high collector efficiencies were obtained, and the mean value was (67.2%) . The use of an auxiliary heater inside the storage tank lead to a waste of energy due to the large heat loss from the storage tank, **Myeong , et al., 2006** showed a collector consists of a network of riser tubes and headers. If the rows of the flat- plate collectors connected in series , they form a large flat- plate collector . They found that the thermal efficiency of the collector assembly is mainly influenced by the number of riser tubes, collector aspect ratio, mass flow rate, thermal conductivity and thickness of absorber plate. Differences in the range of $(2.5\%-8\%)$ were detected depending on the specific parameter tested. **Yi-Mei, et al., 2012,** presented a Thermosyphon solar water heater employed in applications when considerable hot water consumption is required. In this experimental investigation, eight typical Taiwanese solar water heaters were connected in series. The temperature stratification and thermosyphon flow rate in a horizontal tank were evaluated. The system was tested under no-load, intermittent and continuous load conditions. The thermal efficiency for intermittent load conditions is about $(5.8\% \text{ to } 7.0\%)$ higher than the value for the no-load condition. **Khaled, et al., 2012,** presented two systems. The first, Solar Direct Hot Water, which is composed of flat plate collectors and thermal storage tank, the second, a Solar Indirect Hot Water in which they added an external heat exchanger of constant

effectiveness to the first system. The total number of collectors is adjusted to sixty collectors. For the first system, they found the number of series collectors in solar thermal systems must be limited, the same for both direct and indirect systems. Both the series connection and optimized mass flow rate have a positive effect on the system performance, but the range of optimum mass flow rates decreases when a flat plate collector is added in series. The present work is study the effect of parallel and series connections of thermal performance and stratification of storage tank of three flat plate solar collectors array in closed loop system with different flow rates and different inlet and outlet flow directions.

2. EXPERIMENTAL WORK

The components of the experimental test rig consist of three identical flat plate solar collectors in closed loop system, each one with absorbing area of (80cm * 120cm) with one glass cover. Also ,it consists of eight equally spaced parallel copper riser pipes of (10.5mm inner and 11mm outer) diameters , and (1200mm) length. The distance between each centerline of tubes is (10 cm). These pipes are connected with two headers. The headers are made of copper material with (4.1cm) outside diameter and (80cm) length. Each of headers consists of several holes ,two holes in the sides and one in the middle (between riser 4-5) which lead to the inlet and outlet of the collector . The absorbing plate was manufactured in fabricated way through the work as curve surrounds riser pipes to increase the surface area of contacts between the plate and the riser pipe as shown in **Fig.1**. A copper sheet with (0.5mm) thickness is used as the solar radiation absorber The riser pipes are fixed on the absorbing plate by welding lead along the riser pipes as shown in **Fig. 2** . The collector frame is made of aluminum bars of (1.5mm) thick as shown in **Fig.3** . A glass sheet is used as a transparent cover of the collector with (4mm) thickness. A glass wool insulation of (50 mm) thickness was used as insulator to decrease the collector back and side heat losses. A cylindrical galvanized steel tank with (0.58 m) outside diameter and (1 m) height is used for storing hot water. The tank is insulated by a (50mm) thickness glass wool. **Figs. 4-a and 4-b** show the storage tank and position of thermocouple inside it .A plastic pipe of (15mm) diameter is used between the components of the closed loop system. They connect the storage tank, water circulation pump, flow meter and solar collectors with each other as closed loop system. The equivalent length of the closed loop in each system is (11 m) . The pipes in each loop are insulated with (25 mm) thick of glass wool insulation. In order to circulate the water in the system, a small circulation pump (CRS25/4-180) is used in closed loop to make the forced circulation. The water mass flow rate in the closed loop is controlled by using valves and measured with flow meter (Izs-15-Range (60-600LPH) with accuracy 4%. The mass flow rates used, are (60,100 and 150) ℓ/hr. The spray paint (RUSTOLEUM high heat) as the absorber surface paint is used. This Coating has high absorptance (0.92-0.96) for solar radiation is used to substrates with low emittance (0.24) ,**Rhett,2013**.

2.1 Measuring Devices and Data Analyzing

In order to measure the temperature at various points of the absorbing plate, water storage tank, inlet and outlet of collectors, T type thermocouple (copper- constantan) with the accuracy of ($\pm 0.5^{\circ}$ C) is used. The thermocouples were calibrated before beginning of the experiments. The measurement of the temperature distribution of the absorbing plate is done by using three thermocouples, one located at the centerline of the absorbing plate and the others at top and bottom with space distance of (50cm) from the centerline from the absorber plate. All thermocouples are



connected to the data logger, that's connected to a digital electronic thermometer (UT325-0.1C resolution). The data is interfaced to the computer and then displayed as a table. The ambient temperature is measured by using a digital electronic thermometer. The solar power radiation on the collector is record by solar meter with rang varied from (0 to 2000 W/m²). This device measures the total solar radiation (beam and diffuse) per unit area of the collector surface. This device could be recorded the data and save them in (SD Ram). The solar power meter was oriented due to the south at a collector tilt angle (35). This angle has been adopted for all cases of examination. To calculate the solar radiation depending on the recommended average days for months and values of n by months ,**Duffie and Beckman, 2006**. This is the recommended angle maximum yearly useful energy.

The governing relations used in the present work are:

1. Water mass flow rate (\dot{m}_w)

$$\dot{m}_w = \rho_w \cdot \dot{V}_w \quad (1)$$

\dot{m}_w : mass flow rate kg /s

\dot{V}_w : Water volume flow rate (m³/s)

The water density varies with its temperature according to the equation ,**Sinem, E., 2011**.

$$\rho_w = 1000 * (1 - (T + 288.9414)/(508929.2 * (T + 68.12963)) * (T - 3.9863))^2 \quad (2)$$

2. Useful energy (Q_u)

$$Q_u = \dot{m}_w \cdot (C_p)_{water} \cdot (T_{fout} - T_{fin}) \quad (3)$$

Trapezoidal rule has been used to calculate the Useful energy (Q_u) for three flat plate solar collectors array ,**Maytham, 2014**.

$$Q_U = \sum_{ti}^{tf} q_t = b \left[\frac{Q_{U1}}{2} + Q_{U2} + Q_{U3} + \dots + \frac{Q_{Un}}{2} \right] \quad (4)$$

$$q_U = \frac{Q_U}{A_c} \quad (5)$$

3. The total solar radiation for the flat plate solar collectors array

$$Q_R = N * A_c * b * \left[\frac{GT_1}{2} + GT_2 + GT_3 + \dots + \frac{GT_n}{2} \right] \quad (6)$$

4. To calculate the solar collector's array efficiency

$$\eta = \frac{Q_U}{A_c \cdot Q_R} \quad (7)$$

The mean fluid temperature is calculate by



$$T_m = \frac{T_{fin} + T_{fout}}{2} \quad (8)$$

5. To calculate the instantaneous collector efficiency was taken as half an hour for one collector

$$\eta_i = \frac{Q_U}{A_C \cdot G_T} \quad (9)$$

6. The instantaneous collector efficiency for the flat plate solar collectors array

$$\eta_{i \text{ av.}} = \frac{\eta_{i1} + \eta_{i2} + \eta_{i3}}{N} \quad (10)$$

2.2 Test Model

The model, consist of three flat plate solar water collectors connected parallel connection (Z-configuration and I configuration) as shown in **Figs. 5 and 6** and series connection as shown in **Fig.7** In this model three different flow rate of (60,100,150) ℓ/hr. are used in this study.

2.3 Test Procedure

The experiment was carried out in Baghdad from (10th March to 15th April 2014) and these experiments were carried out during sunny days only .The slope angle of three closed looped collectors is (35 deg.). The collectors was tested under steady-state conditions in which the solar intensity, ambient temperature, inlet and outlet temperature difference were considered constant for period of time. The period was taken as half an hour for a clear day. The type of test was to estimate the instantaneous performance of the system. Before each test, the following preparations were made.

- The closed collector loop was filled with water, the glass cover of the collectors were cleaned.
- The storage tank, was filled with water and the pump was operate with the maximum flow rate half an hour every day before starting the experiments, to eliminate trapped air from the system .
- The system was tested with three different flow rates of water through the collector loop.
- In each case, experiments usually started at (8 am and continued until 5 pm).
- In each test and each time period all the measurements of temperatures, solar radiation intensity, the instantaneous efficiency, heat collection and absorbing energy were recorded for each collector.

3. RESULTS AND DISCUSSION

3.1 Relationship between Solar Energy and Useful Energy and Absorber Plate Temperature

Fig.8 shows the relationship between solar energy and useful energy, for three different connections of flat plate solar collectors array at different flow rates and flow directions. It is clear that the useful energy curves have the same trends of the solar radiation. The results show that as the mass flow rate increases, the useful energy gain increase. The useful energy of the series connection is greater than parallel connections when the flow rate at (60) ℓ/hr. But when

the flow rate increases the useful energy of series connection decreases. This effect, because of a long the path that the fluid interrupted by series connection than parallel connection. This confirms that the thermal losses in parallel connection less than series connections when the flow rate increase. In the parallel connection, the useful energy gain of (I-Configuration) greater than (Z-Configuration), because of increase the particle mixing due to increase mass flow rate in the middle risers than side riser pipes and hence the heat transfer coefficient increase. **Tables 1,2 and 3** show the variation of useful energy with time for different flow rates presented in this study. The behavior of useful energy obtained for one collector (Z-Configuration) at the flow rate 100 l/hr. as compared with ,**Maytham, 2014**, as shown in **Fig.9** . In **Fig .10** shows, the temperature distribution of the absorber plate and ambient temperatures with time as shown in. The temperature of the absorber plate is not the same, where ($T_{P3}>T_{P2}>T_{P1}$) because of, the temperature of the absorber plate increase along the direction of water flow in risers.

3.2 Performance Test of Solar Water Heating

The instantaneous collector efficiencies curves for three different connections are shown in **Fig's.** (11 and 12) they observed clearly that when the mass flow rate increases, the instantaneous collector efficiencies increases and the temperature difference decrease. This can be due to the lower mass flow rate which takes more time to absorb solar radiations ,**Duffie and Beckman, 2006**. The decreasing of the temperature difference between absorber plate and ambient lead to decreasing thermal losses in collector, then the collector efficiency will increase, **Peter, 1979**. The instantaneous collector efficiencies curves for parallel connection is higher than series connection at flow rate increase, because of thermal losses in parallel connection less at rates greater than series connections when the flow rate increase. The results show the overall daily efficiency of 100 l/hr. of parallel connection (I-Configuration) is (50%), while parallel (Z-configuration) and series connections are (47.6% and 42%) respectively .For increase mass flow rate to 150 l/hr. , the overall daily collector efficiency increasing. In (I-Configuration) is (55%) while, (Z-configuration) and series connections are (51% and 48.4%) respectively. **Table 4**. Instantaneous collector efficiencies with time at flow rates (100-150 l/hr.).The data of instantaneous collector efficiencies for one collector (Z-configuration) at 150 l/hr. as compared with ,**Herrero , et al .**, as shown in **Fig.13**.

3.3 Effect the Stratification of Storage Tank

Thermal stratification in storage tanks has a significant positive effect on the system efficiency. **Figs. 14 and 15** show the effect of stratification of storage tank for different flow rates. The water temperatures difference between the top and bottom in the storage tank in case of series connection for the mass flow rate of order (60,100 and 150) l/hr. at (11 am) are (11.3 °C, 8.5 °C are 7.8 °C) respectively. While, the water temperature difference in case of parallel connection (Z-Configuration) are (9.3 °C, 6.5 °C and 5.8 °C) respectively, and in case of parallel connection (I-Configuration) are (8.1 °C, 7.1 °C and 6 °C) respectively for the same water flow rates and time period. Therefore the stratification of storage tank in case of series connection is higher than the parallel connection mode. The average water temperature of the storage tank at the end periods (3-5 pm) in case of parallel connection is higher than the series connection. Where the maximum average temperature at (5pm) for the flow 100l/hr. in case of parallel connection (I-Configuration) is (64.2 °C) and in case of (Z-Configuration) is (63.5 °C), while the maximum average temperature in case of series connection is (61.2 °C). This because of the parallel connection stored larger quantities of energy than the series connection. Due to, increase the temperature drops, resulting in higher inlet



temperature to the second and third collectors .That's leads finally to reduce the temperature difference significantly in case of series connection mode .

4. CONCLUSION

From the present work, we can conclude that:

- The efficiency of series connection greater than parallel connection at low flow rate.
- The useful energy gain of (I-Configuration) greater than (Z-Configuration) when increase mass flow rate.
- That higher thermal stratification in the storage tank can be achieved by using a smaller flow rate.
- The stratification of series connection is more than parallel connections.

REFERENCES

- Bong, K.C. NG., and H. BAO., 1993 , *Thermal Performance of a Flat Plate Heat Pipe Collector Array*, Solar Energy, vol. 50 no. 6 , pp 491-498 .
- Duffie , J. A., and Beckman,. W. A., 2006 , *Solar Engineering of Thermal Processes*, Solar energy, laboratory, University of Wisconsin-Madison .
- Herrero Martín, R., García Pinar,A. and Pérez García, J.,2011, *Experimental Heat Transfer Research in Enhanced Flat-Plate Solar Collectors*, World Renewable Energy Congress,Sweden,8-13 May.
- Khaled Z., A. G., Ramzi S., and Chakib K., 2012 , *Solar Thermal Systems Performances Versus Flat Plate Solar Collectors Connected in Series* , Engineering, 4, 881-893.
- - Kuang, R.Z., and L.Q. Yu., 2003, *Experimental Study on Solar Assisted Heat Pump System for Heat Supply* , Energy Conversion and Management, 44 , 1089–1098 .
- Maytham A. J., 2014, *Utilization of Air-Water Solar Collector System for Space Heating*, Master Thesis university of Technology.
- Myeong C. K., Yong H. K. , Sang H. L., and Wongee, C., 2006, *Numerical Analysis on The Thermal Performance of a Roof-Integrated Flat-Plate Solar Collector Assembly*, International Communications in Heat and Mass Transfer, 33 , 976–984.
- Peter J. L., 1979, *Solar Thermal Engineering Space Heating and Hot Water System*, New York, Chichester Brisbane Toronto .
- Rhett N., , 2013 , *The Water Wall – a Passive Solar Collector and Thermal Storage Device for Supplementary Radiant Heating* , Master Thesis , University of Nevada, Las Vegas December.



- Sinem E., 2011, *Assessment of Impact of Reservoirs Contaminated Bottom Sediments on Surface Water Quality by Sediment Water Interaction Model* , Master Thesis , the Graduate School of Engineering and Sciences .
- - Wang., and L.G. WU, 1990, *Analysis and Performance of Flat Plate Solar Collector Arrays*, Solar Energy vol.45, no.2, pp71-78 .
- Yi-Mei, L., Kung-Ming C., Keh-Chin C., and Tsong-Sheng L., 2012, *Performance of Thermosyphon Solar Water Heaters in Series* , Energies, 5, 3266-3278; doi:10.3390/en5093266 .

NOMENCLATURE

A_C =collector area, m^2 .

b = time increments, s

$C_{P\text{ water}}$ =specific heat capacity of water, $kJ/kg.K$.

G_T =incident solar radiation, W/m^2 .

I =hourly solar radiation, J.

N =number of collectors.

n =for i th day of month

Q_U =useful energy, W.

q_u = useful energy per unit area, W/m^2 .

qt =the useful energy with time (b)

Q_R =total solar radiation, W/m^2 .

t_a =ambient temperature, $^{\circ}C$.

T_{fin} =inlet fluid temperature, $^{\circ}C$.

T_{fout} =outlet fluid temperature, $^{\circ}C$.

T_m = mean fluid temperature, $^{\circ}C$.

T_p =absorber plate temperature, $^{\circ}C$.

T_s =storage tank temperature, $^{\circ}C$.

\dot{m}_w =water mass flow rate , kg/s .

ρ_w =water density, kg/m^3 .

η =collector efficiency.

η_i = instantaneous efficiency.

Table 1. The useful energy with time for different connection at flow rate (60ℓ/hr.).

Time	qu-ser.(W/m ²)	qu-Z- (W/m ²)	qu-I-(W/m ²)
8.00am	174.784	196.633	168.54
8.30am	243.45	230.969	218.48
9.00am	287.153	284.033	259.06
9.30am	340.217	315.246	318.362
10.00am	368.306	371.4274	358.94
10.30am	390.158	393.279	396.39
11.00am	415.127	424.4911	440.09
11.30am	399.51	433.854	455.7
12 noon	383.915	446.3387	477.54
12.30am	377.672	424.4911	446.33
1.00pm	337.03	390.158	412
1.30pm	305.879	349.581	349.58
2.00pm	265.304	312.125	324.61
2. 30pm	227.847	268.419	287.15
3.00pm	156.05	221.6	196.62
3.30pm	109.233	162.299	146.68
4.00pm	59.298	109.233	68.65
4.30pm	28.08	46.8	40.56
5.00pm	9.362	18.725	21.846

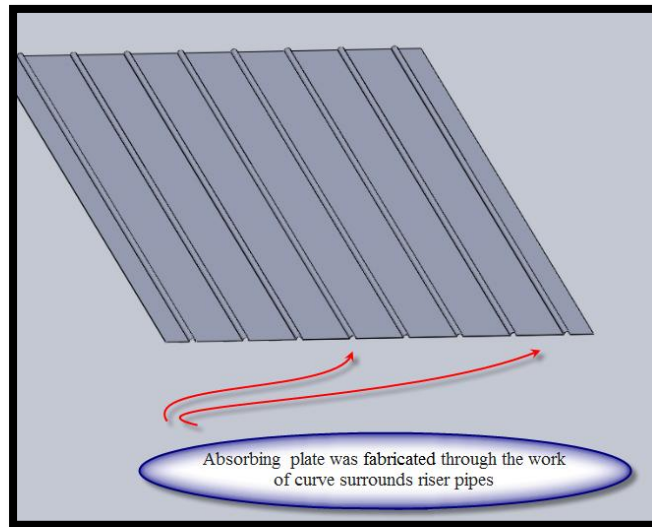
**Figure 1.** Absorber plate geometry.



Figure 2. A copper sheet welding on riser pipes.



Figure 3. Aluminum collector frame.

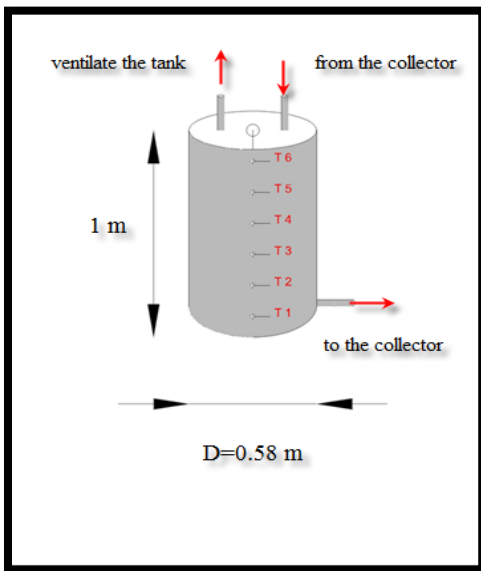


Figure 4-a. Position of thermocouple inside Storage tank



Figure 4-b. Water storage tank

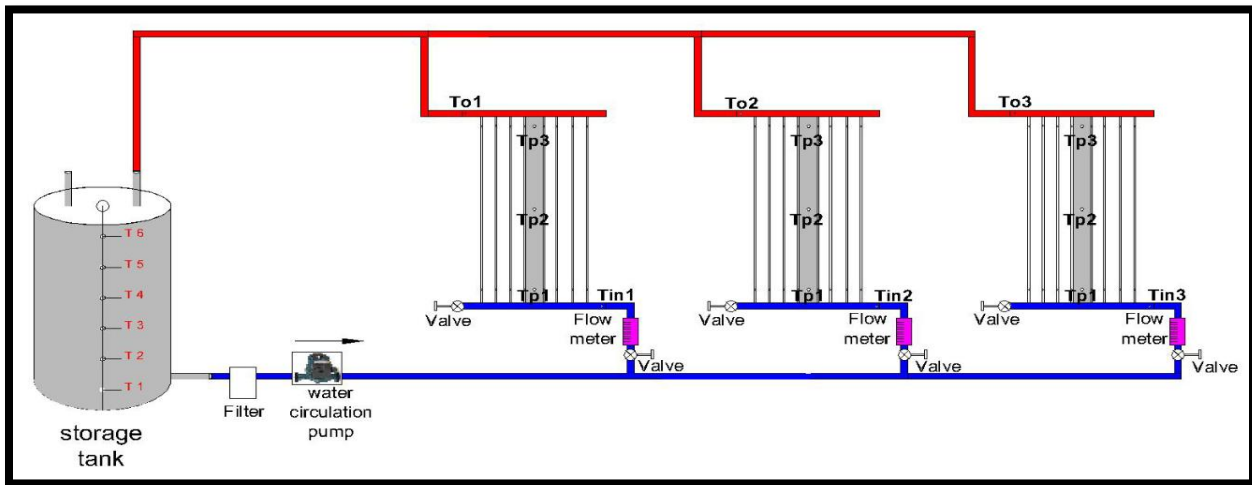


Figure 5. Three flat plate solar collector's connection in parallel mode (Z – Configuration).



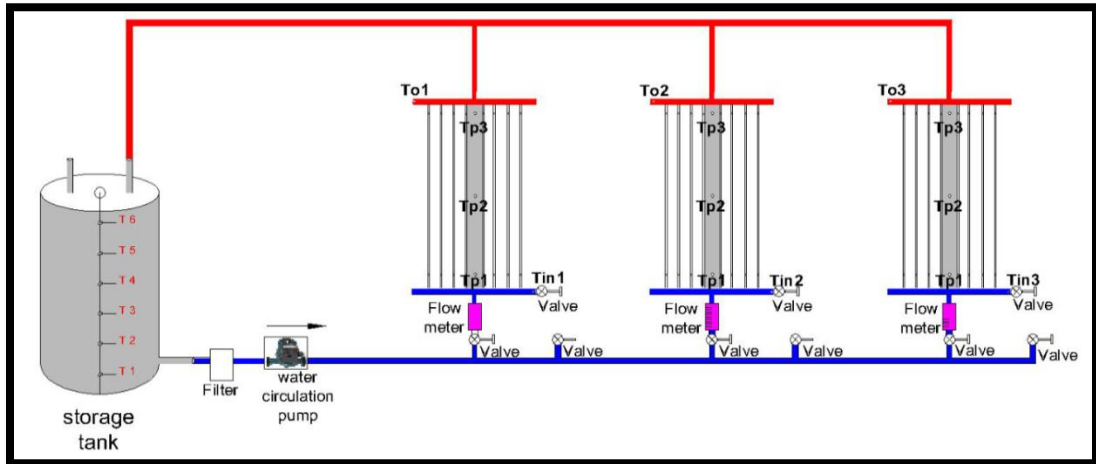
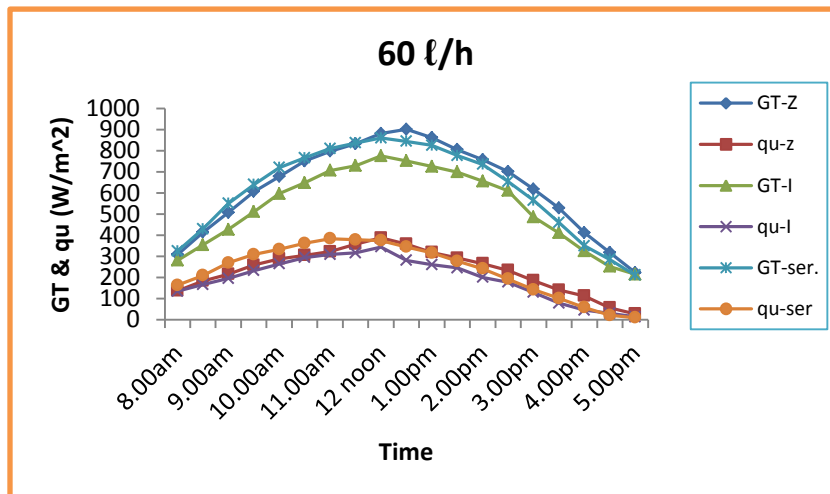


Figure 6. Three flat plate solar collector's connection in parallel mode (I – Configuration).



Figure 7. Three flat plate solar collector's connection in series.



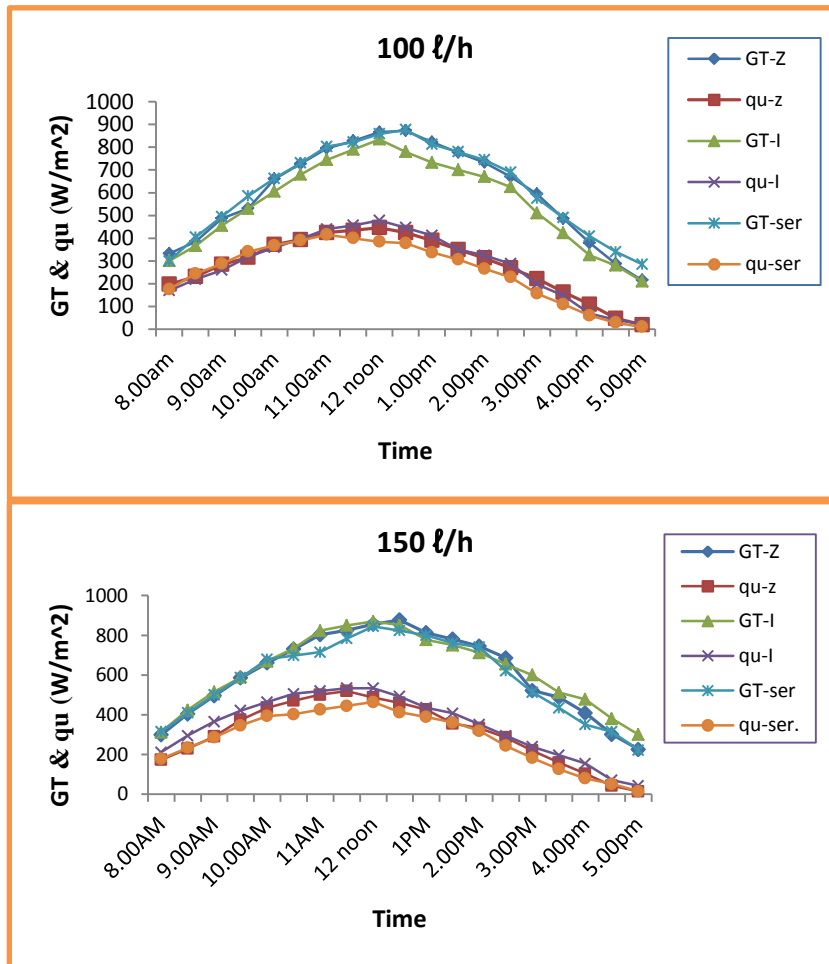


Figure 8. Relationship between the useful energy and solar radiation for different connections.

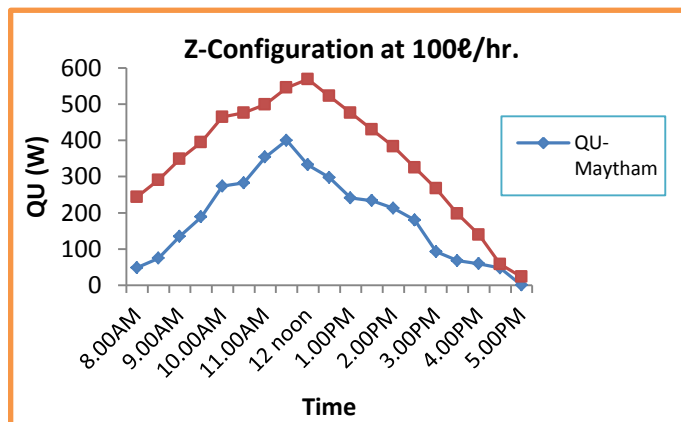


Figure 9. Comparison the behavior of useful energy between the present work and other work.

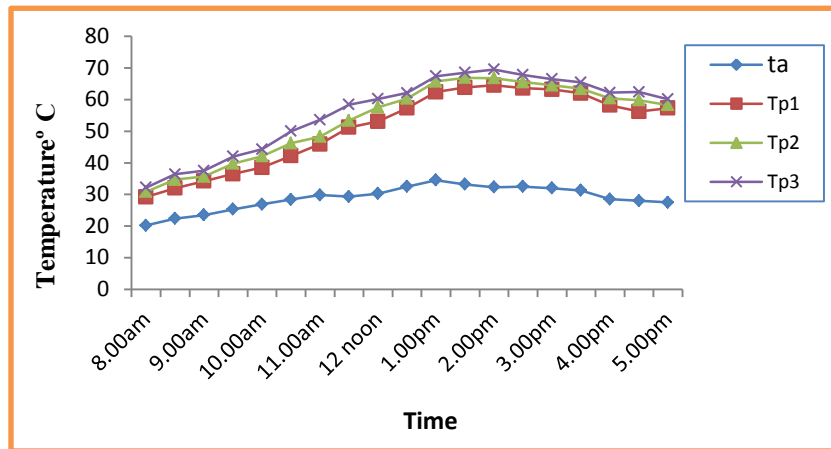


Figure 10. Absorber plate and ambient temperatures during day time at 100 ℓ/hr.

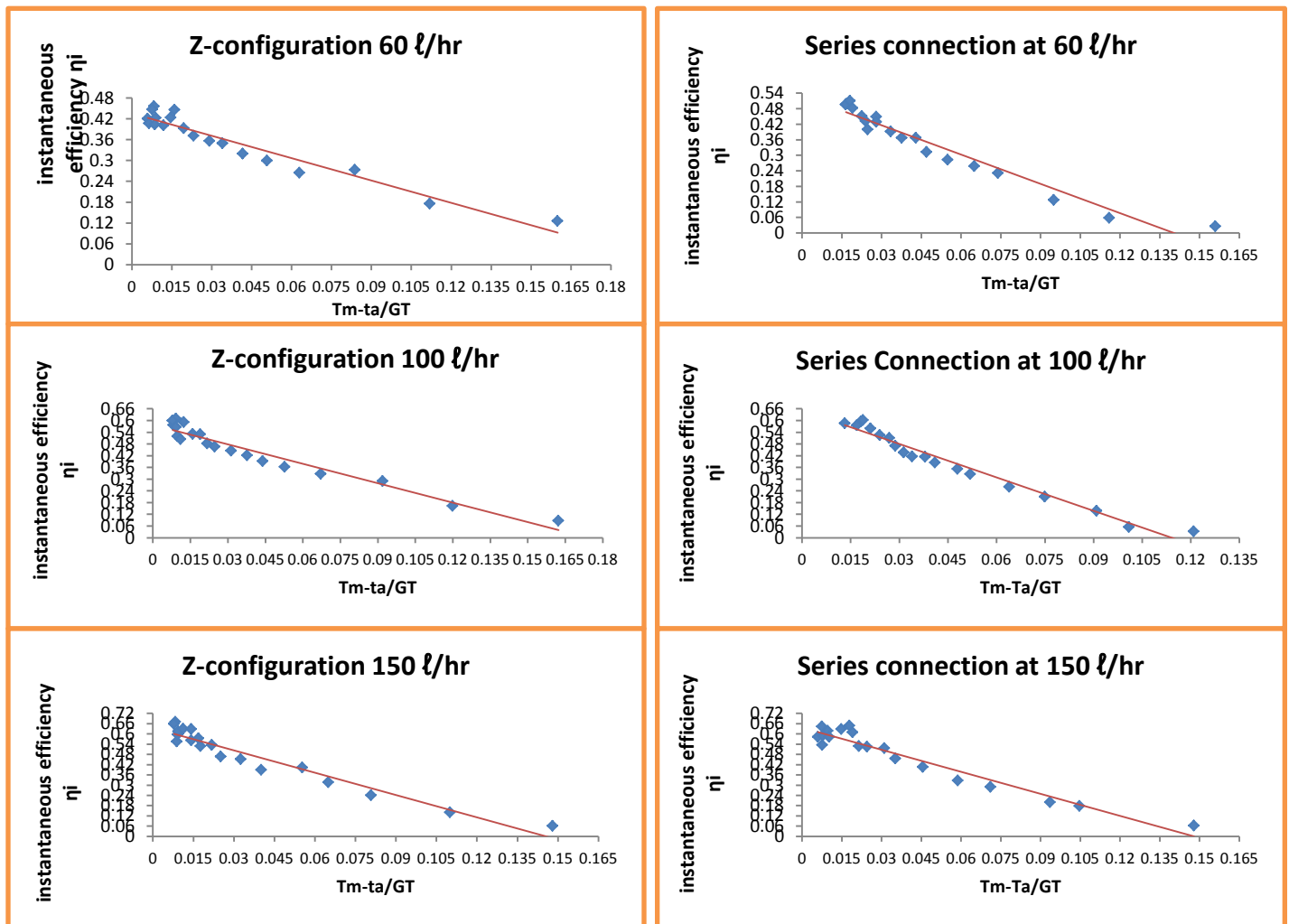


Figure 11. Performance test of series connection and parallel connection (Z-Configuration).

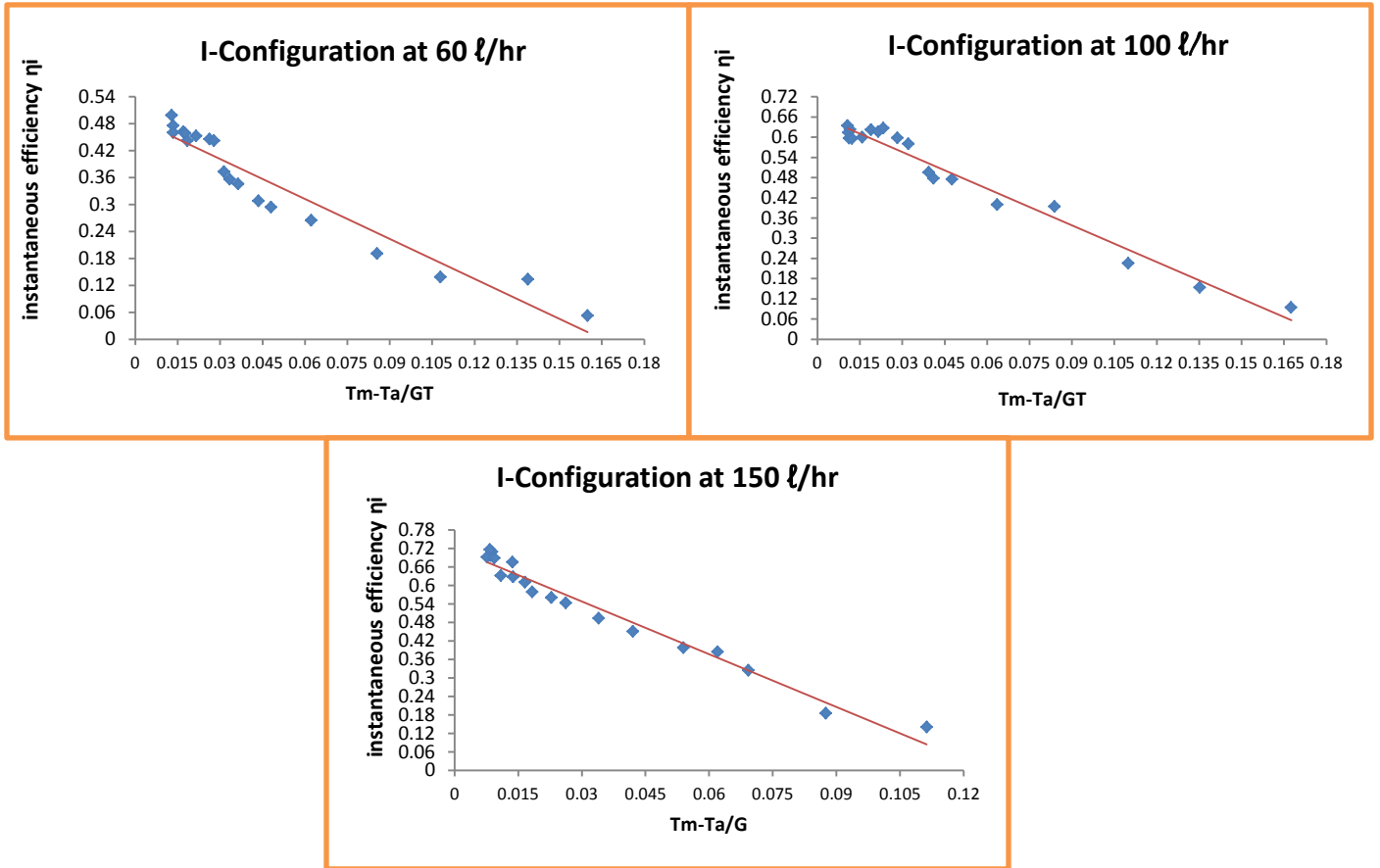


Figure 12. Performance test of I-configuration flat plate solar collectors array.

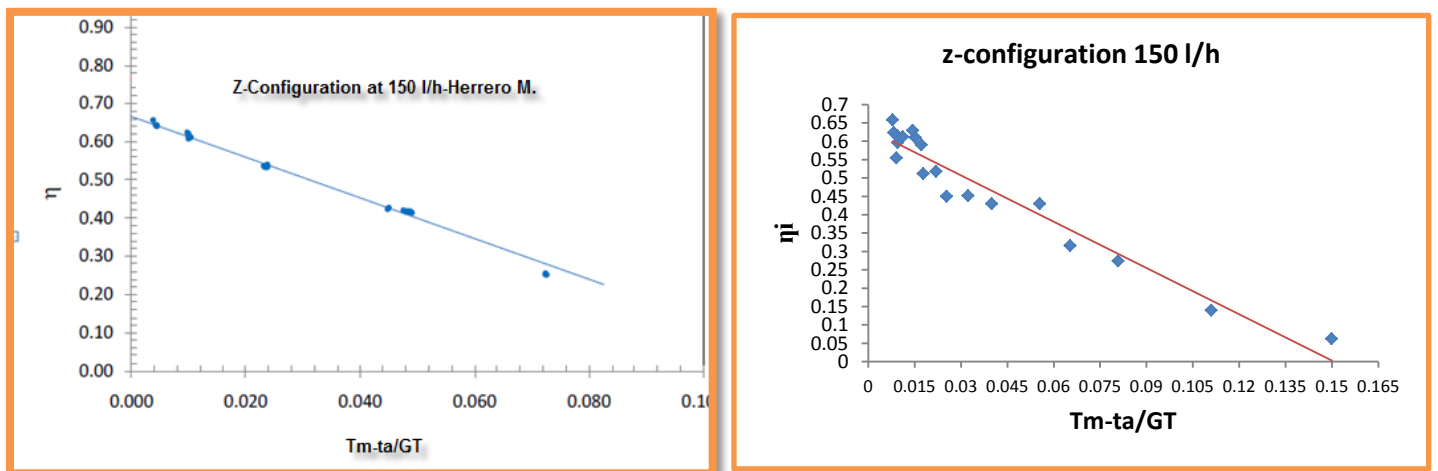


Figure .13 Comparisons the performance test at flow rate 150 l/hr.

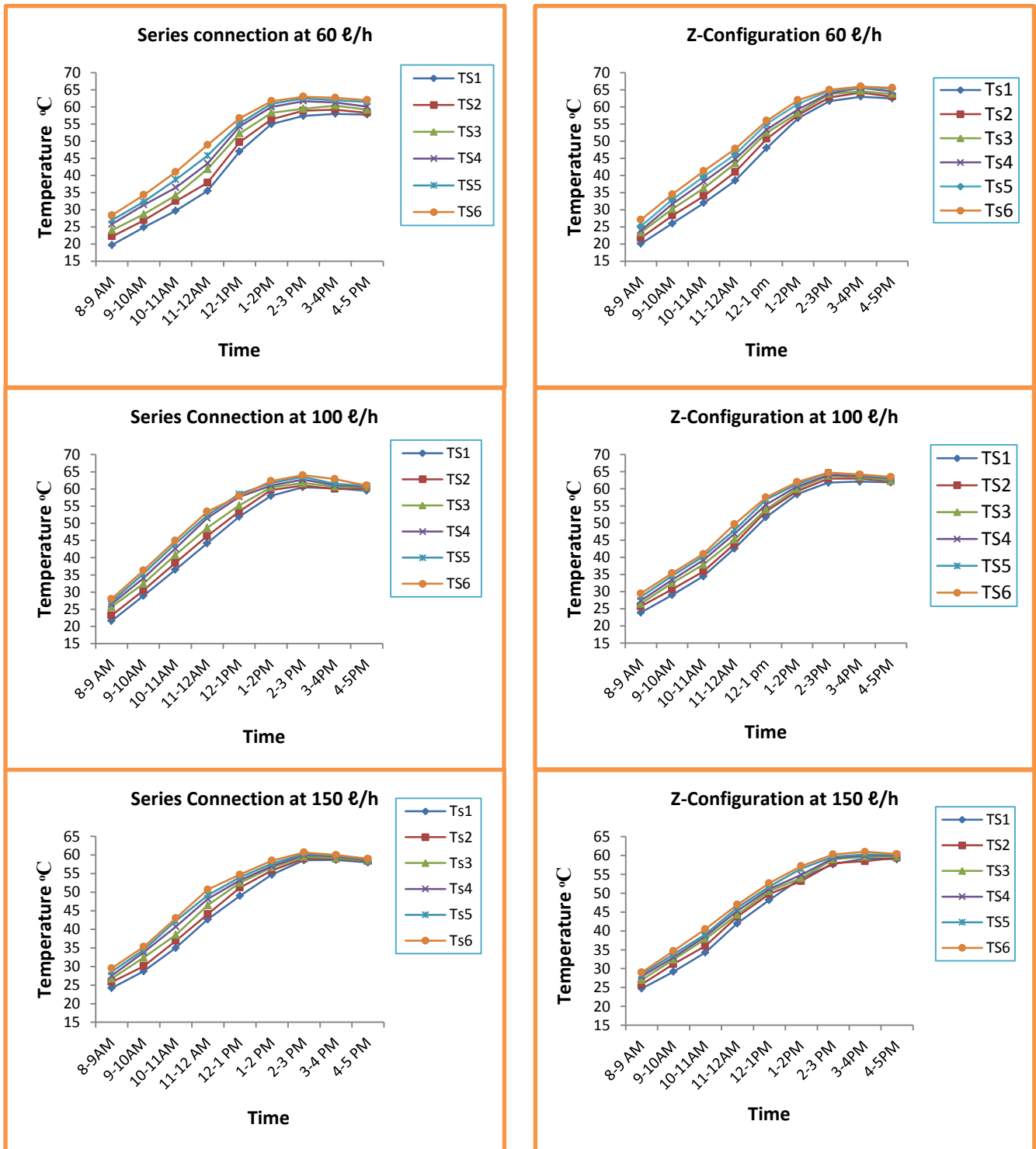


Figure 14. Stratification of storage tank of parallel (Z-Configuration) and series connections.

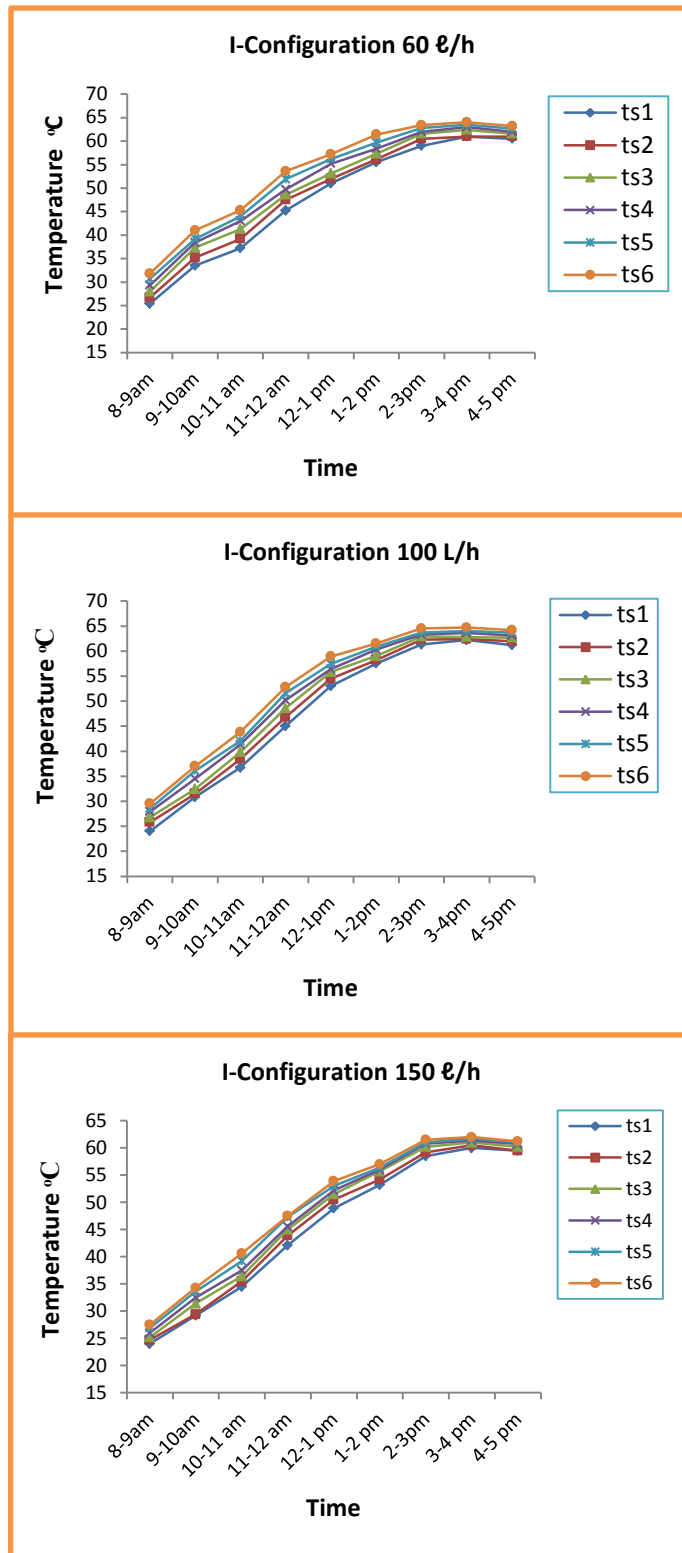


Figure 15 . Stratification of storage tank of parallel connection (I-Configuration).

Strength Improvement of Clay Soil by Using Stone Powder

Ahmed Sameer Abdulrasool

Assistant Lecturer

Department of Building and Construction Engineering Department - University of Technology

ahmeedsameerabd@gmail.com

ABSTRACT

Soil stabilization with stone powder is a good solution for the construction of subgrade for road way and railway lines, especially under the platforms and mostly in transition zones between embankments and rigid structures, where the mechanical properties of supporting soils are very influential. Stone powder often has a unique composition which justifies the need for research to study the feasibility of using this stone powder type for ground improvement applications. This paper presents results from a comprehensive laboratory study carried out to investigate the feasibility of using stone powder for improvement of engineering properties of clays.

The stone powder contains bassanite ($\text{CaSO}_4 \cdot \frac{1}{2} \text{H}_2\text{O}$), and Calcite (CaCO_3). Three percentages are used for stone powder (1%, 3% and 5%) by dry weight of clay. Several tests are made to investigate the soil behavior after adding the stone powder (Atterberg limits, Standard Proctor density, Grain size distribution, Specific gravity, Unconfined Compressive test, and California bearing ratio test). Unconfined Compressive tests conducted at different curing. The samples are tested under both soaked and unsoaked condition. Chemical tests and X-ray diffraction analyses are also carried out. Stone powder reacts with clay producing decreasing in plasticity and The curves of grain size distribution are shifted to the coarse side as the stone powder percentage increase; the soil becomes more granular, and also with higher strength.

Keywords: strength improvement of clay, soil-stone powder mix, effect of stone powder.

تحسين قوة التربة الطينية باستعمال مسحوق الحجارة

احمد سمير عبدالرسول

مدرس مساعد

قسم هندسة البناء و الانشاءات - الجامعة التكنولوجية

الخلاصة

تثبيت التربة بمسحوق الحجارة حل جيد لانشاء الطرق و خطوط السكة الحديد ، وخصوصا تحت الابراج في مناطق الانتقال بين السدة الترابية و الهياكل الصلبة. حيث ان الخواص الميكانيكية للترب الداعمة مؤثرة جدا. مسحوق الحجارة له في اغلب الاحيان تركيب فريد يبرر الحاجة لبحث دراسة عملية لاستعمال هذا النوع من مسحوق الحجارة لتطبيقات تحسين الارضية. يقدم هذا البحث نتائج لدراسة مختبرية شاملة نفذت لتحري عملية استعمال مسحوق الحجارة لتحسين الخواص الهندسية للطين.

مسحوق الحجارة يحتوي على كبريتات الكالسيوم ($\text{CaSO}_4 \cdot \frac{1}{2} \text{H}_2\text{O}$) و كاربونات الكالسيوم (CaCO_3) تم استخدام ثلاث نسب مئوية لمسحوق الحجارة (1% ، 3% و 5%) من الوزن الجاف للطين. تم اجراء العديد من الاختبارات لتحري سلوك التربة بعد اضافة مسحوق الحجارة (حدود اتربرك ، كثافة بروكتر القياسية ، التدرج الحبيبي للتربة ، الوزن النوعي ، اختبار الانضغاط الغير



محصور و اختبار نسبة تحمل كالفورنيا). اختبارات الانضغاط الغير محصور اجريت في معالجة مختلفة. تم اختبار النماذج في اطار كل من حالة المنقع و الغير منقع. الاختبارات الكيميائية و فحص XRD تم تنفيذها ايضا. مسحوق الحجارة يتفاعل مع الطين لينتج انخفاض في اللدونة وكذلك منحنيات التوزيع الحبيبي للتربة تحولت الى الجانب الخشن كما تم زيادة مسحوق الحجارة. لتصبح التربة اكثر حبيبية و ايضا زيادة في القوة بسبب التفاعلات الفيزيائية و الكيميائية بين التربة و مسحوق الحجارة و الماء. الكلمات الرئيسية: تحسين قوة الطين ، خليط التربة – مسحوق الحجر ، تاثير مسحوق الحجارة.

1. INTRODUCTION

Pre-construction treatment of soft and weak deposits is necessary to ensure safety and stability of the building or infrastructure. The conventional method of soil stabilization is to remove the weak soil and replace with a stronger material, **Ingles, and Metcalf, 1972**. The high cost of this method lead to researchers to look for alternative methods, and one of these methods is the process of soil stabilization using stone powder.

Stone powder used may improve the engineering properties of clay to make them suitable for construction. The many advantages of stone powder, including low expansion, even after 48 hours and improved compressive strength. This paper presents a summary of a research project investigating one of the alternatives to improve soil. Specifically the paper presents results of a laboratory investigation of the stabilization properties of clay blended with stone powder.

2. REVIEW OF LITERATURE

Projects of Civil engineering located in soft clay have traditionally considered improving soil properties by using cement, lime and silica fume. Lately projects containing soil mixed with fly ash have been reported, **Reyes and Pando, 2007**. For the particular case the stone powder no literature was found reporting ground improvement applications, constitutes stone powder a cost effective and environmentally beneficial alternative with considerably less capital investment.

3. EXPERIMENTAL PROGRAM

The feasibility of using stone powder is investigated through a comprehensive laboratory experimental program. The program primarily involved assessing the stabilization characteristics of a clay soil when blended with stone powder. The stabilization characteristics are measured in terms of strength and stiffness gain, etc.

The following subsections describe the materials used (clay soil, stone powder), and experimental procedures (sample preparation, and test procedures).

3.1 Materials

Two materials are used for the laboratory experimental program carried out in this research: clay soil and stone powder.

3.1.1 Clay soil

The clayey soil used for this study is obtained from Baghdad city, located in center of Iraq. The geotechnical properties of the clay are determined by conducting grain size distribution, specific gravity, Atterberg limits, standard proctor density, unconfined compressive, and California bearing ratio (CBR). A summary of the main properties of the clay used for this research is presented in



Table 1. A grain size distribution analyses was carried out following ASTM Standard D 422 indicating the clay had 1% sands, 61% silt sizes, and 38% clay sizes. According to the Unified soil Classification system this soil classifies as a CL which corresponds to low plasticity clay.

3.1.2 Stone powder

Stone powder is defining a hard stones for dies characterized by enhanced hardness and low expansion. It can exhibit both pozzolanic and cementations properties. They must have high resistance to compression and abrasion. Stone powder is used in the teeth manufacture, chrome models. The product not classified as hazardous pursuant to directives 67/548/EEC and 1999/45/EC and subsequent amendments and upgrades and does not contain substances classified as being hazardous to human health or the environment pursuant to 67/548/EEC and subsequent amendments. The quantitative X-ray diffraction test is conducted on sample to determine the mineral contents of the stone powder. The State Company of Geological Survey and Mining, Ministry of Industry and Minerals, conducted this test.

Stone powder is contains some Calcite (CaCO_3), and calcium sulfate ($\text{CaSO}_4 \cdot \frac{1}{2} \text{H}_2\text{O}$). A summary of the main properties of the stone powder used for this research is presented in Table 2.

3.2 Experimental Procedures

Prior to soil treatment, the clay soil from Baghdad city is air dried for two weeks and then processed using crushing equipment. The maximum particle size of the soil is restricted to 4.75 mm which corresponds to the opening of a standard Sieve No. 4.

The amount of stabilizer to be used is found from the following formula, **Geiman, 2005**.

$$\text{Amount of stabilizer} = \frac{p_s \times W_{tot}}{(1+w)} \quad (1)$$

where

p_s = Percent by dry weight of stabilizer to be used,

W_{tot} = Wet weight of batch prior to addition of stabilizer, and

w = Moisture content of soil prior to addition of stabilizer, expressed as a decimal.

Soil samples treated with stone powder are prepared with three amounts of stone powder (1, 3, and 5% of stone powder by weight).

The geotechnical properties of the clay stabilized with stone powder are determined by conducting the following laboratory tests.

1. Grain Size Distribution: Tests for sieve, and the hydrometer analysis, are performed after removing any unusually big chunks of clay. The test procedure provided in ASTM test designation D422.
2. Specific Gravity: Values for specific gravity of the soil solids are determined according to (B.S. 1377:1990, test No. 6 B) by placing a known weight of oven-dried soil in a flask, then filling the flask with water.
The weight of displaced water is then calculated by comparing the weight of the soil and water in the flask with the weight of flask containing only water. The specific gravity is then calculated by dividing the weight of the dry soil by the weight of the displaced water.
3. Atterberg Limits: The liquid and plastic limits are determined in accordance with ASTM test designation D4318.

4. Standard Proctor Density: These tests are conducted on the clay samples treated with stone powder for determination of the moisture density relationship (ASTM D698).
5. Unconfined Compressive Tests: The specimens for unconfined compressive strength tests of clay soil blended with stone powder, are all prepared to the same target moisture content of 14.8% (i.e., the optimum moisture content of the untreated soil). The soil- stone powder samples are compacted inside standard proctor mold. The soil- stone powder blends are compacted by placing the mixtures in 3 equal layers and applying 25 blows to each layer using the standard proctor hammer. The sample for unconfined compressive strength tests is prepared 36.5 mm in diameter and 72.5 mm in height. The samples are tested under both soaked and unsoaked. The unsoaked compacted samples are kept in box. The specimens are periodically sprayed with water for curing of 3, 7 and 28 days. At the end of the required curing period, the samples are withdrawn from the box, and kept in unconfined compression test machine. Another set of samples is also kept submerged in water for the periods mentioned as above before testing under soaked condition.
Unconfined compressive tests are also carried out on uncured samples which are tested immediately after compaction, i.e., corresponding to an age of 0 day .A test procedure in general accordance with ASTM Standard D 2166.
6. CBR Tests: California Bearing Ratio tests are conducted using the procedure given in ASTM test designation D 1883-07. The samples are soaked for 4 days before performing the tests. A penetration rate of 1.25 mm per minute was used.

4. LABORATORY TEST RESULTS AND DISCUSSION

4.1 Grain Size Distribution

The grain size distribution curves for soil- stone powder mix, as obtained from sieve and hydrometer analyses are presented in **Fig. 1**. The curves are shifted significantly to the coarser side as the stone powder percentage increases; the soil becomes more granular. This may be caused by the immediately pozzolanic reaction which causes the flocculation of clay particles. The results of tests are listed in **Table 3**.

4.2 Specific Gravity

Fig. 2 shows the specific gravity values of the soil mixed with different percentages of stone powder. Also, it shows the decrease in specific gravity of soil with increasing of stone powder content due to the low values of the specific gravity of stone powder.

4.3 Atterberg Limits

In this section, the clay consistency is investigated during soil stabilization. The effect of adding stone powder to the clay soil on Atterberg limits is shown in **Fig.3**. One can notice a decrease in liquid limit because the calcium of the stone powder exchanges with the adsorbed cations of the clay mineral, resulting in reduction in size of the diffused water layer surrounding the clay particles. This reduction in the diffused water layer allows the clay particles to come into closer contact with one another, causing flocculation/agglomeration of the clay particles. A reduction in plasticity happens when the clayey soil is mixed with stone powder due to converting the soil to the granular mass and at the same time the bonds between the soil particles become stronger due to cation

exchange that takes place between negative ions on the surface clay particles and the calcium ions of the stone powder.

4.4 Compaction Tests

Figure 4 shows the relationship between dry unit weight and water content for different stone powder contents. While **Fig.5** presents the effect of stone powder on the optimum water content, and **Fig. 6** shows the effect of stone powder on the maximum dry unit weight.

It can be seen that there is a decrease in compactive effort due to reduction in the parallel orientation to the clay particles, **Fig.4** while **Fig.5** shows that the optimum water content increases from 14.8% to 17.21% at 5% stone powder. In **Fig.5**, the increase in the optimum moisture content is due, in spite of the reduced surface area caused by flocculation and agglomeration, to the additional fine contents to the samples which requires more water in addition to the stone powder that needs more water for the pozzolanic reactions to take place. The increase in optimum moisture content due to addition of stone powder may be caused by the absorption of water by stone powder.

The variations of maximum dry unit weight and stone powder content showed that stabilizer content decreases the maximum dry unit weight from 17.8 to 17.21 kN/m³, **Fig.6**. The relatively low unit weight of stone powder treated samples of clay coupled with the observed increase in unconfined compressive (as discussed later in the paper) is an important consideration in determining suitability of stone powder treated clay for construction work.

4.5 Unconfined Compressive Tests

The relationship between unconfined compression and time are shown in **Figs.7** and **8** for stone powder in unsoaked and soaked condition respectively. Unconfined compressive tests on untreated soil are shown in **Fig.9**.

From the results for two conditions, it can be observed that the stone powder increases, this will lead to shear strength of the stabilized soil gradually increases with time mainly due to pozzolanic reactions. Interaction between water with stone powder lead to produces calcium hydroxyl. Calcium hydroxide in the soil water reacts with the silicates and aluminates (pozzolans) in the clay to form cementing materials or binders, consisting of calcium silicates and/or aluminate hydrates. For stone powder -soil mixture at the same stone content, the effect of increasing the curing is to increase strength. The curing and temperature has been found to affect the long term reactions between stone powder and clay. The increase factor of the unconfined compression strength in 28 days for the soaked and unsoaked condition is shown in **Table 4** and **Table 5** respectively. the five percent showing little strength gain in comparison with three percent .From unconfined compression test, it has been indicated that the optimum percent of stone powder of 3% from will increase the unconfined compression strength from 114 to 276 kN/m² in 28 days for the soaked condition and from 114 to 338 kN/m² in 28 days for the unsoaked condition.

4.6 CBR Tests

The results of CBR tests for various treated and untreated samples of clay are shown in Table 6. These values are based on 1.25 mm penetration. Comparison of CBR values for the different tests indicates that the significant improvement in CBR values can be achieved by treating samples of clay with stone powder admixtures.



5. CONCLUSIONS

This paper has discussed the results of a laboratory investigation involving use of elite stone powder for ground improvement of clays.

1. A decrease in liquid limit and plasticity index with the addition of stone powder. Pozzolanic reactions occur because of the siliceous and aluminous material which possesses little cementitious value and large particles which produces decrease in liquid limit.
2. A decrease in specific gravity of soil was obtained with increasing of stone powder content due to the low values of the specific gravity of stone powder (2.58).
3. The curves of grain size distribution are shifted significantly to the coarser side as the stone powder percentage increase; the soil becomes more granular. This may be caused by the immediately pozzolanic reaction which causes the flocculation of clay particles.
4. When are increased stone powders, the maximum dry unit weight decreases from 17.8 to 17.21 kN/m³.
5. The optimum moisture content increases with increase of stone powder percents from 14.8% to 17.21%, due to due to the addition of stone powder contents to the samples which needed more water for the pozzolanic reactions to take place.
6. The shear strength of the stabilized soil gradually increases with time mainly due to pozzolanic reactions. Calcium hydroxide in the soil water reacts with the silicates and aluminates (pozzolans) in the clay to form cementing materials or binders.
7. the test results indicate that clay soils treated with stone powder result in adequate ground improvement as evidenced from higher strengths measured from unconfined compressive tests.
8. The five percent showing little strength gain in comparison with three percent.
9. The compressive strength gains were observed primarily in the initial 7 days of the curing period irrespective of stone powder contents used in the stabilized soil cushion and then had a tendency to stabilize showing little strength gain.
10. CBR values also improve with addition of stone powder mixtures to clay due to chemical interactions among soil, stone powder and water to form cementing materials or binders.

6. REFERENCES

1. Al-Saoudi, N.K., Rahil, F.H. and AL-Soudany, K.Y., 2011, *Improvement of Ballast Embankment Resting on Soft Clay by Reed and Asphalt Layers, Engineering and Technology Journal, Vol.29, No.15. pp. 3224-3241.*
2. ASTM D 422-00, *Standard Test Method for Particle Size-Analysis of Soils*, American Society for Testing and Materials.
3. ASTM D 4318-00, *Standard Test Methods for Liquid Limit, Plastic Limit, and Plasticity Index of Soils*, West Conshohocken, Pa.
4. ASTM D 2166-00, *Standard Test Method for Unconfined Compressive Strength of Cohesive Soil*, West Conshohocken, Pa.
5. ASTM D 2487-00, *Standard Practice for Classification of Soils for Engineering Purposes (Unified Soil Classification System)*, American Society of Testing and Materials.
6. ASTM D 698-00, *Standard Test Methods for Laboratory Compaction Characteristics of Using Standard Effort.*



7. Awad, A. A. 1977, *Effect of Lime on Permeability of Compacted Soil*, M.Sc. Thesis, Civil Engineering Department, College of Engineering, University of Baghdad.
8. Bergado, D.T., Anderson, L.R. and Balasubramaniam, A.S., 1996, *Soft Ground Improvement in Lowland and other Environments*, published by ASCE press.
9. Bowles, J. E. 1996, *Foundation Analysis and Design*, the McGraw-Hill Companies, Inc., pp. 1175.
10. British Standard Institution, 1990, *Method of Testing Soils for Civil Engineering Purposes, B.S. 1377*.
11. Broms, B.B. 1987, *Stabilization of Soft Clay in Southeast Asia*, Proceeding 5th International Geotechnical Seminar 2-4 Dec. 1987.
12. Das, B. M. 2002, *Principles of Geotechnical Engineering*, 5th Edition, Wadsworth Group, California, USA.
13. Geiman, C. M. 2005, *Stabilization of Soft Clay Subgrades in Virginia: Phase I Laboratory Study*, M.Sc. thesis, Virginia Polytechnic Institute and State University, at Blacksburg, VA.
14. Gromko, G. J. 1974, *Review of Expansive Soils*, Journal of Geotechnical Engineering Division, ASCE, GT6, pp. 667-687.
15. Ingles, O.G. and Metcalf, J.B. 1972, *Soil Stabilization*, Butterworth pty, limited, Australia.
16. Reyes, A. and Pando, M. 2007, *Evaluation of CFBC Fly Ash for improvement of Soft Clays*, Conference, WOCA, USA.
17. Stone powder sheet, 2013.
18. Terzaghi, K. and Peck R.B 1967, *Soil Mechanics in Engineering Practice*, 2nd edition, John Wiley and Sons, New York.
19. U.S Army Corps of Engineers 1999, *Use of Waste Materials in Pavement Construction ETL.1110-3-503*.

NOMENCLATURE

p_s = percent by dry weight of stabilizer to be used,

W_{tot} = wet weight of batch prior to addition of stabilizer, gram

w = moisture content of soil prior to addition of stabilizer, %

Table 1. Physical and chemical properties of soil.

Properties	Value
Liquid limit	38
Plastic limit	24
Plasticity index	14
Shrinkage limit	17
Specific gravity, G_s	2.72
Maximum dry density (Standard Proctor) (kN/m^3)	17.8
Optimum water content (Standard Proctor) (%)	14.8
Unconfined compressive (kN/m^2)	114
pH	8.45



So ₃ %	0.20
CL%	0.04
SiO ₂ %	35.82
Fe ₂ O ₃ %	5.5
T.S.S	0.25

Table 2. Physical and chemical properties of stone powder.

Properties	Value
Water/powder ratio	25 ml / 100 g
Expansion after 2 h	0.08%
Expansion after 48 h	0.09%
Compressive strength after 1 h	42 MPa
Compressive strength after 48 h	60 MPa
Density	23 kN/m ³
Specific gravity	2.58

Table 3. Grain size distribution analysis results for soil- stone powder mix.

Stone powder %	0%	1%	3%	5%
Sand size %	1%	3%	3%	6%
Silt size %	61%	66%	67%	71%
Clay size %	38%	31%	30%	23%

Table 4. Increase factor of the unconfined compression strength in the soaked condition.

Soil treatment		Normal soil	Increase factor %
Stone powder additive %	Unconfined compression in 28 day	Unconfined compression	
1	206	114	44.6
3	276	114	58.6
5	319	114	64.2

Table 5. Increase factor of the unconfined compression strength in the unsoaked condition.

Treatment soil		Normal soil	Increase factor %
Stone powder additive %	Unconfined compression in 28 day	Unconfined compression	
1	253	114	54.9
3	338	114	66.2
5	378	114	69.8



Table 6. CBR results for soil- stone powder mix.

Stone powder additive %	CBR Results
0	4.5
1	5.2
3	6.0
5	7.1

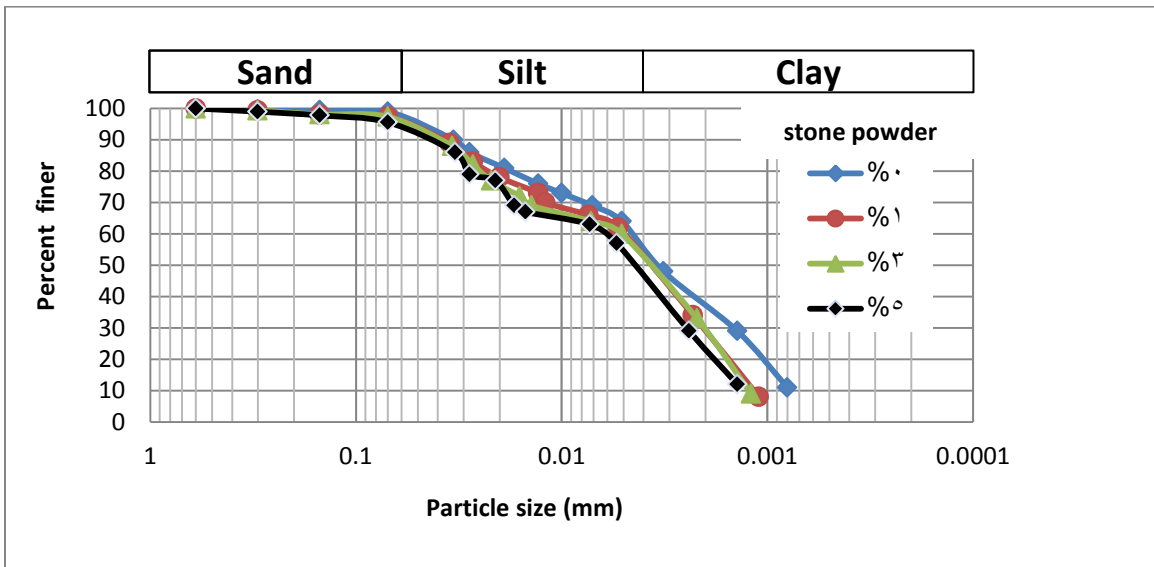


Figure 1. Grain size distribution of the soil stabilized with stone powder.

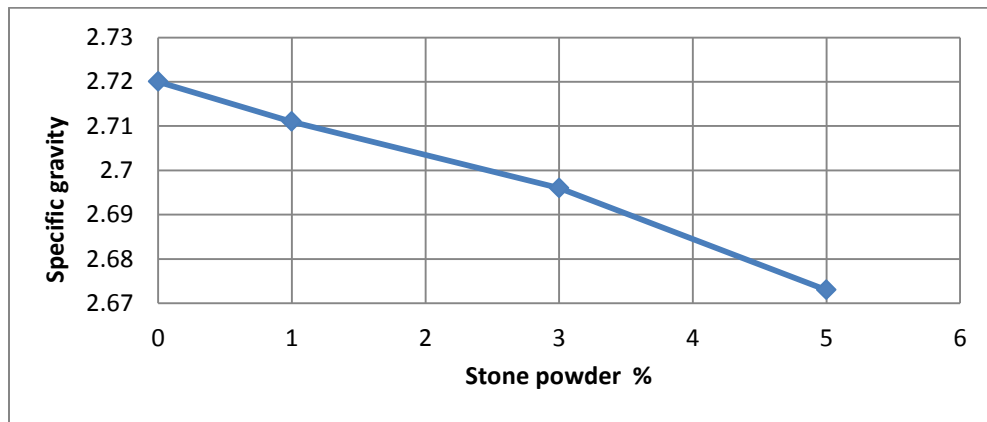


Figure 2. Effect of stone powder content on specific gravity.

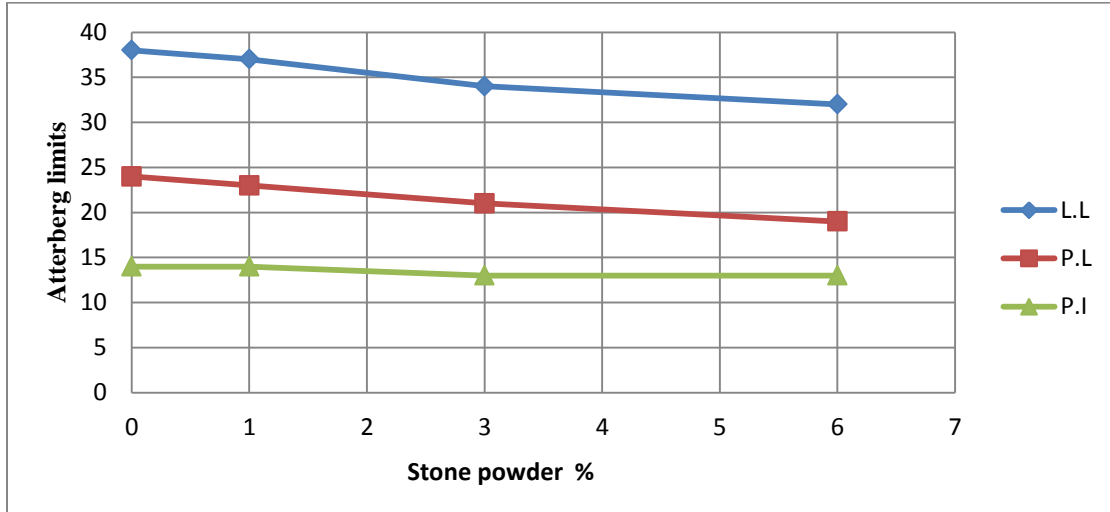


Figure 3. Effect of stone powder content on Atterberg limits.

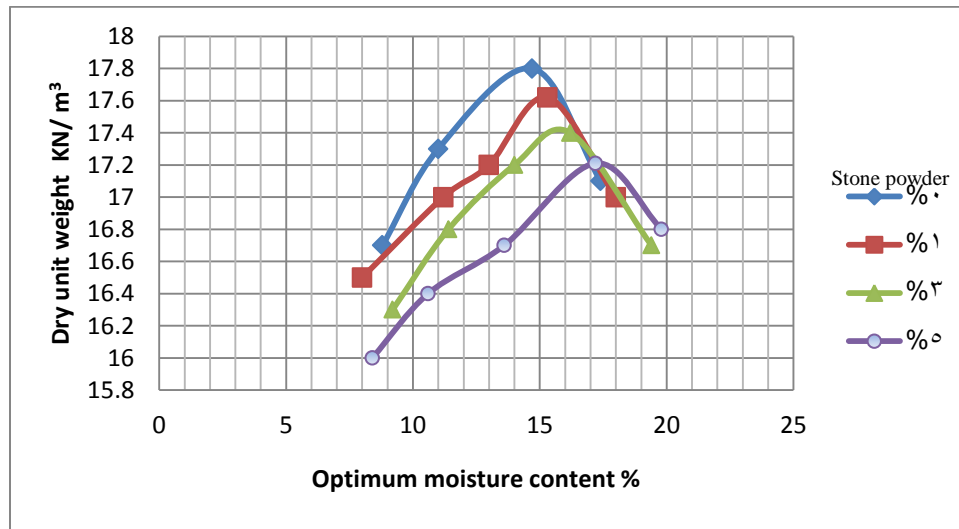


Figure 4. Effect of stone powder content on dry unit weight and optimum moisture content.

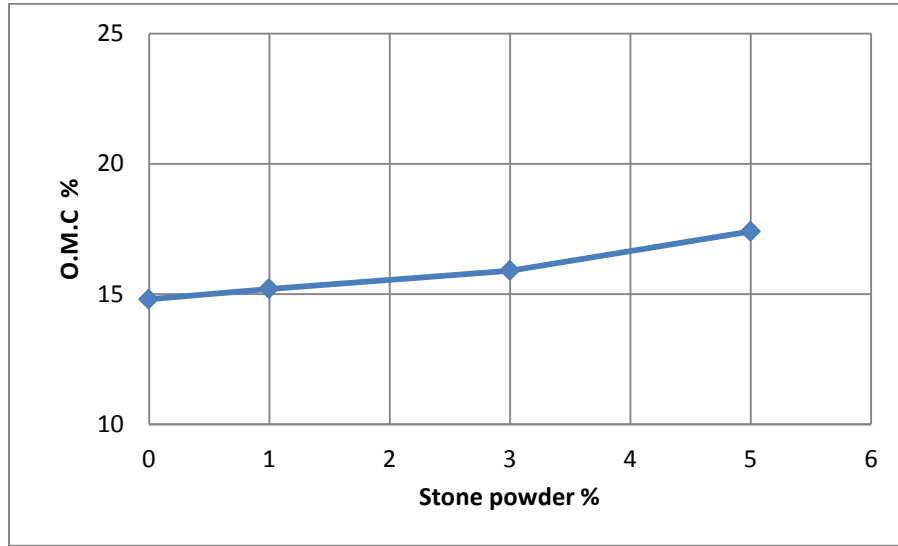


Figure 5. Variation of the optimum moisture content with stone powder percent.

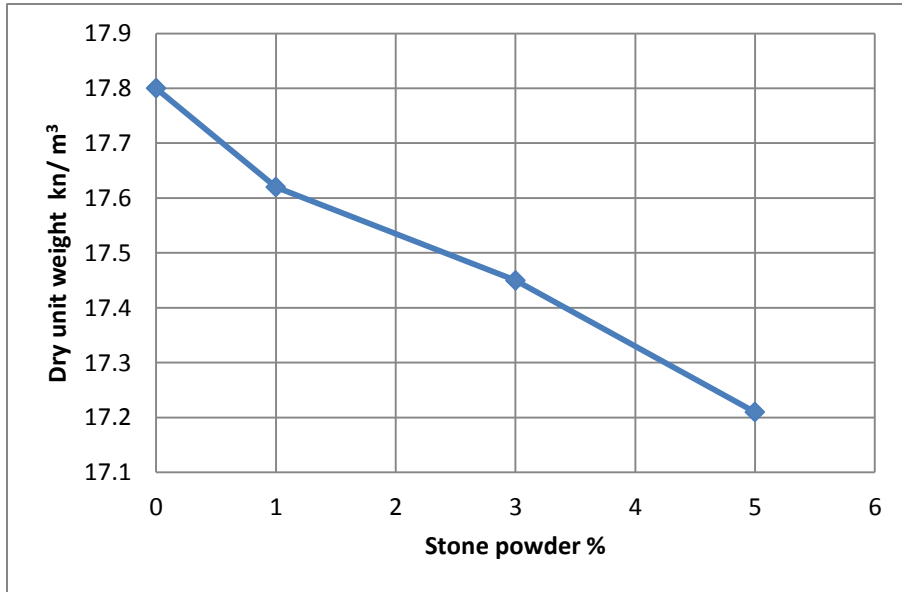


Figure 6. Variation of the maximum dry unit weight with stone powder percent.

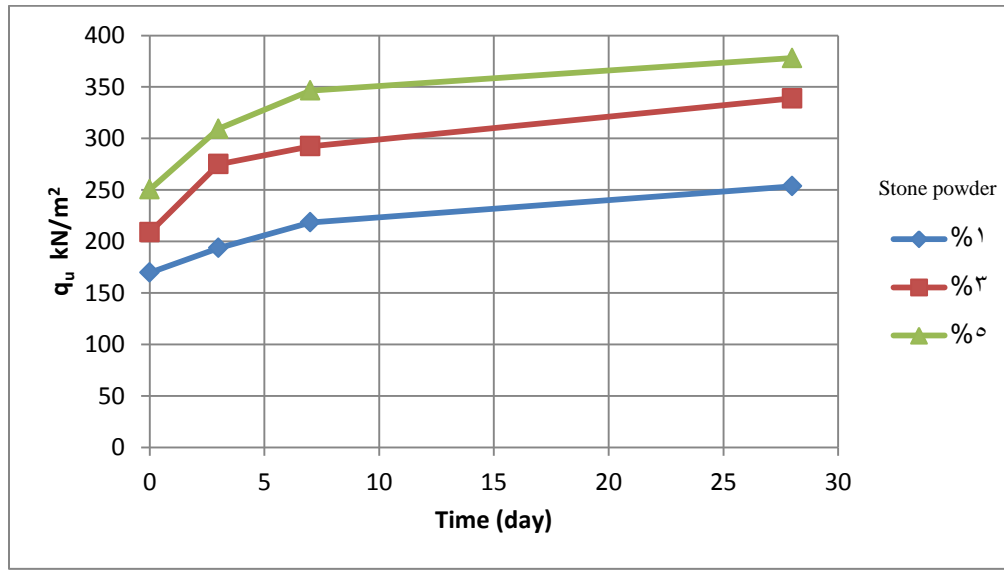


Figure 7. Effect of stone powder content on unconfined compression and time in unsoaked condition.

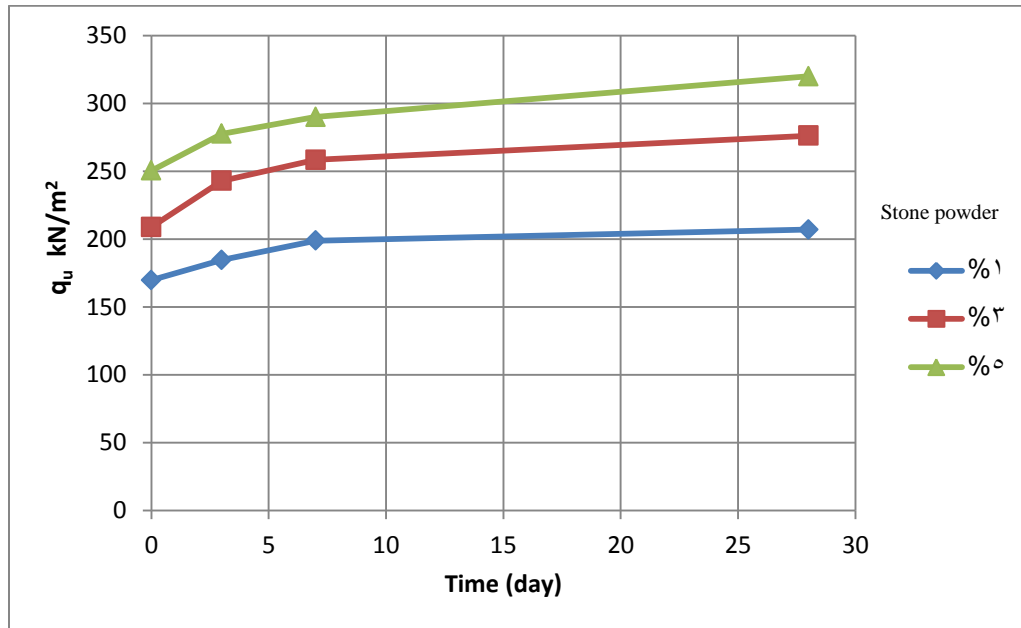


Figure 8. Effect of stone powder content on unconfined compression and time in soaked condition.

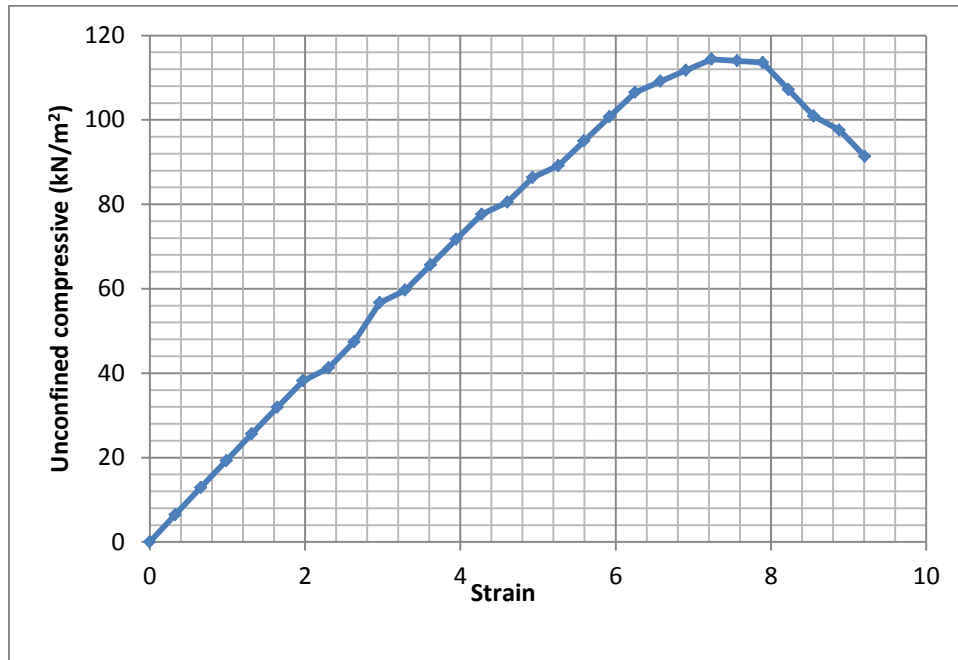


Figure 9. Unconfined compression on normal soil without stone powder corresponding to an age of 0 day.

On Gradient Descent Localization in 3-D Wireless Sensor Networks

Prof. Nuha Abdul Sahib Alwan
Department of Computer Engineering
College of Engineering
Baghdad of University
Email: n.alwan@ieee.org

Alaa Shakir Mahmood
Department of Computer Engineering
College of Engineering
University of Baghdad
Email: alaashaker.am@gmail.com

ABSTRACT

Localization is an essential demand in wireless sensor networks (WSNs). It relies on several types of measurements. This paper focuses on positioning in 3-D space using time-of-arrival-(TOA-) based distance measurements between the target node and a number of anchor nodes. Central localization is assumed and either RF, acoustic or UWB signals are used for distance measurements. This problem is treated by using iterative gradient descent (GD), and an iterative GD-based algorithm for localization of moving sensors in a WSN has been proposed. To localize a node in 3-D space, at least four anchors are needed. In this work, however, five anchors are used to get better accuracy. In GD localization of a moving sensor, the algorithm can get trapped in a local minimum causing the track to deviate from the true path, thereby impairing real-time localization. The proposed algorithm is based on systematically replacing anchor nodes to avoid local minima positions. The idea is to form all possible combinations of five-anchor sets from a set of available anchor nodes (larger than five), and to segment the true path. Iterating through each segment, the sets of anchors that could draw the track to a local minimum are discarded and replaced with possible others to maintain the right track.

Keywords: centralized localization; gradient descent (GD) algorithm; local minima; moving sensor nodes.

ألاء شاكور محمود
قسم هندسة الحاسبات
كلية الهندسة / جامعة بغداد

أ. نهى عبد الصاحب العلوان
قسم هندسة الحاسبات
كلية الهندسة / جامعة بغداد

الخلاصة

إن التوطين مطلب أساسي في شبكات الاستشعار اللاسلكية و هو يعتمد على عدة أنواع من القياسات. هذا البحث يركز على تحديد المواقع في الفضاء الثلاثي الأبعاد باستخدام قياسات المسافة القائمة على وقت الوصول (TOA) بين النواة المراد تحديد موقعها و عدة نوى مرجعية. أن معلومات النواة من المفترض ان تعالج بطريقة مركزية و في قياس المسافات تستخدم أما اشارات الترددات الراديوية (RF) ، الاشارات الصوتية (acoustic) أو الاشارات واسعة النطاق (UWB). عولجت هذه المشكلة باستخدام نسب التدرج التكرارية (GD) و تم اقتراح خوارزمية تكرارية قائمة على نسب التدرج لتحديد مواقع اجهزة الاستشعار المتحركة في شبكة استشعار اللاسلكية. ان عدد التكرارات هي مسألة مفاضلة بين درجة الدقة و استهلاك الطاقة في نوى الاستشعار. لتحديد موقع نواة في الفضاء الثلاثي الأبعاد، هناك حاجة الى ما لا يقل عن اربعة نوى مرتكزة. غير أن في هذا البحث، لقد تم استخدام خمسة نوى مرتكزة للحصول على دقة افضل. عند توطين جهاز استشعار باستخدام نسب التدرج (GD) ، من الممكن ان تعلق الخوارزمية في موقع محلي أدنى مما يتسبب بانحراف المسار عن الطريق الصحيح وبالتالي إضعاف الوقت الحقيقي للتوطين. إن خوارزمتنا المقترحة تستند على الاستبدال المنهجي للنوى المرتكزة لتجنب الوقوع في



المواقف الدنيا المحلية. الفكرة هي تشكيل كل مزيج ممكن مكون من خمس نوى مرتكزة من اصل مجموعة النوى المرتكزة المتاحة (أكثر من خمسة)، و تجزيء المسار الصحيح. مع تكرار كل جزء، يتم تجاهل مجموعة النوى التي من المحتمل أن تجر المسار الى موقع محلي أدنى ويتم استبدالها مع المجموعات الأخرى الممكنة للحفاظ على المسار الصحيح.

الكلمات الرئيسية: التوطين المركزي؛ خوارزمية تدرج الانحدار؛ المواقع الدنيا المحلية؛ نوى الاستشعار المتحركة



1. INTRODUCTION

Wireless sensor networks are widely deployed to perform various tasks in monitoring and control applications such as traffic monitoring, environmental monitoring of air, water, soil quality or temperature, response to earthquakes and building safety, etc. The nodes are usually small radio-equipped low-power sensors scattered over an area or volume of a few tens of square or cubic meters respectively. There is information sharing between sensors and for this information to be meaningful, the nodes or sensors need to be located. Besides, in some applications, the node positions themselves are the information that has to be conveyed such as in warehousing and manufacturing logistics.

Node information is either processed centrally or in a distributed manner. In centralized localization, a central processor collects measurements prior to calculation, whereas in distributed algorithms, the sensors share their information only with neighbors but possibly iteratively. Both methods face the high cost of communication, but, in general, centralized algorithms produce more accurate location information. On the other hand, distributed localization offers more scalability and robustness to link failures.

Node localization relies on measurements of distances between the nodes to be localized and a number of reference or anchor nodes. The distance measurements can be via radio frequency (RF), acoustic or ultra-wideband (UWB) signals. Measurements that indicate distance can be time of arrival (TOA), angle of arrival (AOA), or received signal strength (RSS). TOA measurements seem to be most useful especially in low-density networks, since they are not as sensitive to inter-device distances as AOA or RSS.

Accurate location information is important in almost all real-world applications of wireless sensor networks (WSNs). In particular, localization in a 3-D space is necessary as it yields more accurate results. Trilateration and multilateration positioning methods, **Zhang et al., 2011**, can be employed in a two-dimensional (2-D) and three-dimensional (3-D) space respectively. These methods use geometric properties to estimate the target location, and suffer from poor performance, decreased accuracy and computational complexity especially in the 3-D case. Iterative optimization methods offer an attractive alternative solution to this problem. The most common iterative optimization method is the gradient descent algorithm, which has been widely dealt with in the literature for the 2-D case, **Qiao and Pang, 2011** and **Garg et al., 2010**.

This work addresses localization in a three-dimensional space of stationary and moving wireless sensor network nodes by gradient descent methods. It is assumed that a central processor collects the data from the nodes, and TOA measurements will be assumed throughout. An evaluation analysis of the performance of the localization algorithm considered is performed. In particular, the effect of varying the number of anchor nodes and the effect of measurement noise have been studied. The work also investigates tracking of moving sensors and proposes a method to counteract some associated problems such as falling into local minima.

The rest of the paper will be organized as follows: Section 2 describes the problem of gradient descent localization of sensor nodes in 3-D space and with different scenarios as regards the parameters affecting this problem such as noise types affecting TOA measurements and the number of anchor nodes. Section 3 discusses localization of a moving sensor in 3D space. Section 4 presents results and the corresponding performance evaluation. Finally, Section 5 concludes the paper.

2. PROBLEM DESCRIPTION

Localization in 3-D space is particularly important in real applications of WSNs, but many of its aspects remain unexplored since the typical scenario for WSN localization is investigated in a 2-D plane, **Wang et al., 2010**. In a 3-D space at least four anchor nodes are needed whose locations are known. An estimate of the distance d_i , $i = 1, 2, 3, 4$, between each of the anchor nodes (x_i, y_i, z_i) and the node to be localized (x, y, z) is needed.

The TOA distance measurement technique is assumed. TOA is the time delay between transmission at the node to be localized and reception at an anchor node. This is equal to the distance d_i divided by the speed of light if either RF or UWB signals are used. The backbone of the TOA distance measurement technique is the accuracy of the arrival time estimates. This accuracy is hampered by additive noise and non-line-of-sight (NLOS) arrivals. The measurement errors are modeled as additive zero-mean Gaussian noise. The total additive Gaussian measurement noise will be modeled as $N(\mu, \sigma_{NLOS}^2)$, where the letter N denotes the normal or Gaussian distribution, μ is the mean, and σ_{NLOS}^2 is the variance taking into account NLOS arrivals. The occasional inclusion of a mean accounts for the biased location estimate resulting from NLOS errors, **Gustafsson and Gunnarsson, 2005**. and **Patwari et al., 2005**.

To determine the TOA in asynchronous WSNs, two-way TOA measurements are used. In this method, one sensor sends a signal to another which immediately replies. The first sensor will then determine TOA as the delay between its transmission and reception divided by two, **Patwari et al., 2005**.

Gradient-descent iterative optimization in three dimensions results in slower convergence when compared to the 2-D case due to tracking along an extra dimension. This is typical of all iterative optimization methods. Owing to the limited exploration of 3-D scenarios in the literature, the present work serves to shed light on practical results relating to the GD WSN localization problem in three dimensions. As with all optimization methods, the gradient descent method hinges on the concept of minimizing an objective function. For the problem of WSN localization, it is natural to define the objective function as the sum of the squared distance errors of all anchor nodes. Thus, the objective function is defined as:

$$f(p) = \sum_{i=1}^N \left\{ \left[(x - x_i)^2 + (y - y_i)^2 + (z - z_i)^2 \right]^{1/2} - d_i \right\}^2$$

(1)

$$\text{and } d_i = c(t_i - t_o) \quad (2)$$

where $p = [x, y, z]^T$ is the vector of unknown position coordinates (x, y, z) , t_i is the receive time of the i th anchor node, t_o is the transmit time of the node to be localized, c is the speed of light ($= 3 \times 10^8$ m/s) and N is the number of anchor nodes. The difference $(t_i - t_o)$ is the TOA that can be measured (with measurement noise) in asynchronous WSNs as explained.

The optimization purpose is to minimize the objective function to produce the optimal solution which is the position estimate of the node to be localized. This problem is solved iteratively using gradient descent as follows:

$$p_{k+1} = p_k - \alpha \cdot g_k \quad (3)$$

where p_k is the vector of the estimated position coordinates, α is the step size, and g_k is the gradient of the objective function given by:

$$g_k = \nabla f(x, y, z) = \left[\frac{\partial f}{\partial x}, \frac{\partial f}{\partial y}, \frac{\partial f}{\partial z} \right]^T \quad (4)$$

To start the iteration, the initial position coordinates are required. These may be chosen to be the mean position of all anchor nodes. The number of iterations is a tradeoff between energy consumption, which is critical to WSNs, and the degree of accuracy.

A minimum of four anchor nodes is needed to estimate position in a 3-D space. The estimation accuracy increases as a function of the number of anchor nodes. If the number of anchor nodes is less than four, the estimation problem becomes under-determined (number of simultaneous equations is less than the number of unknowns) and there are an infinite number of solutions that converge iteratively to an erroneous location or position.

The objective function is the sum of the squares of the differences between estimated distances and measured distances. Therefore, distance measurement errors are squared, too. This problem is countered by weighting distance measurements according to their confidence to limit the effect of measurement errors on localization results **,Kwon et al., 2005**. So the objective function accommodating different weights is expressed as:

$$f(p) = \sum_{i=1}^N w_i \left\{ \left[(x-x_i)^2 + (y-y_i)^2 + (z-z_i)^2 \right]^{1/2} - d_i \right\}^2 \quad (5)$$

Weighting, however, results in sub-optimal solutions if only four anchor nodes are used. Since usually there are only a few anchors in a real WSN, **Li et al., 2008** use of five anchor nodes is a good choice to achieve better accuracy without undue deviation from real settings. In this case, weighting according to anchor node confidence gives better results than those obtained with the minimum number of anchor nodes (four) without weighting.

It is worth mentioning that evaluating Eq.(1), i.e. the error objective function $f(p)$ versus p where $p=[x,y,z]^T$, results in a 4-D performance surface with a global minimum and several local minima. To avoid local minima, the gradient descent must run several times with different starting points, which is expensive computationally. To better visualize the local minima problem, localization in a 2-D space is envisaged to enable performance surface plotting in a 3-D space. Three anchor nodes [10 ,100], [100 ,90], and [10 ,70] are considered with $d_i=78.1025$, 64.0312, and 58.3095 corresponding to a point $p=[60 ,40]$. Then, plotting the following objective function

$$f(p) = \sum_{i=1}^3 \left\{ \left[(x-x_i)^2 + (y-y_i)^2 \right]^{1/2} - d_i \right\}^2 \quad (6)$$

results in **Fig. 1** with azimuth= 180° and elevation= 0°.

The presence of a global minimum at p and a neighboring local minimum can be noticed from **Fig. 1**. The search procedure of the performance function therefore often gets trapped in a local minimum especially when the node to be localized is moving. In the following section, a solution will be presented to solve the local minima problem in a moving sensor localization setting.

3. LOCALIZATION OF A MOVING SENSOR IN A 3-D SPACE

With a moving sensor, the gradient descent still functions acceptably to track the target in real time. The measurement sample interval determines the measurement update rate. A bit of care is required in adjusting the sample interval to avoid conflict with moving sensor velocity and motion models which may be completely unknown, **Gustafsson and Gunnarsson, 2005**. The moving node must provide multiple measurements to the anchors as it moves across space. It has the opportunity to reduce environment-dependent errors as it averages over space. Many computational aspects of this problem remain to be explored, **Patwari et al., 2005**.

Agarwal et al., treated the problem of avoiding local minima for moving sensor localization by smart use of available anchors and good initialization. Although these works are also based on minimizing cost functions, they are not general gradient descent-based, which is the focus of this paper. Besides, these works require and exploit good initial estimation of the target location. It is therefore challenging to achieve moving sensor localization, and at the same time, dispense with the initial estimation of the moving target location. As a solution to this problem, we may consider the introduction of diversity in the iterative GD estimation problem.

In this work, the algorithm listed below is presented to localize a moving sensor in a 3-D space with the provision of local minima avoidance. The foreseen success of the proposed method is based on the conception that, as the updated position begins to wander away from the global minimum in the direction of a local minimum, it is highly probable that it would return to the right track if some anchor nodes are replaced due to the consequent change of performance surface shape and hence local minima positions.

Algorithm 1: Proposed GD localization of a moving sensor

1. Estimate a suitable measurement sample interval or update rate.
2. Cluster available anchor nodes into sets of five nodes each. The number of resulting sets P will be:

$$P = \binom{N}{5} = \frac{N!}{5!(N-5)!}$$

where N is the total number of anchor nodes.

3. Randomly draw M sets from P obeying a uniform distribution.
 4. Perform M independent gradient descent localization procedures on the moving sensor using these M sets.
 5. Iterate the gradient descent algorithm up to the L -th update, and calculate the final $f(p)$ for each of the M sets. Discard the sets that produce $f(p)$ greater than a certain threshold γ . Find the point p with the minimum $f(p)$.
 6. Stop the algorithm if the moving sensor tracking halts.
 7. Complete the M sets by randomly choosing other sets from P , and repeat steps 4 to 6 starting with the final position of p that corresponds to the minimum $f(p)$.
-

The different parameters appearing in Algorithm 1 should be properly chosen. These are M , N , L and the threshold γ . As discussed in the problem description, N should not be unduly large in practical settings. Assuming that five anchors per set are involved in localization, N must not be much greater especially when the WSN area or volume is limited. As for M , it naturally determines the computational overhead; GD localization must run M times in each round of

position estimation. To reduce the amount of computation to a minimum, the choice of M must achieve a tradeoff between computational complexity and sufficient diversity of anchor sets in order to cancel unsuitable candidates and retain functional ones. The threshold γ depends on the specific application and how tolerant the latter is to the final value of the error function $f(p)$. In the simulations (Section 4), the moderate value of 7 m^2 is used as a default setting. This means that the estimated squared distance error associated with each anchor is $(7/5) \text{ m}^2$ on average, Eq. (1).

As for L , it has been assigned the value 150 iterations in the present simulation settings, which is, however, an ad-hoc value that worked for the particular settings under consideration. To ensure accurate tracking, a check on the error function of all running estimations can be performed after each certain interval (for example 30 iterations) and then the decision is made whether to proceed or replace the diverging sets.

A final remark concerns the communication overhead; the proposed algorithm does not add to the communication complexity. With each iteration, and after the sensing has been achieved, only one broadcast (communication) of the distance measurement is enough from each of the N anchors. It is in the fusion center that the various combinations of P are sorted out and their associated computations performed.

4. SIMULATION RESULTS

The gradient descent localization problem in a 3-D space is simulated on MATLAB. The anchor node locations are chosen at random in a volume of $200 \times 200 \times 200 \text{ m}^3$. It is assumed that the target node which is to be localized, whether stationary or moving, has all anchor nodes within its radio range. The LOS and NLOS measurement noise is assumed to obey a normal distribution $N(\mu, \sigma^2)$. In the subsequent simulations, a noisy TOA measurement is simulated by adding a random component to the exact value of the time measurement. The latter is readily computed for simulation purposes from knowledge of the exact node position to be localized, the anchor positions, and the speed of light c .

A. Localization of a stationary target node

First, consider three anchor nodes to localize a node of position (60,90,60) in the 3-D space assuming that the standard deviation of the zero-mean Gaussian TOA measurement noise, the convergence factor or step size and the number of iterations to be $\sigma=0.001 \text{ } \mu\text{sec}$, $\alpha=0.25$ and $j=100$ respectively. Simulation results localized the target node as (57.62, 68.16, 52.42) which is clearly erroneous. Using four anchor nodes and the same settings, the localization of the target node improves to (60.28, 84.02, 58.65). Finally, five anchor nodes provide an almost ideal target localization of (60.16, 89.64, 60.09). **Fig. 2** is a plot of the error function versus the number of iterations for this last case of five anchor nodes. Retaining this scenario, another node (70,45,60) is localized as (70.03,45.16,59.85). Obviously, any node within the convex hull of the anchor nodes will be almost exactly localized with five anchors.

The results of **Fig. 2** are repeated in **Fig. 3** taking into account the presence of NLOS arrivals and a greater noise standard deviation. In **Fig. 3**, $\sigma=0.002 \text{ } \mu\text{sec}$, and $\mu_{\text{NLOS}}= 0.003 \text{ } \mu\text{sec}$. A reduction in the localization process accuracy is readily noticed: The point (60,90,60) results in a localization of (60.35, 88.97, 59.40). It is also clear from the figure that the solution is biased due to NLOS arrivals.

The number of iterations in the localization process of a stationary target is a tradeoff between the energy consumption for result refinement and the degree of accuracy achievable through

refining. The issue of energy consumption may appear to disfavor the iterative GD method compared to other optimization methods. This is not the case, however, when the target is moving, since updating would then be a must whether iterative or other methods are employed. In such cases, resorting to distributed algorithms would save energy costs even for iterative methods, since the nodes in a distributed algorithm communicate mostly with neighbors (one hop) as compared to centralized algorithms which are the concern of the present work. This is especially manifested when the number of hops to the central processor exceeds the necessary number of iterations.

B. Localization of a moving target node

In the following scenarios, a moving node is tracked and localized. We assume five anchor nodes since this offers the best estimation accuracy. To better illustrate the proposed algorithm and the effect of the various inherent parameter values, it is assumed that the measured distances are noise-free.

- a. A target node is moving 0.5 m in each of the three x , y , and z axes in each of 200 steps, which gives a true track distance of 100 m. The true track is illustrated by the straight line in **Fig. 4**. The estimated track begins with an initial point of (50, 50, 50) and converges to the true track for a while but then deviates from it due the local minima associated with this problem. This deviation is shown clearly in **Fig. 4**.
- b. The same scenario is repeated except that the track is divided into two segments. The first segment uses the same previous anchor nodes. In the second segment, the anchor nodes have been changed in an attempt to avoid the local minimum and resume tracking the true path. **Fig. 5** shows the corrected tracking behavior and the new set of anchor nodes.
- c. The proposed method of Algorithm 1 is applied with $N=7$ resulting in $P=21$, that is, seven anchor nodes are clustered in 21 sets of five anchor nodes each. M is chosen to be equal to 10 and L equal to 150. The threshold is chosen as $\gamma=7$. At the 150th update, the final $f(p)$ is calculated for each of the 10 sets. The sets that produce an error function greater than 7 are discarded, and other sets from the remaining 11 sets are chosen to complete the 10 sets starting with the final position of p that corresponds to the minimum $f(p)$. Iterative computations are continued for another 150 updates and the optimum set is also found by inspecting the localized point that results in the minimum final $f(p)$. The true and estimated tracks are shown in **Fig. 6**. Simulations show that the optimum set of anchor nodes in the first segment (150 iterations) is different from that of the second segment and no local minimum deviation is noticed.

It is worth noting that in the second segment; the first-segment unsuccessful sets can be replaced in a deterministic manner rather than randomly, since one would by then have an idea of the location of the moving target. This is especially convenient for WSNs with widely scattered sensors, where sets with nodes that are distant from the moving target and that are likely to contribute to poor localization can be discarded.

Future work may consider introducing distance-measurement noise and studying its effect on the performance of the proposed algorithm. In that case, the final $f(p)$ may not be enough indication of the validity of any certain set of anchors due to noisy measurements. So averaging $f(p)$ of the last 10 iterations of each segment of the estimated path, and for all M running sets,



may be considered to obtain a more accurate comparison and a judicious subsequent selection of sets.

5. CONCLUSION

The problem of sensor localization in a 3-D space by the method of gradient descent has been investigated and solutions are presented to some impediments that are associated with the moving sensor case, namely, the local minima problem. The proposed method considers all possible combinations of a certain chosen number of anchor nodes from a larger set of available anchors. The foreseen success of the proposed method stems from the fact that a deviating estimated path towards a local minimum is almost certain to return to the right track if some anchor nodes are replaced. This is true since anchor node replacement entails a change of the shape of the performance along with different local minima positions. The anchor nodes placement is made uniformly random as the true track of the moving sensor to be localized is unpredictable, and it is performed periodically. The simulation results demonstrate the success of this method. The advantage gained is at the expense of increased computational requirements, and the proposed method also necessitates faster data processing in order to perform accurate moving sensor localization in real time.

REFERENCES:

- Agarwal A., Daume H. III, Phillips J. M., and Venkatasubramanian S., 2012, *Sensor Network Localization for Moving Sensors*, Proceedings of the 12th International Conference on Data Mining Workshops, ICDMW 2012, IEEE, pp. 202-209.
- Agarwal A., Phillips J. M., and Venkatasubramanian S., 2010, *Universal Multi-Dimensional Scaling*, Proceedings of the 16th International Conference on Knowledge Discovery and Data Mining, ACM SIGKDD 2010, ACM, pp. 1149-1158.
- Garg R., Varna A. L., and Wu M., 2010, *Gradient Descent Approach for Secure Localization in Resource Constrained Wireless Sensor Networks*, International Conference on Acoustics, Speech and Signal Processing (ICASSP) , IEEE pp. 1854-1857.
- Gustafsson F. and Gunnarsson F. , 2005, *Mobile Positioning using Wireless Networks*, IEEE Signal Processing Magazine, vol. 22, no. 4, pp. 41-53.
- Kwon Y. M., Mechtov K., Sundresh S., Kim W. and Agha G., 2005, *Resilient Localization for Sensor Networks in Outdoor Environments*, Proceedings of the 25th IEEE International Conference on Distributed Computing Systems, ICDCS 2005, , IEEE, pp. 643-652.
- Li X., Hua B., Shang Y. and Xiong Y., 2008, *A Robust Localization Algorithm in Wireless Sensor Networks*, Front. Comput. Sci. China, DOI 10.1007/s11704-008-0018-7, April.
- Patwari N., Ash J. N., Kyperoutas S., Hero A. O. III, Moses R. L. and Correal N. S. , 2005, *Locating the Nodes*, IEEE Signal Processing Magazine, vol. 22, no. 4, pp. 54-69.



- Qiao D. and Pang G. K. H. , 2011, *Localization in Wireless Sensor Networks with Gradient Descent*, IEEE Pacific Rim Conference on Communications, Computers and Signal Processing, IEEE, pp. 91-96.
- Wang J., Ghosh R. K. and Das S. K., 2010, *A Survey on Sensor Localization*, Journal of Control Theory Applications, vol. 8, no. 1, pp. 2-11.
- Zhang L., Tao C. and Yang G. , 2011, *Wireless Positioning: Fundamentals, Systems and State of the Art Signal Processing Techniques, Cellular Networks- Positioning, Performance Analysis, Reliability*, Dr. A. Melikov (Ed.), ISBN: 978-953-307-246-3, InTech. Available from: <http://www.intechopen.com/books> .

NOMENCLATURE

c : speed of light

d_i : distance between the i th anchor node and the target node

$f(p)$: the error function or objective function

g_k : the k th gradient of the objective function

N : number of anchor nodes

p_k : the k th estimate of the position co-ordinates.

t_o, t_i : the transmit time of the target node and the receive time of the i th anchor respectively.

w_i : weight of the i th error term in the objective function.

x, y, z : co-ordinates of the target node

α : the step size or convergence factor

γ : threshold in proposed algorithm

μ : mean

σ : standard deviation

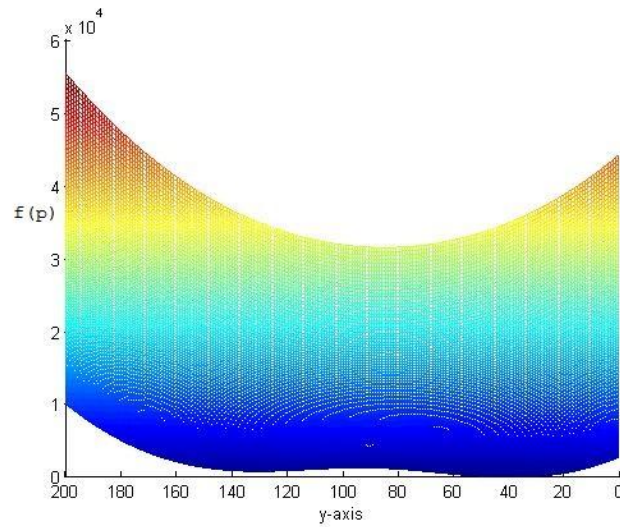


Figure 1. Error function $f(p)$ as a 3-D performance surface with 2-D anchor nodes $[10,100]$, $[100,90]$, and $[10,70]$ and a global minimum at $p=[60,40]$. Azimuth= 180° and elevation= 0° .

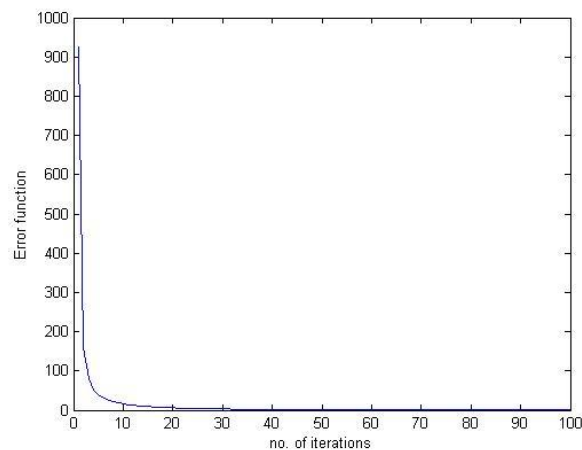


Figure 2. Error function versus the number of iterations when GD localization of a stationary target in 3-D space is performed using five anchor nodes. Convergence factor= 0.25 , standard deviation (SD) of TOA measurement noise = $0.001 \mu\text{sec}$.

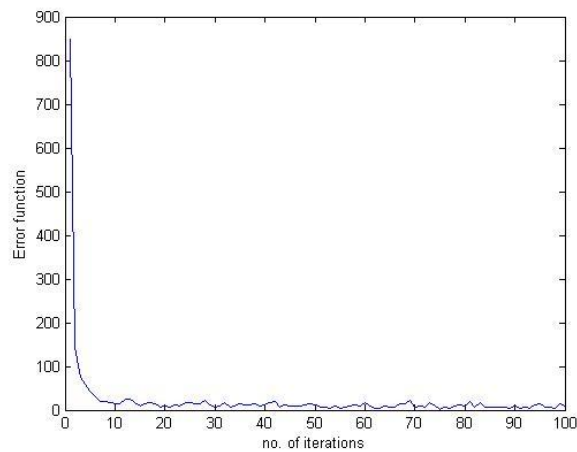


Figure 3. Error function versus the number of iterations when GD localization of a stationary target in 3-D space is performed using five anchor nodes. Convergence factor=0.25, SD of TOA measurement noise =0.002 μ sec and μ_{NLOS} =0.003 μ sec.

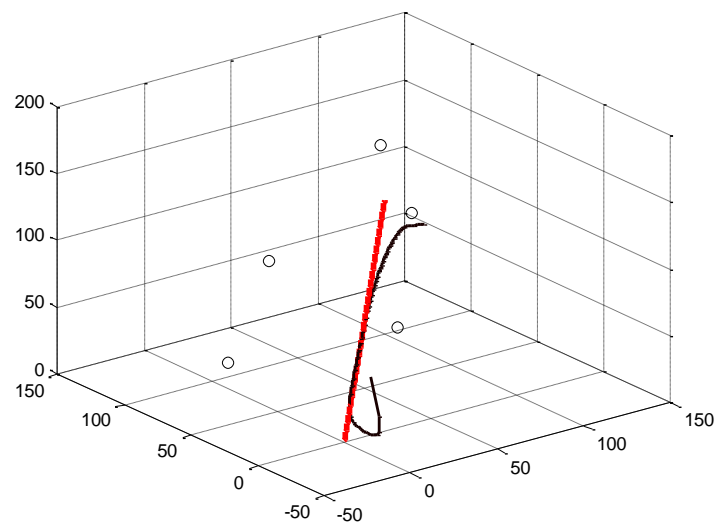


Figure 4. Tracking of a moving sensor in 3-D space using iterative GD with initial point [50,50,50] and a fixed set of anchor nodes (shown by the small circles). Convergence factor=0.1. The true path is shown in red.

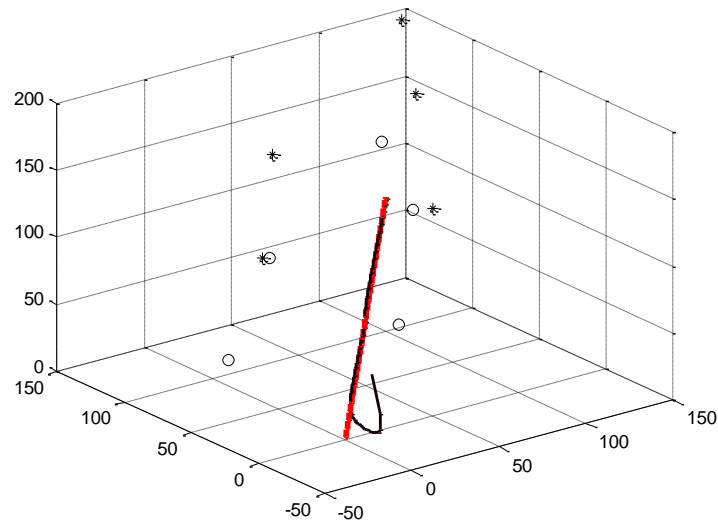


Figure 5. Two-segment true path and track of a moving sensor in 3-D space using iterative GD. Initial point is $[50,50,50]$. Convergence factor=0.1. The small circles are the 1st-segment anchors and the asterisks are the 2nd-segment anchors. The true path is shown in red.

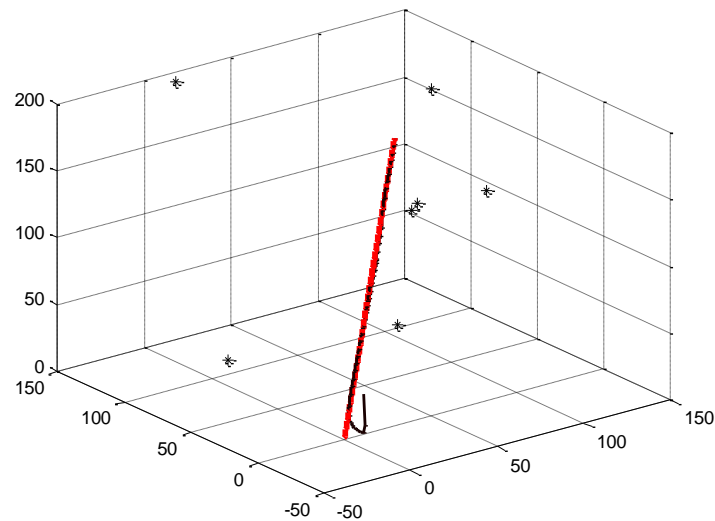


Figure 6. GD tracking of a moving sensor using the proposed algorithm. Initial point is $[50,50,50]$. Convergence factor=0.1. The basic seven anchor nodes are shown as asterisks. The true path is shown in red.



Cooling Load Calculations For Typical Iraqi Roof And Wall Constructions Using Ashrae's RTS Method

Khalid Ahmed Joudi

Professor

College of Engineering-University of Baghdad

E-mail: Khalid47joudi@yahoo.com

Ali Naser Hussien

Lecturer

Mechanical engineering department-University of Technology

E-mail: aaali_n@yahoo.com

ABSERACT

The present work is an attempt to develop design data for an Iraqi roof and wall constructions using the latest ASHRAE Radiant Time Series (RTS) cooling load calculation method. The work involves calculation of cooling load theoretically by introducing the design data for Iraq, and verifies the results experimentally by field measurements. Technical specifications of Iraqi construction materials are used to derive the conduction time factors that needed in RTS method calculations. Special software published by Oklahoma state university is used to extract the conduction factors according to the technical specifications of Iraqi construction materials. Good agreement between the average theoretical and measured cooling load is obtained and the difference between them does not exceed 9.3%.

Key words: Iraqi constructions cooling load.

حسابات حمل التبريد لتركيبيات سقوف وجدران نموذجية عراقية باستخدام نظرية RTS لاشري

علي ناصر حسين

مدرس

قسم الهندسة الميكانيكية- الجامعة التكنولوجية

خالد أحمد جودي

أستاذ

كلية الهندسة- جامعة بغداد

الخلاصة

الدراسة الحالية هي محاولة لتقديم بيانات تصميمية لسقوف وجدران عراقية باستخدام أحدث الطرق المستخدمة من قبل جمعية اشري لحساب حمل التبريد وهي طريقة السلسلة الزمنية للإشعاع (RTS). يتضمن العمل حساب الحمل الحراري نظريا باستخدام ظروف العراق التصميمية، والتحقق منها بالقياسات العملية. تم استخدام المواصفات الفنية لمواد بناء عراقية لاشتقاق المعاملات الزمنية للتوصيل المطلوبة للعمليات الحسابية بطريقة (RTS). وقد استخدم برنامج خاص مصمم من قبل جامعة أوكلاهوما الأميركية لاستخراج المعاملات الزمنية للتوصيل وفقا للمواصفات الفنية لمواد البناء العراقية. وقد تم الحصول على توافق جيد بين معدل حمل التبريد المحسوب نظريا والمقاس عمليا ولم يتجاوز الفرق بينهما ٩,٣%.



1. INTRODUCTION

Among six common ASHRAE methods: Equivalent Temperature Difference (ETD), Total Equivalent Temperature Differential with Time Averaging (TETD/TA), Transfer Function Method (TFM), Cooling Load Temperature Difference/Solar Cooling Load/Cooling Load Factor (CLTD/SCL/CLF), Heat Balance Method (HBM), and Radiant Time Series Method (RTSM), the Radiant Time Series Method (RTSM) is the latest ASHRAE method for calculating the cooling load. RTSM is a simplified method that is “heat-balance based” but does not solve the heat balance equations. The storage and release of energy in the zone is approximated by a set of predetermined zone response factors, called radiant time factors (RTFs), **Spitler, et al., 1997**. The transient conduction calculation is approximated using another set of predetermined thermal response factors, called periodic response factors (PRFs) which relate conduction heat gains directly to temperatures only, **Spitler, and Fisher, 1999a** and, **Chen and Wang, 2005**. By incorporating these simplifications, the RTSM calculation procedure becomes explicit, avoiding the requirement to solve the simultaneous system of Heat Balance (HB) equations. The RTSM shares many of the heat transfer sub-models used by the HBM and has the equivalent principle of superposition used in the Transfer Function Method TFM, **Spitler and Fisher, 1999b**. Moreover, it is a rather simplified method that does not require iterative calculations like the HBM and the TFM. If the radiant time factors (RTFs) and the periodic response factors (PRFs) for a particular zone configuration are known, the RTSM may be implemented in a spreadsheet. The method is useful not only for peak load calculations, but also for estimating component contributions to the hourly cooling loads that is useful for both pedagogy and design, **Iu, 2002**.

Following the development of the RTSM, it was verified by comparing cooling loads predicted by the RTSM with cooling loads predicted by the heat balance method for a wide range of zone configurations. **Rees, et al., 2000**, compared RTSM and heat balance cooling loads for 1296 configurations, which were generated by parametrically varying significant input parameters over a wide range. This analysis conclusively demonstrated that the RTSM always produces a conservative estimate of the cooling load when compared to the heat balance method. However, the over-prediction of the cooling load by the RTSM tends to increase as the fraction of window area in the zone increases. Since the HBM and RTSM share most of the heat transfer models in the cooling load calculation, the Periodic Response Factor (PRF) and the Radiant Time Factor (RTF) models that are used exclusively in the RTSM are considered the most likely sources of error.

A series of investigations of the Radiant Time Series Method (RTSM), in some cases, leading to improvements to the method was introduced by **Nigusse, 2007**. It included sub-models, supporting data, or facilitation of implementation in a wide range of computing environments. These developments comprise the improved RTSM procedure, which accounts for transmission of radiant heat gains back to the outside by conduction through fenestration or other high conductance surfaces. As a result a new set of radiative / convective splits were established to facilitate implementation of the RTSM in a range of computing environments, and parametric investigation to establish the method limitations and provide design guidance.

The radiant time series method (RTSM) has effectively replaced the manual load calculation procedures and has attracted interest, **Nigusse, 2007** due to:



- 1) Its amenability to spreadsheet implementations as opposed to the Transfer Function Method, which requires iteration.
- 2) Captures and depicts the physics involved in the Conduction Time Series Factor (CTSF) and Radiant Time Factor (RTF) coefficients, unlike the Transfer Function Method.
- 3) Has essentially the same accuracy as the TFM.

1.1. The Concluded Concepts from the Previous Studies

From the above, there are some concepts can be concluded such as:

1. The radiant time series method (RTSM) is suitable and applicable to estimate the cooling load using the local climatic data in any region without correction formulas.
2. Because the RTSM approximates the heat balance concepts using set of zone response factors, the accurate results is ensured, beside the simplified equations.
3. The progress in the field of electronic computers, simplifies the insertion of the actual construction data of the local roofs and walls in the cooling load calculations, using RTSM without need to choose the nearest constructions from ASHRAE tables, as in the previous.

1.2. The Object of the Present Work

The present work aims to appraise the ASHRAE's Radiant Time Series Method (RTSM) with the introduction of Iraqi data which includes:

- outside design temperatures
- solar radiation values
- heat transfer coefficients
- building material characteristics

2. CALCULATION PROCEDURE IN RTS METHOD

The general procedure for calculating a cooling load for each load component is shown in **Fig. 1** and includes:

1. Calculate 24 h profile of component heat gains for the design day as follows:

- a. For conduction through walls, and roofs, first account for conduction time delay by applying conduction time series. The Conduction Time Series (CTS) are series of 24 factors tabulated in ASHRAE's issues for different construction types of roofs and walls and grouped according to the thermal properties of structure (U value, mass per unit area, and thermal capacity ($m \cdot c$)). These factors are denoted by c_f in the present study, and represent the hourly percentage of converting the heat conduction across the external construction (walls and roofs) to hourly heat gain. The conduction through exterior walls and roofs is calculated using conduction time series (CTS) as follows:

Wall and roof conductive heat input at the exterior at n hours ago is defined by the familiar conduction equation:

$$Q_{i,t-n} = UA(T_{e,t-n} - T_i) \quad (1)$$

where T_i is the indoor temperature and $T_{e,t-n}$ is the sol-air temperature at n hours ago and is expressed as:



$$T_{e,t-n} = T_{o,t-n} + \frac{\mu}{h_o} I_{t,t-n} - \frac{\varepsilon \Delta R(t)}{h_o} \quad (2)$$

Conductive heat gain through walls or roofs can be calculated using conductive heat inputs for the current hour and past 23 hours and conduction time series , **ASHRAE, 2009**:

$$Q_t = c_{f0}Q_{i,t} + c_{f1}Q_{i,t-1} + c_{f2}Q_{i,t-2} + c_{f3}Q_{i,t-3} + \dots + c_{f23}Q_{i,t-23} \quad (3)$$

c_{f0} , c_{f1} , etc. represent the conduction time factors. Multiplying of the conduction time factors by the U value gives the periodic response factors, p_r and equation (3) may be rewritten as:

$$Q_t = p_{r0}A(T_{e,t} - T_i) + p_{r1}A(T_{e,t-1} - T_i) + \dots + p_{r23}A(T_{e,t-23} - T_i) \quad (4)$$

b. For other components of heat gain (fenestration, ventilation and infiltration, internal, and etc.), the same procedure is applied as in any other method as follows:

i. Solar and thermal heat gain through fenestration is calculated as (ASHRAE 2009):

$$Q_{fs} = I_b * SHGC(\theta) * A_f * IAC(\theta) + (I_d + I_r) * SHGC)_D * A_f * IAC)_D \quad (5a)$$

$$Q_{fth} = U * A_f * (T_o - T_i) \quad (5b)$$

where I is the solar radiation. The subscripts b, d, and r refer to beam, diffuse and reflected portions respectively. $SHGC(\theta)$ and $SHGC)_D$ are the solar heat gain coefficients as a function of the incident angle θ and the diffuse radiation respectively. $IAC(\theta)$ and $IAC)_D$ are the indoor solar attenuation coefficient functions of the incident angle θ and diffuse radiation respectively.

ii. Total heat gain from infiltration or ventilation is

$$Q_{inf} \text{ or } Q_v = \rho_a * \dot{V}_a * \Delta h \quad (6)$$

where Δh is the enthalpy difference.

iii. Heat gain due to lighting, occupancy and equipment are;

For lighting,

$$Q_{Li} = W F_{ul} F_{sa} \quad (7)$$

For occupancy, occupants emit sensible and latent heat at a metabolic rate depending on the state of activity. Tables of ASHRAE summarize design data for common conditions.

For equipment,

$$Q_{em} = (P/E_M) F_{UM} F_{LM} \quad (8)$$

where P is the motor power rating, E_M is the motor efficiency, F_{UM} is the motor use factor, and F_{LM} is the motor load factor.



2. Heat gain through all components, are calculated for each hour, and then divided into two portions according to **Table 1**. The hourly convective portion heat gain, which is converted directly to hourly convective cooling load, and, the hourly radiant portion heat gain.
3. Apply appropriate radiant time series (table 19 and 20 in chapter 18 of, **ASHRAE Handbook of Fundamentals 2009** to the radiant heat gains to account for time delay in conversion to cooling load. The radiant time series are the series of 24 factor denoted by r in the present study and represent the hourly ratio of converting the radiant part of hourly heat gain to hourly cooling load.

The radiant time series or Radiant Time Factors (RTF) are thus generated from heat balance procedures between interior surfaces radiant heat gain and room air for different types of structures, fenestrations, and furnishing. These factors are tabulated for specific cases, (as indicated in table 19 and 20 in chapter 18 of ASHRAE Handbook of Fundamentals 2009) to use them directly for the certain application instead of performing inside surface and room air heat balances. Converting the radiant portion of hourly heat gains into hourly cooling loads is accomplished by the following equation:

$$Q_{clr,t} = r_0 Q_{r,t} + r_1 Q_{r,t-1} + r_2 Q_{r,t-2} + r_3 Q_{r,t-3} + \dots + r_{23} Q_{r,t-23} \quad (9)$$

4. The hourly radiant portion cooling load calculated in 3 above is then added to the hourly convective cooling load to obtain the total hourly cooling load for a certain component.
5. After calculating cooling loads for each component for each hour, sum them to determine the total cooling load for each hour and select the hour with the peak load for design of the air-conditioning system.

Tables 19 and 20 (in chapter 18 of ASHRAE Handbook of Fundamentals 2009) of radiant time factors introduce representative solar and non-solar radiant time series data for light, medium, and heavyweight constructions. The two different radiant time series solar and non-solar are used as follows:

- a. **Solar**, for direct transmitted solar heat gain (radiant energy is assumed to be distributed to the floor and furnishings only) and,
- b. **Non-solar**, for all other types of heat gains (radiant energy assumed to be uniformly distributed on all internal surfaces). Non-solar RTS apply to radiant heat gains from people, lights, appliances, walls, roofs, and floors. Also, for diffuse solar heat gain and direct solar heat gain from fenestration with inside shading (blinds, drapes, etc.), the nonsolar RTS should be used.

The radiant time series representative zone construction for tables 19 and 20 is indicated in table 21 in chapter 18 of, **ASHRAE Handbook of Fundamentals 2009**.

2.1. Evaluation of Periodic Response Factors (PRFs) of Roof and Wall Constructions

Iu and Fisher 2001, published a software program called Periodic Response Factor / Radiant Time Factor (PRF/RTF) Generator. They used the most developed accurate methods to derive the conduction transfer function coefficients and the periodic response factors that are needed to calculate the heat gain from walls and roofs. Giving the physical properties of any structure with any number of layers, this software can yields the conduction transfer function coefficients, the

periodic response factors, and the U value, in addition to the radiant time factors for the certain space. The physical properties that must be given include; thickness, thermal conductivity, density, and specific heat for each layer of a homogeneous material constituting the wall or roof. For non-homogeneous materials and for air gaps and air films in and outside the structure, the equivalent thermal resistance is the input instead of the other physical properties. **Fig. 2** shows the dialog box used for creating the input file

This program is very useful and reasonable when the used structures are different to those mentioned in the ASHRAE issues. Therefore, this software is used in the present study for typical Iraqi construction materials.

3. EXPERIMENTAL VERIFICATION OF RTSM

Fig. 3 shows the schematic floor plan of a 24 hr air-conditioned space in the second floor of the maintenance department building of the medical city in Baghdad (33.3° N latitude and 44.4° E longitude) for the test space. The inlet conditioned air comes through a 24x24 cm ceiling diffuser at 6 m/s supply velocity. The space construction components detailed are in **Table 2**.

Table 3 presents the thermal properties of the materials of the roof and wall constructions.

Inserting the thermal properties of the building materials in the dialog box of PRF/RTF Generator program gives the periodic response factors that are needed to calculate the heat gain of the roof and walls. **Table 4** listed the periodic response factors of roof and wall constructions of **Table 2**.

Thus, the theoretical cooling load can be calculated by apply Eqs. (2, 4, 5a, 5b, and 9). The values of p_r s are taken from **Table 4** for the concrete roof and the thermo-stone walls. The heat gain per unit area for the concrete roof and the thermo-stone wall for the NE and NW directions are given in **Tables 5a. and 5b.** respectively. The fenestration specifications are given in **table 6**, and the values of r_s are selected from table 19 in chapter 18 of, **ASHRAE Handbook of Fundamentals 2009** for heavy weight, no carpet and 10% of glass to wall ratio. **Table 7** lists these r values.

The experimental verification of the calculated cooling load was accomplished by measuring the average indoor air temperature, the supply air temperature and flow rate. The sensible heat extraction was calculated as:

$$Q_{s,h} = \dot{m}_a * c_p * (T_i - T_s) \quad (10)$$

$$\text{where } \dot{m}_a = \rho \dot{V}_s / RT_s \quad (11a)$$

$$\dot{V}_s = v_a * A_c \quad (11b)$$

$$\text{and } c_p = 1.006 + 1.840 * w_s \quad (11c)$$

where the specific heat of dry air and water vapor were taken at 1.006, and 1.840 kJ/kg.K respectively for the range of air conditioning temperatures and w_s is the moisture content. The approximated value of c_p is equal to 1.012 kJ/kg.K.

The heat extraction rate is equal to the cooling load if the indoor temperature of the space is constant. The latent load inside the space was zero for no occupancy.

4. RESULTS AND DISCUSSION

Fig. 4 shows the time delay of the roof and the external wall of the tested space. The time delay of the construction type can be defined as the difference between the hour of the peak heat gain in the space and the hour of the peak heat input at the external surface, **Nigusse, 2007**. The exterior and interior air conductance can be included in the wall and roof constructions. The time of the peak outer heat input to the construction is the time of the peak value of the sol-air temperature. Therefore, the time delay is the difference in the times of the peak heat gain and peak sol-air temperature. The value of the time delay is independent of the direction of the construction or the date at which it is calculated. It is only dependent on the material types of the construction and the inner and outer air conductance. The concrete roof of the tested space has 12 hours' time delay. The presence of the Styrofoam as an insulating material and the heavy weight of the roof slow the heat flow and reduce the peak and total heat gain, in addition, they make the time delay of the peak heat gain longer. The thermo-stone walls of the test space have 8.5 hours' time delay. This is because the thermo-stone has low thermal conductivity which results in a reduction of the heat gain across the wall. This reduces the exterior heat input and delays the hour at which the peak load occurs.

Fig. 5 shows the components of heat gain and cooling load of the test space using RTS method on July 8, 2011. The effect of the weight construction on the damping of the cooling load values is clearly apparent. The fenestration load component is the largest component because of the big area of the window, in spite of the shading of the concrete curtain wall. **Fig. 6** shows the comparison between total theoretical cooling load and the measured heat extraction rate. Also, it shows the indoor and supply air temperatures. The values of the measured load (heat extraction rate) fluctuate at the early hours of the morning and the last hours of the evening because of small fluctuations in the measured indoor temperature at these hours. The average values of the measured load and the calculated (theoretical) cooling load along the day are 1864.4 and 1690.3 W respectively. The underestimate of the calculated value is about 9.3%.

Good agreement between the average theoretical and measured cooling load is obtained from the comparison. This means that the calculated values of the cooling load of the Iraqi tested roof and wall using the RTS method and the procedure in the present paper is satisfied. Also the values of heat gains that are calculated in **Tables 5a. and 5b** can be adopted by engineers as design data for estimation the cooling load in Iraq for similar construction without needing correction formulas.

5. CONCLUSIONS

The following conclusions are found pertinent for the calculations of cooling load:

1. Radiant Time Series Method (RTSM) can be used to estimate the cooling load without correction formula and gives a good agreement with the measured cooling load. The underestimate of the average calculated value not exceeds 9.3% for the case in the present study.
2. The measured load average value is 1864.4 W, whereas the calculated (theoretical) cooling load average value is 1690.3 W along July 8, 2011 for the tested space.



3. The roof construction of 15 cm of high density concrete, 1cm of felt and membrane, 5 cm of Styrofoam, 5 cm of sand, 4 cm of cement shtyger, with suspended ceiling has 12 hours' time delay.
4. The wall construction of 30 cm thermo-stone, with 3 cm of cement plaster in the outside and 1.5cm juss plaster and 1 cm gypsum plaster in the inside delays the peak load by 8.5 hours.

References

- ASHRAE, 2009, *Handbook of Fundamentals*.
- Chen, Y., and Wang, S., 2005, *A new Procedure for Calculating Periodic Response Factors Based on Frequency Domain Regression Method*, International Journal of Thermal Sciences, vol. 44, No. 4, PP. 382-392.
- Iu, I. S., 2002. *Experimental Validation of The Radiant Time Series Method for Cooling Load Calculations*, M. Sc. thesis, Oklahoma State University.
- Nigusse, B. A., 2007, *Improvements to the Radiant Time Series Method Cooling Load Calculation Procedure*, Ph.D. dissertation, Oklahoma State University.
- Rees, S.J., Spitler, J.D., Holmes, M.J. and Haves, P., 2000, *Comparison of Peak Load Predictions and Treatment of Solar Gains in the Admittance and Heat Balance Load Calculation Procedures*, Building Services Engineering Research & Technology, vol. 21, No. 2, PP.125–38.
- Spitler, J. D., Daniel E. Fisher, and Pedersen, C. O., 1997, *Radiant Time Series Cooling Load Calculation Procedure*, ASHRAE Transactions, vol.103, No. 2, PP. 503-515.
- Spitler, J. D., and Fisher, D. E., 1999a, *Development of Periodic Response Factors for Use with the Radiant Time Series Method*, ASHRAE Transactions, vol. 105, No. 1, PP. 491-509.
- Spitler, J. D., and Fisher, D. E., 1999b, *On the Relationship between the Radiant Time Series and Transfer Function Methods for Design Cooling Load Calculations*, HVAC and Research, vol. 5, No. 2, PP. 125-138.

NOMENCLATURE

A	Area,	m^2
c_p	Specific heat of air,	kJ/kgK
c_f	conduction time factor	
E_m	Motor efficiency	
F_{LM}	Motor load factor	
F_{ul}, F_{um}	lighting, motor using factor	
F_{sa}	lighting special allowance factor	



h	specific enthalpy,	kJ/kg
h_i, h_o	inside, outside heat transfer coefficient,	$\text{W/m}^2\text{K}$
I	solar radiation,	W/m^2
m_a	air mass flow rate,	kg/s
P	motor power rating,	W
p	atmospheric pressure,	pa
p_r	periodic response factor,	$\text{W/m}^2\text{K}$
Q	heat,	W
R	gas constant of air,	kJ/kg.K
R^b, R^f	back, front face reflected of glass	
ΔR	The difference between the long wave radiation incident on the surface from the sky and surroundings, and the radiation emitted by a black body at the outdoor air temperature	
		W/m^2
r	radiant time factor	
SHGC	solar Heat Gain Coefficient	
T	temperature,	$^{\circ}\text{C}$
t	time,	sec
U	overall heat transfer coefficient,	$\text{W/m}^2\text{K}$
v_a	air supply velocity,	m/s
V_s	air supply volume flow rate,	m^3/s
V_a	ventilation air volume flow rate,	m^3/s
w_s	moisture content,	$\text{kg}_{\text{water}}/\text{kg}_{\text{air}}$

Greek Symbols

ϵ	emittance of the surface	
m	absorptivity of the surface	
ρ_a	air density,	kg/m^3
θ	incident angle,	degrees
τ_v	visible transmittance	
α_k^f	front absorptance of layer k of glass	

Subscripts

a	air
b	beam
c	cross sectional (diffuser area)
d	diffuse
e	sol-air (Temperature)
f	fenestration
fs	solar fenestration
fth	thermal fenestration
i	indoor
o	outdoor
r	reflected (radiation)
s	supply
t	total (solar radiation), time (others)



Abbreviations

- CL Cooling load, W
- CLF Cooling load factor,
- CLTD Cooling load temperature difference, °C
- CTS Conduction Time Series
- ETD Equivalent temperature difference, °C
- HG Heat gain, W
- IAC Indoor solar attenuation coefficient
- LCav Average calculated load, W
- LMav Average measured load, W
- PRF Periodic response factor, W/m²K
- RTS Radiant time series
- RTSM Radiant time series method
- SCL Solar cooling load, W/m²
- SHGC Solar heat gain coefficient
- TETD/TA Total equivalent temperature differential with time averaging, °C
- TFM Transfer function method

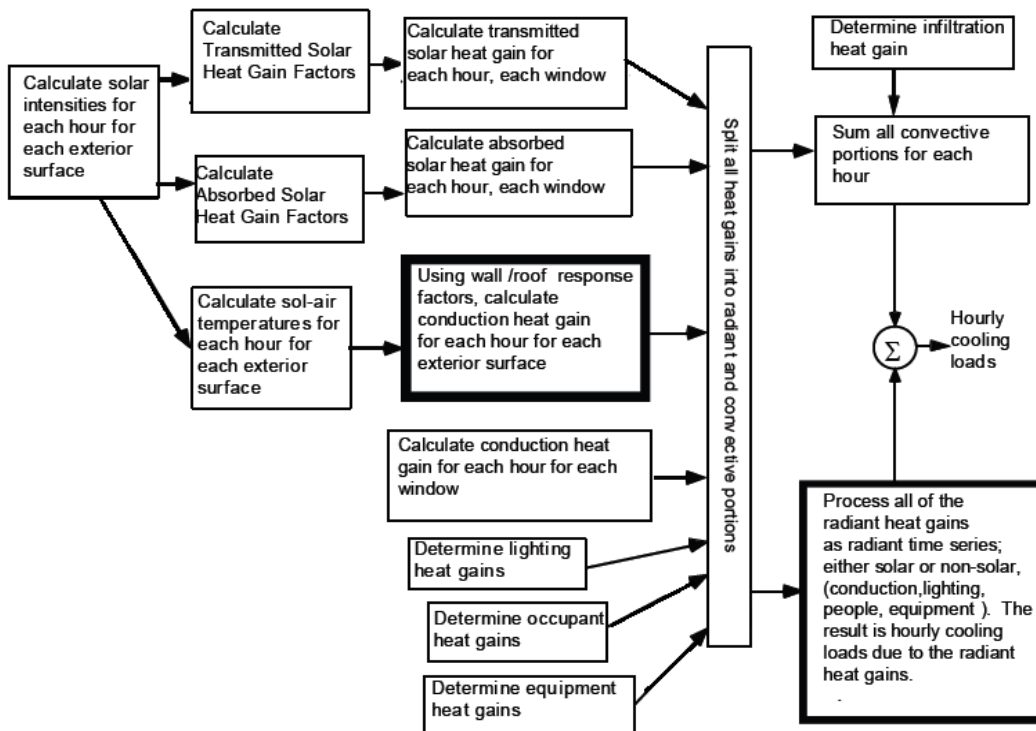


Figure 1. Overview of the (RTS) method.

Table 1. Recommended radiative/convective splits for heat gains components* , Nigusse, 2007. and adopted by , ASHRAE, 2009.

Heat Gain Type	Recommended Radiative Fraction	Recommended Convective Fraction
Occupants, typical office conditions	0.60	0.40
Lighting	Varies	
Recessed fluorescent luminaire with lens	0.40 to 0.50	0.61 to 0.73
Infiltration	0.00	1.00
Conduction heat gain		
Through walls and floors	0.46	0.54
Through roof	0.60	0.40
Through windows	0.33 (SHGC > 0.5) 0.46 (SHGC < 0.5)	0.67 (SHGC > 0.5) 0.54 (SHGC < 0.5)
Solar heat gain through fenestration		
Without interior shading	1.00	0.00
With interior shading	varies	

* Notes

1. For solar radiation through fenestration with interior shading tables 13A to 13G in Chapter 15 in ASHRAE 2009 can be reviewed.
2. For lighting table 3 and for different equipment, tables 6 to 12 in Chapter 18 in ASHRAE 2009 can be reviewed.

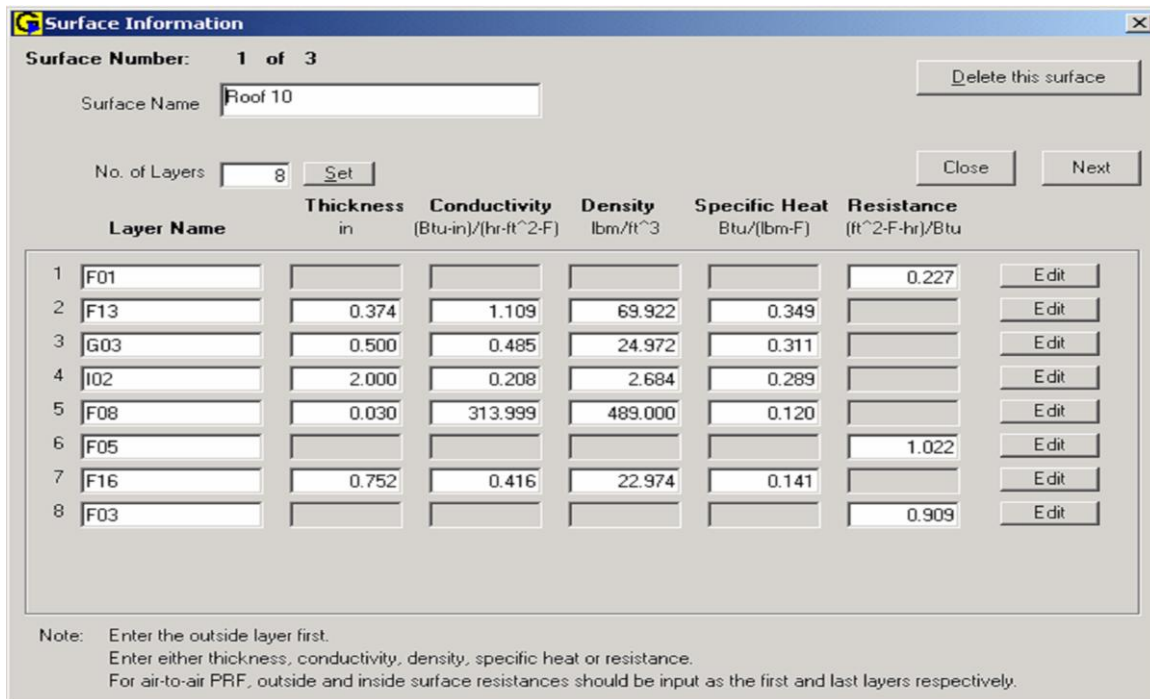


Figure 2. The dialog box of PRF/RTF generator program.

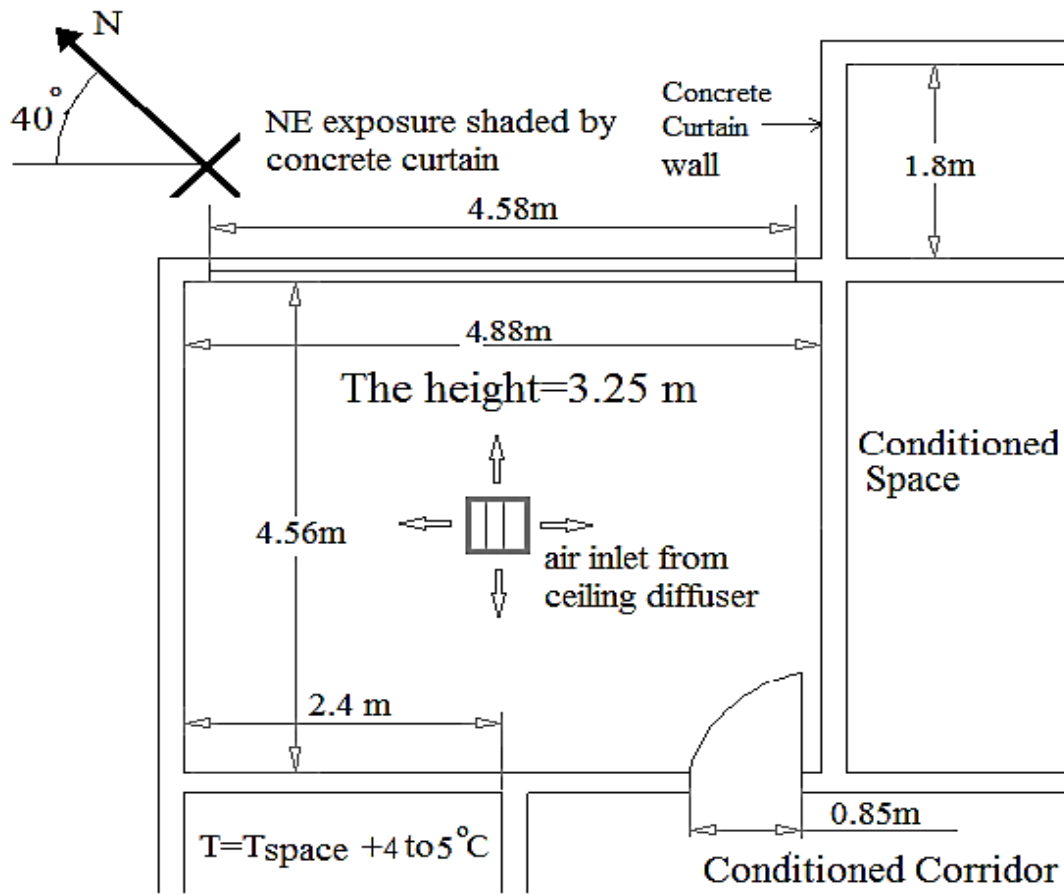


Figure 3. Schematic floor plan of tested space.

Table 2. Space construction components.

Part	Area (m ²)	U-value W/m ² K	Details
Roof	22.25	0.371	4 cm of cement shtyger+5 cm of sand+1cm of felt and membrane +5 cm of sty-rubber+15 cm of high density concrete+air gap+acoustic tiles in suspended ceiling
NE exterior wall	8.32	0.5747	3 cm of cement plaster +30 cm thermo-stone+1.5cm juss plaster+1 cm gypsum plaster
NW exterior wall	15.05	0.5747	3 cm of cement plaster+30 cm thermo-stone+1.5cm juss plaster+1 cm gypsum plaster
Window	7.8		5.75 m ² of glazing area + 2.035 m ² of aluminum frame area in NE(shaded) direction
SW partition	7.8	2.45	1 cm gypsum plaster +1.5cm juss plaster +20 cm hollow block +1.5cm juss plaster +1 cm gypsum plaster
floor	22.25	0.99	20 cm of high density concrete+3cm cement mortar+2.5cm mozaek tile

**Table 3.** Thermal properties of the building materials*.

Material	Thermal conductivity W/mK	density kg/m ³	Specific heat kJ/kgK	Thermal resistance m ² K/W
Outside air film				0.044
Inside horizontal surface air film (ceiling)				0.163
Inside vertical surface air film				0.12
Inside horizontal surface air film (floor)				0.11
Ceiling air space				0.176
Thermo-stone blocks	0.21	760	0.8	
High-density concrete	1.49	2300	0.84	
Styrofoam	0.03	30	2.03	
Concrete roofing tile (shytyger)	0.85	2220	0.837	
Sand (under roofing)	0.25	1450	0.84	
Cement plaster	1.08	2050	0.84	
Juss	0.72	1858	0.84	
Gypsum	0.57	1200	0.84	
Acoustic tile	0.061	481	0.84	
felt	0.35	1400	1.67	
Asphalt	0.041	1121	1.25	

* These thermal properties of the building materials are based on more than one source to insure an actual case, some of them are:

- 1- Center of building research issues /Baghdad University 1977.
- 2- The specific heats of the materials are taken according to the ASHRAE issues for the similar building materials that used in present study.
- 3- Previous studies of Iraqi building materials.

Table 4. PRFs of the test space roof and wall constructions as obtained by (PRF/RTF) generator program.

Hours	Concrete roof	Thermo-stone wall	Hours	Concrete roof	Thermo-stone wall
0	0.0138	0.0136	12	0.0171	0.0359
1	0.0134	0.0124	13	0.0170	0.0342
2	0.0132	0.0119	14	0.0168	0.0322
3	0.0134	0.0132	15	0.0166	0.0300
4	0.0140	0.0169	16	0.0163	0.0278
5	0.0148	0.0221	17	0.0160	0.0257
6	0.0156	0.0275	18	0.0157	0.0236
7	0.0162	0.0321	19	0.0154	0.0216
8	0.0166	0.0353	20	0.0151	0.0197
9	0.0169	0.0371	21	0.0148	0.0180
10	0.0171	0.0376	22	0.0144	0.0164
11	0.0171	0.0371	23	0.0141	0.0149



Table 5a. Heat gain of roof of tested space in W/m^2 with corresponding outdoor temperature on July 21.

Hours	0	1	2	3	4	5	6	7	8	9	10	11
T _{out} (°C)	34.41	34.06	33.9	33.66	33.41	34.61	36.18	38	39.95	41.9	43.93	46.29
Heat gain (W/m ²)	10.68	10.67	10.64	10.58	10.5	10.41	10.31	10.19	10.07	9.95	9.84	9.76
Hours	12	13	14	15	16	17	18	19	20	21	22	23
T _{out} (°C)	47.49	48.24	49	48.24	47.49	46.29	44.73	42.9	40.95	39	37.18	35.61
Heat gain (W/m ²)	9.71	9.7	9.73	9.8	9.91	10.04	10.18	10.32	10.45	10.55	10.63	10.67

Table 5b. Heat gain of thermo-stone wall in W/m^2 with corresponding outdoor temperature on July 21.

Hours	T.out °C	NE (shaded)	NW	Hours	T.out °C	NE (shaded)	NW
0	34.41	12.60	14.38	12	47.49	9.87	10.75
1	34.06	12.66	14.47	13	48.24	9.79	10.59
2	33.90	12.61	14.42	14	49.00	9.82	10.53
3	33.66	12.48	14.24	15	48.24	9.94	10.58
4	33.41	12.26	13.96	16	47.49	10.14	10.75
5	34.61	11.99	13.59	17	46.29	10.43	11.04
6	36.18	11.66	13.16	18	44.73	10.76	11.45
7	38.00	11.31	12.70	19	42.90	11.14	11.97
8	39.95	10.94	12.23	20	40.95	11.52	12.57
9	41.90	10.59	11.77	21	39.00	11.89	13.17
10	43.93	10.28	11.36	22	37.18	12.21	13.71
11	46.29	10.04	11.01	23	35.61	12.45	14.12

Table 6. Glass specifications of tested space , **ASHRAE, 2009.**

Clear glass 6mm thickness double pane with 0.5" air space, aluminum frame with thermal break							
Center glazing τ_v	U_f W/m ² K		Total Window SHGC at Normal incidence		Total Window τ_v at Normal Incidence		
	Fixed	Operable	Fixed	Operable	Fixed	Operable	
0.78	3.18	3.31	0.64	0.64	0.7	0.69	
Center-of-Glazing Properties							
Properties	Incident angle						
	0.0 (normal)	40	50	60	70	80	Hemis., diffuse
SHGC	0.70	0.67	0.64	0.58	0.45	0.23	0.60
τ	0.61	0.58	0.55	0.48	0.36	0.17	0.51
R^f	0.11	0.12	0.15	0.20	0.33	0.57	0.18
R^b	0.11	0.12	0.15	0.20	0.33	0.57	0.18
\mathcal{A}_1^f	0.17	0.18	0.19	0.20	0.21	0.20	0.19
\mathcal{A}_2^f	0.11	0.12	0.12	0.12	0.10	0.07	0.11

Table 7. Non-solar RTS values for the tested space (Table 19 in chapter 18 of ASHRAE Handbook of , **Fundamentals, 2009** for heavy weight construction, no carpet, and glass to wall percentage is 10%).

Hours	0	1	2	3	4	5	6	7	8	9	10	11
RTS%	22	10	6	5	5	4	4	4	4	3	3	3
Hours	12	13	14	15	16	17	18	19	20	21	22	23
RTS%	3	3	3	2	2	2	2	2	2	2	2	2

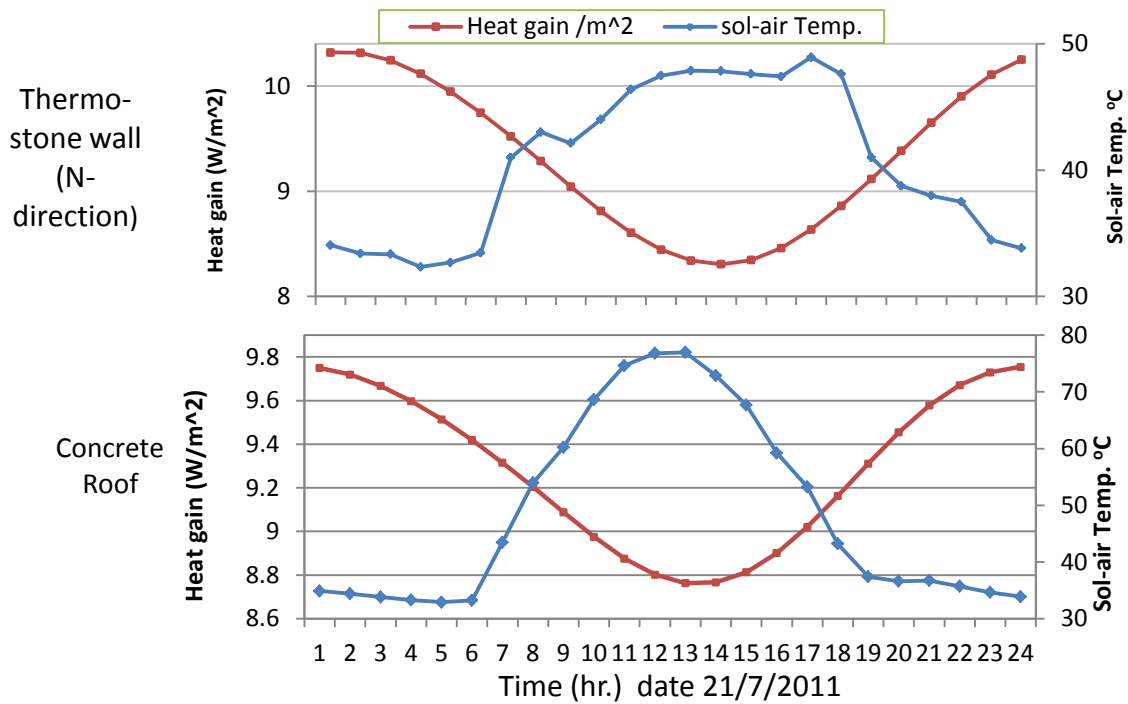


Figure 4. Conduction time delay of Thermo-stone wall and concrete roof of tested space.

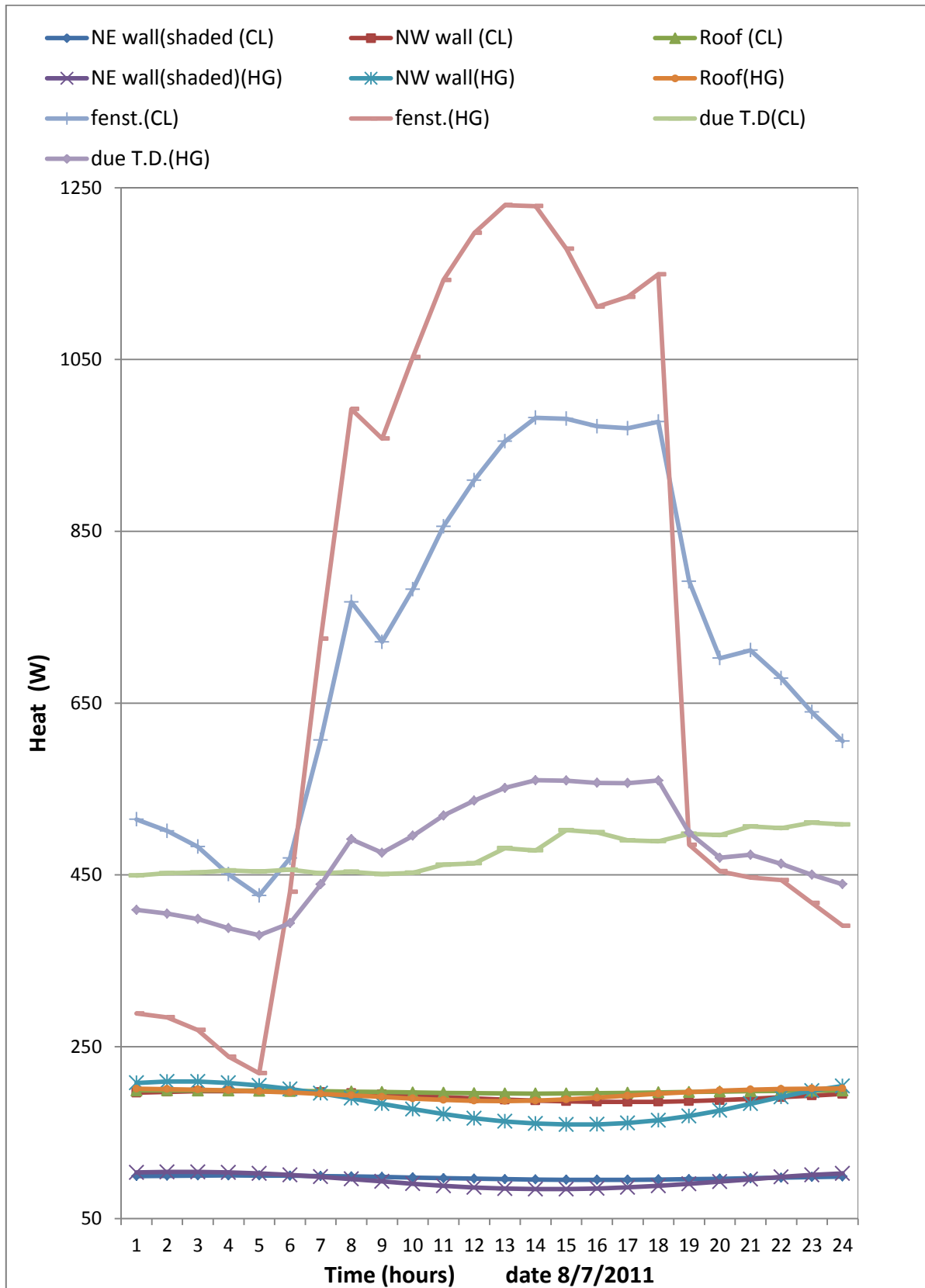


Figure 5. Theoretical components of cooling load and heat gain of tested space.

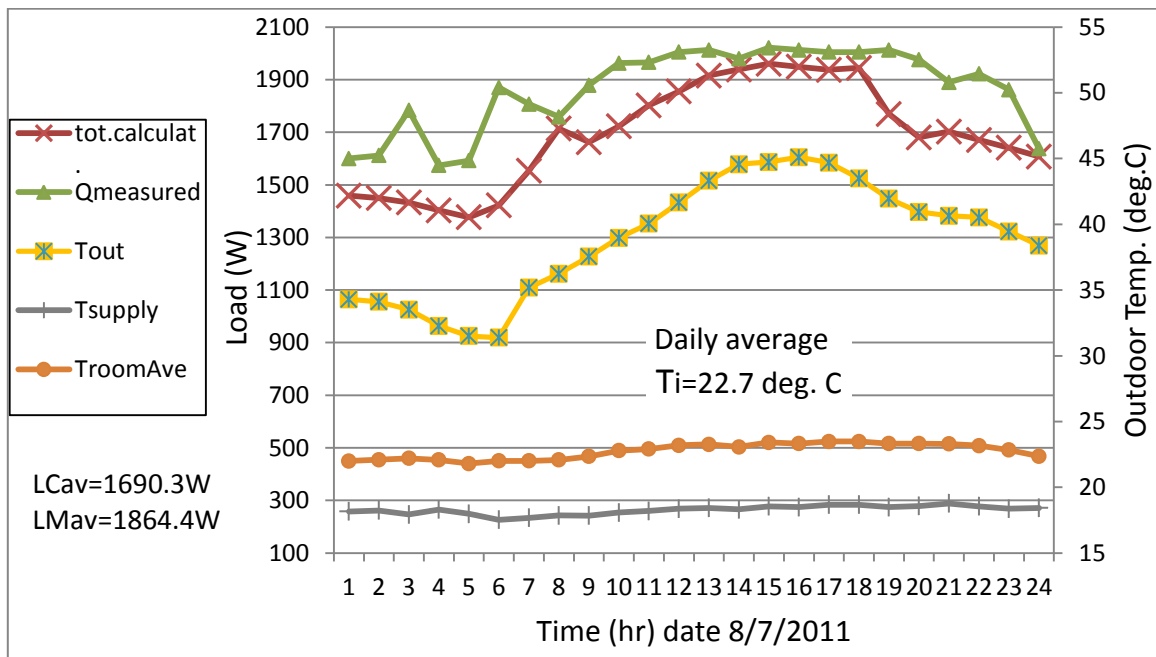


Figure 6. The comparison between the calculated and measured cooling loads for the test space.



Using Spatial Videos, Google Earth™ and Geographic Information System to Dynamically Monitor Built Environment Changes In a Challenging Environment: Baghdad, Iraq.

Husham AbdMunaf Atta

Instructor

Computer Center -University of Baghdad
husham@uobaghdad.edu.iq

Andrew Curtis

Associate Professor

College of Arts and Sciences Kent State University
acurti13@kent.edu

ABSTRACT

Urban expansion and its environmental and safety effects are one of the critical information needed for future development planning, safety considerations and environmental management. This work used two methods to monitor urban expansion and its environmental and safety effects, the first is based on Google Maps for the years 2002 and 2010, and the second was the usage of spatial videos for the year 2013. Although the usage of satellite images is critical to know and investigate the general situation and the total effects of the expansion on a large piece of area, but the Spatial videos do a very detailed fine scale investigation, site conditions regarding both environmental and safety cannot be easily distinguished from satellite images. Another advantage of spatial videos is new houses can be recognized and separated visually even if they are attached or derived from one house. This article shows that the working conditions for the workers do not comply with the standards especially their health and safety procedures.

Also the municipality services are at the lowest level because of all the debris left in the street, lack of regulation and law enforcement that protect the health of neighborhood residents.

Keywords: GIS, google maps, spatial videos and urban environment.

استخدام الفيديو المكاني، برنامج جوجل إيرث ونظام المعلومات الجغرافية لرصد التغييرات الحوية للبيئة الحضرية في بيئة مليئة بالتحديات: بغداد، العراق.

الأستاذ أندرو كورتيس
كلية الآداب والعلوم - جامعة كنت

المدرس هشام عبدمناف عطا
مركز الحاسبة - جامعة بغداد

الخلاصة

بعد التوسع العمراني وتأثيراته على البيئة والسلامة من المعلومات المهمة جداً واللازمة لخطط التطوير المستقبلية وأعتبرت السلامة والأدارة البيئية للمدن في هذا العمل تم استخدام اسلوبين لمتابعة التوسع العمراني وتأثيراته على السلامة والبيئة المدنية ، في الأسلوب الأول تم الاعتماد على خرائط غوغل لسنة ٢٠٠٢ وللسنة ٢٠١٠ ، اما الأسلوب الثاني فأعتمد على الفيديو المكاني لسنة ٢٠١٣ . بالرغم من اهمية استعمال الصور الفضائية لمعرفة وتحديد الوضع العام وكذلك التأثيرات الكلية للتوسع على منطقة كبيرة ، لكن الفيديو المكاني تقوم برصد التغييرات الدقيقة وظروف الموقع بشكل لا يمكن للصور الفضائية تحقيقه . كما ان للفيديو المكاني فائدة اخرى ، هي فرز المنازل الجديدة وتحديدتها بالرويا حتى لو بنيت بشكل متلاصق أو اشتقت من نفس المنزل . أظهر هذا العمل ان ظروف عمل العمال غير متوافقة مع معايير السلامة المهنية والصحة . ولقد أظهرت الدراسة ان



الخدمات البلدية في اوطأ مستوياتها بسبب ترك الأنقاض في الطرقات وغياب تطبيق القوانين والتشريعات التي تحافظ على صحة سكان المنطقة .

الكلمات الرئيسية : نظم المعلومات الجغرافية ، خرائط غوغل ، الفيديو المكثية والبيئة الحضرية

1. INTRODUCTION

It is estimated that the population growth associated with urban areas in less developed countries will grow from 2.7 Billion in 2011 to 5.1 Billion capita in 2050 UN, 2012. The increase in urban population will result in more construction for domiciles and industry, the need for more (and better) roads, and general service provision ,Wong and Jusuf, 2011 and Farooq and Ahmed , 2008. This type of development can have a devastating effect on the urban ecosystem, including increases in solid waste generation, air pollution from a variety of human sources, a higher runoff rate and a general depletion of resources ,Yangfan, et al., 2010.

In China, Yanjun , and Ying, 2011. found dramatic increases in environmental pollution and an over consumption of resources because of an extremely fast growing urban economy with little planning oversight or general policy guidance. Unfortunately for many environments where these factors combine; dramatic urban development with little planning control resulting in multiple environmental problems, also suffer from a lack of data that can be used to monitor the situation.

A challenge in many of these environments is the lack of data needed to create baselines and assess change. From a spatial perspective, census information is often missing, and often the only source of data is remotely sensed(high resolution aerial photorgaph and satelite data). Although these can provide broader impressions of the change in urban areas, such as where development as a whole is occuring, fine scale data, and espicially dynamic fine scale data are extremely difficult to collect. For example, Erener, et al.,2012. estimated that there was a 135.72% increase in the built-up area in Göcek Bay in the south western coast of Turkey with an associated 29.38% vegetation loss ,Haregeweyn,et al., 2012. Using a similar approach found that the horizontal expansion in Bahir dar (North west of Addis Ababa, Ethiopia) increased from 279 ha in 1957 to 4830 ha in 2009, at an average growth rate of about 31% (88 ha year⁻¹). A further challenge for many of these urban environments is the issue of security, which as a result lead to the adoption of new methodologies to collect spatial data ,Cohen, and Arieli, 2011. One such environment, and the focus of this paper, is Baghdad, Iraq. This is not to say that there is no ground-level geographic information system (GIS) use in the Baghdad area or Iraq in general, for example one study considered the pattern of violence and ethnic segregation in the city ,Weidmann and Salehyan, 2013. Increasing urbanization in Basra province (southern part of Iraq) was estimated to be approximately 15% from 1990 to 2003 , Hadeel,et al., 2009. again using remotely sensed imagery.

This paper will consider the dynamic environment of Baghdad, where the urban landscape is contionually changing, where offical (spatial) data is sparse, and where on-the-ground security issues hamper field data collection. More specicially it will focus on one neighborhood in Baghdad to show how expansion and new construction can be captured using a ubiquitous tool for fine scale data collection, a spatial video. Through this method this paper will explore the

environmental impacts and work safety issues in the new construction in a typical dynamically changing neighborhood of the city.

2. STUDY AREA

Baghdad has an estimated population of more than 11 million people ,**Salah, and Saleh, 2007**. In the South Western part of Baghdad is the Hitten district, **Fig.1** . The focus of this paper, is section 622 of the Hitten district **Fig.2** , an administrative division smaller than a district. section 622 was built in the late 1960s and initially contained 682 houses. The area is fully serviced including residential connections to piped water, sewer systems, electricity and phone lines. This section (neighborhood) was considered during the period 1970s until the late 1990s to be wealthy and full of large houses (an average size of approximately 600 Sq.Meter). The section also had from the full range of education access, from kindergarten to highschools, and generally good infrastructure including roads and commercial areas. However a high demand for urban growth has led to the construction of many new houses in the section, despite the fact that there are few remaining open spaces. Although local “knowledgeis that existing buildings and parcels are being turned into multiple living units, the situation is hard to monitor because of lack of spatial data and associated cadstral maps, Therefore, there is little official record of any assessed properties and building footprints, nor is new construction or modifications to existing structures centralized and available for mapping.

This paper presents a proof of concept analysis for this section, showing how spatial video can be used to capture fine scale urban processes, including visual evidence of neighborhood change.

3. METHODOLOGY

Although there are many advantages in using remotely sensed imagery to “map” data-poor urban environments, such studies tend to be cross-sectional and limited to coarse scale mapping. Fine scale mapping challenges from such data sources include building separation where multiple units are adjoined, especially if there is no separation by gardens or corridors, or if the houses share the same roof. Indeed these remotely sensed sources do not capture the dynamic context of the built environment; the look from the curbside, the general condition of the structure, and general human activity such as building activity, building changes, potential safety and environmental problems. To overcome these problems spatial camera and field interviews with owners took place to identify the dynamism of urban morphology, property specific histories, and environmental impact.

Spatial video is a near-scale data collection approach that has been used in multiple situations in the United States, including capturing built environment change after a disaster ,**Curtis, et al., 2013**. ,**Mills, and Curtis ,2008**. **Curtis, and Fagan, 2013**. The general process of using a spatial video for fine-scale mapping is that fieldwork collects video which is encoded with a coordinate stream. Upon playback, the video image can be identified on a map, and attributes from the video digitized into a spatial package, with a GIS or Google Earth. Although different systems have been used in previous research projects, for this study a Contour + HD video camera was used to record the visual conditions of the construction sites. There are several advantages in choosing this camera including affordability, the wide angle high definition lens which is excellent for capturing street-level built environment data (See **Fig.3** for an example), and the built-in GPS receiver. In addition, as this camera was designed for extreme sports, it is sport

which makes it more inconspicuous, rugged and simple to use. The camera is powered by an internal battery boosted by a charger for use in a car's cigarette lighter. Data is stored onto an internal micro SD card (32GB). Both battery life and disk storage allow for up to 5 to 6 hours of data collection.

For this proof of concept study one Contour + camera was attached to the driver's window. In other locations multiple cameras would collect different angles around the car, but as only one camera was used here each road had to be driven twice. Pre-data collection experimentation were important to determine the right angle for the camera, optimum car velocity and the GPS accuracy data collection included approximately 15 hours of recording and interviews over three days. The only streets omitted in the analysis were those that were closed to traffic.

Once captured the video data were downloaded into the associated free-software (Storyteller) which is a user friendly system that allows for both the video and data collection path to be viewed simultaneously. Storyteller can be downloaded by anyone even without a camera purchase which facilitates the easy dissemination of video data. The software has basic functionality including the ability to zoom in and out of the data collection path (displayed on Google Maps), some speed controls, and a GPS extraction function.

Fig.3 Shows the Interface window of the camera software. The red box represents the normal viewer for the video including a time counter with play/pause button. The Blue box shows the GPS part for this Camera. The video collection path is displayed as a yellow line with the exact location of the image displayed represented as a yellow circle, with associated speed, elevation and length of path to that point. The image can be progressed by clicking onto the map path, or by sliding the bottom progress bar.

After data collection, the part of the Google Earth™ started.

Although digitizing can occur directly into ArcGIS 10.1, there are benefits for using Google Earth as an intermediate platform. Firstly, it is free meaning that digitizing can occur irrespective of any GIS license, or GIS skillset. Secondly, the imagery used in Contour Storyteller is the same as Google Earth making digitizing easier. Thirdly, the digitizing framework in Google Earth allows for points, lines and polygons to be digitized, with additional notes added, in an uncoffing format. Digitizing in ArcGIS 10.1 has more restrictions in terms of data structure, and database attribute structure.

A two screen system was utilized whereby the spatial video played on one, and attribute information was digitized into the other. Example data extractions included the locations of debris and changed houses each represented as a separate point, with additional written context added into the dialogue box. After completion, both the spatial video collection path and the digitized points were exported to the ArcGIS as KMZ file.

Google Earth also provided the source for a historical comparison of structures. In addition to the quantity and size of the houses in 2013 was extracted from the spatial video, the historic imagery function in Google Earth™ was used to add two further time periods; 2002 and 2010. After the digitized data were imported into ArcGIS 10.1 data were separated into two categories; debris, new houses construction sites. New columns have been added to the attribute table like the time window of construction for the new houses, this time window was found through the comparison of the 2002 and 2010 images and the 2013 spatial videos.

4. RESULTS AND DISCUSSION

1- Urban Expansion:

The debris location and the current new houses construction sites in 2013 were displayed in **Fig .4** .

By comparing the historical imagery in Google Earth between 2002 and 2010, thirty four new buildings were constructed, eight on empty land and the others either in the grounds of an existing house, or as multiple rebuilds on the site of a demolished house. By comparing the imagery in 2010 with the spatial video in 2013, eighty new houses had been constructed, 13 of them are built in empty lands. In total there were 114 new units built between 2013 and 2002. In order to visualize the urban expansion, numbers were assigned to each parcel condition: if only one house were built the digit 1 will be assigned, if there was two houses built the digit 2 will be assigned and so on.

Then subtracting the number of houses we have in 2010 and 2013 from the baseline in 2002. **Fig.5** Shows the Urban expansion in 2010. The map shows that few houses was expanded to 3 houses (7 only) and 2 lands become 4 houses, others are increased by 1 house only .

While in 2013, **Fig.6** shows that one parcel increased to six houses, two parcels increased from one house to five houses, seven parcels increased from one house to four houses. Six land parcels built to be 14 houses in total.

The period from 2002 till 2010 showed a limited expansion in this area due to the war in 2003, and the security situation in the years from 2007 till 2009. During this period most of the new houses were for the same family expanding their living arrangements within the bounds of their existing property. More rapid expansion occurred between 2010 to 2013 because of the better security situation, and the fact that the neighborhood was fully serviced while many other areas of Baghdad had little or no service provision. A further reason for the expansion was that the government had started to give loans for building new houses; also some real estate companies bought old houses and divided them into sections on demand.

As a result of the urban expansion, new governmental buildings were also constructed in the neighborhood; Police station, clinic, new School and municipality building.

2- Environment and safety

A- In some cases, the new houses areas were less than 50 Sq. Meter, that will cause very poor ventilation which will lead to serious respiratory diseases and allergies especially for children ,**Zuraimi,et al., 2007**. also poor Indoor air quality could lead to 6-9% less performance and productivity ,**Wyon, 2004**.

B- Lack of safety; the safety in the construction sites are in the lowest level ,**Fig.7** and **Fig.8** shows that the site has no warning signs of any type, non-secured scaffold and large heavy materials (large white marble boards) .

Fig.9 and **Fig.10** shows that the workers are not wearing PPE (Personal Protection equipment).

In Australia, 138 works related death occurred, 120 workers and 18 bystanders two of them were children ,**Australia, 2012**. In the United States 4,609 work related deaths ,**BLS, 2012**.



Environmental problems with the construction site is the debris of old houses, the debris may contain asbestos, sharp metals and leaded paint. **Fig.11** shows the regular debris of the demolished houses left on the curb side without any covering or securing for long time. Asbestos can cause several severe diseases such as lung cancer, malignant mesothelioma and pleural effusion ,**Jamrozik, 2011. ,Farfels, et al., 2003.** Stated that lead paint from old demolished houses increase the concentration of lead by 81 fold. Lead poisoning can cause serious neural disability. Also having all these debris and new construction materials can contribute to higher suspended material concentration in the ambient air.

5. CONCLUSION

There are several factors affecting the urban expansion, the security situation, the services in the area, location and the prices of land. Although the use of satellite images is critical in investigating and evaluating the general situation and total effects of the expansion on a large piece of area; the Spatial videos do a very detailed fine scale investigation, site conditions regarding both environmental and safety which cannot be easily distinguished from satellite images .

Another advantage of spatial videos is, new houses can be recognized and separated visually even if they are attached or they derived from one house.

This article shows that the working conditions for the workers do not comply with the standards especially their health and safety procedures.

Also the municipality services are at the lower levels because of all the debris left in the street and lack of regulation and law enforcement to protect the health of neighborhood residents.

Bibliography

- Australia, S. W.,2012, *Notified Fatalities Statistical Report 2010–11*, Safe Work Australia.
- BLS. ,2012, *National Census Of Fatal Occupational Injuries In 2011*, US.Department of Labor.
- Curtis,A., Blackburn, J. K., Widmer,J.M., and Morris Jr, J.G.,2013, *A Ubiquitous Method For Street Scale Spatial Data Collection And Analysis In Challenging Urban Environments: Mapping Health Risks Using Spatial Video In Haiti*, International Journal of Health Geographics, Vol.12, No. 21 PP. 1- 14.



- Curtis, A., and Fagan, W.F.,2013, *Capturing Damage Assessment With Spatial Video:An Example Of A Building And Street Scale Analysis Of Tornado- Related Mortality In Joplin,Missouri,2011*, Annals of the Association of American Geographers .
- Cohen, N., and Arieli, T.,2011, *Field Research In Conflict Environments: Methodological Challenges And Snowball Sampling*, Journal of Peace Research, Vol. 48,No.4,PP.423-435.
- Dr. Salah A. H. and Saleh, D. S.-B.,2007,*Evaluation And Forecasting Of Baghdad City Public Services By Gis Techniques*. Retrieved from http://www.saudigis.org/FCKFiles/File/69_E_SalahSaleh_IRAQ.pdf
- Erener,A., Düzgünb,S., and Yalcinerc,A. ,2012 , *Evaluating Land Use/Cover Change With Temporal Satellite Data And Information Systems*, Procedia Technology, Vol. 1,PP.385 – 389.
- Farfel,M.R., Orlova A.O., Lees, P.S., Rohde, C., Ashley, P.J., Chisolm, J.J Jr.,2003, *A Study of Urban Housing Demolitions as Sources of Lead in Ambient Dust:Demolition Practices and Exterior Dust Fal*. Environmental Health Perspectives, Vol. 111, No. 9,PP.1228-1234.
- Farooq, S. , and Ahmed, S.,2008,*Urban Sprawl Development Around Aligarh City:A Study Aided By Satellite Remote Sensing And GIS*,Indian Society of Remote Sensing,Vol.36, No. 1 , PP.77–88.
- Hadeel A.S., Mushtak T. J., and Xiaoling C. ,2009, *Application of Remote Sensing and GIS to the Study of Land Use/Cover Change and Urbanization Expansion in Basrah Province, Southern Iraq*, Geo-spatial Information Science , Vol. 12 No. 2,pp.135-141.
- Haregeweyn,N., Fikadu,G., Tsunekawa,A., Tsubo,M., and Meshesha,D.,2012, *The Dynamics Of Urban Expansion And Its Impacts On Land Use/Land Cover Change And Small-Scale Farmers Living Near The Urban Fringe: A Case Study of Bahir Dar, Ethiopia*, Landscape and Urban Planning , Vol. 106, No. 2,PP.149– 157.
- Jamrozik, E. d. ,2011, *Asbestos-related disease. Internal Medicine Journal*,Vol. 41 No. 5, PP.372–380.
- Leick, G. ,2002,*Mesopotamia: The Invention of the City*. USA: Penguin.
- Mills, J.W., Curtis, A.,2008, *The Spatial Video Acquisition System as an Approach to Capturing Damage and Recovery Data After a Disaster: A Case Study from the Super Tuesday Tornadoes*. University of Colorado Natural Hazards Center.
- UN. ,2012, *World Urbanization Prospects The 2011 Revision*. New York: United Nation.



- Weidmann, N. B., & Salehyan, I. ,2013, *Violence and Ethnic Segregation: A Computational Model Applied to Baghdad*. International Studies Quarterly , Vol. 57, No.1,PP.52–64.
- Wong, N.H., and Jusuf, S.K.,2011, *Integrated Urban Microclimate Assessment Method as A Sustainable Urban Development and Urban Design Tool*. Landscape and Urban Planning,Vol. 100 ,No.4 pp.386–389.
- Wyon, D. P. ,2004,*The Effects Of Indoor Air Quality on Performance And Productivity*. Indoor Air, Vol. 14,PP.92-101.
- Yangfan, L., Xiaodong, Z., Xiang, S., & Feng, W. ,2010, *Landscape Effects Of Environmental Impact On Bay-Area Wetlands Under Rapid Urban Expansion And Development Policy: A Case Study Of Lianyungang, China*. Landscape and Urban Planning, pp.218–227.
- Yanjun, L., & Ying, W. ,2011, *Study on Resource-environment Response to the Rapid Urban Expansion in China*. Energy Procedia,Vol. 5, PP.2549–2553.
- Zuraimi, M. S.,Tham,K.W., Chew,F. T. and Ooi, P. L. ,2007, *The Effect Of Ventilation Strategies Of Child Care Centers On Indoor Air Quality And Respiratory Health Of Children In Singapore*. Indoor Air, Vol. 17,No. 4 ,PP.317-327.

Table 1. Summarizes the urban expansion details.

Details	Urban Expansion differences between	
	2010 and 2002	2013 and 2013
New houses built	34 (8 on empty lands)	80 (13 on empty lands)
Houses demolished	5	2
Houses expanded to 6 houses	nil	1
Houses expanded to 5 houses	nil	2
Houses expanded to 4 houses	2	7
Houses expanded to 3 houses	7	2

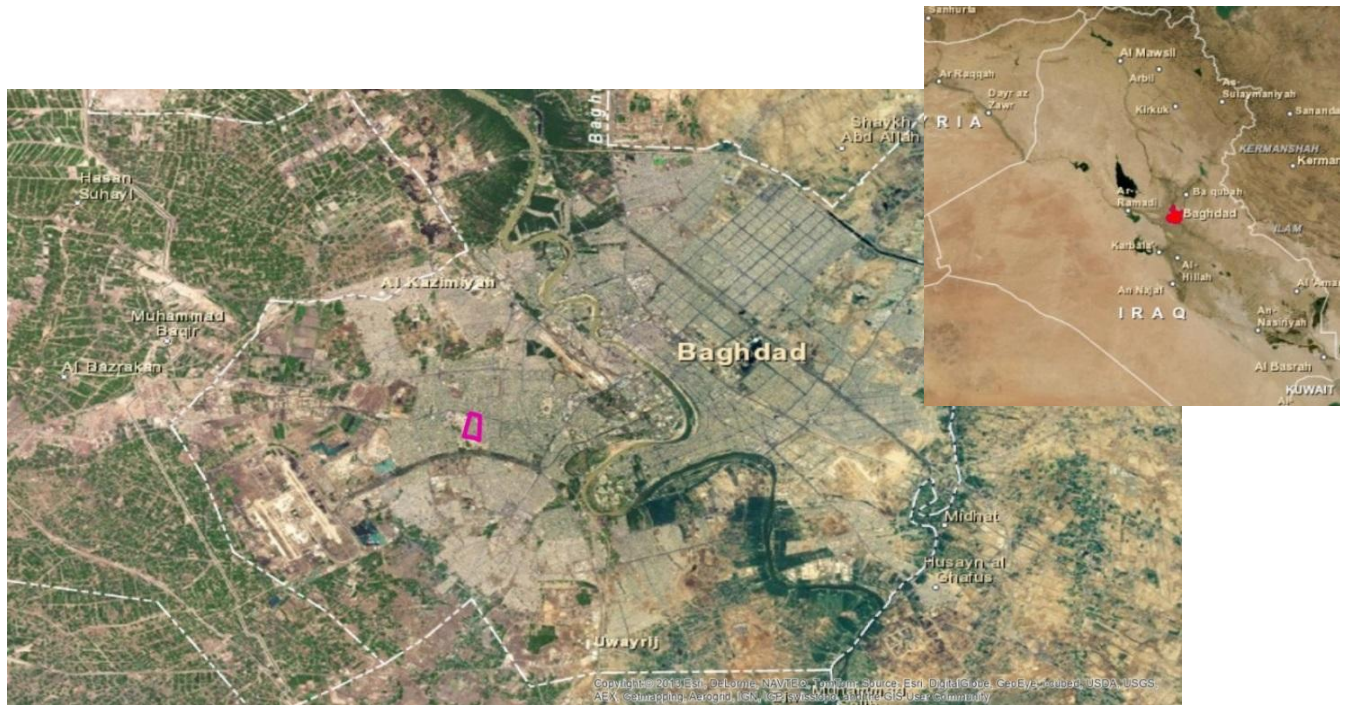


Figure 1. Satellite images locates the district within Baghdad Governorate .

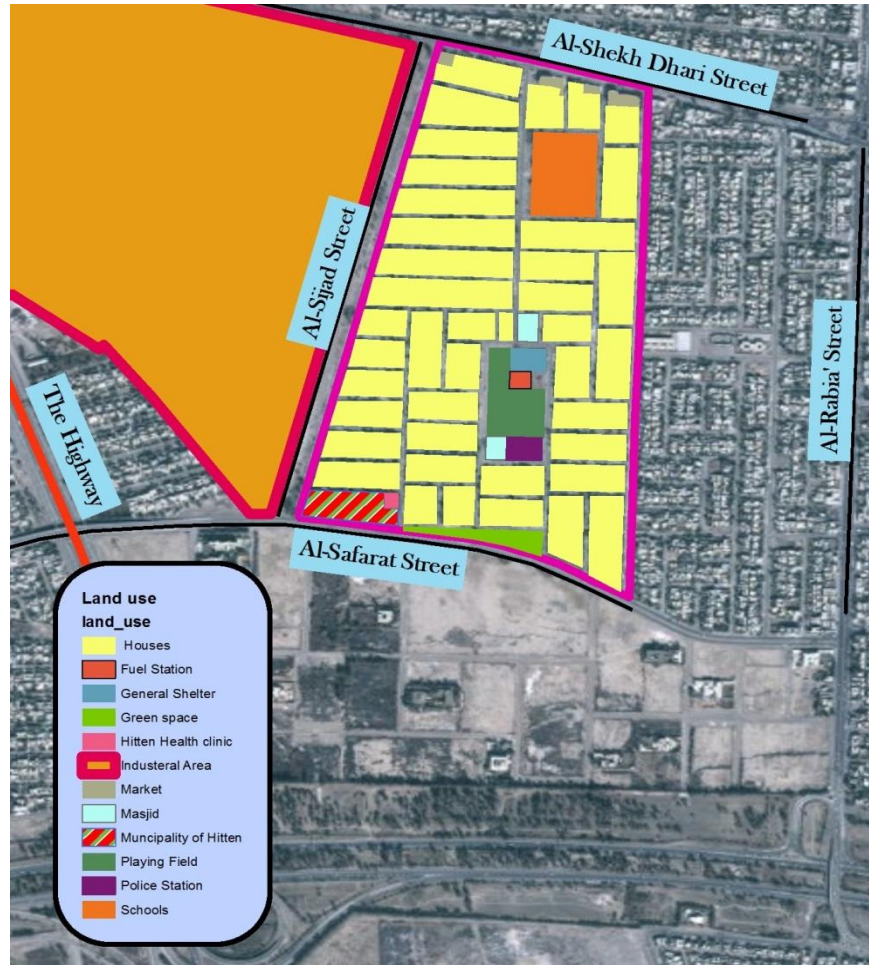


Figure 2. Land use of the study area.



Figure 3. The interface window of the spatial video camera.

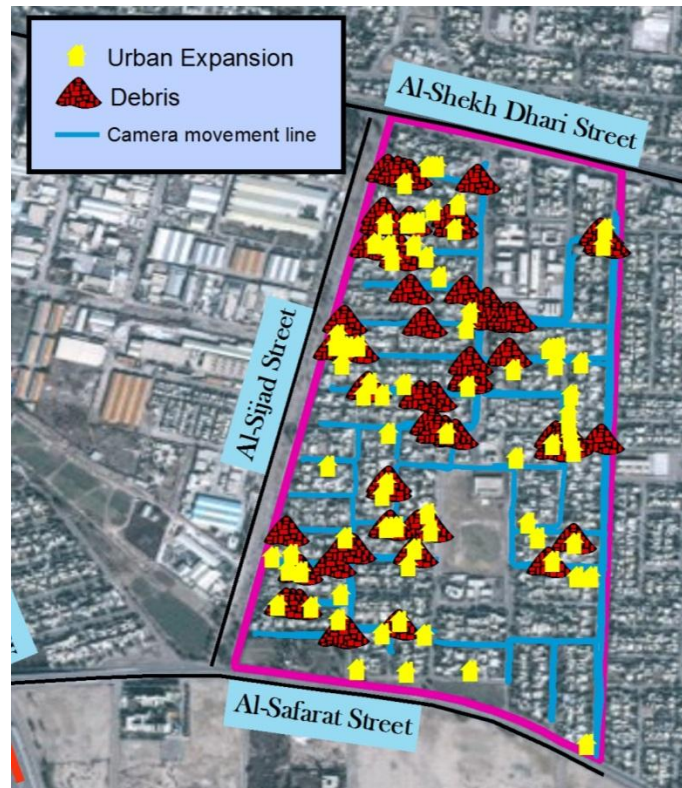


Figure 4. The debris and location of new houses in 2013.

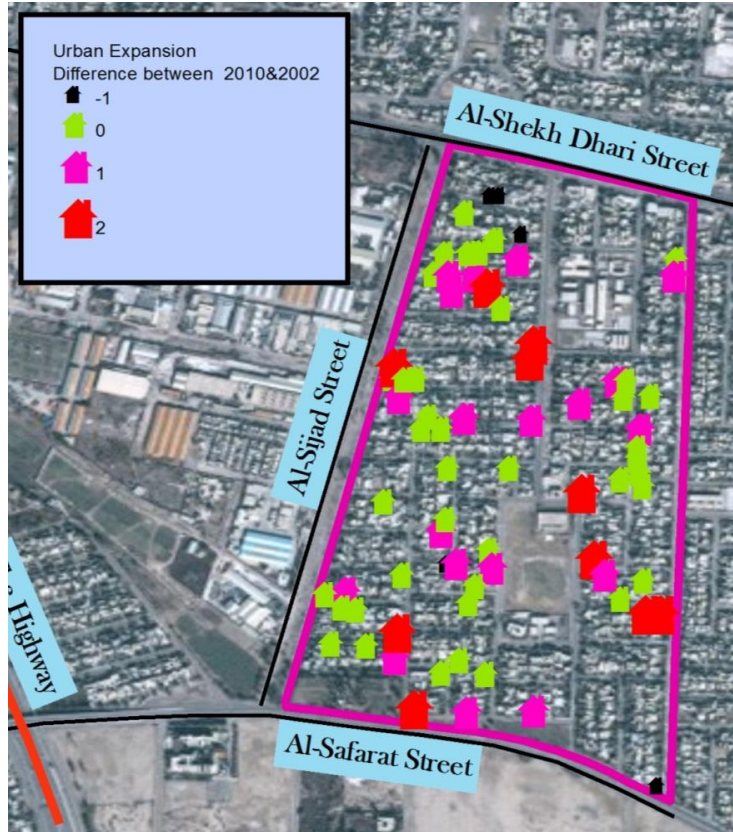


Figure 5. The urban expansion in 2010.

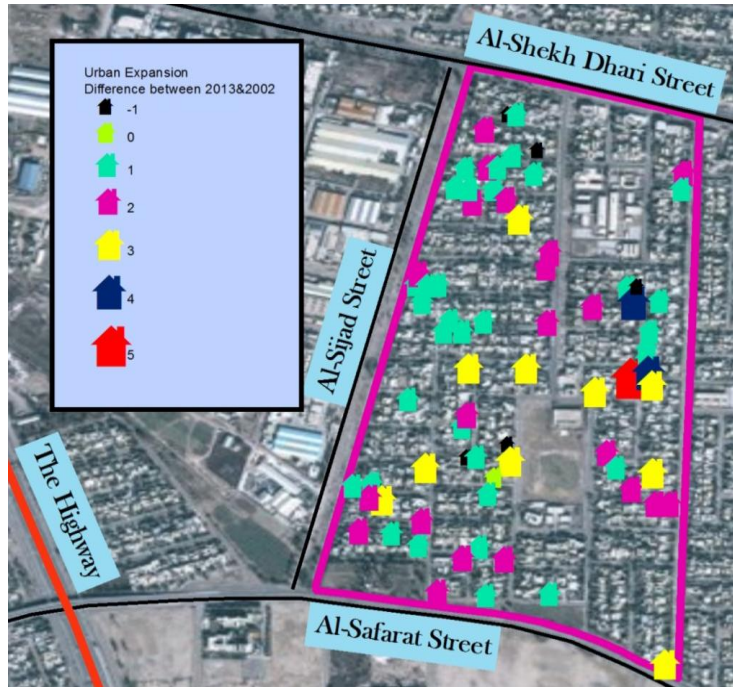


Figure 6. Urban expansions in 2013.



Figure 7. Non secure site with large heavy marble boards and unattended scaffold.



Figure 8. Non secured site, no warranty signs and potential falling objects.



Figure 9. Workers without hard hats, gloves or any other personal protection equipment.



Figure 10. Workers without hard hats, boots, gloves, and respirator.



Figure 11. Debris from demolished houses; contain Brick, sharp metal and other building materials.

قائمة المحتويات

القسم العربي:

الصفحة	العنوان
21-1	تحليل عددي لجريان المائع وانتقال الحرارة بالحمل القسري في مجرى ذي سطح يحتوي مقاطع نصف دائرية ومملوء بمادة مسامية

موفق علي حمادي

د.أمير سلطان داود



تحليل عددي لجريان المائع وانتقال الحرارة بالحمل القسري في مجرى ذي سطح يحتوي مقاطع نصف دائرية ومملوء بمادة مسامية

د.أمير سلطان داود
أستاذ مساعد
كلية الهندسة / جامعة الموصل

موفق علي حمادي
ماجستير هندسة ميكانيك / موانع وحراريات
كلية الهندسة / جامعة الموصل

الخلاصة

أجريت في هذا البحث دراسة عددية لمحاكاة انتقال الحرارة بالحمل القسري الناتج عن جريان مائع داخل مجرى ذي سطح يحتوي مقاطع نصف دائرية ومملوء بوسط مسامي. وقد افترض أن جريان المائع يكون طباقياً ومستقرًا و غير قابل للانضغاط ودرجة حرارته أقل من درجة حرارة أسطح المقاطع ، وقد استخدمت تقانات الفروق المحددة لتمثيل المعادلات الحاكمة (الكتلة و الزخم و الطاقة) ، وقد تم توليد الشبكة التفاضلية داخل الحيز باستخدام معادلات بوزن التفاضلية البيضاوية ، أما المعادلات الحاكمة بصيغتها الجبرية فقد حُلَّت عددياً باستخدام طريقة الحل العددية خط بعد خط (LSOR) . وقد دُرِسَ في هذا البحث تأثير تغيير شكل القناة في جريان المائع وانتقال الحرارة لحالتين الاولى: عند أنصاف الأقطار ($r = 0.25H, 0.5H, \text{and } 0.75H$) ، وثانياً عند المسافة بين أنصاف اقطار المقاطع ($P = 3r, 5r, 7r, \text{and } 9r$). كما تم دراسة تأثير تغيير عدد رينولدز عند قيم ($Re=50, 100, 150, \text{and } 200$). النتائج بينت أن زيادة انصاف أقطار المقاطع والمسافة فيما بينها يؤدي إلى زيادة في كمية الحرارة المنتقلة ؛ كذلك فأن زيادة عدد رينولدز يقابلها زيادة في معدل انتقال الحرارة . وأن وجود المادة المسامية قد منع حدوث ظاهرتي الانفصال وتكون الدوامات في الجريان .

الكلمات الرئيسية : الوسط المسامي ، الحمل القسري ، الجريان اللادارسي .

Numerical Analysis of Fluid Flow and Heat Transfer by Forced Convection in Channel with one-sided Semicircular Sections and Filled with Porous Media

Mouwaffaq A. Hammadi
M.Sc. Mech. Eng./Thermal and Fluid
Collage of Engineering - Mosul University
E-mail : mahs_19862000@yahoo.com

Dr. Amir S. Dawood
Assistant professor
Collage of Engineering - Mosul University
E-mail : amirsd1954@yahoo.com

ABSTRACT

This research presents a numerical study to simulate the heat transfer by forced convection as a result of fluid flow inside channel's with one-sided semicircular sections and fully filled with porous media. The study assumes that the fluid were Laminar , Steady , Incompressible and inlet Temperature was less than Isotherm temperature of a Semicircular sections .Finite difference techniques were used to present the governing equations (Momentum, Energy and

Continuity). Elliptical Grid is Generated using Poisson's equations . The Algebraic equations were solved numerically by using (LSOR) .This research studied the effect of changing the channel shapes on fluid flow and heat transfer in two cases ,the first: changing the radius ($r = 0.25H$, $0.5H$,and $0.75H$) . and changing the distance between these radiuses ($P = 3r$, $5r$, $7r$,and $9r$) . also the effect of changing the Reynolds number in ($Re=50$, 100 , 150 ,and 200) is study .The results showing that the increase in the Radius , the distance between the sections and Reynolds number lead to increase the rate of heat transfer . and the presence of porous media prevents the phenomena of separation and vortex formation in flow.

Keywords : Porous Media, Forced Convection, Non Darcian Flow .

المقدمة

إن علوم انتقال الحرارة وميكانيكا الموائع تعد من العلوم المهمة لما لها من تطبيقات واسعة في كافة المجالات لاسيما الهندسية والصناعية منها ، ويعد انتقال الحرارة بالحمل الذي يلعب فيه جريان المائع دور بارزاً ومهماً من أهم أنواع انتقال الحرارة الجدير بالدراسة، ويكون انتقال الحرارة بالحمل القسري نتيجة التفاعل الحراري الناتج عن مرور المائع وجريانه على سطح معين إذ تنتقل الحرارة من السطح إلى المائع أو بالعكس اعتماداً على الفرق في درجات الحرارة بين السطح والمائع **Jiji,2006**. إن انتقال الحرارة بالحمل القسري واحد من أهم المواضيع ذات التطبيقات الصناعية الواسعة كما في المراحل البخارية والمفاعلات الكيميائية المُحفَزة بالعامل المساعد والخلايا الشمسية؛ وإن إدارة انتقال الحرارة لتحسينها أو تقليل حجم هذه المعدات يعد مهمة ضرورية جداً لحفظ وتوفير الطاقة في آن واحد، ويشكل عام فأن الخلايا الشمسية تُصمم عادةً كخلايا مستوية ذات تجاويف مفرغة لكن خلايا امتصاص الطاقة تكون مختلفة الأشكال مثل (المتعرجة)، وإن القناة ذات السطح المتعرج واحدة من عدة أجزاء تُوظف لتحسين كفاءة انتقال الحرارة في هذه المعدات **Heidary and, 2012**. وقد أشار **بيجان (Bejan)** إلى ظهور مجال منفصل في دراسة انتقال الحرارة وجريان المائع داخل القنوات وهو انتقال الحرارة وجريان المائع خلال الأوساط المسامية وذكر بأنه أخذَ حيزاً من فصل انتقال الحرارة بالحمل القسري **Bejan, and Kraus, 2003**. ونتيجة لأهمية نمط انتقال الحرارة بالحمل القسري والجريان داخل القنوات الحاوية على مواد مسامية فضلاً عن كونه مجال بحثي حديث ومُهم فقد سعى الكثير من الباحثين إلى دراسة هذا النمط سواءً من اهتَم بدراسة أنموذج الجريان الدارسي أو اللادارسي لوصف تحليل مُعادلة حفظ الزخم التي تحكم الحالة الفيزيائية لديناميكية جريان المائع داخل الوسط المسامي ومن هذه البحوث .

قام الباحث **Nakayama et al.,1988** بإجراء دراسة باستخدام الحل المثالي والتقريبي لدراسة انتقال الحرارة بالحمل القسري في قناة مستوية ومملوءة بمادة مسامية لنموذج جريان لا دارسي؛ إذ تجهز الحرارة من سطحي القناة العلوي والسفلي بفيض حراري ثابت ، النتائج أعطت تقارب كبير بين الحل بالطريقتين حتى في إيجاد مخططات توزيع السرعة ودرجة الحرارة داخل القناة . كذلك تم اشتقاق صيغة مثالية (Exact Expression) لحساب عدد نسلت تحت شروط الفيض الحراري الثابت على الجدار. أما الباحث **Kaviany, 1985** فقد قام بدراسة عددية لجريان المائع وانتقال الحرارة بالحمل القسري داخل قناة مستوية مملوءة بمادة مسامية و ذات جدارين بدرجة حرارة ثابتة ، وقد أُسُخدم الأنموذج اللادارسي لتحليل معادلة حفظ الزخم ولكن بحذف حد مربع السرعة ، نتائج الدراسة أظهرت بأن عدد نسلت يزداد للجريان المكتمل النمو بزيادة معلمة الشكل للمادة المسامية $(H^2\phi/K)^{0.5}$ وعدد دراسي ، كما أظهرت الدراسة بأن الانخفاض بالضغط يقل بزيادة المعلمة المذكورة. وأجرى **Kim et al.,2001** دراسة عملية لمعرفة تأثير وجود هيكل أسفنجي من الألمنيوم على جريان المائع وانتقال الحرارة داخل قناة سطحها العلوي بدرجة حرارة ثابتة فيما سطحها السفلي معزول . وقد

تم دراسة تأثير كل من معامل الاحتكاك وعدد نسلت بوجود المادة المسامية داخل القناة ، وقد استنتج الباحثون بأن معامل الاحتكاك يكون ذا قيمة عالية جداً عندما تكون النفاذية قليلة وفي نفس الوقت تزداد قيم عدد نسلت الذي يعد مؤشر على تحسين انتقال الحرارة .

أما دراسة تأثيري التموج في سطح القناة و وجود المادة المسامية داخلها فيعد مجال بحثي حديث جداً لذا فان البحوث التي اختصت بدراسة هذا المجال قليلة جداً ومن جملتها الدراسة التي قام بها الباحثان **Mansoor, and Dawood 2013**, إذ قام الباحثان بإجراء تحليل عددي لجريان المائع وانتقال الحرارة بواسطة الحمل القسري داخل مجرى متموج مملوء بمادة مسامية ؛ وقد درس الباحثان تأثير التموج و وجود المادة المسامية على طبيعة الجريان وانتقال الحرارة ، وقد دُورس تأثير التموج من خلال تغيير شكله لحالتيه. النتائج أكدت أن تمويج سطح القناة بوجود المادة المسامية يعطي زيادة في معدل انتقال الحرارة بمقدار 18% تقريباً مقارنة بالسطح المستوي . أما الباحثان **Heidary, and Kermani 2012**, فقد قاما بإجراء دراسة عددية لجريان المائع وانتقال الحرارة داخل قناة سفلي متموج فيما سطحها العلوي كان مستوياً ، والقناة محتوية على المادة المسامية ضمن الحيز من الأعلى إلى منتصف القناة ، وقد دُرس تأثير التموج في السطح لمدى من أعداد رينولدز تراوح بين (100-1000) من خلال عاملين هما عدد الموجات وسعة الموجة . النتائج بينت أنه من خلال التحكم في عدد الموجات من خلال الطول وسعة الموجة وكذلك عدد رينولدز يمكن زيادة معدل انتقال الحرارة بنسب عالية. وقد أجرى الباحث **Al-Sammarai,1999**, دراسة عملية لانتقال الحرارة بالحمل القسري من اسطوانة مسخنة في صف من الاسطوانات الأفقية خلال وسط مسامي لجريان متعامد تحت شرط ثبوت درجة حرارة سطح الاسطوانة المسخنة. شملت الدراسة بيان تأثير كل من سرعة الجريان وموقع الاسطوانة المسخنة والمسافة بين الاسطوانات على قابلية هذه الاسطوانة لتبديد الحرارة . النتائج بينت أن قابلية الاسطوانة المسخنة على تبديد الحرارة تعتمد على سرعة جريان المائع وموقع هذه الاسطوانة ضمن الصف والمسافات بين الاسطوانات. إذ تزداد هذه القابلية بزيادة سرعة الجريان ، وقد لوحظ أن هذه القابلية تصل أعلى قيمة لها عند نسبة مسافة فاصلة مقدارها ($S/D = 1.6$) في كلتا حالتي الاسطوانات الطليقة والمغموسة في وسط مسامي ، كما أظهرت الاسطوانة المسخنة الموضوعة في أي موقع في الصف ولأغلب نسب المسافة الفاصلة ضمن حالتي الاسطوانات الطليقة والمغموسة زيادة في انتقال الحرارة مقدارها الأعظم (21%) مقارنة بأسطوانة مفردة طليقة أو مغموسة في وسط مسامي ، كذلك لوحظ أن أعلى قيمة تحسن في انتقال الحرارة من الاسطوانة المسخنة نتيجة استخدام الوسط المسامي كانت أكثر بخمس أضعاف انتقال الحرارة من نفس الصف ضمن حالة الاسطوانات الطليقة عند سرعة الجريان نفسها.

تمثيل الشكل الهندسي للمسألة

الانموذج المقترح في هذه الدراسة هو مقطع من قناة تحتوي مقاطع نصف دائرية على سطحها العلوي يتم فيها انتقال الحرارة من هذه المقاطع الى المائع المار عبر القناة . كما يمكن أن يكون شكل المسألة مقطوعاً لمجمع جريان لمنظومة شمسية تمثل المقاطع النصف دائرية فيها الخلايا الشمسية (ينظر الشكل (1)). أما رياضياً فيمكن تمثيل الشكل على وفق المعادلات التالية :

فيما يخص السطح السفلي فان معادلتها تكون بالصيغة التالية :

$$y_b = 0 \quad 0 \leq x \leq L \quad (1)$$

أما فيما يخص السطح العلوي المستوي فان معادلتها تكون كما يأتي :

$$0 \leq x \leq L_i$$

$$y_t = H \begin{cases} (L_i + 2r) \leq x \leq (L_i + p) \\ (L - L_e) \leq x \leq L \end{cases} \quad (2)$$

وفيما يخص السطح العلوي الحاوي على مقاطع نصف دائرية فإن معادلته تكون كما يأتي:

$$\begin{aligned} y_t &= H - \sqrt{r^2 - [(x - L_i) - r]^2} && \text{المقطع الأول} \\ y_t &= H - \sqrt{r^2 - [(x - (L_i + p)) - r]^2} && \text{المقطع الثاني} \end{aligned} \quad (3)$$

الفرضيات

- 1- المادة المسامية تملأ القناة بالكامل؛ وتكون متجانسة الخواص من نفاذية ومسامية وغيرها.
- 2- المائع المفترض نيوتني (Newtonian Fluid) وغير قابل للانضغاط وجريانه يكون مستقراً وطباقياً.
- 3- جداري القناة العلوي والسفلي معزولين حرارياً وغير نفاذيين.
- 4- اعتبار الحالة المدروسة حالة استقرار حراري؛ وجميع الكميات تؤخذ في اتجاهي (x,y) فقط 2-Dimensions
- 5- درجة حرارة المقاطع النصف دائرية ثابتة وبنفس الوقت أعلى من درجة حرارة المائع الداخل إلى القناة .
- 6- عدم تغير كل من الحرارة النوعية والموصلية الحرارية واللزوجة والكثافة وغيرها من الخواص.
- 7- يخضع انسياب المائع داخل المجرى إلى قانون دارسي المطور .

المعادلات الحاكمة

إن مُعادلات حفظ الكتلة وحفظ الزخم وحفظ الطاقة هي المعادلات المتحكمة بالمسألة ، وباعتماد الفرضيات الواردة أعلاه ، فإن المعادلات تمثل بالصيغ الآتية . Mansoor, and Dawood, 2013. and ,Hadim, and North, 2005.

معادلة حفظ الكتلة (الاستمرارية)

$$\frac{\partial u}{\partial x} + \frac{\partial v}{\partial y} = 0 \quad (4)$$

معادلة حفظ الزخم

$$\frac{\rho_f}{\phi^2} \left(u \frac{\partial u}{\partial x} + v \frac{\partial u}{\partial y} \right) = -\frac{\partial p}{\partial x} - \frac{\mu_f}{K} u - \frac{\rho_f \cdot F}{\sqrt{K}} \sqrt{u^2 + v^2} \cdot u + \frac{\mu_f}{\phi} \left(\frac{\partial^2 u}{\partial x^2} + \frac{\partial^2 u}{\partial y^2} \right) \quad \text{in } x\text{-direction} \quad (5)$$

$$\frac{\rho_f}{\phi^2} \left(u \frac{\partial v}{\partial x} + v \frac{\partial v}{\partial y} \right) = -\frac{\partial p}{\partial y} - \frac{\mu_f}{K} v - \frac{\rho_f \cdot F}{\sqrt{K}} \sqrt{u^2 + v^2} \cdot v + \frac{\mu_f}{\phi} \left(\frac{\partial^2 v}{\partial x^2} + \frac{\partial^2 v}{\partial y^2} \right) \quad \text{in } y\text{-direction} \quad (6)$$

معادلة حفظ الطاقة

$$u \cdot \frac{\partial T}{\partial x} + v \frac{\partial T}{\partial y} = \alpha_f \left[\frac{\partial^2 T}{\partial x^2} + \frac{\partial^2 T}{\partial y^2} \right] \quad (7)$$

المعادلات الحاكمة بصيغتها اللابعدية

باعتقاد المقاييس المميزة للمسألة (Characteristic Scales) وهي $(T_h, u_o, \rho u_o^2, H)$ تم كتابة جميع المتغيرات بصيغتها اللابعدية وفق الصيغ الآتية ومن هذه المتغيرات تم كتابة المعادلات الحاكمة بصيغتها اللابعدية :

$$\left[x^* = \frac{x}{H}, y^* = \frac{y}{H}, T^* = \frac{T-T_i}{T_h-T_i}, u^* = \frac{u}{u_o}, v^* = \frac{v}{u_o}, \omega^* = \frac{\omega H}{u_o}, r^* = \frac{r}{H}, \psi^* = \frac{\psi}{u_o H} \right]$$

معادلة حفظ الكتلة (الاستمرارية) بصيغتها اللابعدية

$$\frac{\partial u^*}{\partial x^*} + \frac{\partial v^*}{\partial y^*} = 0 \quad (8)$$

معادلات حفظ الزخم بصيغتها اللابعدية

إن معادلات حفظ الزخم في اتجاهي (x, y) بعد تحويلها إلى الصيغة اللابعدية ستكون :

$$\frac{1}{\phi^2} \left(u^* \frac{\partial u^*}{\partial x^*} + v^* \frac{\partial u^*}{\partial y^*} \right) = -\frac{\partial p^*}{\partial x^*} - \frac{1}{ReDa} u^* - \frac{F}{\sqrt{Da}} \sqrt{u^{*2} + v^{*2}} \cdot u^* + \frac{1}{Re\phi} \left(\frac{\partial^2 u^*}{\partial x^{*2}} + \frac{\partial^2 u^*}{\partial y^{*2}} \right) \quad (9)$$

$$\frac{1}{\phi^2} \left(u^* \frac{\partial v^*}{\partial x^*} + v^* \frac{\partial v^*}{\partial y^*} \right) = -\frac{\partial p^*}{\partial y^*} - \frac{1}{ReDa} v^* - \frac{F}{\sqrt{Da}} \sqrt{u^{*2} + v^{*2}} \cdot v^* + \frac{1}{Re\phi} \left(\frac{\partial^2 v^*}{\partial x^{*2}} + \frac{\partial^2 v^*}{\partial y^{*2}} \right) \quad (10)$$

ومن المعادلتين أعلاه نشق معادلة النقل الدوامية (Vorticity Transport Equation) وصيغتها اللابعدية هي **Mansoor, and Dawood, 2013.**

$$\frac{1}{\phi} \left[\frac{\partial \psi^*}{\partial y^*} \frac{\partial \omega^*}{\partial x^*} - \frac{\partial \psi^*}{\partial x^*} \frac{\partial \omega^*}{\partial y^*} \right] = \frac{1}{Re} \left[\frac{\partial^2 \omega^*}{\partial x^{*2}} + \frac{\partial^2 \omega^*}{\partial y^{*2}} \right] - \frac{\phi}{ReDa} \omega^* - \frac{\phi F}{\sqrt{Da}} |V^*| \omega^* + \frac{\phi F}{\sqrt{Da}} \left[\frac{\partial \psi^*}{\partial x^*} \frac{\partial |V^*|}{\partial y^*} + \frac{\partial \psi^*}{\partial x^*} \frac{\partial |V^*|}{\partial x^*} \right] \quad (11)$$

$$|V^*| = \sqrt{u^{*2} + v^{*2}} \quad (12)$$

معادلة حفظ الطاقة بصيغتها اللابعدية

$$\frac{\partial \psi^*}{\partial x^*} \frac{\partial T^*}{\partial x^*} + \frac{\partial \psi^*}{\partial x^*} \frac{\partial T^*}{\partial y^*} = \frac{1}{Pe} \left[\frac{\partial^2 T^*}{\partial x^{*2}} + \frac{\partial^2 T^*}{\partial y^{*2}} \right] \quad (13)$$

الشروط الحدية للمسألة

لكي يتم حل أي معادلة تفاضلية لابد من توفر هذه الشروط ، إذ وزعت كما موضح في الشكل (3) وقد تم كتابتها بالصيغة اللابعدية وكما يأتي :

منطقة دخول المائع إلى القناة (A): $u^* = u_o^* = 1, v^* = 0, \psi^* = u_o^* \cdot y^* = y^*, \omega^* = 0, T^* = 0$

$$\frac{\partial u^*}{\partial x^*} = 0, \quad \frac{\partial \psi^*}{\partial x^*} = 0, \quad \frac{\partial \omega^*}{\partial x^*} = 0, \quad \frac{\partial T^*}{\partial x^*} = 0 \quad \text{: (B) منطقة خروج المائع من القناة}$$

$$u^* = 0, \quad v^* = 0, \quad \frac{\partial T^*}{\partial y^*} = 0, \quad \psi^* = u^* \cdot y^*, \quad \omega^* = -\frac{\partial^2 \psi^*}{\partial n^{*2}} \quad \text{: (C) عند السطح العلوي المعزول}$$

$$\psi^* = V^* / y^*, \quad \omega^* = -\frac{\partial^2 \psi^*}{\partial n^{*2}}, \quad T^* = 1 \quad \text{: (D) عند السطح العلوي المتموج}$$

$$u^* = 0, \quad v^* = 0, \quad \frac{\partial T^*}{\partial y^*} = 0, \quad \psi^* = 0 \quad \text{: (E) عند السطح السفلي للقناة}$$

حساب أعداد نسلت الموضوعي والمعدل

يعد عدد نسلت أهم معلمة في البحوث التي تهتم بدراسة عملية انتقال الحرارة بالحمل ، وقد تم حساب قيمته الموضوعية من خلال بالصيغة الآتية. **Mansoor, and Dawood, 2013.**

$$Nu_x = \frac{h_{c_x} H}{k_f} = -\frac{\partial T^*}{\partial n^*} \frac{1}{(1-T^*_b)} \quad (14)$$

إذ إن (T^*_b) تمثل معدل لدرجات الحرارة للمائع (bulk temperature) ويمكن حسابها من المعادلة الآتية:

$$T^*_b = \frac{\int_{y_b}^{y_t} u^* T^* dy}{\int_{y_b}^{y_t} u^* dy} \quad (15)$$

أما معدل عدد نسلت فقد تم حسابه من خلال العلاقة الآتية :

$$\overline{Nu} = \frac{1}{s} \int_0^s Nu_x \cdot ds \quad (16)$$

تقانات الفروق المحددة

بعد أن تم إيجاد المعادلات التفاضلية المتحكممة بالشكل الفيزيائي للمسألة قيد الدراسة لابد من تقطيع هذه المعادلات عددياً ، وهذا يعني أن يتم تحويل كل جزء من المعادلات التفاضلية إلى ما يقابله في الحل العددي لينتم إدخاله إلى الحاسبة الالكترونية ، ومن ثم التعامل معه عن طريق كتابة برنامج حاسوبي وفق خوارزمية حل تُنشأ لهذا الغرض . وتعتمد تقانات الفروق المحددة بالإسناد على متوالية تايلور التي يتم تقطيعها عند الحد المطلوب للمشتقة سواء كانت الأولى أو الثانية أو أية قيمة أخرى. ولكي تطبق هذه الطرائق لابد من تحديد نقاط معينة داخل الحيز يتم عندها حل المعادلات بالأسلوب الامثل واختيار صيغة الفتح المناسبة لمواقع تلك النقاط، وهذه النقاط تنتج عن تقاطع الاحداثيين الافقي والعمودي في حالة كون الشكل منتظماً، أما في حالة كون الشكل غير منتظم كما في دراستنا الحالية فسيتم اللجوء إلى ما يعرف بـ " توليد الشبكة " إذ يتم تكوين شبكة جديدة من المحاور الافتراضية التي تكون فيها المسافات متساوية ، وهو الشرط اللازم لتطبيق تقانات الفروق المحددة. **Chapra, and Canale, 2002.**

التوليد الشبكي

لكي يتم حل المعادلات التفاضلية التي تصف جريان المائع وانتقال الحرارة داخل حيز الدراسة لابد من توفير فضاء من النقاط الناتجة عن تقاطع المحاور ، وهذه النقاط تسمى بـ " الشبكة " وتسمى سلسلة الاجراءات والعمليات التي ينتج عنها تكوين هذه النقاط بـ " التوليد الشبكي " وهذا الاجراء يسبق عملية حل المعادلات التفاضلية بعد تمثيلها عددياً ويكون

هذا الاجراء ضرورياً جداً ومهماً في نفس الوقت ، كما أن اختيار نوع التوليد وشكله أيضاً يلعب دوراً مهماً في الحل العددي إذ يؤدي عدم التوليد الجيد للشبكة إلى نتائج غير صحيحة، وربما يؤدي إلى عدم حصول تقارب عند الحل . في الشكل (2) يلاحظ شبكة النقاط التي تم توليدها داخل الحيز وفق اسلوب التوليد الشبكي التفاضلي باستخدام معادلات بوزن التفاضلية البيضوية . وقد استخدمت دالة التجميع المتناظر لتركيز النقاط عند مناطق العمليات على السطح العلوي والسفلي لغرض زيادة دقة الحل من خلال الاعتماد على عدد كبير من النقاط الامامية او الخلفية عند ايجاد قيمة متغير معين بالاعتماد على قيم سابقة او لاحقة .Fletcher,1988.

تحقيق صحة البرنامج

لكي يتم اختبار دقة وصحة البرنامج الحاسوبي الذي تم انشاءه باستخدام برنامج ماتلاب Matlab، فقد تم اختباره من خلال مقارنة النتائج التي تم التوصل إليها لحالة معينة مع قيم بحوث سابقة ، إذ تم مقارنة مخطط توزيع السرعة الذي تم الحصول عليه من الدراسة الحالية الشكل (5(a)) مع ما توصل إليه الباحثان .Mansoor, and Dawood, 2013, والباحث .Kaviany, 1985, كما في الشكل (5(b)) . كذلك فإن الحصول على مخطط توزيع قيم عدد نسلت الموضوعي (الشكل (6)) خلال قناة مستوية وعلى السطحين العلوي والسفلي وفيه استقرت قيمة عدد نسلت عند 4.93 تقريباً وهي القيمة التي ذكرها بيجان .Bejan,1983, وهذا التحقيق لحساب قيم عدد نسلت يعطي البرنامج الموثوقية اللازمة للحصول على نتائج الدراسة الحالية ، إذ إن صحة نتائج عدد نسلت الموضوعي تؤكد صحة تمثيل معادلات الزخم والطاقة مجتمعة .

النتائج و المناقشة

تأثير عدد دارسي في جريان المائع وانتقال الحرارة

يمثل عدد دارسي النسبة بين نفاذية المادة المسامية (K) إلى مربع ارتفاع القناة (H) أو ما يعرف بـ (Characteristic length scale) ويعطي مؤشر لوجود أو عدم وجود المادة المسامية و كذلك يُعطي مؤشراً أيضاً لكثافة المادة المسامية داخل الحيز ؛ فإن كان مقداره كبيراً دلّ على قلة المادة المسامية وبالعكس ، أما تأثيره على شكل مركبة السرعة داخل القناة فيكون واضح جداً كما في الشكل (7) إذ إنه لقيم عدد دارسي العالية تكون مركبة السرعة الاقضية ذات سرعة عالية في منتصف القناة ثم بنقصان قيمة عدد دارسي تقل مركبة السرعة في منتصف القناة مع زيادة ملحوظة لقيمة السرعة قرب الجدار ، والسبب هو ان عدد دارسي العالي دليل على قلة المادة المسامية وبالتالي فإن نمو الطبقة المتاخمة يأخذ مسافة معينة حتى يكتمل، مع تلاشي إجهاد القص في منتصف القناة فتأخذ السرعة شكلها المغزلي، أما في حالة عدد دارسي القليل والقليل جداً فإن الوجود الكثيف للمادة المسامية يعيق حركة المائع ويجعله يأخذ شكل منتظم مع تلاشي تكون الطبقة المتاخمة وهذا الامر ضروري جداً إذ إن زيادة مركبة السرعة قرب الجدار يعني زيادة انتقال الحرارة بالحمل وهو الغرض المنشود من الدراسة الحالية . أما في الشكل (8) فيلاحظ ان نقصان عدد دارسي (زيادة كثافة المادة المسامية) يؤدي إلى كبح خطوط ثبوت درجة الحرارة ودفعها جانباً وهذا الامر ضروري جداً إذ أنه كلما قل ميل خطوط ثبوت درجة زاد معامل انتقال الحرارة وبالتالي زاد عدد نسلت وكمية الحرارة المنتقلة .

تأثير تغيير أنصاف اقطار المقاطع النصف دائرية في جريان المائع وانتقال الحرارة

من الشكل (9) يلاحظ ان زيادة نصف قطر المقطع أدى إلى زيادة مركبة السرعة عند مناطق التخصر وذلك بسبب نقصان مقطع مساحة التدفق وطبقاً لمعادلة حفظ الكتلة فإن أي نقصان في مساحة المقطع تقابلها زيادة في سرعة جريان المائع للحصول على قيمة تدفق ثابتة . أما فيما يخص اشكال خطوط دالة الانسياب (11)(12)(13) فيلاحظ ان كثافة تلك الخطوط تتبع تغيير نصف قطر المقطع نصف الدائري وتأخذ تعجيل أنه مع نقصان المقطع تزداد السرعة وزيادة السرعة يعني دمج وتكاثف خطوط الانسياب في تلك المنطقة. أما تأثير نصف القطر في انتقال الحرارة فيلاحظ أن زيادة نصف القطر (زيادة مساحة المصدر الحراري) تؤدي إلى زيادة في كمية الحرارة المنتقلة ويلاحظ ذلك من خلال الوان الطيف المائل إلى الاحمرار وهذا يعني إن المائع في حالة زيادة نصف القطر يمتص كمية حرارة أكبر وكما يلاحظ في الشكل (10) والسبب هو زيادة نشاط تيارات الحمل في هذه الحالة وهذه الزيادة في نشاط تيارات الحمل يعبر عنها فيزيائياً بزيادة عدد نسلت أي بمعنى زيادة معدل انتقال الحرارة .

تأثير تغيير المسافة بين أنصاف اقطار المقاطع في جريان المائع وانتقال الحرارة

تؤثر المسافة بين مركزي انصاف اقطار المقاطع النصف دائرية في جريان المائع وانتقال الحرارة ويلاحظ ذلك أولاً من خلال خطوط دالة الانسياب إذ يلاحظ أنه عندما تكون المسافة بين المراكز ($P=3r$) فإن خطوط دالة الانسياب تكون بعيدة عن الجدار (بين المقطعين) وهذا مؤشر واضح على نقصان السرعة في تلك المنطقة والسبب يعود إلى حالة الركود التي يعاني منها المائع في تلك المنطقة ، أما مع زيادة المسافة فإن المائع يبدأ بالحركة ويبدو ذلك جلياً من خلال أشكال خطوط دالة الانسياب كما في الأشكال (11)(12)(13) وهذا الحالة مهمة جداً في عملية انتقال الحرارة . كما يلاحظ من خلال الشكل (14) أن توزيع أعداد نسلت على المقطع الأول أكثر منه على المقطع الثاني وذلك بسبب الفرق الكبير في درجات الحرارة بين السطح الساخن والمائع فضلاً عن نشاط تيارات الحمل بشكل كبير على المقطع الأول وأقل منه على المقطع الثاني خاصة عندما تكون المسافة ($P=3r$) لان هذه المسافة تجعل المقطع الثاني يقع في منطقة انفصال خطوط الانسياب خلف المقطع الأول فيكون نشاط تيارات الحمل أقل على المقطع الثاني ، لكن هذا النشاط لتيارات الحمل على المقطع الثاني يزداد مع زيادة المسافة بين المقطعين . أما تأثير المسافة في انتقال الحرارة فيلاحظ من خلال الاشكال (15) انه بثبوت نصف القطر وعدد رينولدز فإن زيادة المسافة تؤدي إلى دفع خطوط ثبوت درجة الحرارة والسبب يعود إلى أنه مع زيادة المسافة فإن المائع المار على المقطع الأول يمتص كمية من الحرارة ثم يمتزج مع المائع الذي مر دون المقطع ولم يكتسب حرارة فيفقد المائع الساخن كمية من حرارته ثم يمرره مرة اخرى على المقطع الثاني يكتسب كمية إضافية من الحرارة ، أما في حالة المسافة القليلة ($P=3r$) فإن المائع بعد أن أكتسب كمية من الحرارة من المقطع الأول لا تكون له فرصة الامتزاج بمائع غير ساخن نتيجة قصر المسافة بين المصدرين الحراريين فيمر مباشرة بالمقطع الثاني لكنه لا يكتسب كمية حرارة إضافية كبيرة لان درجة حرارة عالية نسبياً ومن المعلوم أن المائع الساخن يكتسب حرارة إضافية قليلة . كما يلاحظ من خلال الاشكال (16)(17)(18) فإن زيادة عدد رينولدز بثبوت انصاف اقطار المقاطع والمسافة فيما بينها يؤدي الى زيادة عدد نسلت وبالتالي زيادة في انتقال الحرارة .

الاستنتاجات

- 1 - تؤدي زيادة عدد رينولدز إلى زيادة في انتقال الحرارة من خلال زيادة معدل أعداد نسلت على المقاطع نصف الدائرية
- 2 - يؤدي تقليل عدد دارسي بشكل كبير إلى انتظام مركبة سرعة جريان المائع داخل القناة مع تلاشي تكون الطبقة المتاخمة الهيدروليكية ، فضلاً عن كبح خطوط ثبوت درجة الحرارة ودفعها باتجاه السطح.
- 3 - إن قيم كل من نصف قطر المقطع ($r = 0.75H$) والمسافة بين مركزي المقاطع ($P=9r$) تمثل القيم المثلى من بين القيم التي درست وعند جميع قيم أعداد رينولدز .
- 4 - يلعب تغيير نصف قطر المقطع الدور البارز في جريان المائع وانتقال الحرارة أكثر من تغيير عاملي المسافة بين المقاطع أو تغيير عدد رينولدز .
- 5 - إن وجود المادة المسامية بشكل كثيف داخل القناة قد منع حدوث ظاهرتي الانفصال وتكون الدوامات .

References

المصادر

- Jiji L. M., 2006, *Heat Convection*, Third Edition, Springer-Verlag, Inc., Berlin Heidelberg, Netherland.
- Heidary H.,and Kermani M. J.,2012, *Enhancement of Heat Exchanger in a Wavy Channel Liked to a Porous Domain ; a Possible Duct Geometry for Fuel Cells*, Int. Communications in Heat and Mass Transfer, Vol,39, PP. 112-120.
- Bejan A.,and Kraus A. D., 2003, *Heat Transfer Handbook*, John Wiley and Sons, Inc., Hoboken, New Jersey, USA.
- Nakayama A., Koyama H.,and Hamamats J.L.,1988, *An Analysis on Forced Convection in a Channel Filled with a Brinkman-Darcy Porous-Medium: Exact and Approximate Solutions*, *Warme-und Stoffubertragung*, Vol.23, 291-295.
- Kaviany M.,1985, *Laminar Flow through a Porous Channel Bounded by Isothermal Parallel Plates*, Int. J. Heat Mass Transfer, Vol. 28, No. 4, PP.851-858.
- Kim S. Y., Kang B. H.,and Kim J.-H.,2001, *Forced Convection from Aluminum Foam Materials in an Asymmetrically Heated Channel*, Int. J. Heat Mass Transfer,Vol.44, PP. 1451-1454.
- Mansoor F.S., Dawood A. S.,2013, *Numerical Investigation of Heat Transfer and Fluid Flow Characteristics inside Wavy Channels Fully Filled with Porous Medium*, Canadian Center of Science and Education, Vol.3, No.2.13-27.
- Al-Sammarai A.T.,1999, *An Experimental Study on Forced Convection Heat Transfer From a Heated Cylinder in Free And Embedded Horizontal Cylinders Array in a Porous Medium in Cross Flow*, M.sc Thesis , Tikrit University.

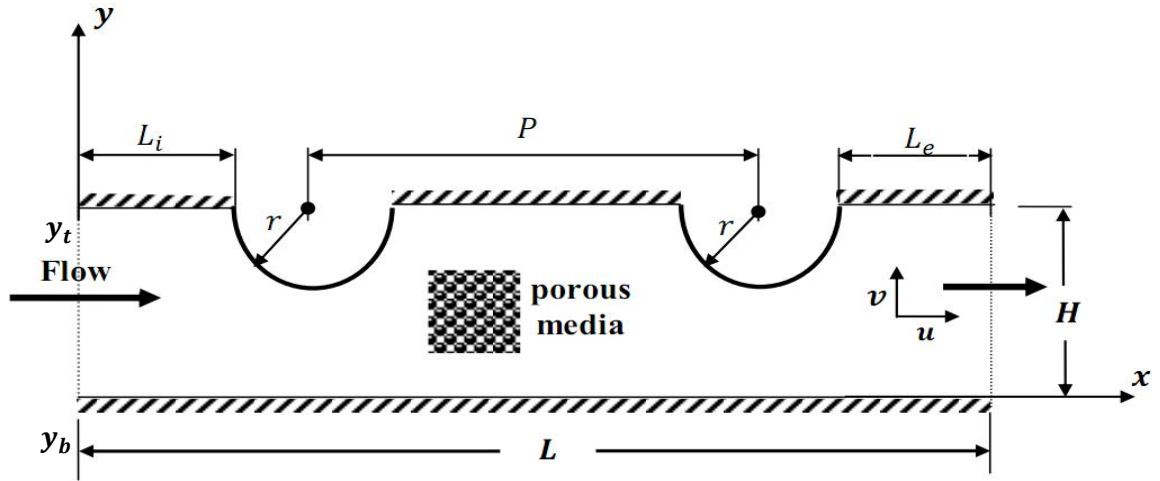


- Hadim H., North M.,2005, *Forced Convection in a Sintered Porous Channel with Inlet and Outlet Slots*, Int. J. Thermal Sciences, Vol.44, PP.33-42.
- Bejan A.,1983, *Natural Convection Heat Transfer in a Porous Layer with Internal Flow Obstructions* ,Int.J. Heat Mass Transfer Vol.26, No.6, PP.815-822.
- Chapra,S.C.,Canale,R.P.2002,*Numerical Methods for Engineers*, McGraw-Hill, USA.
- Fletcher C. A. J., 1988, *Computational Techniques for Fluid Dynamics 2*, Springer-Verlag Berlin Heidelberg, USA.

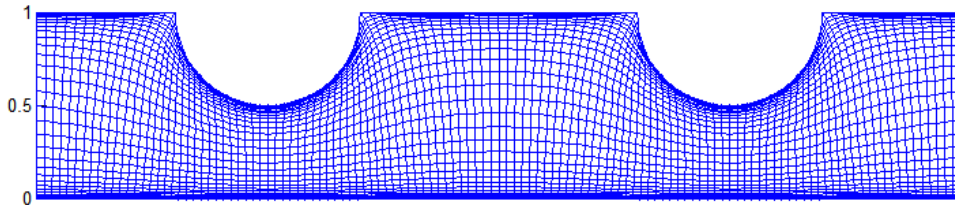
الرموز

الوحدة	تعريفه	الرمز
J/kg. K	الحرارة النوعية بثبوت الضغط	C_p
—	عدد دارسي $K/H^2 =$	Da
—	معامل فروكهايمر $= 1.75/\sqrt{150\phi^3}$	F
m	ارتفاع المجرى (القناة)	H
W/m ² . K	معامل انتقال الحرارة بالحمل	h_c
W/m. K	الموصلية الحرارية	k
m ²	نفاذية المادة المسامية	K
—	عدد نسلت الموضعي	Nu_x
—	معدل عدد نسلت $= h_c H / k_f$	\overline{Nu}
Pa(N/m ²)	الضغط	p
m	البعد بين مركزي المقاطع نصف الدائرية	P
—	عدد برانتل $= \mu_f \cdot C_{p_f} / k_f$	Pr
—	عدد رينولدز $= u \cdot H / \nu$	Re
K	درجة الحرارة	T
—	درجة الحرارة اللابعدية	T^*
m/s	مركبة السرعة في الاتجاه الأفقي	u
m/s	سرعة المائع الداخل إلى القناة	u_0
m/s	مركبة السرعة في الاتجاه العمودي	v
—	مركبة السرعة اللابعدية في الاتجاه الأفقي	u^*
—	مركبة السرعة اللابعدية في الاتجاه العمودي	v^*

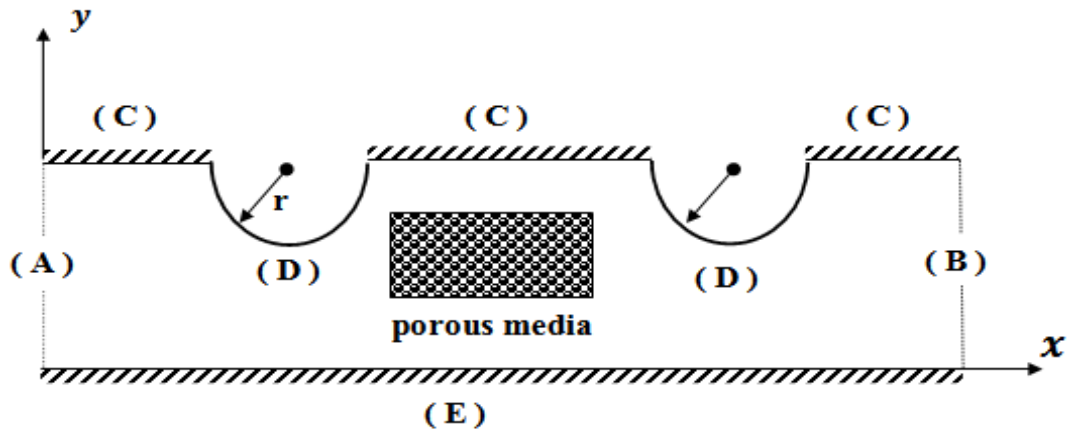
m/s	محصلة السرعة في الاتجاهين الأفقي والعمودي	$/V/$
الرموز الاغريقية		
m^2/s	الانتشارية الحرارية	α
$kg/m.s$	اللزوجة الديناميكية	μ
m^2/s	اللزوجة الكينيمائية	ν
—	المحوران الأفقي والعمودي في المستوي الحسابي	ξ, η
kg/m^3	الكثافة	ρ
—	المسامية	ϕ
m^2/s	دالة الانسياب	ψ
$1/s$	دالة الدوامة $-\nabla^2\psi = \omega$	ω
الرموز العلوية والسفلية		
—	معظم (bulk)	b
—	مائع	f
—	لأبعدي	*
—	علوي	t
—	سفلي	b



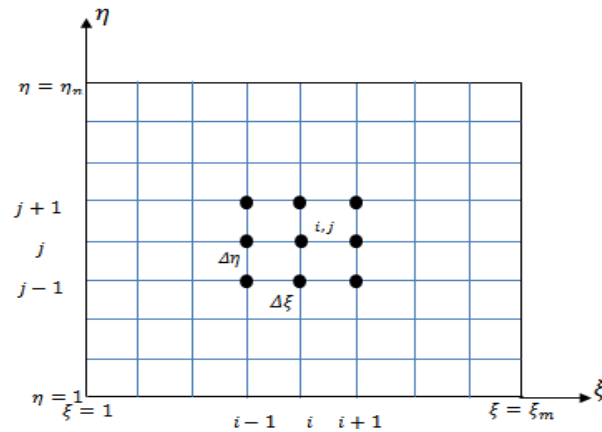
الشكل (1) : يوضح الانموذج الفيزيائي للمسألة.



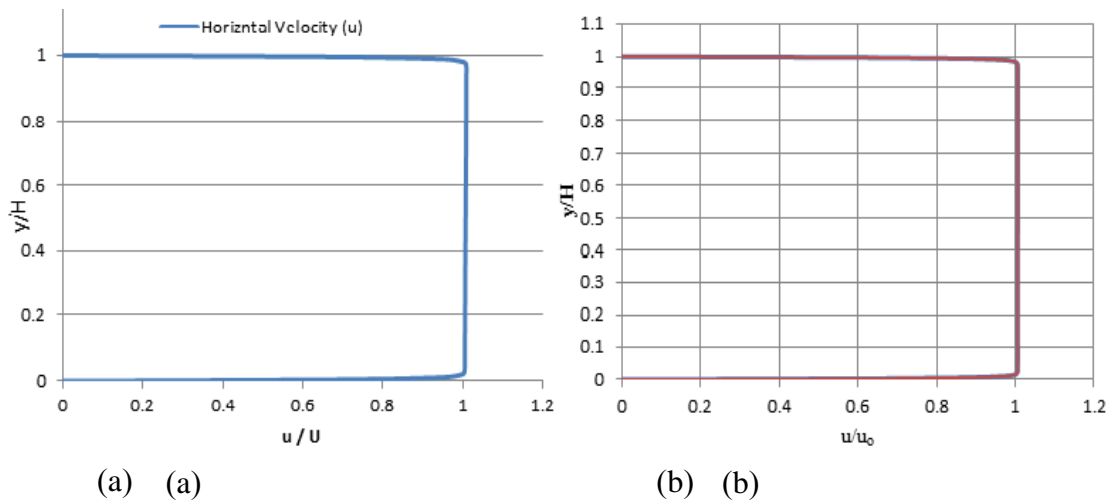
الشكل (2) : يوضح الشبكة المولدة داخل الحيز باستخدام معادلات بوزن التفاضلية.



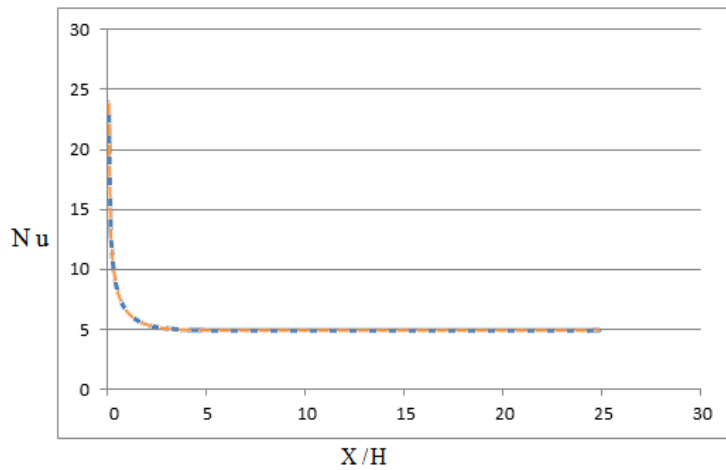
الشكل (3) : يمثل مناطق توزيع الشروط الحدية للمسألة.



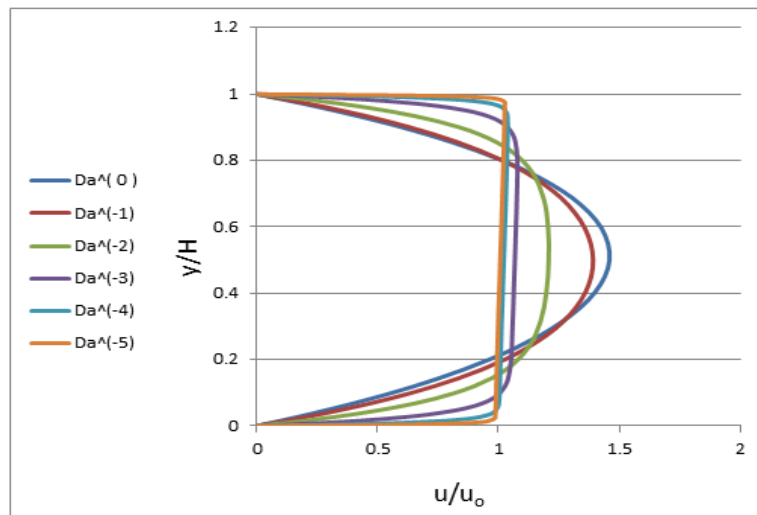
الشكل (4) : يوضح النقاط العقدية المستخدمة في التحليل العددي.



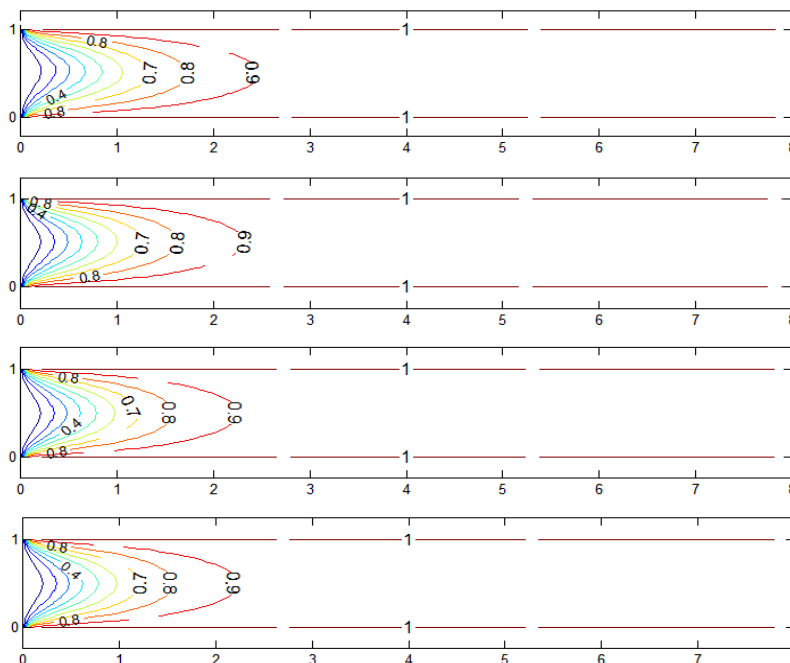
الشكل (5) : مقارنة مخطط توزيع السرعة داخل قناة مستوية الذي تم الحصول عليه من الدراسة الحالية (a) مع ما توصل إليه الباحثان Mansoor and Dawood, 2013 والباحث Kaviany, 1985 كما في الشكل (b).



الشكل(6): قيم عدد نسلت الموضعي على السطحين العلوي والسفلي على طول قناة مستوية عندما عدد رينولدز $Re=100$.

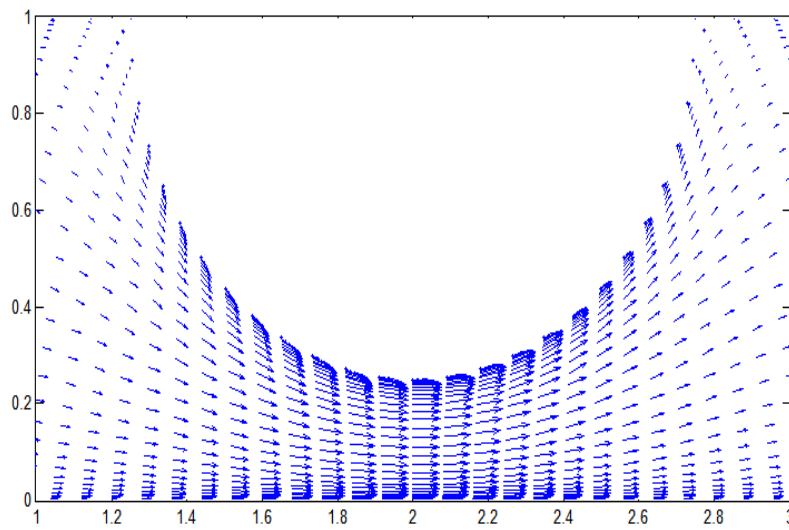
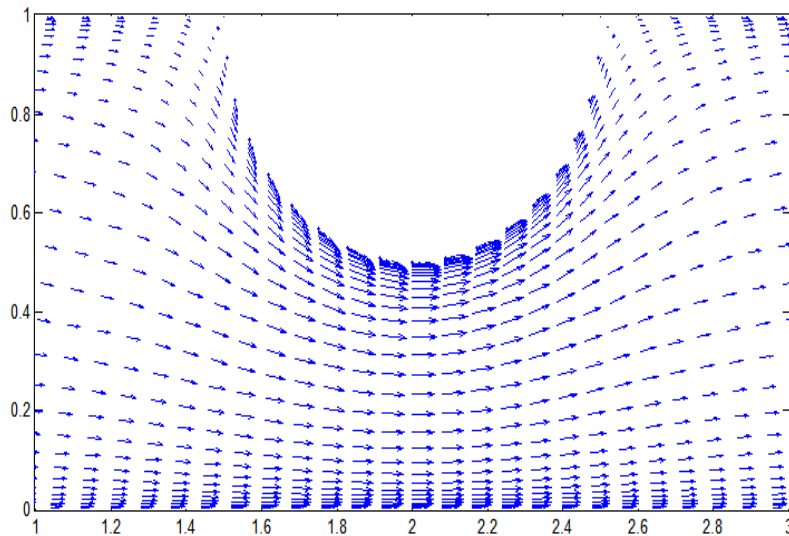
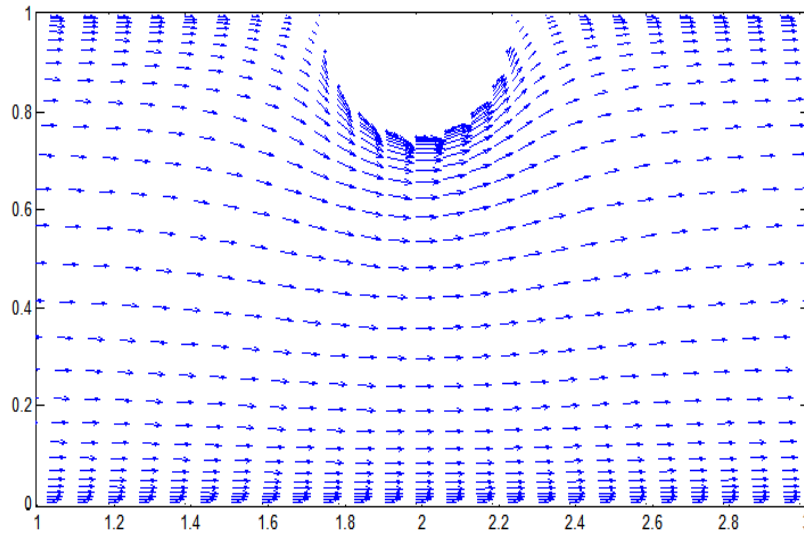


الشكل (7): شكل مركبة السرعة في الاتجاه الأفقي على طول المحور العمودي ولقيم مختلفة من عدد دارسي داخل قناة مستوية الجريان فيها مكتمل النمو.

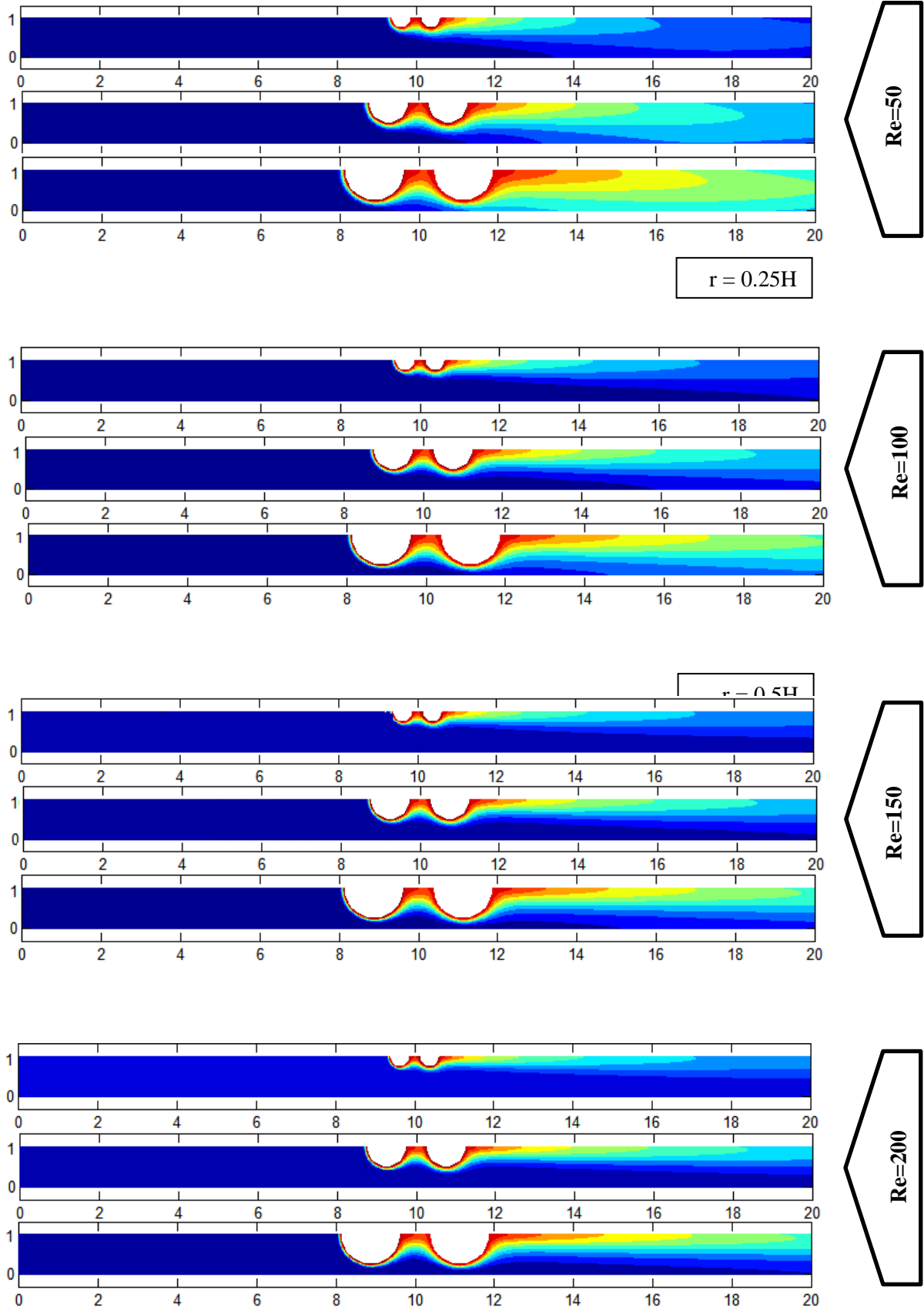




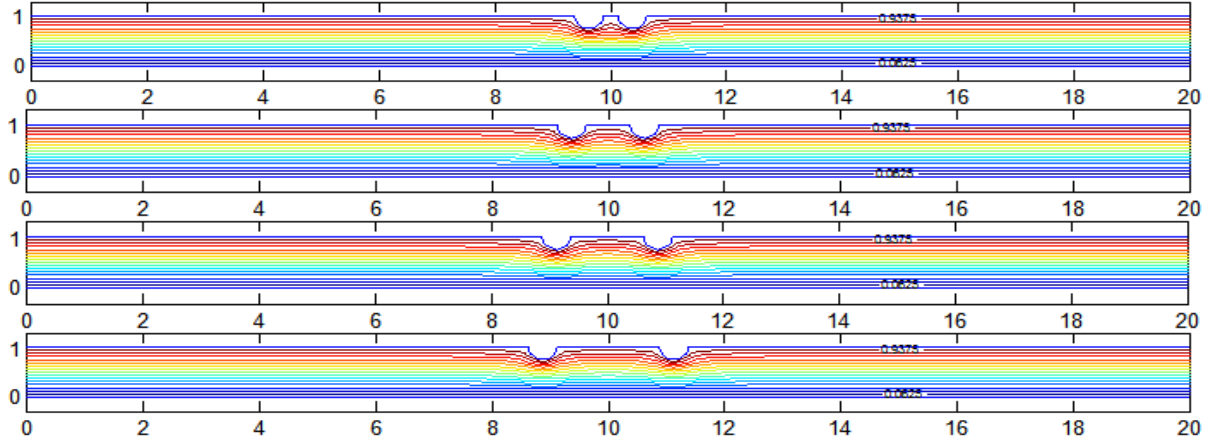
الشكل (8) : توزيع خطوط ثبوت درجات الحرارة داخل قناة مستوية عندما تكون قيم كل من عدد رينولدز والمسامية $Da = (10^{-2}, 10^{-3}, 10^{-4}, 10^{-5})$ ولقيم مختلفة من أعداد دارسي ($Re = 10, \phi = 0.9$)



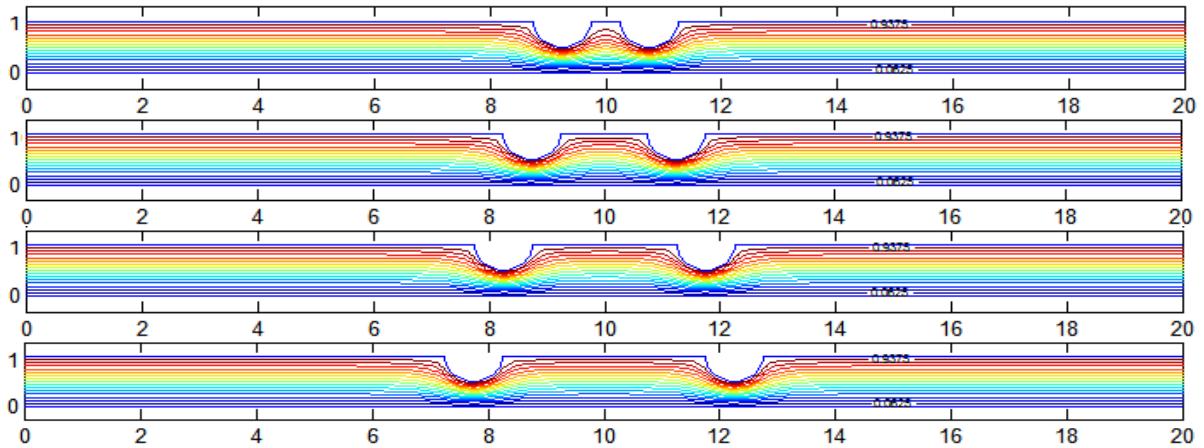
الشكل (9) : مقاطع توضح متجهات السرعة لحظة مرور المائع في مناطق التخصر عند $Re=50$ ولانصاف اقطار مختلفة $(r = 0.25H, 0.5H, 0.75H)$.



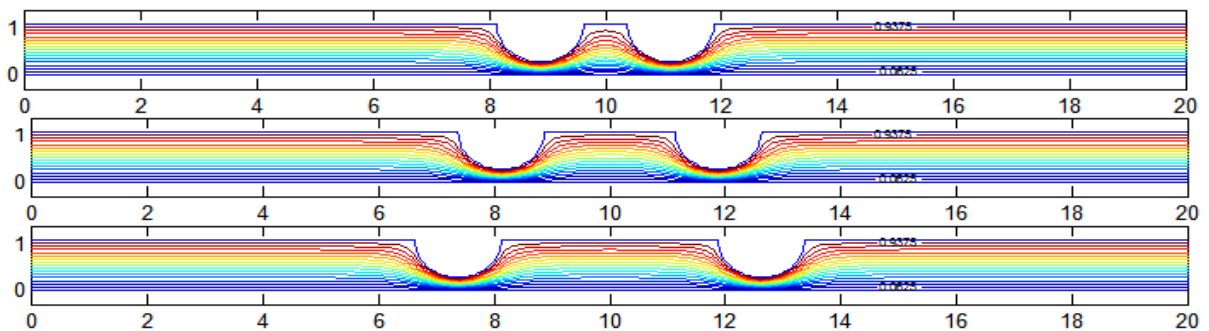
الشكل (10) : خطوط ثبوت الحرارة عند $r = 0.25H, 0.5H, 0.75H$ وعندما تكون المسافة فيما بين المقاطع نصف الدائرية $P = 3r$ ولقيم مختلفة من أعداد رينولدز.



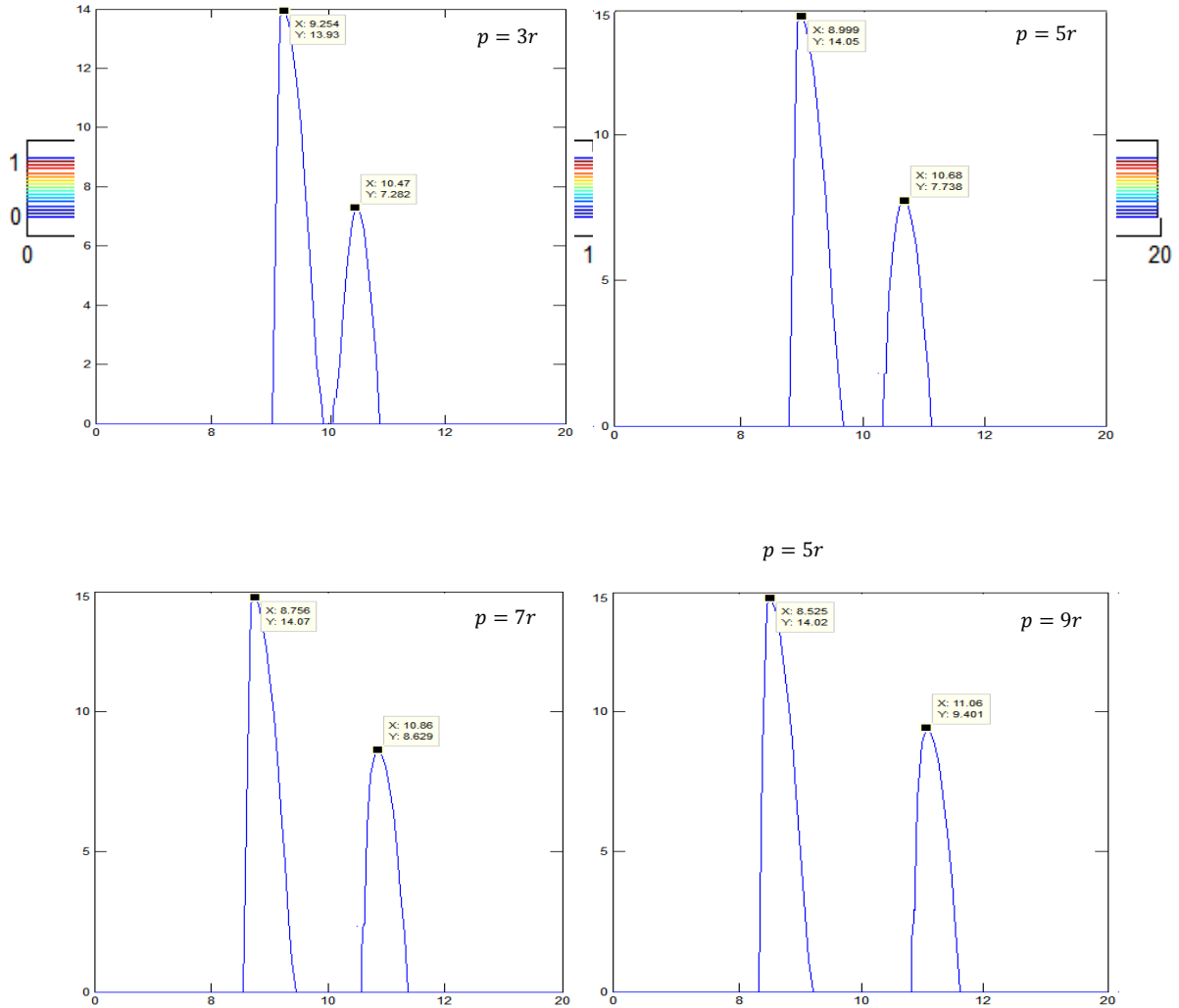
الشكل(11):خطوط دالة الانسياب للمائع عند $Re = 50, r = 0.25H$ ولقيم مختلفة من المسافة فيما بين المقاطع النصف دائرية .



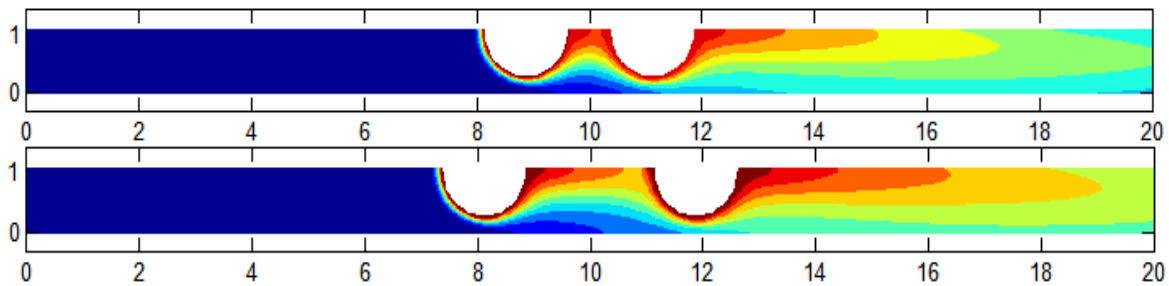
الشكل(12):خطوط دالة الانسياب للمائع عند $Re = 50, r = 0.5H$ ولقيم مختلفة من المسافة فيما بين المقاطع النصف دائرية .



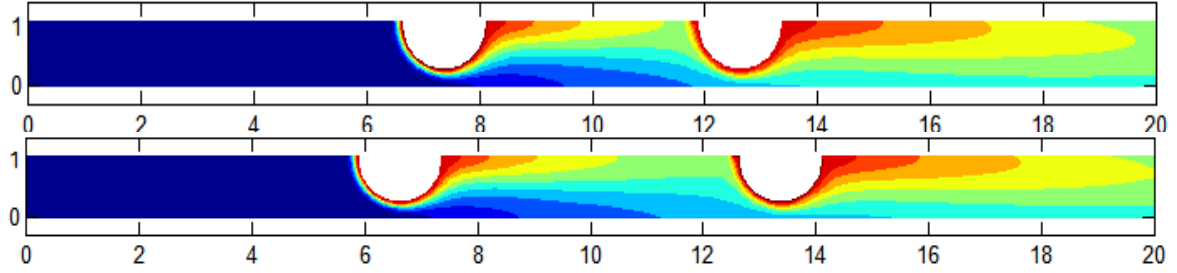
الشكل (13): خطوط دالة الانسياب للمائع عند $Re = 50, r = 0.75H$ ولقيم مختلفة من المسافة فيما بين المقاطع النصف دائرية .

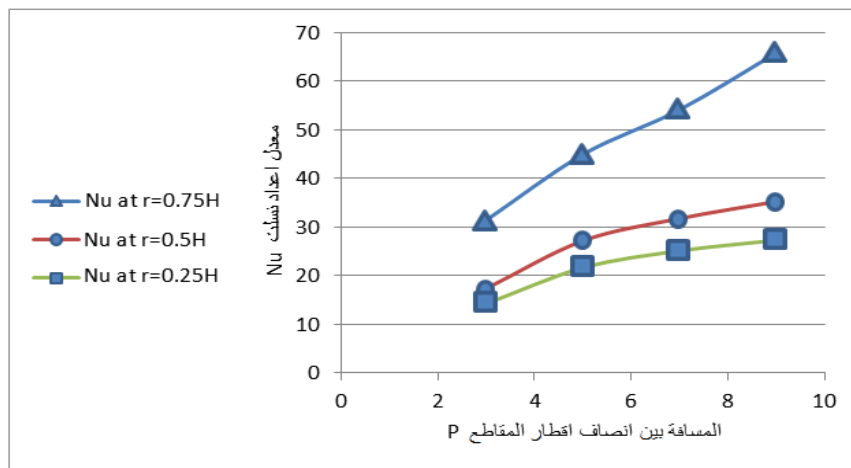


الشكل (14) : توزيع قيم عدد نسلت الموضعي على المقاطع النصف دائرية عند $(r = 0.25H, Re = 50)$ ولأربع قيم مختلفة من المسافة بين مركزي هذه المقاطع .

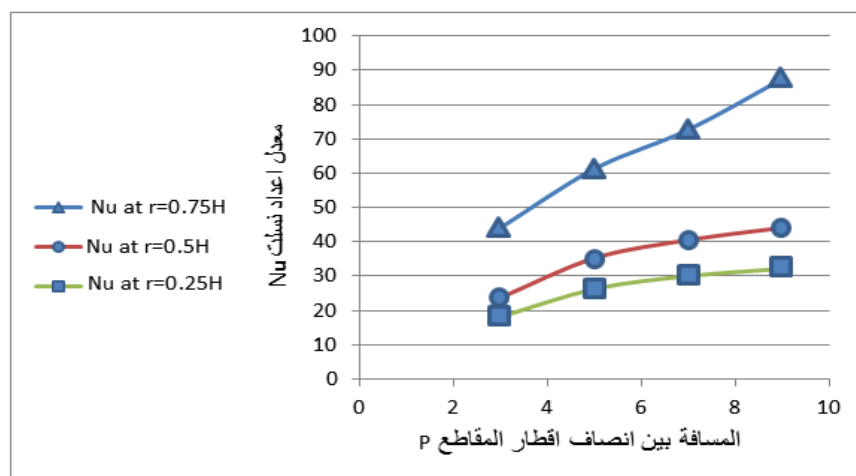


الشكل (15) : خطوط ثبوت درجات الحرارة عند $Re = 50, r = 0.75H$ ولقيم مختلفة من المسافة فيما بين المقاطع النصف دائرية .

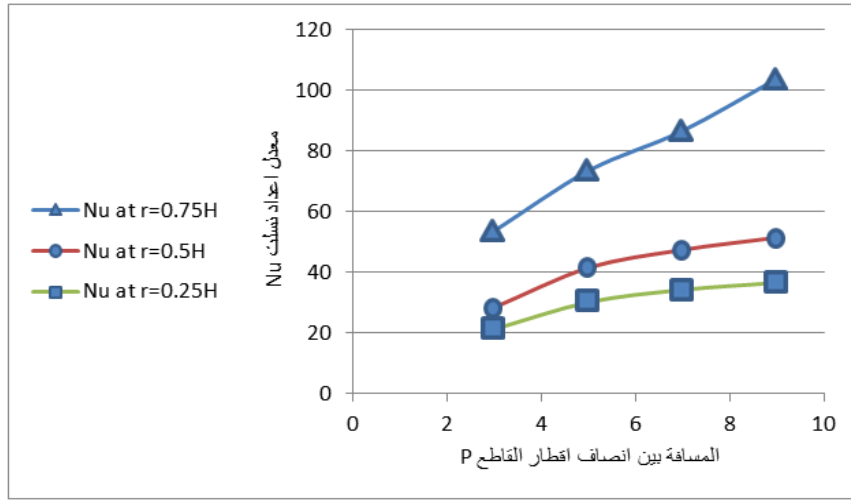




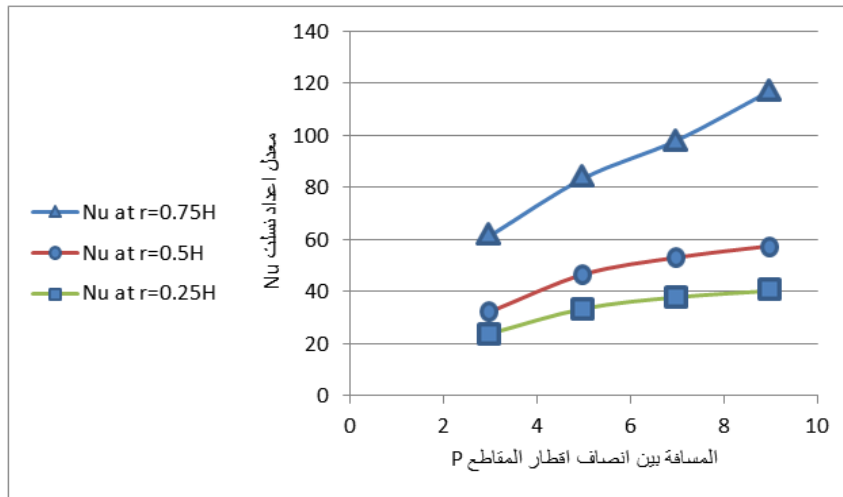
الشكل (16) : معدل اعداد نسلت لقيمة انصاف اقطار مختلفة وعند مسافات مختلفة بين المقاطع وفي حالة عدد رينولدز $Re=50$



الشكل (17) : معدل اعداد نسلت لقيمة انصاف اقطار مختلفة وعند مسافات مختلفة بين المقاطع وفي حالة عدد رينولدز $Re=100$



الشكل (18) : معدل اعداد نسلت لقيمة انصاف اقطار مختلفة وعند مسافات مختلفة بين المقاطع وفي حالة عدد رينولدز $Re=150$



الشكل (19) : معدل اعداد نسلت لقيمة انصاف اقطار مختلفة وعند مسافات مختلفة بين المقاطع وفي حالة عدد رينولدز $Re=200$

الجدول (1) : يبين أفضل مسافة (P) بين المقاطع نصف الدائرية التي أعطت أفضل أداء حراري للمصدر الأول والثاني ؛ عند قيم أعداد رينولدز مختلفة .

	$r = 0.25H$	$r = 0.5H$	$r = 0.75H$
$Re = 50$	$P=7r$	$P=5r$	$P=9r$
$Re = 100$	$P=5r$	$P=5r \text{ \& } 7r$	$P=9r$
$Re = 150$	$P=9r$	$P=5r$	$P=7r$
$Re = 200$	$P=9r$	$P=7r$	$P=7r$



الجدول (2) : يبين أفضل مسافة (P) بين المقاطع نصف الدائرية التي أعطت أفضل أداء حراري للمصدر الحراري الثاني ؛ عند قيم أعداد رينولدز مختلفة

	$r = 0.25H$	$r = 0.5H$	$r = 0.75H$
$Re = 50$	$P=9r$	$P=9r$	$P=9r$
$Re = 100$	$P=9r$	$P=9r$	$P=9r$
$Re = 150$	$P=9r$	$P=9r$	$P=9r$
$Re = 200$	$P=9r$	$P=9r$	$P=9r$